Advanced BEM-based methodologies to identify and simulate wave fields in complex geostructures

DISSERTATION

zur Erlangung des Doktorgrades
"Dr.-Ing."
der Mathematisch-Naturwissenschaftlichen Fakultät
der Christian-Albrechts-Universität zu Kiel

Vorgelegt von
Min Bahadur Basnet

Kiel, 2023

Gutachter:

1. Prof. Dr.-Ing. habil Frank Wuttke
   Kiel University
2. Prof. Dr. Petia S. Dineva
   Bulgarian Academy of Sciences

Tag der mündlichen Prüfung: 16.02.2023
Zum Druck genehmigt: 28.02.2023

Der Dekan

I would like to dedicate this thesis to my loving parents ...

Eidesstattliche Erklärung

Hiermit versichere ich eidesstattlich, dass die vorliegende Arbeit, abgesehen von der Beratung durch den Betreuer, nach Inhalt und Form selbstständig und ohne unzulässige Hilfsmittel von mir angefertigt wurde. Die vorliegende Arbeit hat weder in Teilen noch im Ganzen an anderer Stelle im Rahmen eines Prüfungsverfahrens vorgelegen und wurde nicht veröffentlicht oder zur Veröffentlichung eingereicht. Weiterhin versichere ich, dass die Arbeit unter Einhaltung der Regeln guter wissenschaftlicher Praxis der Deutschen Forschungsgemeinschaft angefertigt wurde. Dies ist mein erster Promotionsversuch. Mir wurde kein akademischer Grad entzogen.

Kiel, 13.12.2022 Min Bahadur Basnet

Vorwort des Herausgebers

Die vorliegende Promotionsschrift von Herrn Dr.-Ing. Min Bahadur Basnet ist dem Forschungs- und Arbeitsgebiet „Bodendynamik“ und der „Erdbebeningenieurwesen“ zuzuordnen. In dieser Dissertation wurden neue Modelle zur Beschreibung und Identifizierung von elastischen Wellenfeldern in der Ebene in homogenen oder natürlich inhomogenen Medien mit unterschiedlichen Arten von Heterogenitäten für die Nutzung in der Randelemente-Methodik entwickelt. Dazu wurde die Wellenausbreitung in inhomogenen und heterogenen Halbraum im Frequenz- und Zeitbereich weiterentwickelt, verifiziert und implementiert. Insbesondere wurden inverse Methoden mit der Boundary- Element-Methode unter Verwendung hybrider globaler Optimierungsmethoden als auch hybride BEM-Finite-Elemente-Methodenmodell basierend auf dem Makro-Finite-Elemente-Konzept grundlegend weiterentwickelt. Zur Umsetzung der benannten Modelle, wird ein verschiebungsbasiertes BEM-Modell für die P-SV-Wellenausbreitung in einer homogenen elastischen isotropen Halbebene genutzt. Für die Identifikation der Heterogenitäten wurde eine vollständige Wellenforminversion im Frequenzbereich entwickelt und verifiziert. Dabei erfolgte die Identifikation der inhomogenen Strukturen basierend auf Grenzintegralgleichungen (BIE) für den homogenen, elastischen, isotropen Halbraum anstelle der Fundamentlösungen. Die Optimierung und Bestimmung der Variablen in den BIEs basierend auf den seismischen Daten am Standort, erfolgte durch ein hybrides Partikel-Schwarm-Gradienten-Verfahren. Dieses hybride BEM-PSO-Modell verbessert die Effizienz des BEM für die Ausbreitung seismischer Wellen in beliebig inhomogenen und heterogenen Medien unter Verwendung eines BEM-Modells mit stark reduzierten Freiheitsgraden. Für die Lösung und Verbesserung der numerischen Effizienz, erfolgte die Inversion durch CPU- und GPU-parallelisierte Rechenprozesse, welche im Rahmen der Arbeit erstellt wurden. Die Dissertationsschrift beinhaltet die konsequente Weiterentwicklung, Kopplung von bisherigen Ansätzen und Neuentwicklung von Modellen in Anwendbarkeit von BEM zur bodendynamischer Simulationen und Identifikationen in heterogenen Halbräumen durch die Verwendung von numerischer Optimierung, FEM-BEM-gekoppelten Modellen und der Verbesserung der Recheneffizienz von FWI durch parallele Berechnung in der GPU.

Kiel, im Dezember 2022 Frank Wuttke

Acknowledgements

I would like to use this opportunity to gratefully acknowledge those who have directly or indirectly supported me while working on my thesis.

First and foremost, I would like to express my deep gratitude and sincere appreciation to my supervisor Prof. Dr.-Ing. habil Frank Wuttke for providing me with an environment from which my scientific development greatly benefited. His valuable input and scientific guidance through many fruitful discussions was decisive factor in completing this thesis. Also, I would like to express my deep gratitude and sincere appreciation to my second supervisor Prof. Dr. Petia S. Dineva for providing valuable knowledge and guidance throughout the development of this thesis. Without her guidance, remarks, and motivation, the dissertation would not have been completed to this level. I would like to express my sincere gratitude towards the chairperson of the examination committee Prof. Dr. Sebastian Bauer and the other members of the committee Prof. Dr. rer. nat. Thomas Meier and Prof. Dr.-Ing. Ludger Klinkenbusch for agreeing to be on the committee and for their encouraging remarks.

Also, I would like to express my gratitude to my colleagues at Kiel University, especially Dr.-Ing. Zargham H. Rizvi for his always encouraging advice and support in academic, professional, and personal matters throughout the years. My special gratitude to Binod, Dinesh, Henok, Hem, Hendrawan, Amir, Aycan, Shadi, Hao, and Nils for their valuable assistance and scientific discussions during my research. I would also like to thank Mr. Robin Stechert for his sincere technical support in the laboratory. I would also like to thank Mrs. Nadja Glenewinkel, Mrs. Gesa Koberg, and Dr. Miriam Tanhua for their valuable administrative support during my study and the process of defense.

I would also like to express my gratitude to the officers in the Nepalese Army, especially Lt.Col. Sanjaya, Major Nishant, and my batchmates, for their valuable suggestions and support during my serpentine journey of scientific research. I am grateful to my friends from Bauhaus Universität-Weimar, specially Sheelu, Bigyan, and Kamal, for their continuous support and motivation during my study. Finally, I would like to thank all my family members and friends. I owe great debt and gratitude to my parents, wife Prava, my daughter Aavya, and my son Aaryav for their endless love, patience, and continuous support throughout my journey.

Abstract

The primary purpose of this study is to propose mechanical models describing in-plane elastic wave propagation in homogeneous or naturally inhomogeneous media with different types of heterogeneities. With this aim, the following computational tools for P-SV wave propagation in inhomogeneous and heterogeneous half-plane are developed in frequency domain, verified, and inserted in detail simulation: ***(a)*** inverse computational technique by Boundary Element Method (BEM) using Particle Swarm Optimization (PSO); ***(b)*** hybrid BEM-Finite Element Method (FEM) model based on macro-finite element concept. To develop these models, a pure displacement BEM model for P-SV wave propagation in homogeneous elastic isotropic half-plane, and seismic Full Waveform Inversion (FWI) by Finite Difference Method (FDM) in frequency domain are developed and verified. Additionally, the enhancement of computational efficiency of FWI for P-SV waves in time domain by parallel computation using Central Processing Unit (CPU) and Graphics Processing Unit (GPU) is studied.

Inverse modeling of seismic wave propagation in inhomogeneous and heterogeneous half-plane is implemented in BEM using PSO. The Boundary Integral Equation (BIE)s based on the fundamental solutions for homogeneous elastic isotropic continuum are modified by assuming the variable Lame parameters and density over each node-element pair in the BEM mesh. PSO is implemented to compute the variables in the BIEs based on the seismic measurement data. The BIEs with the computed variables are used to calculate the site-dependent impedance functions. This hybrid BEM-PSO model improves the efficiency of the BEM for seismic wave propagation in arbitrarily inhomogeneous and heterogeneous media using a BEM model with strongly reduced Degrees of Freedom (DOFs).

A hybrid BEM-FEM approach is developed for the evaluation of the seismic response of a complex poroelastic soil region containing an underground structure. The domain under consideration is divided into far-field and near-field regions. The far-field semi-infinite geological region is modeled via BEM, and the near-field finite geological region by FEM. The BEM influence matrices are converted into equivalent stiffness and damping matrices, which are directly coupled to the global FEM stiffness and damping matrices using macro-finite-element concept. The main contribution of this model is the capability to describe the entire wave path from the seismic source to the local site under consideration in one model.

The parallel computation of seismic FWI algorithms by CUDA C in GPU shows a performance gain of up to 90 times the serial execution. In summary, the thesis shows a way forward for the enhancement in the applicability of BEM for geomechanical modeling by using numerical optimization, FEM-BEM coupled models and the improvement in computational efficiency of FWI by parallel computation in GPU.

Zusammenfassung

Das Ziel der Dissertationsarbeit besteht im wesentlichen in der Neuentwicklung von Modellen, welche die Ausbreitung elastischer Wellen in der Ebene in homogenen oder natürlich inhomogenen Medien mit unterschiedlichen Arten von Heterogenitäten mit Hilfe der BEM erlauben. Für dieses Ziel werden weiterführende Berechnungswerkzeuge in der P-SV-Wellenausbreitung für inhomogene und heterogene Halbräume im Frequenzbereich entwickelt, verifiziert und in Detailsimulationen implementiert: ***(a)*** inverse Berechnungstechnik durch Randelementmethode (BEM) unter Verwendung der Particle Schwarmoptimierung (PSO); ***(b)*** hybrides BEM-FEM-Modell basierend auf dem Makro-Finite-Elemente-Konzept. Zur Entwicklung dieser Modelle werden ein Verschiebungs-BE-Modell zur P-SV-Wellenausbreitung in einer homogenen elastischen isotropen Halbebene und ein seismisches FWI durch FDM im Frequenzbereich entwickelt und verifiziert. Zusätzlich wird eine High-Performance-Simulation der FWI für P-SV-Wellen im Zeitbereich durch eine Code-Erweiterung für eine parallele Berechnung mit CPU und GPU implementiert.

Inverse Modellierung der Ausbreitung seismischer Wellen in inhomogenen und heterogenen Halbebenen in BEM wurde durch PSO implementiert. Die BIEs, basierend auf den Fundamentallösungen für das homogene elastische isotrope Kontinuum, wurden so modifiziert, dass die variablen Lame-Parameter und die Dichte über jedem Knoten-Element-Paar im BEM-Netz angenommen werden können. Die PSO wurde implementiert, um die Variablen in den BIEs basierend auf den seismischen Daten am Standort zu berechnen. Die BIEs mit den berechneten Größen werden zur Berechnung der standortabhängigen Impedanzfunktionen verwendet. Dieses hybride BEM-PSO-Modell verbessert die Effizienz des BEM für die Ausbreitung seismischer Wellen in beliebig inhomogenen und heterogenen Medien unter Verwendung eines BEM-Modells mit stark reduzierten Freiheitsgraden (DOFs).

Alternativ wurde ein hybrider BEM-FEM-Ansatz zur Bewertung der seismischen Reaktion einer komplexen poroelastischen Bodenregion entwickelt, welcher eine unterirdische Struktur enthält. Die semi-unendliche geologische Fernfeldregion wird mittels BEM und die endliche geologische Nahfeldregion durch FEM modelliert. Die BEM-Einflussmatrizen werden in äquivalente Steifigkeits- und Dämpfungsmatrizen umgewandelt und unter Verwendung des Makro-Finite-Elemente-Konzepts direkt mit den globalen FEM-Steifigkeits- und Dämpfungsmatrizen gekoppelt. Der Hauptbeitrag dieses Modells ist die Fähigkeit, den gesamten Wellenweg von der seismischen Quelle bis zum betrachteten lokalen Standort in einem Modell zu beschreiben.

Die parallele Berechnung seismischer FWI-Algorithmen durch CUDA C in der GPU zeigt einen bis zu 90-fachen Leistungsgewinn bzw. Reduktion in der Berechnungsdauer. Zusammenfassend gibt die Dissertation einen Weg für eine methodische Erweiterung in der Anwendbarkeit von BEM zur geomechanischen Modellierung durch die Verwendung von numerischer Optimierung, FEM-BEM-gekoppelten Modellen und der Verbesserung der Recheneffizienz von FWI durch parallele Berechnung in der GPU.

Table of contents

List of figures

List of tables

List of Abbreviations

BEM Boundary Element Method

BFGS Broyden–Fletcher–Goldfarb–Shanno

BIE Boundary Integral Equation

BIEM Boundary Integral Equation Method

BVP Boundary Value Problem

CPU Central Processing Unit

CQM Convolution Quadrature Method

CUDA Compute Unified Device Architecture

DOF Degree of Freedom

DOFs Degrees of Freedom

FDM Finite Difference Method

FEM Finite Element Method

FWI Full Waveform Inversion

GPR Ground Penetrating Radar

GPU Graphics Processing Unit

l-BFGS Limited-memory Broyden–Fletcher–Goldfarb–Shanno

OQM Operational Quadrature Method

PDE Partial Differential Equation

PML Perfectly Matched Layers

PSO Particle Swarm Optimization

Chapter 1

Introduction

1.1 Background and motivation

The geological formation in the earth's crust is mostly heterogeneous. The inhomogeneity due to irregular topography, geological layers, cavities, inclusions, discontinuities, anisotropy, porosity, and complex material parameters affect the geomechanical behavior of the geological formation. Seismic waves traveling through this type of medium are subjected to a complex wave distortion by the processes such as reflection, refraction, diffraction, scattering, attenuation, site effects, etc., see Manolis and Kausel (2000). These phenomena highly affect the dynamic behavior of the infrastructures built on them. All civil engineering infrastructures are built-up on the earth's crust; hence their dynamic behavior is affected by the soil on which they are built. Many important problems faced in earthquake engineering involve significant components of seismic mechanics and geophysics. Moreover, the safety of sensitive structures such as nuclear power plants, radioactive waste disposal areas, gas pipelines, dams, motorways, tunnels, ports, bridges, and industrial structures is vital because their failure can lead to disasters. Adequate knowledge of the seismic wave field in the close vicinity is of great significance for the protection against earthquakes. The evaluation of local amplification or deamplification patterns is of great importance for the seismic design of highly sensitive and strategically important structures. The simulation of elastic wave propagation in the earth and their interaction with different types of heterogeneity is of interest in many instances. The adequate mechanical models describing the seismic wave propagation have to incorporate such information as:

(i) Characteristics of the seismic source: geometrical, kinematic, fracture, dynamic, etc.

(ii) Characteristics of the wave path, such as: non-elastic behavior, anisotropy, inhomogeneity, heterogeneity, damping of soil, soil saturation, layering, etc.

(iii) Characteristics of the local geological region, such as: inhomogeneity, layering, surface and subsurface relief, and the existence of discontinuities as cracks, inclusions, and flows on a variety of scales; and engineering structures such as foundations, tunnels, bridges, buildings, etc.

(iv) Characteristics of the seismic motion in spatial dimensions.

For several reasons, incorporating all these effects in seismic design codes has been proven difficult. Different numerical modeling techniques have their benefits and drawbacks in modeling of seismic wave propagation. The main advantage of the BEM is that only the domain boundaries (and possibly interfaces) are discretized, leading to the reduction of the number of DOFs, and avoiding cumulative effects of grid dispersion. BEM is considered a very accurate computational technique in modeling of seismic wave propagation problems. BEM is also efficient in modeling the infinite/semi-infinite domains to model the infinite space that arises in geomechanical modeling effectively because the exact satisfaction of radiation conditions is built into the formulation. However, some limitations of BEM in modeling seismic wave propagation in naturally existing geological formations need to be addressed. Some of the major limitations of BEM in modeling seismic wave propagation are as follows:

(i) The elastodynamic fundamental solutions that are the main component of the BEM exist mainly for homogeneous medium and limited cases of variable material properties. Several Green's functions for elastic isotropic half-space exist for homogeneous, stratified, and continuously varying media, see Appendix C. But in reality, the earth's crust usually consists of a heterogeneous formation. In such cases, the existing solutions of BIEs fail to model the wave propagation correctly. This limits the applicability of BEM for modeling seismic wave propagation in realistic scenarios.

(ii) Modeling of elastic material behavior is efficiently done in BEM. However, modeling of nonlinear behavior such as elastoplastic or plastic ones is inefficient in BEM. The solutions are primarily obtained along the boundary. The solution in the domain can be computed after those along the boundary are obtained at additional computational costs. On the other hand, domain-based methods such as FEM can model nonlinear material behavior efficiently. However, as opposed to BEM, they are inefficient in modeling of wave propagation in infinite domain. This is a motivation to apply coupled BEM-FEM models, where BEM is used to model far-field infinite or semi-infinite regions, and FEM is used to model near-field finite regions.

The first limitation discussed above has two-fold problems: *(a)* Obtaining the information of subsurface material and the features such as cavities and inclusions is a challenging task; *(b)* even after having the information about the geological features, the solutions of the BIEs for such an arbitrarily real problem does not exist. One of the ways to solve these problems is inverse and optimization procedures. FWI is a widely used inverse algorithm in exploration geophysics to obtain a high-quality subsurface image based on seismic measurements. In FWI, the subsurface parameters are obtained by minimizing the misfit between the observed data from the seismic measurements and the modeled data in an iterative manner. FWI is widely used in domain-based numerical methods such as FDM and FEM, but are seldom found to be used in BEM. Several algorithms are being used in FWI. However, finding one that works to solve a complex elastodynamic inverse problem in BEM is tough. One simple yet powerful optimization tool finding its space in FWI is PSO. In PSO, a swarm of particles, where each particle is a set of solutions, interact with each other to find the best solution that fits the observed or measured data. The search algorithms are inspired by the social behavior of animals, such as a flock of birds flying in search of food. The existence of such a simple yet powerful algorithm shows the possibility of application of FWI in BEM to solve seismic wave propagation problems.

Another vital aspect in numerical modeling by BEM or hybrid BEM-FEM is the computational requirement. The matrices in BEM are fully populated, which takes a long time to solve. FWI and other optimization algorithms are iterative procedures that multiply the computational volume of the wave propagation simulation model. However, modern computers come with parallel computation capability using CPU and GPU. To solve the models in a reasonable time, the following methods can be applied: *(a)* reduce the model size by optimization techniques, and *(b)* apply parallel computation using CPU and GPU.

Overall, the primary motivation is to develop a BEM methodology for wave propagation in naturally occurring arbitrarily inhomogeneous and heterogeneous geological regions. As an effort to move towards this generic goal, the dissertation investigates three major areas as follows: *(a)* apply and validate an efficient optimization procedure for inverse seismic wave propagation modeling in BEM; *(b)* develop, verify and study hybrid BEM-FEM models for the numerical simulation of seismic wave propagation problems; *(c)* improve the computational efficiency of FWI algorithm.

1.2 Objective

The followings are the objectives of this thesis.

(i) To study and develop a BEM-based seismic forward model for inplane wavefield using available fundamental solutions for elastic isotropic continuum in homogeneous and discrete inhomogeneous half-plane.

(ii) To study seismic FWI in FDM using local optimization techniques.

(iii) To study and develop BEM optimization models based on synthetic data of field measurements using PSO.

(iv) To study and develop BEM-FEM coupled models for seismic wave propagation modeling in homogeneous and inhomogeneous, elastic, and poroelastic half-plane.

(v) To enhance the computational efficiency of FWI models by CPU and GPU-based parallel computations.

In order to achieve these objectives, the dissertation is structured as shown in the next section.

1.3 Organization of Dissertation

The remaining part of the dissertation is organized as follows:

Chapter 2: A BEM tool for seismic wave propagation is reviewed for P-SV wavefield in a homogeneous elastic isotropic medium with multiple domains and layered media. The state-of-the-art review, the mathematical statement of the problem, its Boundary Integral Equation Method (BIEM) reformulation, and the numerical implementation using BEM are presented. The numerical scheme is verified with existing literature. This chapter develops the BEM base tool and the forward model for the inverse and optimization problems by BEM.

Chapter 3: FWI in P-SV wave-field using PSO is discussed. A state-of-the-art review of full waveform inversion is followed by the formulation of forward and inverse problems using FDM. Broyden–Fletcher–Goldfarb–Shanno (BFGS) method is used as a numerical optimization tool. The applicability of a similar strategy in BEM is discussed.

Chapter 4: A method for estimating site-specific impedance function values for P-SV wavefield in inhomogeneous and heterogeneous media is discussed. The mathematical statement of the problem and its BIEM reformulation based on the fundamental solution for homogeneous elastic isotropic continua are presented. The wave velocities are considered the variables dependent on the node-element pairs in the BEM mesh which are taken as inversion parameters. Synthetic data of seismic wave propagation are developed for elastic isotropic half-plane with surface relief and embedded cavities, which are taken as true seismic data. Finally, the elastodynamic impedance matrices are estimated by modified PSO.

Chapter 5: A hybrid BEM-FEM model is developed for P-SV wavefield in a homogeneous elastic and poroelastic isotropic half-plane. The in-house BEM model developed by the author is used in conjunction with FEM software ABAQUS, Smith (2009). The BEM matrices are transformed into stiffness and damping matrices and included in the FEM model as a macro-finite element using the substructure approach.

Chapter 6: High-performance numerical schemes using parallel computation is developed for the computational enhancement of FWI. In-plane seismic FWI in time domain is studied by CPU-based parallel computation using OpenMP and GPU-based parallel computation using CUDA C environments. The focus lies on improving the model's computational efficiency for real-time applications using commonly available and affordable hardware (CPU and GPU).

Chapter 7: A summary of the implemented techniques, the outcomes of the study, their applicability, drawbacks, and further improvements are discussed. Conclusions for the study and future perspectives to improve the modeling technique are presented.

Chapter 2

A review of seismic wave propagation in elastic half-plane by boundary element method

2.1 Introduction

A closer look into the Earth on a scale of hundreds of *km* reveals its heterogeneity due to the surface and subsurface reliefs, non-parallel layers, cavities, inclusions, cracks, faults and underground engineering constructions. The Earth's heterogeneous geological features, such as depth-dependent geo-material gradient, nonlinear stress-strain states, etc., cause a significant spatial variation of ground motion, leading to large amplifications during earthquakes. A quantitative prediction of strong ground motion manifestation at a given site involves dealing with the source of seismic waves, the path of propagation, and the local site effects. A possible way of shedding some light on understanding the site-response phenomena and their sensitivity to the type and properties of the seismic source, inhomogeneity and heterogeneity of the wave path lies in developing high-performance numerical methods for the simulation of seismic wave propagation phenomena. Mesh-reducing BIE-based methods are considered in this chapter for numerical modeling of elastic wave motion in naturally occurring inhomogeneous and heterogeneous media. The main reason to choose BIE-based methods is the presence of the free surface of the Earth, whereby large categories of problems involve continua with a small surface-to-volume ratio. As BIEM requires only the surface to be discretized, substantial savings can be realized in terms of the mesh size compared to the domain-type numerical methods under most circumstances.

This chapter is restricted to in-plane elastodynamic problems in an elastic isotropic half-plane containing different types of heterogeneities that are subjected to incident time-harmonic or transient in-plane P/SV waves or waves emitted by embedded dynamic sources. The heterogeneities may include free-surface reliefs, layers, deposits, multiple cavities or multiple elastic isotropic inclusions, unlined/lined tunnels, embedded foundations, and other underground structures. The presented mechanical models and corresponding computational tools are based on BEM using the frequency-dependent fundamental solution of the governing wave equation for elastic isotropic continua.

2.2 State-of-the-Art:BEM

2.2.1 A historical perspective of BEM

BEM is based on BIEM which belongs to the family of integral equations theory. The first remarkable work in integral equations encountered in potential theory is from a Swedish mathematician Erik Ivar Fredholm published in Fredholm (1903). Although the development of differential and integral equations can be traced back to the eighteenth and nineteenth centuries, the work by Fredholm is considered the first rigorous work in the theory of integral equations. It paved the way for the advancement in BIEM and BEM for elastic potential problems. With the advancement of digital computers in the 1960s, classical integral formulations were required to be derived into numerical formulations. The direct BEM formulations, where the boundary is discretized, and the integral equations are transferred into a system of algebraic equations for 2D potential problems, are published in Jaswon (1963), Symm (1963). The term BEM, which first appeared in the works of Brebbia (1978), indicates the surface discretization characteristics of the method, where the shape functions are derived from FEM. The first boundary integral formulation in elastodynamics is used by Cruse and Rizzo (1968). In that publication, the formulation is performed in Laplace domain with subsequent inverse transformation to time domain to achieve the results for transient behavior. The corresponding formulation in Fourier Domain, i.e., frequency domain, is presented in Dominguez and Roesset (1978a,b). The first boundary element formulation directly in time domain is developed by Mansur and Brebbia (1982a) and Mansur (1983). The extension of the elastodynamic time domain formulation to non-zero initial conditions is presented by Antes (1985). A detailed formulation of BEM for elastodynamics is presented in Brebbia (1978), Beskos (1987b, 1997), Dominguez (1993). More detailed reviews of the early development of BEM for wave propagation in elastic solids can be found in Beskos (1987b), Manolis and Beskos (1988), Dominguez (1993).

2.2.2 BEM formulation in elastodynamics

Four classes of BEM formulations commonly used in elastodynamics are:

(i) **Time domain boundary element method (TD-BEM):** The solutions are formulated directly in time domain. The first direct time-domain BE formulation is presented for anti-plane elastodynamics by Friedman and Shaw (1962). Time domain BEM formulations are presented in: Mansur (1983) for 2D problems, Mansur and Brebbia (1982a,b) for 1D and 2D problems, respectively, and Karabalis and Beskos (1984) for 3D problems. Other pioneering works concerning mesh-reducing BEM are those in Antes (1985), Banerjee et al. (1986), Beskos (1987a,b, 1997), Manolis and Beskos (1988).

(ii) **Frequency or Laplace domain BEM:** Use of the fundamental solution in the Fourier or Laplace domains: Cruse and Rizzo (1968) – first work for in-plane elastodynamics, Manolis and Beskos (1988), Dominguez (1993).

(iii) **Dual reciprocity BEM:** Based on the fundamental solutions of elastostatics, see Nardini and Brebbia (1983), Partridge et al. (1992).

(iv) **Convolution Quadrature Method (CQM) for dynamic transient problems:** Proposed by Schanz and Antes (1997a,b), this approximation is based on Operational Quadrature Method (OQM). The convolution integral is substituted by a quadrature formula in Lubich (1988, 1994), whose weights are computed using Laplace transform of the fundamental solution and a linear multi-step method. A detailed comparison of the advantages and disadvantages of time-domain BEM, frequency domain BEM, and CQM-BEM for transient elastodynamics can be seen in García-Sánchez and Zhang (2007), Furukawa et al. (2014), Manolis and Dineva (2015). The final solution to the problem is obtained in time domain.

2.3 BIEM formulation for P-SV wave

The 2D elastodynamic wave equation in frequency domain is given by Equation (2.1). The Partial Differential Equation (PDE) is derived by combining constitutive equation (Hooke's law), kinematic equation, and equation of motion for dynamic equilibrium, see Dominguez (1993), Fontara (2015).

$$\eta u_j(X,\omega)_{,ji} + \mu u_i(X,\omega)_{,jj} + (\omega^2\rho - i\omega\upsilon)\, u_i(X,\omega) + \Psi b_i(x,\omega) = 0 \qquad (2.1)$$

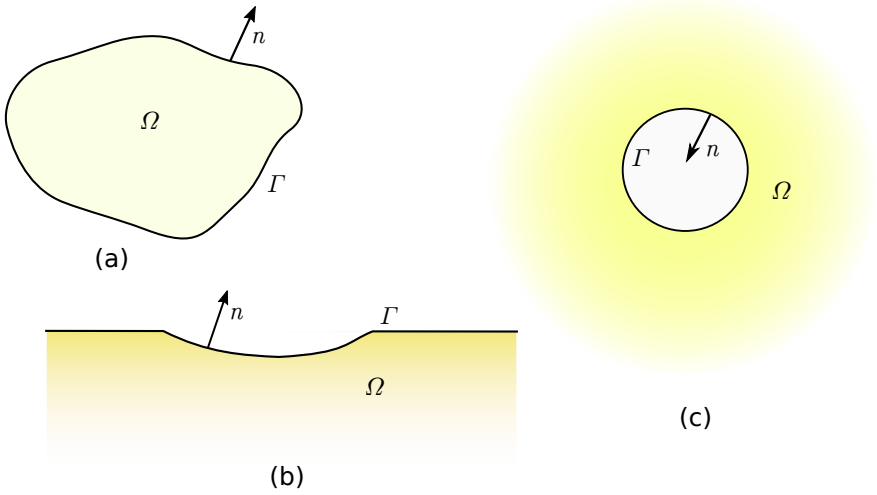

Fig. 2.1 Bounded domains Ω with boundary Γ and outward normal direction n: (a) Finite domain; (b) Semi-infinite domain; (c) Infinite domain.

Where: $\eta = \lambda + 2\mu$; λ and μ are Lame constants; υ is the viscous damping factor; u is the displacement variable; ω is the circular frequency; $X(x_1, x_2)$ is the position variable; $b_i = f_{0i}\delta(X - X_0)$ is a time-harmonic $e^{i\omega t}$ body force located at position $X_0(X_{01}, X_{02})$, with amplitude f_{0i}. $i = 1,2$ and $j = 1,2$ represent the unit vectors along the principle directions in a two-dimensional space. In the case of existing dynamic source radiated P/SV wave $\Psi = 1$, while in its absence $\Psi = 0$.

The BIEM solution is achieved by reformulating the corresponding boundary-value problem described via PDE into integral equations along the existing boundaries via the combination of reciprocity theorems and fundamental solutions of the governing equation, see Rizzo et al. (1985), Beskos (1987a,b, 1997), Kobayashi (1983, 1987), Manolis et al. (2017). The BIE representation of the governing equation (2.1) in frequency domain is given by Equation (2.2), see Dominguez (1993).

$$c_{ij}\, u_i(x,\omega) = \int_\Gamma u^*_{ij}(x,\xi,\omega)\, t_j(\xi,\omega)\, d\Gamma - \int_\Gamma \tau^*_{ij}(x,\xi,\omega)\, u_j(\xi,\omega)\, d\Gamma + \zeta_{ij}(x,\omega) \qquad (2.2)$$

Where: $x(x_1, x_2)$ and $\xi(\xi_1, \xi_2)$ are the position vectors of the source and the field points, respectively; u^*_{ij} is the frequency-dependent displacement fundamental solution, and τ^*_{ij} is the corresponding traction, see Equations (D.1-D.2); ζ_{ij} is the term that stands for the possible domain integral terms such as body sources or incident wave-fields; c_{ij} is the jump term depending upon the local geometry. $c_{ij} = I$ in $(x \in \Omega, x \notin \Gamma)$; $c_{ij} = 0.5\delta_{ij}$ in $x \in \Gamma$, when the

boundary is smooth. For non-smooth surfaces, the values of c_{ij} can be calculated indirectly using the principle of rigid body motion, see Dominguez (1993).

2.3.1 Problem formulation

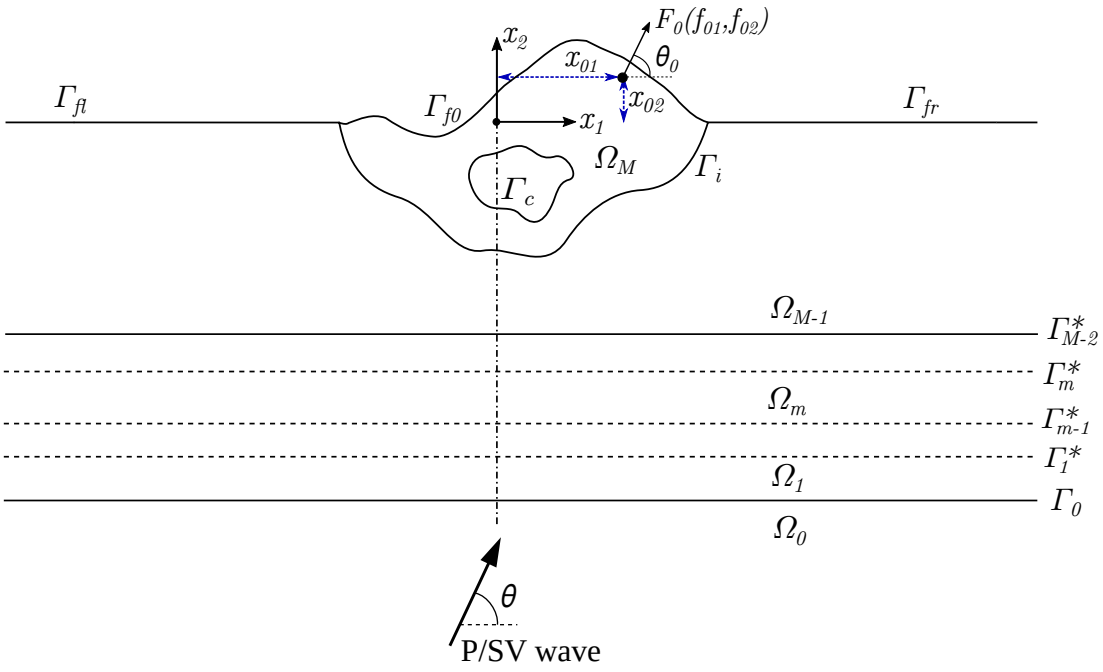

Fig. 2.2 A finite geological region with free surface relief and an embedded arbitrarily shaped cavity resting on a half-plane

In a Cartesian coordinate system O_{x_1,x_2,x_3}, consider a finite elastic isotropic geological region Ω_M with free surface relief and an arbitrarily shaped unlined cavity on a stratified elastic isotropic half-plane with $M-2$ number of layers Ω_m, where $(m = 0,1,2,...,M-1)$, see Figure 2.2. The finite region Ω_M consists of an arbitrarily shaped cavity bounded by Γ_c. The half-plane Ω_0 is bounded by the interface Γ_0. The stratified layers Ω_m, where $(m = 1,2,3,...,M-2)$, are bounded by $\Gamma_m = \Gamma^*_{m-1} \cup \Gamma^*_m$. The domains Ω_{M-1} and Ω_M are bounded by $\Gamma_{M-1} = \Gamma^*_{M-2} \cup \Gamma_i \cup \Gamma_{fl} \cup \Gamma_{fr}$ and $\Gamma_M = \Gamma_i \cup \Gamma_{f0} \cup \Gamma_c$, respectively. $\Gamma_f = \Gamma_{f0} \cup \Gamma_{fl} \cup \Gamma_{fr}$ is the free surface boundary. The layered boundaries extend towards the positive and negative infinity along O_{x_1} direction. The dynamic loads comprise either **(a)** an incident time-harmonic P or SV wave traveling at an incident angle θ with respect to axis O_{x_1} or **(b)** in-plane waves generated by an embedded seismic line source F_0 located at a point $x_0(x_{01},x_{02},0)$ inside the domain Ω_M. The in-plane deformation state is considered in the plane $x_3 = 0$. The governing elastodynamic equation is Equation (2.1). The reformulation of

the problem by BIE and the corresponding boundary conditions along the existing boundaries are discussed in Section 2.3.2.

2.3.2 BIEM reformulation for the posed problem

The BIEM reformulation of the Boundary Value Problem (BVP) defined in Section 2.3.1 is applied to each domain Ω_m, where $(m = 1,2,3,...,M)$. The integral representation of the wave equation for each domain Ω_m, bounded by Γ_m, is given by Equation (2.3), see Dominguez (1993).

$$\begin{aligned} c_{ij}\, u_i^{sc}(x,\omega) = & \int_{\Gamma_m} u_{ij}^*(x,\xi,\omega)\, t_j^{sc}(\xi,\omega)\, d\Gamma \\ & - \int_{\Gamma_m} \tau_{ij}^*(x,\xi,\omega)\, u_j^{sc}(\xi,\omega)\, d\Gamma \\ & + \Psi_m\, f_{0j}\, \tilde{g}(\omega)\, u_{ij}^*(x,x_0,\omega) \qquad \text{for } x \in \Gamma_m,\ i = 1,2 \text{ and } j = 1,2 \end{aligned} \tag{2.3}$$

Where: the superscripts $()^{sc}$ represent the scattered wave motion; c_{ij} is the jump term depending upon the local geometry; $x(x_1,x_2)$ and $\xi(\xi_1,\xi_2)$ are the position vectors of the source (collocation) and field (integration) points, respectively; u_{ij}^* is the frequency-dependent fundamental solution for homogeneous elastic isotropic medium, and τ_{ij}^* is the corresponding traction; $\Psi_m = 1$ when the domain Ω_m contains seismic source, else $\Psi_m = 0$; f_{0j} is the magnitude and $\tilde{g}(\omega)$ is the Fourier transform of the time function of the seismic source located at position x_0.

The complete ground motion in the homogeneous elastic isotropic half-plane with cavities, free-surface relief, and interfaces between the layers comprises the primary (incoming) and the scattered (by the heterogeneities) waves. The primary waves, also known as the free field motion (u_i^{ff}, t_i^{ff}), are expressed analytically by solving a simple wave propagation problem for a homogeneous elastic isotropic half-plane in the absence of heterogeneity and free-surface relief subjected to incident plane P/SV wave. The displacement and traction fields for the scattered waves are labeled as (u_i^{sc}, t_i^{sc}). The total wave field (u,t) at any point in the half-plane is defined as a superposition of the free field motion (u^{ff}, t^{ff}) and scattered wave field (u^{sc}, t^{sc}), such that:

$$\begin{aligned} & u_i = u_i^{ff} + u_i^{sc};\ t_i = t_i^{ff} + t_i^{sc} && \text{where } (i = 1,2) \text{ in } \Omega_0 \\ & u_i^{ff} = 0;\ t_i^{ff} = 0;\ u_i^{sc} = u_i;\ t_i^{sc} = t_i && \text{where } (i = 1,2) \text{ in } \Omega_m\ (m = 1,2,3,...,M) \end{aligned}$$

The free field solutions for displacement u^{ff} and traction t^{ff} in a homogeneous elastic isotropic half-plane in frequency domain are derived in Achenbach et al. (1973), see Appendix B. Rewriting the equation for total wave field, the BIEs for the problem with the geometry shown in Figure 2.2 are given by Equations (2.4)−(2.6):

$$\begin{aligned} c_{ij}\ \Big(u_i(x,\omega)-u_i^{ff}(x,\omega)\Big) &= \int_{\Gamma_0} u_{ij}^*(x,\xi,\omega)\ \Big(t_j(x,\omega)-t_j^{ff}(x,\omega)\Big)\ d\Gamma \\ &\quad - \int_{\Gamma_0} \tau_{ij}^*(x,\xi,\omega)\ \Big(u_j(x,\omega)-u_j^{ff}(x,\omega)\Big)\ d\Gamma \\ &\quad \text{for } x\in\Gamma_0;\ \xi\in\Gamma_0;\ i=1,2 \text{ and } j=1,2 \end{aligned} \tag{2.4}$$

$$\begin{aligned} c_{ij}\ u_i(x,\omega) &= \int_{\Gamma_m} u_{ij}^*(x,\xi,\omega)\ t_j(\xi,\omega)\ d\Gamma - \int_{\Gamma_m} \tau_{ij}^*(x,\xi,\omega)\ u_j(\xi,\omega)\ d\Gamma \\ &\quad \text{for } x\in\Gamma_m;\ \xi\in\Gamma_m;\ (m=1,2,...M-1);\ i=1,2 \text{ and } j=1,2 \end{aligned} \tag{2.5}$$

$$\begin{aligned} c_{ij}\ u_i(x,\omega) &= \int_{\Gamma_M} u_{ij}^*(x,\xi,\omega)\ t_j(\xi,\omega)\ d\Gamma - \int_{\Gamma_M} \tau_{ij}^*(x,\xi,\omega)\ u_j(\xi,\omega)\ d\Gamma \\ &\quad +\ f_{0j}\ \tilde{g}(\omega)\ u_{ij}^*(x,x_0,\omega) \\ &\quad \text{for } x\in\Gamma_M;\ \xi\in\Gamma_M;\ i=1,2 \text{ and } j=1,2 \end{aligned} \tag{2.6}$$

The BIEs (2.4−2.6) are subjected to free surface boundary conditions and coupled to each other by satisfying the interface boundary conditions as follows:

(a) Free surface boundary condition:

$$t_i(x,\omega)=\sigma_{ij}\eta_j=0;\ \text{where } x\in\Gamma_f\cup\Gamma_c \text{ and } i=1,2 \tag{2.7}$$

(b) Interface boundary condition:

$$\begin{aligned} u_i^{(\Omega_{m-1})}(x,\omega) &= u_i^{(\Omega_m)}(x,\omega); \\ t_i^{(\Omega_{m-1})}(x,\omega) &= -t_i^{(\Omega_m)}(x,\omega) \\ &\quad \text{where } x\in\Gamma_m(m=1,2,3,.....M) \text{ and } i=1,2 \end{aligned} \tag{2.8}$$

(c) Boundary conditions along the boundary Γ_0:

$$\begin{aligned} u_i^{(\Omega_0)}(x,\omega) &= u_i^{ff}(x\in\Gamma_0,\omega)+u_i^{sc}(x\in\Gamma_0,\omega)=u_i^{(\Omega_m)}(x,\omega); \\ t_i^{(\Omega_0)}(x,\omega) &= t_i^{ff}(x\in\Gamma_0,\omega)+t_i^{sc}(x\in\Gamma_0,\omega)=-t_i^{(\Omega_m)}(x,\omega) \end{aligned} \tag{2.9}$$

Upon having the solutions for the displacement and traction along the existing boundaries, one can find displacement and traction at any point in the half-plane by Equations (2.10−(2.12)):

$$u_i(x,\omega) = \int_{\Gamma_0} u^*_{ij}(x,\xi,\omega)\, t_j(x,\omega)\, d\Gamma - \int_{\Gamma_0} \tau^*_{ij}(x,\xi,\omega)\, u_j(x,\omega)\, d\Gamma$$
$$\text{for } x \in \Omega_0;\ x \notin \Gamma_0;\ \xi \in \Gamma_0;\ i = 1,2 \text{ and } j = 1,2 \tag{2.10}$$

$$u_i(x,\omega) = \int_{\Gamma_m} u^*_{ij}(x,\xi,\omega)\, t_j(\xi,\omega)\, d\Gamma - \int_{\Gamma_m} \tau^*_{ij}(x,\xi,\omega)\, u_j(\xi,\omega)\, d\Gamma$$
$$\text{for } x \in \Omega_m;\ x \notin \Gamma_m;\ \xi \in \Gamma_m;\ \ (m = 1,2,...M-1);\ i = 1,2 \text{ and } j = 1,2 \tag{2.11}$$

$$u_i(x,\omega) = \int_{\Gamma_M} u^*_{ij}(x,\xi,\omega)\, t_j(\xi,\omega)\, d\Gamma - \int_{\Gamma_M} \tau^*_{ij}(x,\xi,\omega)\, u_j(\xi,\omega)\, d\Gamma$$
$$+\ f_{0j}\, \tilde{g}(\omega)\, u^*_{ij}(x,x_0,\omega)$$
$$\text{for } x \in \Omega_M;\ x \notin \Gamma_M;\ \xi \in \Gamma_M;\ i = 1,2 \text{ and } j = 1,2 \tag{2.12}$$

For the problem under consideration, the elastodynamic fundamental solutions are used as the reciprocal quantities u^*, τ^*. The elastodynamic fundamental solutions for elastic isotropic homogeneous continuum, given in Dominguez (1993), are included in Appendix D. The singularities of the integrals and their solutions obtained after discretization are discussed in detail in Manolis et al. (2017). The weak singularity of type $O(\ln r)$ occurs in integrals with displacement fundamental solution-based kernels at $r \to 0$. They are solved by the usage of special Gauss quadrature. The strong singularity of type $O(1/r)$ occurs in traction fundamental solution-based kernels at $r \to 0$. The rigid body motion concept (see Dominguez (1993)) is applied to avoid the computation of both the free terms c_{ij} and the integrals with strong singularity. The rigid body motion concept cannot be directly applied to an open polygon geometry. However, to follow the rigid body motion philosophy, the half-plane is supplemented to an enclosed geometry by using extra elements. Only the static part of the traction fundamental solution contains strong singularity in the equation, which is frequency-independent. Thus, the static part of the traction fundamental solution is computed in the beginning from the enclosed model. The solution is combined with the dynamic part of the traction fundamental solution for each frequency, see Kamalian et al. (2003), Panji et al. (2013b). When constant elements are used, the singularity occurs only when the collocation and the integration nodes coincide. For this case, the analytical solution exists within the integration limit $(0, \frac{1}{2}l_e)$, where l_e is the length of the boundary element, see Dominguez (1993). The regular parts of the integrals are calculated by using numerical integration by standard Gaussian quadrature.

2.4 Numerical implementation in BEM

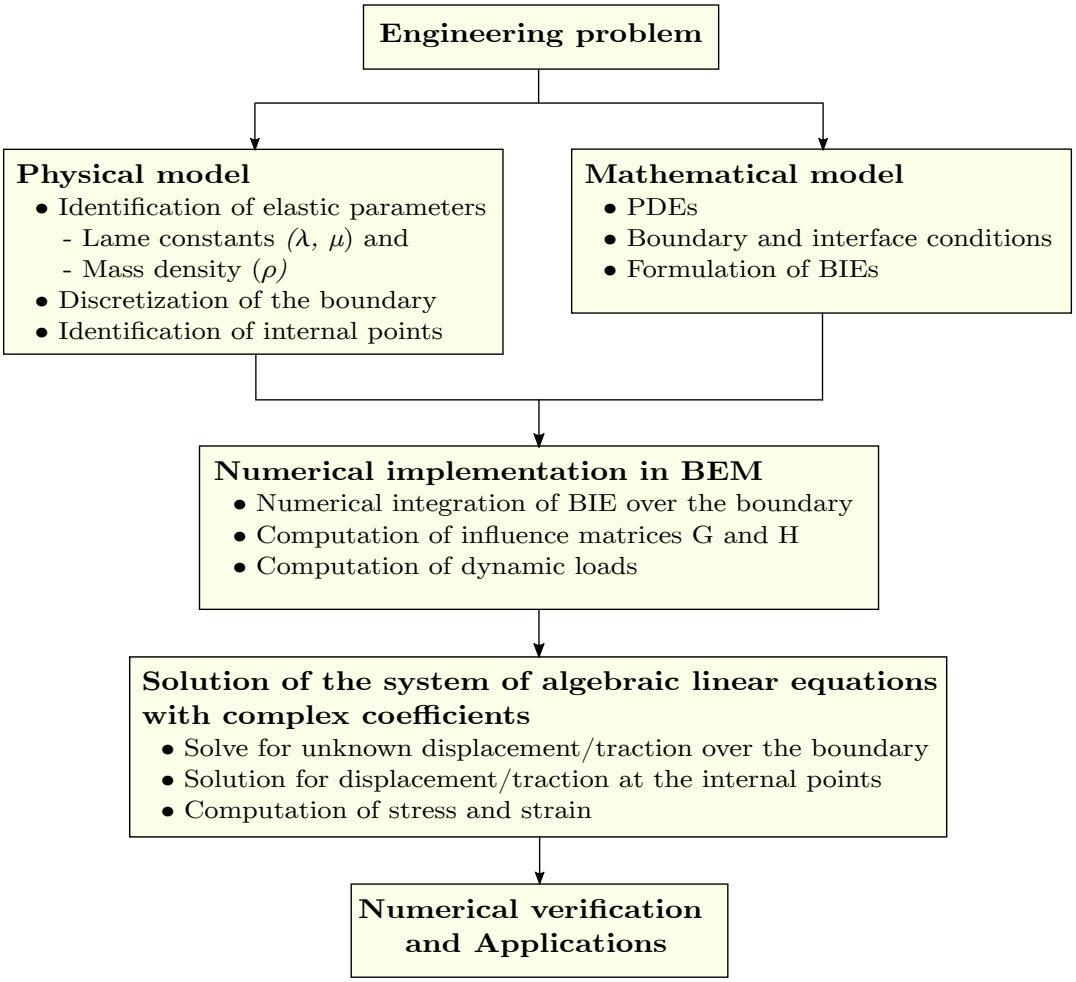

Fig. 2.3 A basic numerical scheme for the simulation of elastodynamic problems by BEM.

The basics numerical scheme for the solution of an elastodynamic problem by BEM is presented in Figure 2.3. The system of BIEs (2.4−2.6) is discretized by boundary elements, see Dominguez (1993). After satisfaction of the boundary conditions, the BIEs transform into a system of linear algebraic equations as given in Equation (2.13).

$$c_m\, u_m(\omega) = G_m(\omega)\, t_m(\omega) - \hat{H}_m(\omega)\, u_m(\omega) + \zeta_m(\omega) \tag{2.13}$$

Where: $(m = 1,2,3,.....M)$; G_m and $\hat{H}_m$ represent the integrals of fundamental solutions u^*_{ij} and τ^*_{ij} in discrete form, respectively. Equation (2.13) can be further rewritten as:

$$\begin{gathered} H_m(\omega)\, u_m(\omega) = G_m(\omega)\, t_m(\omega) + \zeta_m(\omega) \\ \text{where } H = c + \hat{H} \end{gathered} \tag{2.14}$$

Where: G_m and H_m are the BEM influence matrices; ζ_m is a vector related to the domain integral arising from the incident wave field or the seismic sources; and u_m and t_m are displacement and traction vectors, respectively, at circular frequency ω for the domain m. To get the global influence matrices for M domains, the system of linear equations (2.14) are coupled by satisfying the interface conditions in Equation (2.9), such that the global influence matrices G_m and H_m are recovered. However, due to the opposite signs of the displacement and traction balance along the interface, it becomes difficult to implement them in the numerical algorithms. With rearrangement and multiplying with G_m^{-1}, where the superscript $(^{-1})$ represents the inverse of the matrix, the equation can be simplified to the form of Equation (2.15).

$$\begin{gathered} S_m(\omega) \cdot u_m(\omega) = t_m(\omega) + \hat{b}_m(\omega) \\ \text{where, } S_m = G_m^{-1} H_m \text{ and } \hat{b}_m = G_m^{-1} \zeta_m \end{gathered} \tag{2.15}$$

The system of M matrix equations now can be coupled by applying the interface boundary conditions (2.9) to obtain the global system of N linear equations (where N is the total number of nodes in the global system) in Equation (2.16).

$$S(\omega) \cdot u(\omega) = t(\omega) + \hat{b}(\omega) \tag{2.16}$$

Where: S is the global influence matrix, $\hat{b}$ is the global body traction vector due to the incident wave field and the seismic sources; u and t are global nodal displacement and nodal traction vectors, respectively, at circular frequency ω.

The influence matrix S is a fully populated of size $2Nx2N$, where N is the number of boundary nodes. After proper rearrangement and satisfaction of the boundary conditions, the system of algebraic equations (2.16) transforms into the standard form $AX = B$. Once the solution for the field variables along the boundaries is obtained, the displacement, traction, strain, and stress at any observer point inside the domain Ω_m can be determined via the solution of Equations (2.10−2.12), see Manolis et al. (2017).

2.5 Verification study

This section aims to evaluate the accuracy and convergence of the developed BEM solution by comparing the author's solution with the available solutions in the literature for homogeneous elastic isotropic half-plane with different types of heterogeneities.

Test example A: Homogeneous elastic isotropic half-plane with semi-circular canyon under time-harmonic P/SV wave

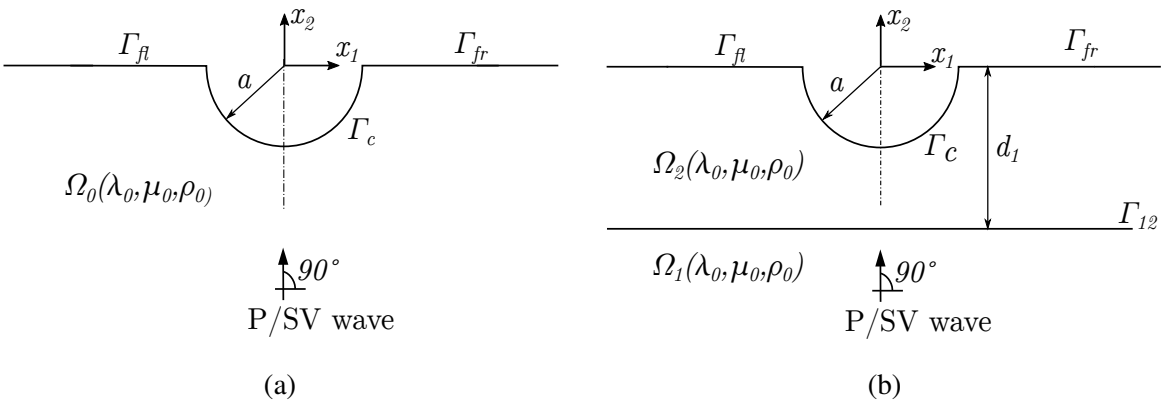

Fig. 2.4 A semi-circular canyon in a homogeneous elastic isotropic half-plane under vertically incident P/SV wave: (a) without domain decomposition, (b) domain decomposition into two stratified layers

Consider a semi-circular canyon with radius a in a homogeneous elastic isotropic half-plane Ω_0 with elastic medium parameters $(\lambda_0, \mu_0, \rho_0)$ and bounded by a free surface boundary $\Gamma_f = \Gamma_{fl} \cup \Gamma_c \cup \Gamma_{fr}$ under vertically incident P/SV waves, Figure 2.4a. Many authors have solved this example in the past: **(a)** Wong (1982) by a generalized inversion technique; **(b)** Sanchez-Sesma and Campillo (1991) by indirect BEM; **(c)** Álvarez Rubio et al. (2004) by direct BEM; **(d)** Parvanova et al. (2014) by direct BEM based on sub-structure technique. For a homogeneous elastic isotropic domain $\Omega_0(\lambda_0, \mu_0, \rho_0)$ with primary and shear wave velocities c_1 and c_2, respectively, a non dimensional frequency is introduced as $\eta = 2a/l_w$, where l_w is shear wavelength given by $l_w = (2\pi/\omega)\, c_2$.

Additionally, for the validation of the stratified model, the half-plane Ω_0 is decomposed into stratified layers Ω_1 and Ω_2 by an interface Γ_{12} at a depth d_1 from the free surface, as shown in Figure 2.4b. The domains Ω_1 and Ω_2 consist of the same elastic medium parameters as Ω_0, and the final displacement along the free surface Γ_f should be the same from both homogeneous and stratified models.

A simulation is performed for $\eta = 1.0$ with the radius of the canyon $a = 10m$, shear wave velocity $c_2 = 223.33m/s$, Poisson's ratio $\nu = 1/3$ and the mass density $\rho = 2000.0kg/m^3$.

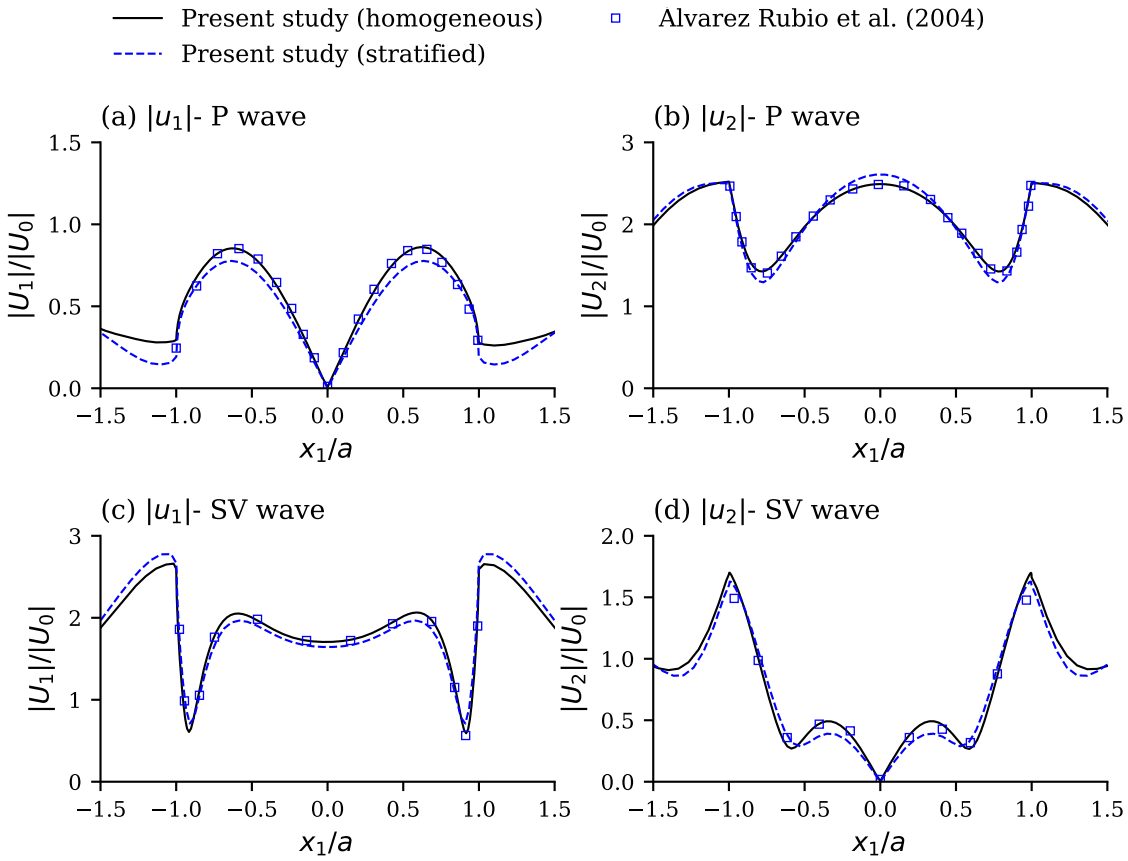

Fig. 2.5 Displacement amplitudes normalized by the amplitude of the vertically incident time-harmonic **(a, b)** P wave and **(c, d)** SV wave with non-dimensional frequency $\eta = 1$ versus x_1/a, i.e., along the free-surface of a homogeneous elastic isotropic half-plane with a semi-circular canyon of radius a. A comparison of the results by Álvarez Rubio et al. (2004) with the author's BEM solutions using a homogeneous and stratified model.

The depth of the interface in the stratified model is $d_1 = 2a$. Constant boundary elements, with the length of boundary elements $l_e = l_w/30$, are used to discretize the boundaries and the interfaces. For the homogeneous model in Figure 2.4a, the flat free surfaces Γ_{fl} and Γ_{fr} are discretized within the length $L = \pm 3.1a$. Satisfying this criteria, the boundary Γ_f is discretized with 158 boundary elements (94 along the canyon surface and 32 each along Γ_{fl} and Γ_{fr}). Similarly, for the stratified model in Figure 2.4b, a total of 620 constant boundary elements (173 each along the left and right flat free surfaces Γ_{fl} and Γ_{fr}, 48 along the canyon Γ_c and 226 along the interface Γ_{12}) are used to discretize the system. The interfaces/boundaries Γ_{12} and Γ_f are discretized to $\pm 20m$ and $\pm 40m$, respectively. The normalized horizontal and vertical displacement amplitudes along the free surface for vertically incident P and SV wave fields with $\omega = 70.16$ ($\eta = 1.0$) from both models are compared with the solution given in Álvarez Rubio et al. (2004), see Figure 2.5. The obtained

solutions illustrate an excellent verification of the BEM solutions developed by the author. It is also observed that the stratified model requires the free surfaces to be discretized to a longer distance towards $\pm\infty$ along x_1 axis.

Test example B: Homogeneous elastic isotropic half-plane with an embedded circular cavity under time-harmonic P/SV wave

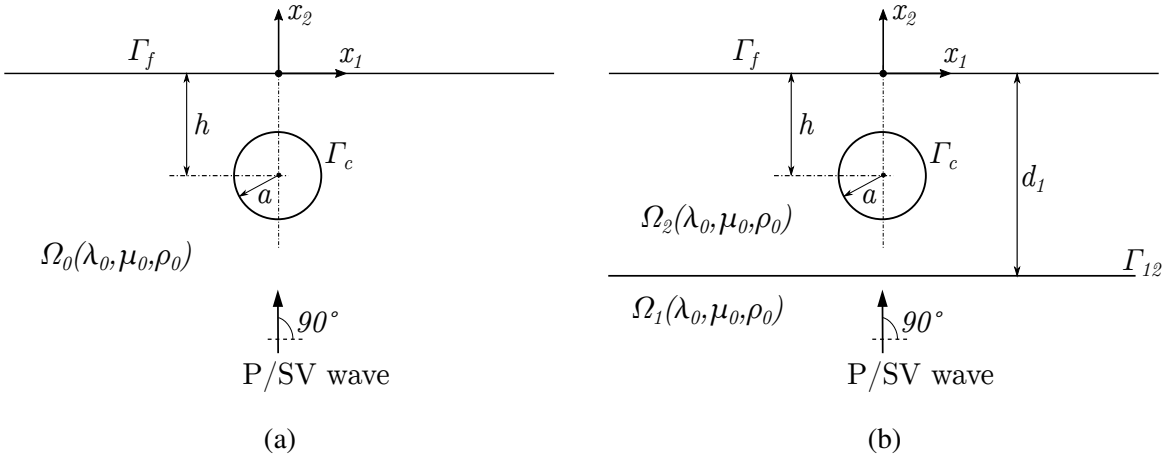

Fig. 2.6 An embedded circular cavity in a homogeneous elastic isotropic half-plane under vertically incident P/SV wave: (a) without domain decomposition; (b) domain decomposition into two stratified layers

Consider an unlined circular cavity with radius a embedded at depth h in a homogeneous elastic isotropic half-plane Ω_0 with elastic medium parameters $(\lambda_0, \mu_0, \rho_0)$ and bounded by boundary $\Gamma_0 = \Gamma_f \cup \Gamma_c$, see Figure 2.6a. Where, Γ_c is the free boundary of the cavity, and Γ_f is the horizontal free surface. The half-plane is subjected to a vertically incident P/SV wave. This example is solved in Luco and de Barros (1994) by indirect boundary integral equation method based on the two-dimensional Green's functions for a viscoelastic half-plane, in Yu and Dravinski (2009) by direct boundary integral equation method, and in Alielahi et al. (2013) by time-domain BEM. For a homogeneous elastic isotropic domain $\Omega_0(\lambda_0, \mu_0, \rho_0)$ with primary and shear wave velocities c_1 and c_2, respectively, a non dimensional frequency is introduced as $\eta = 2a/l_w$, where l_w is shear wavelength given by $l_w = (2\pi/\omega)\, c_2$.

Additionally, for the validation of the stratified model, the half-plane Ω_0 is decomposed into stratified layers Ω_1 and Ω_2 by an interface Γ_{12} at depth $d_1 = 2h$ from the free surface, as shown in Figure 2.6b. The domains Ω_1 and Ω_2 consist of the same elastic medium parameters as Ω_0, and the final displacement along the free surface Γ_f should be the same from both homogeneous and stratified models.

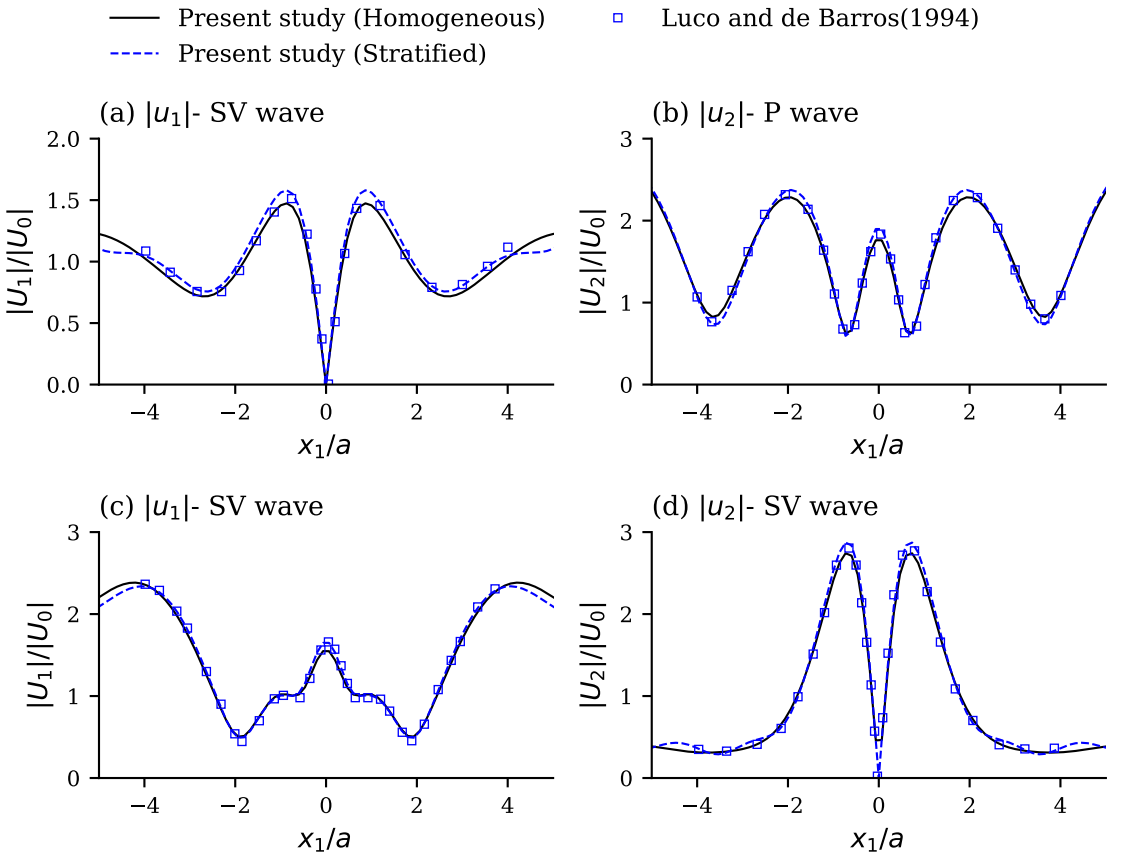

Fig. 2.7 Displacement amplitudes along the free surface normalized by the amplitude of the vertically incident **(a, b)** P-wave, **(c, d)** SV-waves in a homogeneous elastic isotropic half-plane with embedded cavity $(h/a = 1.5)$ and at a fixed non-dimensional frequency $\eta = 0.5$. Comparison of the author's BEM solutions using a homogeneous and stratified model with the solutions in Luco and de Barros (1994).

Simulations are performed with the following parameters: radius of the embedded cavity $a = 10m$, depth of the center of the cavity $h = [1.5a, 2.0a]$, shear wave velocity $c_2 = 223.33m/s$, Poisson's ratio $\nu = 1/3$ and medium density $\rho = 2000.0kg/m^3$. The length of boundary elements l_e is considered as $l_e \leq l_w/30$, which fits well to the highest value in the frequency interval under consideration. In the homogeneous model, the flat free surfaces Γ_f are discretized in the length $L = \pm 20a$. Satisfying this criterion, the boundary Γ_0 is discretized with: 600 boundary elements along the free surface Γ_f and 189 along the cavity Γ_c. Similarly, a total of 1295 constant boundary elements (750 along the free surface Γ_f, 95 along the cavity wall Γ_c and 450 along the interface Γ_{12}) are used to discretize the stratified model. The interfaces/boundaries Γ_{12} and Γ_f are discretized to $\pm 20m$ and $\pm 40m$, respectively.

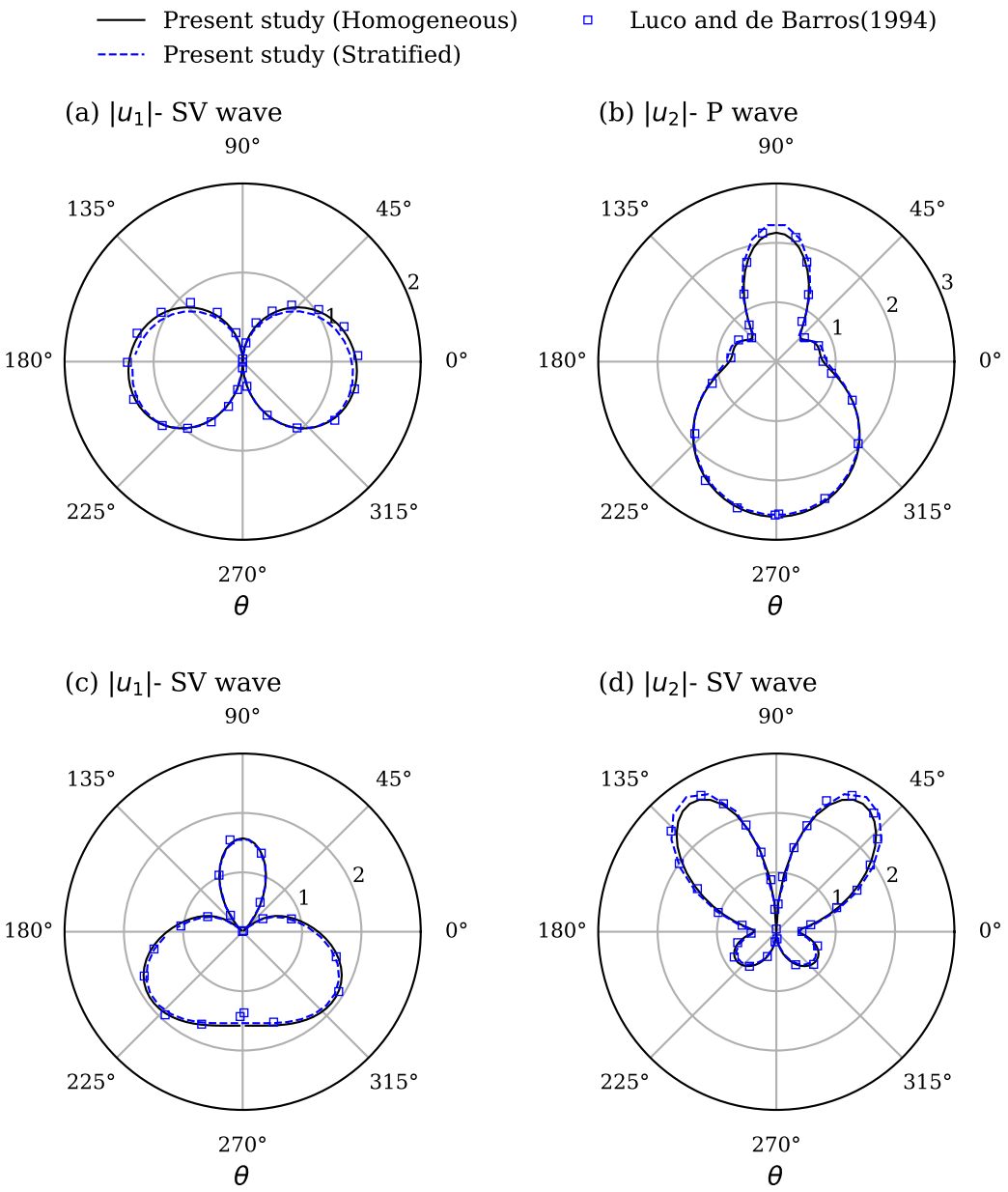

Fig. 2.8 Displacement amplitudes along the cavity wall normalized by the amplitude of the vertically incident **(a, b)** P-wave, **(c,d)** SV-waves in a homogeneous elastic isotropic half-plane with embedded cavity $(h/a = 1.5)$ and at a fixed non-dimensional frequency $\eta = 0.5$. Comparison of the author's BEM solutions using a homogeneous and stratified model with the solutions in Luco and de Barros (1994).

The normalized horizontal and vertical displacement amplitudes along the free surface and cavity wall for vertically incident P and SV wave field are presented for **(a)** $\eta = 0.5$ and $h/a = 1.5$, compared with the solutions obtained by Luco and de Barros (1994) (see Figure

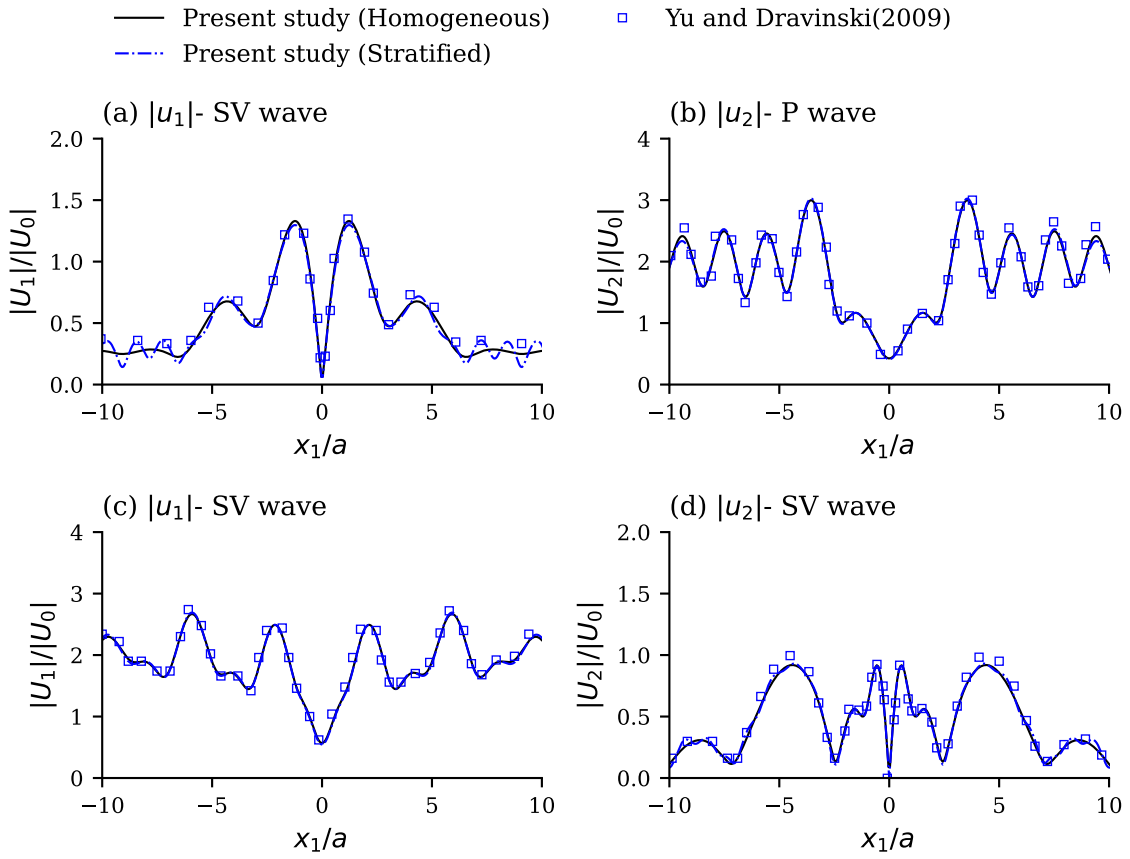

Fig. 2.9 Displacement amplitudes along the free surface normalized by the amplitude of the vertically incident time-harmonic **(a, b)** P wave and **(c,d)** SV wave with a non-dimensional frequency $\eta = 1$ in a homogeneous elastic isotropic half-plane with an embedded cavity of radius a and depth $h = 2a$. A comparison of the author's BEM solutions using homogeneous and stratified models with the results by Yu and Dravinski (2009).

2.7 and 2.8 for the displacements along the free surface and the cavity wall, respectively); **(b)** $\eta = 1.0$ and $h/a = 2.0$, and compared with the solutions presented by Yu and Dravinski (2009), see Figure 2.9. The comparison of the author's BEM solutions for the homogeneous and stratified model with the benchmark results from the corresponding literature shows excellent verification of the BEM solutions developed by the author.

Test example C: Homogeneous elastic isotropic half-plane with an embedded alluvial basin under time-harmonic P/SV wave

Consider a semicircular alluvial deposit with radius a rested on a homogeneous elastic isotropic half-plane under vertically incident P/SV waves, see Figure 2.10. The example is solved by the transition matrix method, see Yeh et al. (2007). A non-dimensional frequency is

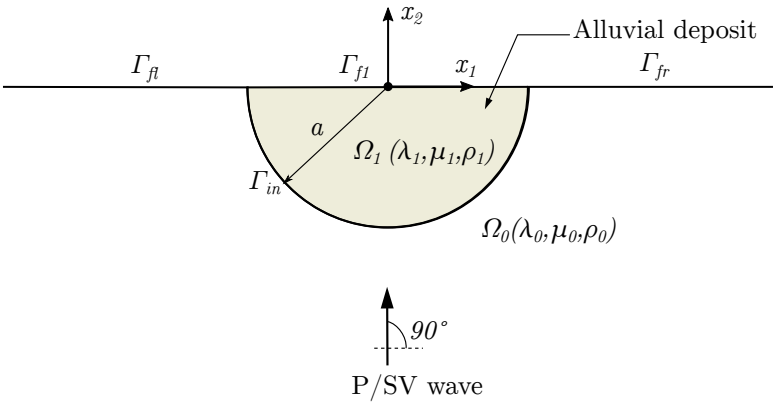

Fig. 2.10 An alluvial basin rested on a homogeneous elastic isotropic half-plane under vertically incident P/SV wave field

introduced as $\eta = 2a/l_w$, where l_w is shear wavelength given by $l_w = (2\pi/\omega)\, c_2^{(0)}$, where l_w is the shear wavelength and $c_2^{(0)}$ is the shear wave velocity of the homogeneous half-plane. The material properties of the half-plane and the alluvial deposit are chosen such that: Poisson's ratio $\nu^{(0)} = \nu^{(1)} = 1/3$, shear modulus $\mu^{(0)} = 6\mu^{(1)}$ and the mass density $\rho^{(0)} = 1.5\rho^{(1)}$, where the superscripts $^{(0)}$ and $^{(1)}$ represent the homogeneous half-plane and alluvial deposit, respectively.

Figure 2.11 shows the normalized horizontal and vertical displacement amplitudes along the free surface for vertically incident *P* and *SV* wave fields. A boundary element model is developed using 348 constant elements, where the top free surface is discretized between $\pm 10a$ with 300 elements and the semicircular interface with 48 elements. The material properties for the homogeneous half-plane are chosen as shear wave velocity $c_2^{(0)} = 300m/s$, Poisson's ratio $\nu^{(0)} = 1/3$ and the mass density $\rho^{(0)} = 2000kg/m^3$. The comparison of the results obtained with the results in Yeh et al. (2007) shows an excellent verification of the BEM solutions developed by the author.

2.6 Conclusion

BEM is formulated, developed, and verified for the simulation of seismic wave propagation in homogeneous and stratified elastic isotropic half-plane. The development is based on the existing BIE formulations for frequency domain fundamental solutions in elastic isotropic continua. The output is verified by comparison with the numerical and analytical solutions from existing benchmark problems. It is observed that BIEM can be implemented

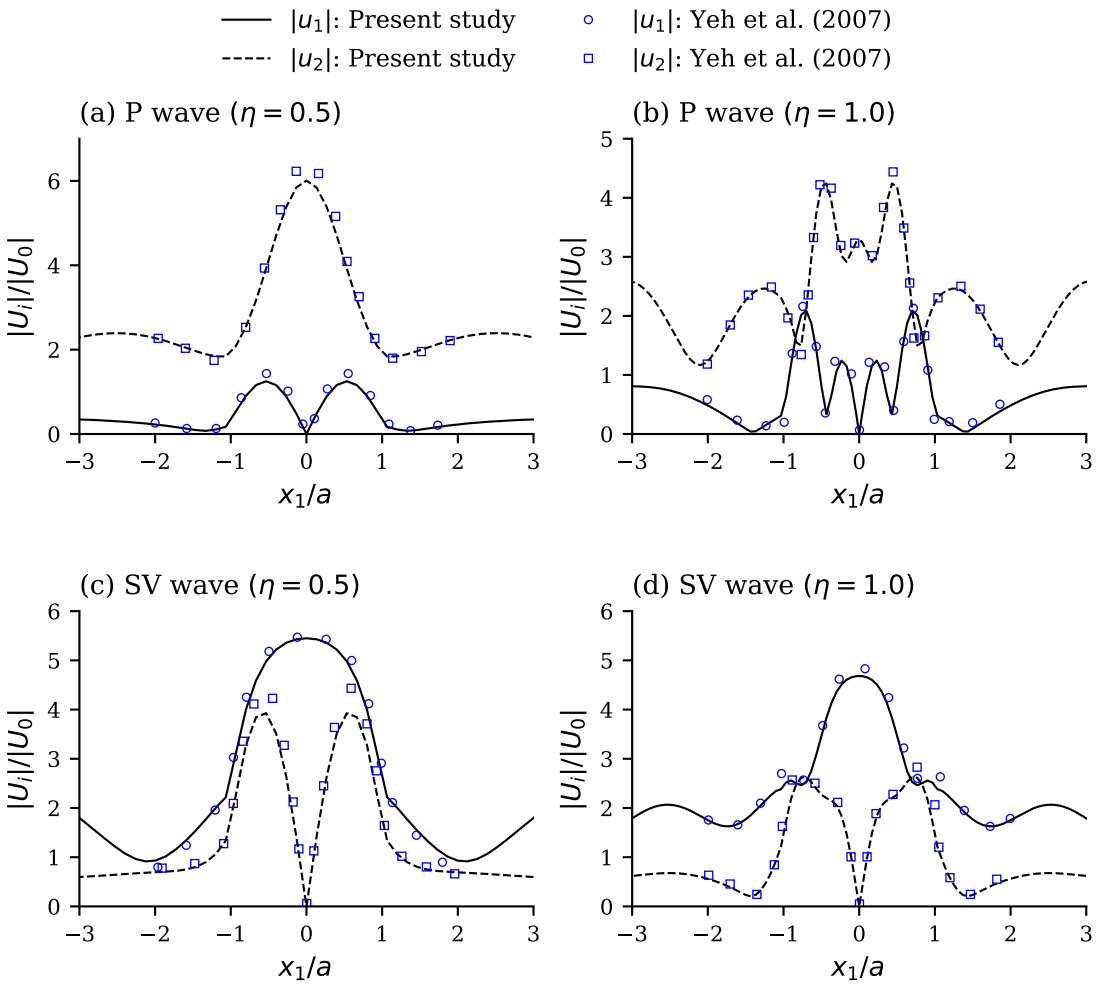

Fig. 2.11 Displacement amplitudes along the free surface normalized by the amplitude of the vertically incident time-harmonic waves in an alluvial basin rested in a homogeneous elastic isotropic half-plane **(a)** P wave ($\eta = 0.5$), **(b)** P wave ($\eta = 1.0$), **(c)** SV wave ($\eta = 0.5$) and **(d)** SV wave ($\eta = 1.0$). A comparison of the author's BEM solutions with the results in Yeh et al. (2007).

successfully to simulate the whole seismic path starting from the source of the seismic waves, traveling through the heterogeneous region from the source to the local geological region with its specific mechanical properties and geometry, containing different types of heterogeneities such as reliefs, cavities, layers, inclusions.

The observations in this chapter show that the existing boundaries have to be discretized to a considerable extent to get reasonably accurate solutions for multiple layers with finite depths and infinite extensions in the horizontal directions. The conclusion is two-fold: (a) The BIEM solutions need further optimization so that the models with more heterogeneities can be solved; (b) The computational efficiency of BEM needs improvement so that more

extensive models can be solved within a practically feasible duration. This chapter also serves as a preliminary verification of the BEM formulations used in the rest of the chapters, where the applicability of the mesh-reducing BEM is further extended for more complex engineering problems. The basic BEM formulation and the numerical implementation in this chapter provide the basis for further development to solve inverse problems and hybrid 2D dynamic soil-structure interaction models.

Chapter 3

A review of full waveform inversion of P-SV wavefield in frequency domain

3.1 Introduction

Exploration of the geological formation underneath the surface and determination of the physical parameters to the desired accuracy plays a crucial role in the successful numerical modeling and analysis of a geomechanical problem. FWI is gaining popularity in exploration geophysics because it delivers highly detailed information about the wave velocity of the subsurface based on seismic monitoring data. As the data obtained are based on the directly measured seismic signals, the estimated subsurface parameters become more reliable for further elastodynamic modeling of the geological region. Full waveform inversion is primarily common in domain-based methods such as FDM and FEM. The main objective of this chapter is to review, investigate and validate the full waveform inversion models by FDM to apply a similar strategy in optimizing the P-SV wavefield in mechanical models based on BEM. A state-of-the-art review of full waveform inversion is presented in Section 3.2. A seismic forward FDM using an optimized 9-point stencil is presented in Section 3.3. Inverse formulation of P-SV wavefield for seismic full waveform inversion is presented in Section 3.4. Section 3.5 briefly discusses the optimization strategies and BFGS algorithm. A short description of the numerical implementation in seismic monitoring of dykes is presented in Section 3.6.

3.2 State-of-the-Art: Full Waveform Inversion

The first introduction and numerical implementation of FWI was made in the 1980s. Pratt et al. (1998) mentioned that the first attempt at waveform inversion was made in 1983 by Lines & Kelly, who computed the partial derivatives of seismograms with respect to the coordinates of a wedge-shaped model using a numerical difference scheme via a finite difference forward modeling technique. The nonlinear inverse problem for seismic reflection data is solved by an iterative algorithm consisting of forward propagation of the actual sources and the time-reversed propagation of the data residuals in an acoustic approximation by Tarantola (1984a,b). The inversion algorithm is numerically implemented by Kolb et al. (1986) for 1D medium and by Gauthier et al. (1986) for 2D medium. The implementation of full waveform inversion for elastic waves is studied in Mora (1987), Tarantola (1988). Nonlinear inversion in a laterally invariant medium is presented in Pica et al. (1990). A comparison between traveltime tomography and full waveform inversion is made by Pratt et al. (2002), showing that the improved resolution is obtained in waveform methods. However, the robustness is reduced in waveform methods as compared to traveltime tomography. The time domain FWI approach is later implemented in the frequency domain approach in Pratt (1990b), Pratt and Worthington (1990). The performance of the frequency domain approach of FWI is optimized by parallel computation in Sourbier et al. (2009a,b).

FWI finds its application in various geophysical and engineering fields. Pratt (1999), Pratt and Shipp (1999) applied Full Waveform Inversion by ultrasonic measurement on a simple block model in a laboratory, which proved its efficacy in laboratory measurements. FWI is widely used for the inversion of: **(a)** acoustic waves in time domain Köhn (2011), Wei et al. (2014), Yang et al. (2018) and in frequency domain Ben-Hadj-Ali et al. (2008), Plessix (2009), Brossier et al. (2010), Malinowski et al. (2011), Jeong et al. (2012), **(b)** seismic waves for elastic isotropic or viscoelastic medium in time domain Köhn (2011), Fabien-Ouellet et al. (2017), Charara et al. (2000), Pan et al. (2020) and in frequency domain Brossier et al. (2009), Brossier (2011), Operto et al. (2013), Trinh et al. (2019), Pan et al. (2020). With the advancement in parallel processing capability of modern-day computers, FWI is gaining popularity in exploration geophysics. Some of the applications of FWI in nondestructive exploration geophysics can be found: for radially anisotropic structures by Fichtner et al. (2010), inversion of deep water bottom dataset by Plessix and Perkins (2010), seismic tomography of southern California crust by Tape et al. (2010), to reveal the structure of the European upper mantle by Zhu et al. (2012), for ocean bottom cable data by Operto et al. (2015). Wang et al. (2021) employed frequency domain acoustic FWI to acquire rock wave velocity in tunnels.

Traditionally, the steepest descent has been the choice of optimization method for most of the FWI algorithms. However, with the advancement of computers, other advanced optimization methods are being tested and implemented. Gauss-Newton and full Newton methods in frequency space seismic waveform inversion are presented in Pratt et al. (1998). Truncated Newton and quasi-Newton methods for full waveform inversion are implemented in Brossier et al. (2009), Brossier (2011), Métivier et al. (2013), Matharu and Sacchi (2019). Castellanos et al. (2015) used source encoding and second-order optimization methods and found that Limited-memory Broyden–Fletcher–Goldfarb–Shanno (l-BFGS) algorithm required the lowest computational cost. Pan et al. (2017) used l-BFGS preconditioned conjugate-gradient algorithm as Hessian-free Gauss-Newton full waveform inversion. Lee and Ha (2019) applied l-BFGS optimization in Laplace domain waveform inversion.

The state-of-the-art review shows that full waveform inversion is developed to a faster and more robust form by better optimization strategies, including quasi-Newton algorithms and global optimization methods. However, there are very limited studies of 2D elastic waveform inversion in the frequency domain for the inversion of all three parameters (P-wave velocity, S-wave velocity, and density) by using a quasi-Newton optimization algorithm.

3.3 Seismic forward model

3.3.1 FD discretization of wave equation

The frequency domain elastic wave equation (2.1) in 2D space can be restated for horizontal and vertical displacement components as:

$$(\lambda+2\mu)\frac{\partial^2 u_1}{\partial x_1^2}+\mu\frac{\partial^2 u_1}{\partial x_2^2}+(\lambda+\mu)\frac{\partial^2 x_2}{\partial x_1\partial x_2}+\left(\rho\omega^2-i\omega\upsilon\right)u_1+b_1=0 \tag{3.1}$$

$$\mu\frac{\partial^2 u_2}{\partial x_1^2}+(\lambda+2\mu)\frac{\partial^2 u_2}{\partial x_2^2}+(\lambda+\mu)\frac{\partial^2 u_1}{\partial x_1\partial x_2}+\left(\rho\omega^2-i\omega\upsilon\right)u_2+b_2=0 \tag{3.2}$$

where: $u(u_1,u_2)$ are displacement components; $b(b_1,b_2)$ are the body forces along Cartesian direction $x(x_1,x_2)$; λ, and μ are Lame constants; ρ is the mass density; and υ the viscous damping coefficient.

The numerical solution to the frequency domain elastic and scalar wave equations using FEM and FDM was developed as early as 1972 (Lysmer and Drake (1972)). Kelly et al. (1976) examined the homogeneous and heterogeneous formulation of the wave equation for modeling synthetic seismograms in a finite difference approach. A nine-point finite

difference stencil is found to be primarily used in finite difference implementation of seismic wave propagation in the frequency domain. A classic nine-point scheme, based on spatial approximations of Kelly et al. (1976), is developed in Pratt (1990a). Following this development, the 9-point scheme is continuously being optimized by various researchers so that the grid dispersion can be minimized with less number of grid points per wavelength. Jo et al. (1996) developed an optimal nine-point scheme using a rotated coordinate system and averaging the mass acceleration terms, where the phase velocity errors are minimized to obtain the optimization coefficients. Incorporating the method from Jo et al. (1996) and staggered-grid technique, Štekl and Pratt (1998) proposed an optimal nine-point scheme for 2D frequency-domain elastic wave equation. Chen and Cao (2016) presented an average-derivative optimal nine-point scheme for modeling frequency domain elastic wave equation. Li et al. (2018) proposed a general optimal scheme for modeling the frequency-domain elastic-wave equation. In this chapter, the average-derivative optimal nine-point scheme by Chen and Cao (2016) is used to model seismic wave propagation in FDM. The finite difference discretization of wave equations (3.1−3.2) using the nine-point average derivative stencils are included in Appendix A.

3.3.2 Initial and boundary conditions

The frequency domain wave equation does not consist of the time variable, and each frequency equation is independent of the others. Thus, the initial condition is inapplicable in modeling the frequency domain wave equation. For modeling geological domains and geo-structural interaction problems, the important boundary conditions are Sommerfeld's radiation condition and a traction-free surface. One of the shortcomings of the domain-based methods is that the boundaries often exist in the numerical model of a physically unbounded region. The general physical meaning of Sommerfeld's radiation condition in such boundary value problems is that the boundary in the numerical model is not supposed to reflect the outgoing waves. Numerically, this is achieved by damping the waves that arrive at the boundary. Traditionally, the waves are damped by absorbing boundaries and Perfectly Matched Layers (PML), among which the latter is more efficient. In PML, the damping of the waves is achieved by stretching the coordinates, which creates an exponential decay of the waves in the absorbing boundary frame. Berenger (1994) applied PML for absorption of electromagnetic waves. Details of unsplit convolutional perfectly matched layers can be found in Komatitsch and Martin (2007), Martin et al. (2008), Martin and Komatitsch (2009). The numerical implementation of PML for seismic FWI is found in Köhn (2011) in time domain and Köhn et al. (2017) in frequency domain. The implementation of PML in 2D finite difference grid for acoustic and visco-acoustic waves is found in Operto et al. (2009).

Chen and Cao (2016), Li et al. (2018) explain the implementation of PML along with 9-point finite difference stencil, see Appendix A.

3.3.3 Matrix formulation and FD solution

The discretized form of the wave equation in 2D for the displacement variables u_1, u_2 consists of $2n$ equations, where $n = n_1 \times n_2$ is the number of computational nodes; n_1 and n_2 represent the number of computational grids in Cartesian directions x_1 and x_2, respectively. Thus, two equations exist for each computational node, and the total system of linear equations takes the form:

$$\mathbf{S}\, u = \mathbf{f} \tag{3.3}$$

Where: $\mathbf{S}$ is called the impedance matrix of shape $(2n, 2n)$; $u(u_1, u_2)$ is the displacement vector; $\mathbf{f}$ is the vector of seismic source terms. It is worth noting that the elements of the matrix and vector are complex numbers. Each node in the finite difference grid contributes to two rows (corresponding to the two DOFs) of the matrix equation. Using the nine-point stencil, each node contributes to a maximum of $9 \times 2 = 18$ non-zero columns in each row. Depending upon the formulations, some of the elements among these 18 terms are zero, which for the average-derivative optimal formulation by Chen and Cao (2016) is 13. For this reason, the impedance matrix is a sparse banded matrix. The displacement vector u is a vector of size $2n$ corresponding to the two DOFs for n number of computational nodes. Similarly, the seismic source vector $\mathbf{f}$ corresponds to the displacement vector u in the size and the DOFs. It is worth noting that the elements of the vector $\mathbf{f}$ are all zero except for the nodes and the DOFs in which the seismic sources are applied.

3.4 Seismic inverse model

The inverse problem in seismic wave propagation is often referred to as full waveform tomography or FWI. The physical sense of seismic inversion can be understood as recovering the unknown physical parameters of geological or structural features based on seismic measurements. The seismic signals recorded in the receivers are the functions of the seismic sources and the path through which the wave propagates. Thus, the recorded signal should carry the information about the physical properties of the medium through which it has traveled. So, it is a systematic way of backtracking or estimating the physical parameters of the medium through which the wave is propagated based on seismic records. However, it is an inverse problem, and the solution may not be unique. Additionally, the inversion

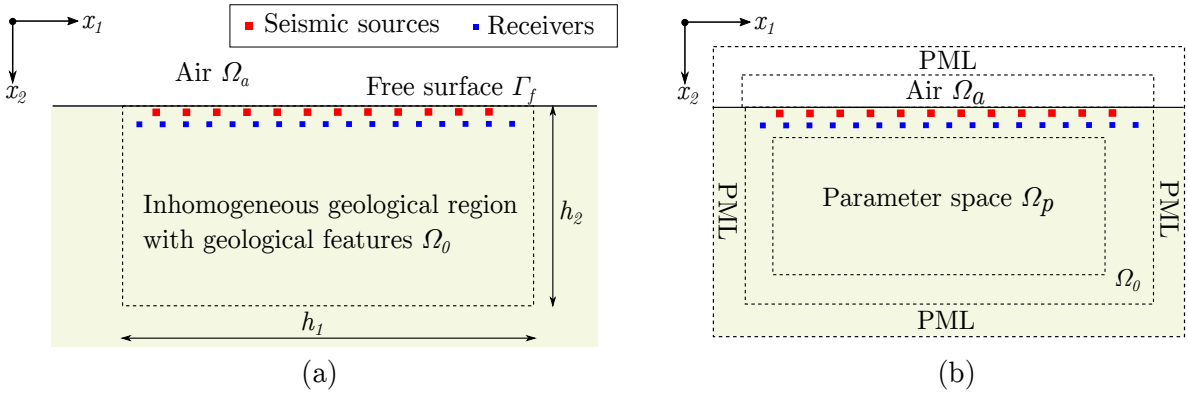

Fig. 3.1 A full waveform inversion model of a geological half plane: **(a)** physical model; **(b)** computational model.

procedure is expensive in terms of computational efficiency, and the solution may not always be possible.

3.4.1 Inverse formulation

Let us consider a geological region as shown in Figure 3.1. A block of width h_1 and depth h_2 is discretized with finite difference grids. The PML grids towards the edges in the numerical model represent the unbounded domain in the physical model. A free surface is considered by assigning the elastic properties of air. Consider seismic sources and the receivers in the respective locations as shown in Figure 3.1. The finite difference forward model for this problem, as defined in Section 3.3, can be represented by the system of linear equations (3.3). The system of linear equations for each discrete circular frequency ω is independent of the others. The amplitude of excitation is included in the source vector $\mathbf{f}$ at the node index corresponding to their Cartesian location and the Degree of Freedom (DOF) corresponding to the excitation direction. The system of linear equations is solved for vector u of length $2n$ for the total number of computational nodes n and two DOFs. Here, u is referred to as model displacement.

On the other hand, the displacements at the receivers, referred to as the observed displacement or observed data d, are obtained from the seismic investigation. Seismic full waveform inversion aims to minimize the difference between the modeled and the observed data by estimating the appropriate model parameters. The function of the data misfit is known as a misfit function or an objective function. The behavior of different types of objective functions for full waveform inversion in frequency and Laplace domains is compared in Shin and Ha (2008). The most commonly used objective function, also referred to as energy norm, is $\mathbf{l_2}$-norm and is defined as:

$$E(p) = \frac{1}{2} \sum_{k=1}^{N_\omega} \sum_{j=1}^{N_s} \sum_{i=1}^{N_r} |u_{ijk} - d_{ijk}|^2 \tag{3.4}$$

Where: $E(p)$ is the objective function of model parameter p that is to be estimated; N_r, N_s and N_ω are the total number of receivers, shots, and angular frequencies in the model; and ijk are the corresponding subscripts, respectively. The aim of the inverse problem is to minimize the value of the objective function $E(p)$ by searching the appropriate model parameters p. Numerically, the summations over the range of the shots $j = [0,\ N_s]$ and angular frequency $k = [0,\ N_\omega]$ are the sum of independent solutions, whereas the summation over the receivers $i = [0,\ N_r]$ is obtained from the solution of the same system of linear equations. For complex matrix algebra, the objective function can be defined as follows, see Pratt et al. (1998):

$$\delta d_i = u_i - d_i, \quad i = (1,2,3,.....,N_r) \tag{3.5}$$

$$E(p) = \frac{1}{2}\ \delta d^T\ \delta d^* \tag{3.6}$$

Where: δd is the vector of the differences between the modeled and the observed data; the subscript i represents the corresponding receiver node and the DOF; the superscript T represents the transpose; the superscript $*$ represents the complex conjugate of a complex-valued vector. The calculated objective function is a real-valued scalar, which can be summed over the shots and the frequencies to obtain the value of the objective function.

3.4.2 Parameter space

The medium parameters in the governing equations (3.1) and (3.2) are Lame constants λ, μ and mass density ρ. For the medium discretized in FDM λ, μ, and ρ are assigned to each of the nodes so that the total medium parameters are:

$$\lambda_{ij},\ \mu_{ij},\ \rho_{ij},\ \text{ where, } (i = 1,2,...,N_x);\ j = (1,2,...,N_z)$$

where: i and j are the grid indices in x and z directions, respectively; N_x and N_z represent the number of grids in the respective directions in the 2D finite difference grid. Normally, there are thousands of these parameters, and it is always wise to reduce the parameters that are already known or assumed to be known. Thus, p is a subset vector of the set of total medium parameters λ_{ij}, μ_{ij} and ρ_{ij}, see Figure **??**. When both Lame constants and density are to be inverted, the values are not of the same order, which results in a poorly scaled inverse model. For example, the order of λ and μ can be of the order of $10^{(7-10)}$ and that of

ρ is generally 10^3. To improve the scaling of the model, the parameters are normalized to the initial model such that:

$$\begin{aligned} \lambda_{ij} &= \lambda_{ij}^0(1+p_k), \\ \mu_{ij} &= \mu_{ij}^0(1+p_k), \\ \rho_{ij} &= \rho_{ij}^0(1+p_k) \text{ and} \\ k &= (1,2,3,....,N_p) \end{aligned} \tag{3.7}$$

Where: p_k is a set of new inversion parameters; N_p is the total number of parameters; k is the respective parameter index. The superscript ^{0} represents the initial medium parameters which are constant throughout the inversion procedure. This provides the flexibility to assign the initial value of all the elements in the parameter vector to zero and set the same bound for all the parameters in the search space while preventing the model from being poorly scaled. The sensitivity of the parameters may be further adjusted by using scalar multipliers to p_k in Equation (3.7). The choice of initial parameters is important for the convergence of the FWI model. The parameters are chosen in such a way that the initial assumption remains close to the expected output. The values are generally obtained from field experiments, known parameters from similar geological formations, or some previous experiences.

3.4.3 Frequency selection strategy

One of the advantages of the frequency domain approach of FWI is that each frequency is independent, and the computation can be performed only for the required frequencies. Additionally, a multi-scale inversion is possible that the inversion can be initially carried out for lower frequencies which gives a low-resolution image, and gradually the inversion in the higher frequencies can be done for high-resolution images. A frequency discretization method is proposed by Sirgue and Pratt (2004) where a much larger frequency sampling interval is taken for an efficient waveform inversion algorithm. The selection of frequency is based on wave numbers, and the inversion is done for a single frequency separately, starting from the lowest to the highest frequency in the range. Bunks et al. (1995) proposed the frequency overlap grouping method as an extension of the time domain multi-grid method. In the overlap grouping method, a small group of low frequencies is taken in the first step. Higher frequencies are added in every next step such that the lower bound is the same for each group, and the upper bound of the frequency is increased in every iteration. Individual grouping method of a frequency selection is employed by Pratt (1999) in which the frequencies sorted from low to high are grouped in many groups, and the inversion is applied for the group of

frequencies stepwise from low to high frequencies. Kim et al. (2011) has compared these strategies and shown that the individual grouping method, where the frequency increment is selected from the discretization method based on wave number, is found to be the most efficient. In the individual grouping method, the individual frequencies satisfy the wave number range as given in Equations (3.8−3.9), see Kim et al. (2011):

$$k_{z\min} = \frac{4\pi f}{c_0\sqrt{1+R_{\max}^2}} \tag{3.8}$$

$$k_{z\max} = \frac{4\pi f}{c_0} \tag{3.9}$$

Where: $k_{z\min}$ and $k_{z\max}$ are the minimum and maximum wave numbers considered; f is the frequency; c_0 is the minimum shear wave velocity in consideration; $R_{\max} = h_{\max}/z$ where $h_{\max}$ is half width of the model and z is the depth of the model. After getting the lowest and the highest frequencies from equation (3.8) and (3.9), the next frequencies are chosen by Equation (3.10).

$$f_{k+1} = f_k\sqrt{1+R_{\max}^2}, \;\; k = 1,2,3,..... \tag{3.10}$$

3.5 Optimization problem

The numerical goal of FWI is to minimize the objective function $E(p)$ defined in Equation (3.6). It is an optimization problem, and various minimization strategies exist, see Nocedal and Wright (2006). BFGS, a Quasi-Newton class of optimization method and a gradient-based method, is used in this chapter. Although several derivative-free methods exist, many optimization problems in computational mechanics and FWI do not succeed without the computation of gradients. Figure 3.2 presents a workflow diagram for full waveform inversion.

3.5.1 Computation of gradients

The computation of gradients is the heart of many optimization algorithms. This gives information about the direction towards which the objective function increases or decreases from the given point. Nocedal and Wright (2006) describes the methods for computation of gradients for general numerical optimization. The computation of gradients for FWI in FDM is described in Pratt et al. (1998). In this section, the gradients are derived in simple algebraic terms based on the description in Pratt et al. (1998).

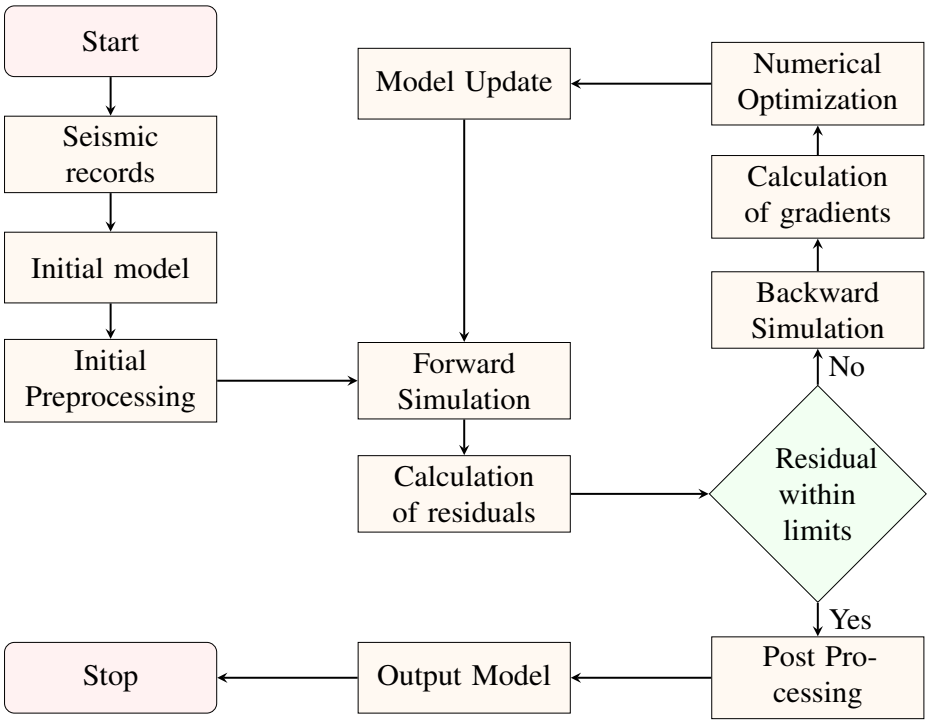

Fig. 3.2 A flowchart of Seismic Full Waveform Inversion by numerical optimization.

The gradient of objective function $E(p)$, formulated in Equation (3.6), is given by:

$$\begin{aligned} \nabla_p E &= \frac{\partial E}{\partial p} \\ &= \mathrm{Re}\left(\frac{1}{2}\,\frac{\partial}{\partial p}\left(\delta d^T\ \delta d^*\right)\right) \end{aligned} \tag{3.11}$$

The gradient of the objective function $\nabla_p E$ in Equation (3.11) is a vector of length N_p, where N_p is the number of parameters. Using the product rule of derivative, the gradient with respect to a single parameter p_i $(i = 1, 2, ..., N_p)$ is given by Equation (3.12).

$$\frac{\partial E}{\partial p_i} = \frac{1}{2}\,\mathrm{Re}\left(\delta d^T \frac{\partial\left(\delta d^*\right)}{\partial p_i} + \frac{\partial\left(\delta d^T\right)}{\partial p_i}\delta d^*\right) \tag{3.12}$$

Now, applying the following properties of complex numbers and matrix algebra, the gradient is expressed by Equation (3.13).

1. The derivative of a complex conjugate is the conjugate of the derivative, i.e. $\frac{\partial f^*}{\partial x} = \left(\frac{\partial f}{\partial x}\right)^*$
2. $\mathrm{Re}\left(A^*B\right) = \mathrm{Re}\left(AB^*\right)$ and $\mathrm{Im}\left(A^*B\right) = -\mathrm{Im}\left(AB^*\right)$
3. Properties of matrix transpose: $\left(A^T\ B\right)^T = B^T A$ and for a scalar $A^T = A$.

$$\frac{\partial E}{\partial p_i} = \mathrm{Re}\left(\left(\frac{\partial \delta d}{\partial p_i}\right)^T \delta d^*\right) \tag{3.13}$$

The solution of Equation (3.13) requires the computation of the partial derivative of δd with respect to the inversion parameters, which in the current problem definition are Lame constants λ, μ and density ρ of the medium at the concerned nodes in the finite difference grid. Taking partial derivative to Equation (3.5), where the vector d is the observed displacement thus are constants i.e. $\frac{\partial d}{\partial p_i} = 0$, the partial derivative formulation can be written as:

$$\frac{\partial \delta d}{\partial p_i} = \frac{\partial (u-d)}{\partial p_i} = \frac{\partial u}{\partial p_i} \tag{3.14}$$

$\frac{\partial u}{\partial p_i}$ is referred to as the partial derivative wavefield. Equations (3.13) and (3.14) show that the gradients can be obtained by computing partial derivative wavefields. In this chapter, the partial derivative wavefield is computed from the derivative of the impedance matrix with respect to the parameters as presented by Pratt et al. (1998). Taking the partial derivative of Equation (3.3) with respect to the parameter p_i, we get:

$$\frac{\partial (\mathbf{S}\, u)}{\partial p_i} = \frac{\partial \mathbf{f}}{\partial p_i} \tag{3.15}$$

The elements in the vector $\mathbf{f}$ in Equation (3.3) are seismic source terms, which are observed from the field, i.e., they are constant terms, and the derivatives are zero $\left(\frac{\partial \mathbf{f}}{\partial p_i} = 0\right)$. Inserting this to Equation (3.15) and applying the product rule of derivative, the following expression is obtained:

$$\mathbf{S}\frac{\partial u}{\partial p_i} + \frac{\partial \mathbf{S}}{\partial p_i} u = 0 \quad \text{i.e.} \tag{3.16}$$

$$\frac{\partial u}{\partial p_i} = -\mathbf{S}^{-1}\frac{\partial \mathbf{S}}{\partial p_i} u \tag{3.17}$$

Substituting Equation (3.17) into Equation (3.14) and applying the matrix transpose properties, the following expression is obtained:

$$\left(\frac{\partial \delta d}{\partial p_i}\right)^T = \left(\frac{\partial u}{\partial p_i}\right)^T = \mathbf{J^{-1}} \tag{3.18}$$

$$\text{where: } \mathbf{J^{-1}} = u^T \frac{\partial \mathbf{S}^T}{\partial p_i}\left(\mathbf{S^T}\right)^{-1} \tag{3.19}$$

Substituting Equation (3.18) in Equation (3.13) the necessary numerical values of the gradient of the objective function with respect to the i^{th} parameter is given as:

$$\frac{\partial E}{\partial p_i} = \text{Re}\left(\mathbf{J}^{-\mathbf{1}}\ \delta d^*\right) \tag{3.20}$$

And the gradient vector is given as:

$$\nabla_p E = \left[\frac{\partial E}{\partial p_1}, \frac{\partial E}{\partial p_2}, \frac{\partial E}{\partial p_3}, ..., \frac{\partial E}{\partial p_{N_p}}\right] \tag{3.21}$$

Numerically, the gradient computation becomes part of the forward problem. The computation of matrix $\mathbf{J}$ in Equation (3.19) consists of three terms. The matrix S is the same sparse impedance matrix in the forward problem, and the intermediate steps for its inversion can be taken from the solution for the forward problem. The displacement vector u is taken from the solution of the forward problem. The partial derivative term $\frac{\partial S}{\partial p_i}$ is derived by differentiating the impedance matrix S with respect to the nodal parameters. In finite difference operators of order 2, the operators are linear. Their derivatives are constant and localized to the node and its neighboring element. Though the matrix size can be huge, only a few elements are non-zero. The computation of the non-zero elements of matrix $\frac{\partial S}{\partial p_i}$ is presented in Appendix A.

Many works of literature explain this process of gradient computation as a back propagation method. The physical sense of the final expression (3.20) is the solution of the back propagated wave field. The matrix $\mathbf{J}$ in Equation (3.19) is equivalent to the backward impedance, and the vector d^* serves as the back-propagated source. The conjugate of the misfit function in the frequency domain is regarded as the time-reversed wave propagation from the adjoint sources.

3.5.2 BFGS algorithm

BFGS algorithm, named after the inventor of the algorithm Charles George Broyden, Roger Fletcher, Donald Goldfarb, and David Shanno, belongs to the Quasi-Newton class of optimization methods. Quasi-Newton methods, similar to the gradient descent method, require the gradient of the objective function to be computed in each iteration. However, compared to Newton's method, they do not require the second derivative of the objective function to be computed. Quasi-Newton methods are considered as a balance between Newton's method and the Gradient descent method. They are computationally much more efficient than Newton's method. On the other hand, the rate of convergence is higher compared to Gradient descent methods. BFGS algorithm is one of the most popular quasi-Newton methods. The

parameter update in each iteration of a quasi-Newton algorithm is expressed as Equation (3.22), see Nocedal and Wright (2006).

$$\begin{aligned} p_{(k+1)} &= p_k + \eta_k \, \delta p_k, \quad k = (0,1,2,3,.....,N_k) \text{ and} \\ \delta p_k &= -\mathbf{B_k}^{-1} \, \nabla_p E_k \end{aligned} \tag{3.22}$$

Where: p_k and p_{k+1} are the parameter vectors of size n in k^{th} and $k+1^{\text{st}}$ iterate, respectively; $\nabla_p E$ is the gradient of the objective function; η_k is the step length in k^{th} iterate; and $\mathbf{B_k}$ is a symmetric positive definite matrix of size $n \times n$ in k^{th} iterate. The analogous replacement to $\mathbf{B}_k$ in the gradient descent method is the Identity matrix $\mathbf{I}$, and that in Newton's method is the exact Hessian of the objective function $\nabla_p^2 E$. In BFGS algorithm, the inverse of matrix $\mathbf{B}$ is updated directly by Equation 3.23 avoiding the expensive computation of matrix inversion, see Nocedal and Wright (2006).

$$\mathbf{H}_{k+1} = (1 - \rho_k s_k y_k^T) \, \mathbf{H}_k \, (1 - \rho_k s_k y_k^T) + \rho_k s_k s_k^T \tag{3.23}$$

Where, $\mathbf{H}_k = \mathbf{B}_k^{-1}$ and the vectors ρ_k, s_k and y_k are given by:

$$s_k = p_{k+1} - p_k = \eta_k \delta p_k \tag{3.24}$$

$$y_k = \nabla_p E_{k+1} - \nabla_p E_k \tag{3.25}$$

$$\rho_k = \frac{1}{y_k^T s_k} \tag{3.26}$$

It can be observed from Equation (3.23) that the matrix $\mathbf{H}_k$, and hence $\mathbf{B}_k^{-1}$ updates in every iterate, is calculated from its value in the previous iteration. The matrix in the first step, i.e., $\mathbf{H}_0$, is often set as a multiple of identity, i.e., $\beta \mathbf{I}$, or the inverse of the Hessian $\nabla_p^2 E$.

3.5.3 Global and local minima

The goal of FWI or any other minimization problem is to find the global minima within the given bound of parameter space. The gradient-based optimization algorithms start with an initial model and follow the negative gradient towards the minimum possible value of the objective function, which might not be the most minimal value in the whole system under consideration. Instead, it might be a local minimum. One of the necessary conditions in this class of optimization algorithms is that the start model should be at such a point in the parameter space that the path in each iteration leads toward the global minimum. Failing to meet this criterion leads the model toward the local minimum and hence the false

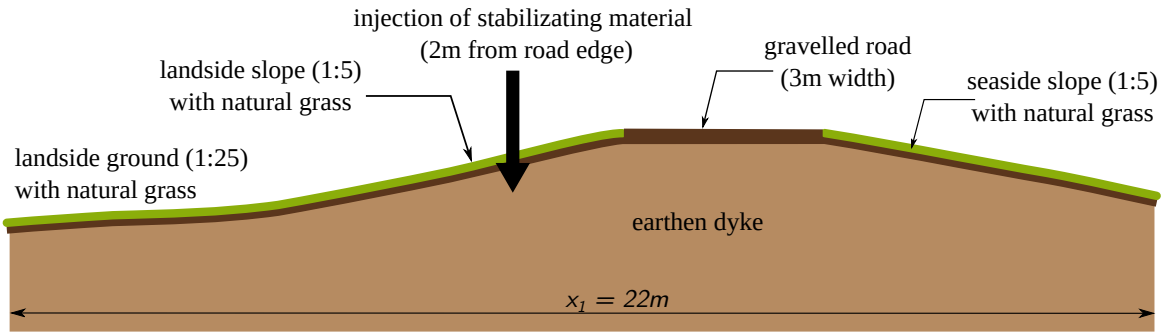

Fig. 3.3 A section of dyke considered for seismic monitoring and full waveform inversion

inversion results. This is one of the limitations of local optimization algorithms compared to global optimization algorithms. The study in this chapter is limited to the local optimization algorithm and requires the initial model near the global minima.

3.6 Numerical Application

This section aims to implement the discussed theoretical development into a numerical application for the inverse computation of FWI. A numerical simulation tool is developed in Python programming environment based on the theoretical formulations given above. For the simulation, an earthen dyke with a cross-section, as shown in Figure 3.3, is considered. An experiment for soil improvement by injection of chemical/biological material is done in the dyke. Seismic measurements are conducted along the surface as a means of non-destructive testing to obtain the information of the soil improvement around the region where the injection is done.

Table 3.1 The mean values of the medium parameters in the initial model of the dyke

Generations	Notation	$c_1(m/s)$	$c_2(m/s)$	$\rho(kg/m^3)$
Free surface	A	0.0	0.0	1.5
Dyke material	B	700	300	1200
Subsurface layer	C	1200	500	2000
Stabilized material	D	800	350	1250

The field measurements are obtained using 72-channel vertical seismic receivers with $0.25m$ spacing. The system is excited at $0.5m$ spacing by the shots of P waves acting in the vertical direction, out of which 8 representative shots are taken for FWI computations (see Figure 3.5). The seismic traces are bandpass filtered with a low corner frequency of $50Hz$

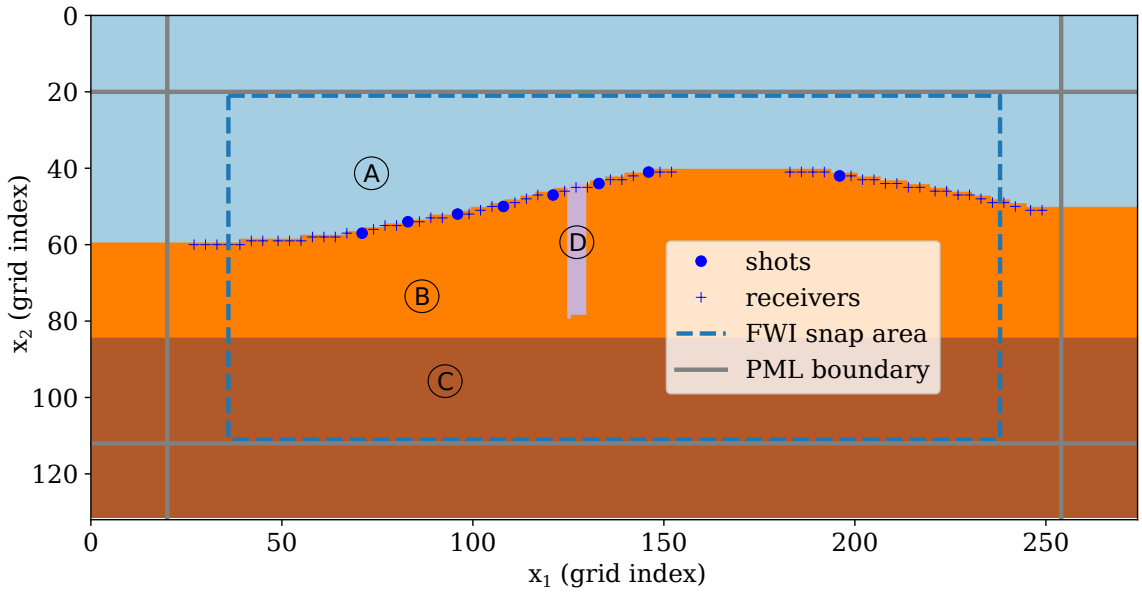

Fig. 3.4 A finite difference model of the dam with initial model parameters referred to Table 3.1.

and a high corner frequency of $120Hz$. The time history of the receiver seismogram located nearest to the source of excitation in each representative shot is presented in Figure 3.6a, and their frequency content normalized to its maximum amplitude in the considered range $(50-120Hz)$ in 3.6b. A finite difference model is developed for $22m$ range of horizontal extent (Figure 3.4). The number of grids taken in the horizontal and the vertical direction is $nx_1 = 276$, $nx_2 = 105$ with grid size $dx_1 = dx_2 = 0.08m$. 20 perfectly matched layers are used in all four directions. The medium parameters for the initial model are taken as random uniform distribution with the mean values as shown in Table 3.1 in a range of $[0.75, 1.25]$ of the mean values. Air parameters are taken with minimum density and zero wave velocities to avoid division by zero and provide free surface boundary conditions. The local optimization method requires the initial model to be close to the expected outcome to obtain an accurate estimate of the final model. A small inclusion is introduced in the start model at the area where the change in the material due to the soil stabilization curtain is expected.

The results of FWI are shown in Figure 3.7. The results show the material with higher primary and shear wave velocity and a similar density in the stabilized region of the dyke.

3.7 Conclusion

FWI, as applied to the geomechanical problems, is reviewed and implemented in a numerical simulation. A state-of-the-art review of FWI is performed, and a suitable strategy that can be

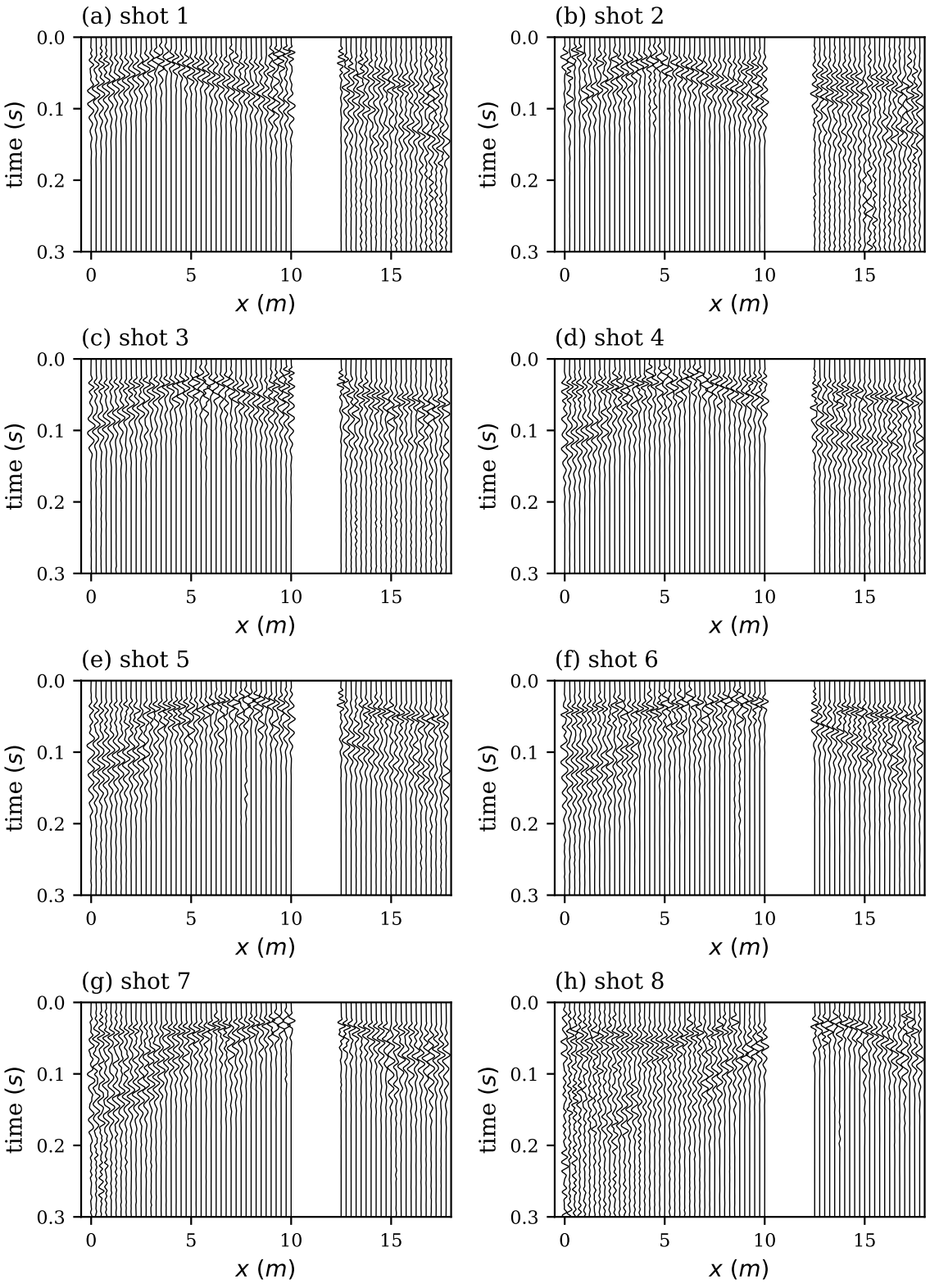

Fig. 3.5 Normalized seismic traces at receiver locations

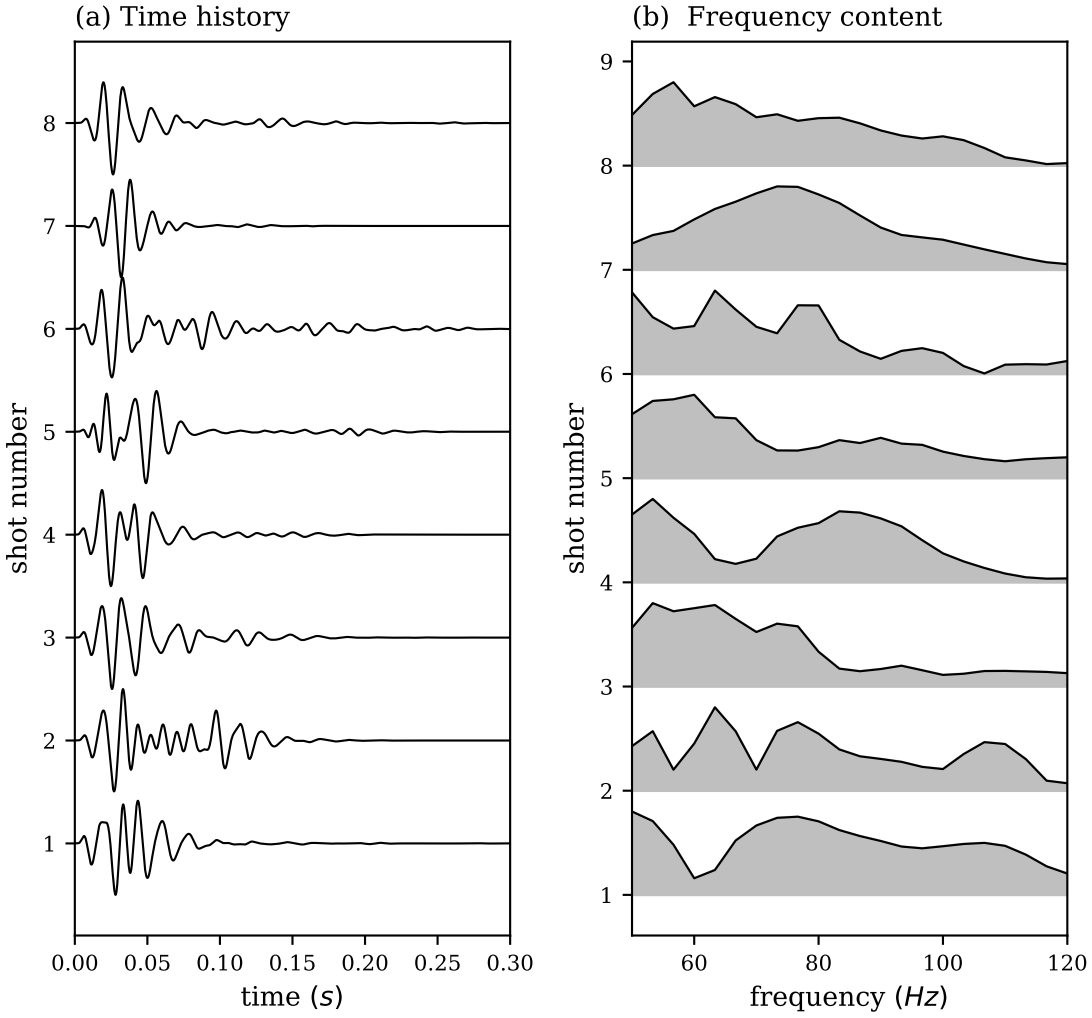

Fig. 3.6 The seismogram recorded at the receiver locations nearest to the source of excitation of the eight representative shots: *(a)* normalized time history, *(b)* frequency amplitudes between the window of $(50-120Hz)$ normalized by the maximum frequency in the given window.

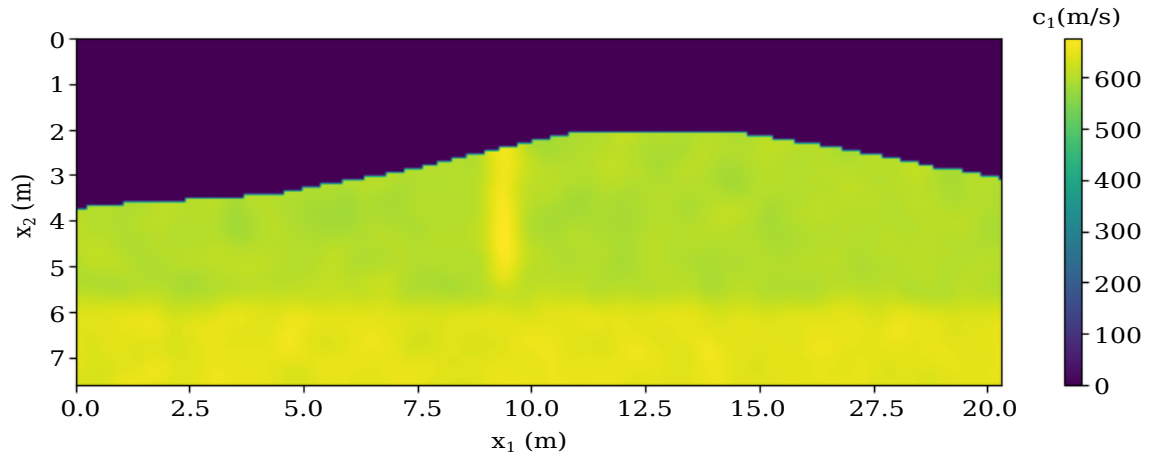

(a)

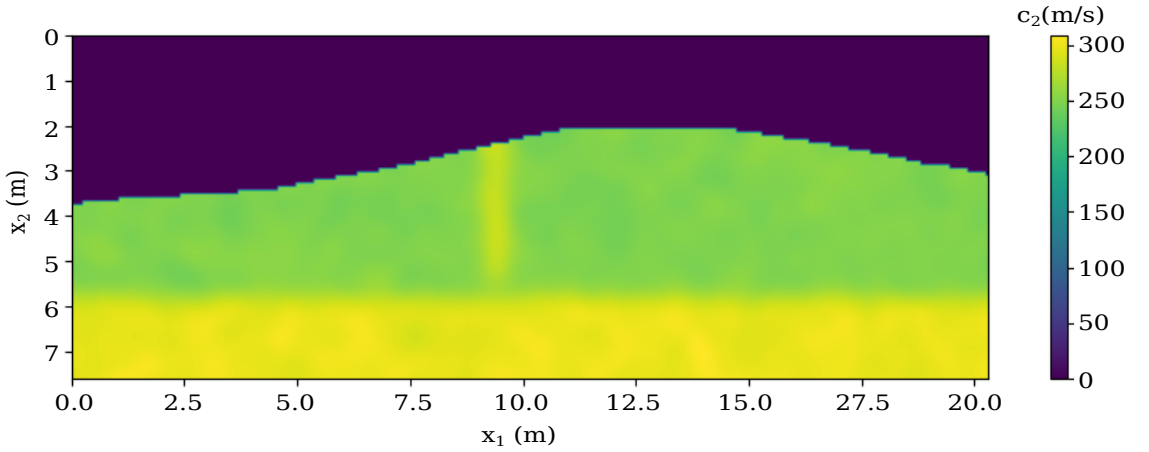

(b)

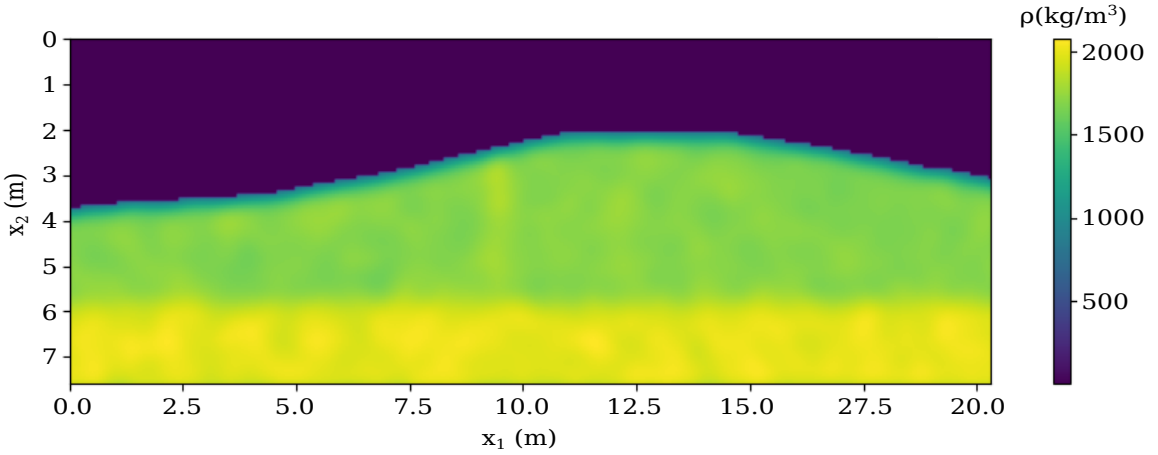

(c)

Fig. 3.7 Medium parameters in the dyke estimated by full waveform inversion: *(a)* P-wave velocity, *(b)* S-wave velocity, *(c)* Mass density

inherited into BEM is discussed. The mathematical derivations are developed into numerical simulation in a Python programming environment and applied for a seismic FWI study in a dyke stabilized with the injection of chemical substances or biological organisms. FDM is taken as the base numerical method, and the BFGS algorithm is considered a tool for numerical optimization. The computation of gradients by applying the partial differential to the impedance matrices is performed. This provides a basis for the computation of gradients in BEM, where the differential wave field can be calculated by differentiating the BEM influence matrices. It is also observed that the local optimization algorithms, including BFGS, depend on the start model. They often fail to converge to the global minima in a highly nonlinear search space. In summary, the basics of inverse simulation and the numerical computation of partial derivative wavefield are reviewed. The partial derivative wavefield and the gradient of the objective function are computed by the numerical differentiation of impedance matrices. A similar approach can be implemented in BEM to obtain the partial derivative wavefield. The system of BIEs in elastodynamics is a system of linear equations. However, due to the type of functions involved in fundamental solutions or Green's functions, the space of possible solutions is highly nonlinear. The local optimization algorithms may not be suitable for inverse problems in BEM. Supplementing the gradient-based search to global optimization algorithms may help to improve the convergence and hence obtain the solution to the BIEs in elastodynamics.

Chapter 4

Site-specific impedance function by particle swarm optimization in boundary element method

4.1 Introduction

BEM is based on the reformulation of a BVP presented by governing PDE into BIEs that are regarded as the exact solutions to the problem under consideration. The solution is obtained along the boundary by fitting the boundary conditions into the integral equations. The solutions inside the domain can be computed via integral representation formulae based on the solutions along the boundary. Due to these characteristics of BEM, the obtained solutions are highly accurate. On the other hand, the dimension of the problem is highly reduced because the method requires the discretization of the existing boundaries only. A major limitation of BEM in the dynamic analysis is that the fundamental solutions and Green's functions are limited for homogeneous media or the inhomogeneous ones with linear, quadratic, or exponential material gradients. However, the medium we encounter in nature is often inhomogeneous and irregular, which limits the applicability of BEM. On the other hand, there exist infinitely long boundaries along the surface of natural geological formations, and they may contain various known and unknown cavities, inclusions, or interfaces. These geometric features contribute to fully-populated BEM influence matrices of large dimensions, which demand higher computational resources. In summary, the limited applicability to the type of medium and the requirement to discretize the boundaries in the region, even if they are not of interest, can be regarded as some of the major limitations of BEM. These disadvantages can be overcome by numerical optimizations.

Numerical optimization is becoming popular in recent years for the improvement of numerical accuracy and computational efficiency. The modeling of elastic waves using BEM and the optimization techniques for seismic full waveform inversion are discussed in Chapter 2 and Chapter 3, respectively. However, the discussion in Chapter 3 primarily involves numerical methods other than BEM. The research in the field of numerical optimization in BEM for elastic waves is scanty. The local optimization methods, as mentioned in Chapter 3, often fail to converge to the accurate solution in the highly nonlinear space of BIEM solutions. PSO, a member of the global optimization class of numerical optimization methods, is considered in this chapter to avoid the solution being trapped in local minima. PSO has arisen from a radical idea of combining the social behavior of animal beings for scientific computations. Kennedy, a social psychologist, and Eberhart, an electrical engineer, worked together to develop an intelligent computational algorithm that is analogous to social interaction in a group of animals. Kennedy and Eberhart (1995) proposed the PSO simulations based on the social interaction within the flock of birds to find the best location for food. Since then, the method has continuously evolved and is applied as an intelligent optimization tool to solve complex scientific problems.

In recent years, PSO has been widely used in inverse modeling in geophysics and computational mechanics. Shaw and Srivastava (2007) implemented PSO on multilayered vertical electronic sounding and magnetotelluric data. Yuan et al. (2009) applied PSO for wavelet inversion in seismic data. Pekşen et al. (2014) implemented PSO in one-dimensional resistivity modeling for the interpretation of anisotropic media. Kaplanvural et al. (2020) implemented PSO for 1D waveform inversion of Ground Penetrating Radar (GPR) traces. Chen and Wang (2017) implemented PSO for seismic FWI, where the gradient of misfit is added in PSO update algorithm to improve the robustness of the algorithm. Moura et al. (2020) implemented PSO for seismic FWI of underground data in a progressive manner, starting from the known parameters on the surface, and interpreting the parameters step-wise towards the depth. In this chapter, the PSO algorithm is implemented in BEM to obtain the site-specific impedance functions. A small portion of the boundary, where the impedance function needs to be calculated, is discretized by boundary elements. The information about the remaining boundaries, interfaces, and inclusions that may or may not be known is discarded in the model. However, the effect of the discarded part of the boundary and material behavior is accounted for by optimization of the solution on the considered boundary. The optimized site-specific function is used for the computation of the impedance of the system, which can be further used for the computation of mechanical quantities such as displacement, traction, stress, strain, etc.

4.1.1 Significance of the study

BEM is one of the most accurate numerical methods, and it is efficient in modeling unbounded domains. However, the availability of solutions mainly for homogeneous media limits its applicability in many real-world problems. On the other hand, the fully populated BEM influence matrices are computationally expensive. The proposed optimization algorithm significantly reduces the size of the model only to the region of interest while accounting for the influence due to the remaining part of the physical model. Thus, the obtained impedance matrix remains significantly small and computationally efficient in further calculations. Similarly, the material inhomogeneity, which is normally impossible to model by BEM, can also be accounted for in the optimized solutions. The concept opens up a research space in optimization in BEM in the following directions: *(a)* using different forms of fundamental solutions and Green's functions for numerical optimization in BEM; *(b)* numerical optimization in the hybrid models where BEM and other numerical methods such as FDM, FEM, etc. are coupled.

4.1.2 Limitation of the study

The proposed method is a concept put forward in order to get the solution of BEM by using optimization rather than the direct solution. A modified form of the elastodynamic fundamental solution for a homogeneous elastic isotropic continuum is considered the basic function. The elastic wave parameters are reinterpreted as the function of the node-element pair and considered optimization parameters. The considered solution and the technique to choose the optimization parameters may not represent the solution in all the cases and have to be verified on a case-by-case basis before applying it to real-world problems. Extensions of this study to other types of functions and different parametrization techniques may improve the accuracy and applicability of the concept. Similarly, the proposed method directly optimizes the solution to obtain the site-specific optimized impedance matrices. It is worth noting that the realistic medium parameters are not recovered in the proposed method of inversion.

4.2 BIEM formulation

4.2.1 Problem statement

In a Cartesian coordinate system O_{x_1,x_2,x_3}, consider an elastic isotropic heterogeneous half-plane Ω_0 with an arbitrary free surface relief Γ_f and an arbitrarily shaped embedded cavity

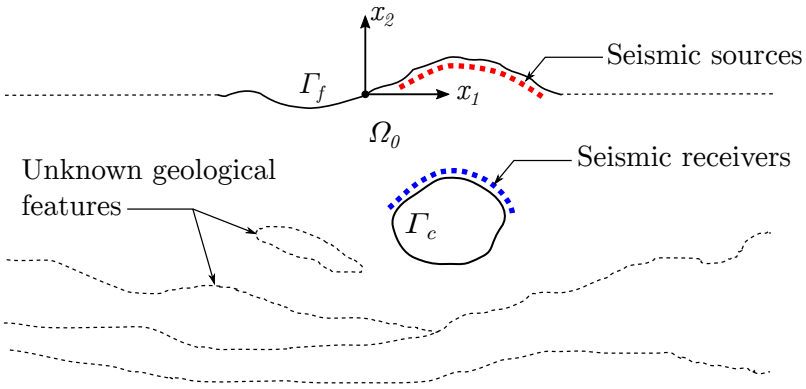

Fig. 4.1 An inhomogeneous and heterogeneous elastic isotropic half-plane

Γ_c (see Figure 4.1). There might be additional layers and interfaces which are less known or not important (denoted by dotted lines in the figure). The effective boundary for the domain Ω_0 is given by $\Gamma_0 = \Gamma_f \cup \Gamma_c$. All other boundaries and interfaces that may exist are not considered in the numerical model, which has to be addressed in the solution of the system differently, i.e., in the fundamental solution or Green's function. Seismic measurements are performed using near-surface P/SV seismic sources, and the seismic signals are measured using seismic receivers at the free surface and/or along the surface of the cavity. The seismic signals due to the near-surface dynamic point loads are denoted by observed displacements u_{obs}. The in-plane deformation state is considered in the plane $x_3 = 0$.

The objective here is to obtain the impedance function along the boundary Γ_0, which should include the effect of the unconsidered part of the boundaries, interfaces, and inclusions and the effect of the heterogeneous medium parameters. The objective includes neither the identification of the location of the additional boundaries, interfaces, and inclusions, nor the interpretation of the medium parameters.

4.2.2 BEM forward model

The BIEM formulation for the problem defined in Section 4.2.1 can be written as:

$$\begin{aligned} c_{ij}\, u_j(x,\omega) = &\int_{\Gamma_0} u^*_{ij}(x,\xi,\omega)\, t_j(\xi,\omega)\, d\Gamma - \int_{\Gamma_0} \tau^*_{ij}(x,\xi,\omega)\, u_j(\xi,\omega)\, d\Gamma \\ &+ f_{sj}\, \tilde{g}_s(\omega)\, u^*_{ij}(x,x_s,\omega) \\ &\text{for } x \in \Gamma_0;\ i = 1,2;\ j = 1,2; \text{ and } s = 1,2,.....,N_s \end{aligned} \tag{4.1}$$

Where: c_{ij} is the jump term dependent upon the geometry of the boundary at the collocation point x; u^*_{ij} and τ^*_{ij} are the displacement fundamental solution and its corresponding

traction, respectively; u_j and t_j are the displacement and the traction solutions, respectively, in the Cartesian direction j; f_{sj} is the magnitude of the s^{th} source acting at position x_s, and $\tilde{g}_s$ is the respective Fourier domain function of the time history function. N_s is the total number of sources acting on the system. Due to the consideration of elastic isotropic medium, the superposition of the system of BIEs for N_s number of sources is possible. However, the BIEs can be stated separately for each source or a group of sources as well.

The BIE (4.1) can be rewritten in matrix form as follows:

$$H(\omega)\, u(\omega) = G(\omega)\, t(\omega) + \zeta(\omega) \tag{4.2}$$

where,

$$\begin{aligned} H_{ij} &= c_{ij} + \hat{H}_{ij} \\ &= c_{ij} + \int_{\Gamma_j} \tau^*_{ij}(x, \xi, \omega)\, d\xi \end{aligned} \tag{4.3}$$

$$G_{ij} = \int_{\Gamma_j} u^*_{ij}(x, \xi, \omega)\, d\xi \tag{4.4}$$

$$\zeta^{(s)}_j = f_{sj}\, \tilde{g}_s(\omega)\, u^*_{sj}(x, x_s, \omega) \tag{4.5}$$

In Equations (4.3) - (4.4), the integrals are over the boundary Γ_j of j^{th} element.

4.2.3 Fundamental solution and Green's function

In Equation (4.1), apart from the solutions u_j and t_j, the reciprocal displacement and traction u^*_{ij} and τ^*_{ij} are unknown for a real inhomogeneous and heterogeneous medium. Depending upon the physical properties of the geological medium, various fundamental solutions and Green's functions in various homogeneous and inhomogeneous continua can be used as reciprocal displacement and traction for the solution of the system of BIEs, see Appendix C. The problem under consideration in this chapter may involve different types of inhomogeneity, such as the existence of unknown cavities, inclusions, geological layers, relief peculiarities, etc., which are unknown. Additionally, the boundary under consideration is not the complete boundary bounding the domain, which needs to be accounted for in the solution of the system. Due to the lack of analytically derived fundamental solutions for arbitrary inhomogeneous continuum, it is almost impossible to find the solution for such an arbitrary problem. The goal of the rest of this chapter is to estimate the solution of the system of BIEs by numerical optimization based on seismic measurements. The fundamental solution for a homogeneous elastic isotropic continuum is considered the basic functional expression. The optimization parameters are considered by parametrizing the wave velocities and density over the boundary

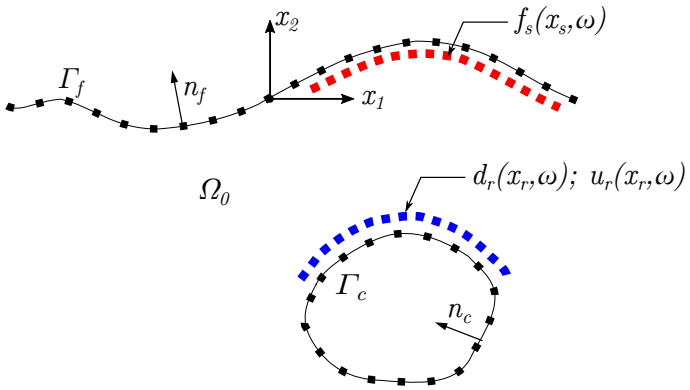

Fig. 4.2 A boundary element model for the problem geometry in Figure 4.1

mesh aiming to decrease the difference between the measured and the computational field variables.

4.3 Inverse formulation

4.3.1 Objective function

The problem formulation in Section 4.2 requires the estimation of the parameters or their functions based on the experimental observations. This can be achieved by minimization of the misfit between the observed and modeled data. Mathematically, it is an optimization (minimization) problem.

Let us consider the problem geometry in Figure 4.1, N_s number of seismic sources of magnitude $f_s(f_{s1}, f_{s2})$ at location $x_s(x_{s1}, x_{s2})$ with Fourier domain function $\tilde{g}_s(\omega)$ are applied simultaneously. The seismic response is measured in N_r number of displacement sensors located at x_r along the surfaces, whose Fourier domain amplitudes are known as the field data or the observed data, denoted by d_r. A boundary element model is developed assuming a homogeneous elastic isotropic half-plane with boundary $\Gamma_0 = \Gamma_f \cup \Gamma_c$, see Figure 4.2. The displacements at the receiver locations x_r are obtained from the numerical model, whose Fourier domain amplitudes are denoted by u. Provided that the numerical model with the assumed parameters represents the true physical model, the measured and the modeled outputs u and d should be equal. However, the problem under consideration is neither a homogeneous elastic isotropic continuum nor all the boundaries, and the interfaces in the physical model are accounted for in the numerical model. The function of the difference between the observed data and the modeled data is known as the misfit function or the

objective function. Among various types of misfit functions, L_2 or energy norm is widely used in geomechanics. The energy norm is given by Equation (4.6).

$$E(p) = \frac{1}{2}\ \delta d^T\ \delta d^* \tag{4.6}$$

Where: $\delta d = u - d$ is the misfit between the observed and the modeled data; the superscript * represents the complex conjugate. $E(p)$ is energy norm as the function of parameter p. The inversion parameter p, which is undefined until this point, is defined later in Section 4.3.2.

4.3.2 Optimization parameters

In domain-based methods like FDM or FEM, the inversion parameters are usually wave-velocities or Lame parameters and density at the individual grid points or nodes. However, in BEM, only the boundary is discretized, and the whole domain is homogeneous or a function of medium parameters. There are very few inhomogeneous functions with uniform, quadratic, or exponential material gradient over the depth, for which the fundamental solution and Green's functions are derived, see Appendix C. Hence, the problem is two-fold: *(a)* it is difficult to define the inversion parameters over the boundary, and *(b)* the recovery of the inhomogeneous medium parameters in the domain is not possible with the current state-of-the-art. However, many engineering problems in structural dynamics, soil dynamics, and soil-structural interaction problems require only the computation of the impedance of the system rather than recovering the physical parameters of the geological region. A quality estimate of the impedance at the concerned nodes, without knowing the medium parameters, is often necessary and sufficient for the mechanical analysis of the system. This section focuses on the computation of impedance matrices by the estimation of impedance function values based on parameters that may not have physical significance.

In Equations (4.2) - (4.5), the influence matrices G, H and vector ζ are the functions of reciprocal displacement or traction, which in turn are the functions of the position and the medium parameters. Thus, estimation of reciprocal displacement and traction u^* and τ^* gives the influence matrices and hence the impedance of the system. Let us define a functional expression of displacement fundamental solution u^* and its corresponding traction τ^*, which is presented by Equation (4.7), having in mind the expressions (D.1−D.6) for a homogeneous elastic isotropic medium.

$$\beta_{ij}^* = f(X, p) \tag{4.7}$$

Where: $\beta_{ij}^{*} \in \left(u_{ij}^{*}, \tau_{ij}^{*}\right)$ denotes the reciprocal displacement and traction terms; $X \in (x, \xi, x_s)$ is the positional argument and $p \in (c_1, c_2, \rho)$ are wave velocities and density of the homogeneous elastic isotropic half-plane; i, j are the row and the column indices in the influence matrices.

In the fundamental solution for homogeneous elastic isotropic continuum, see Equations (D.1−D.6), the medium parameters c_1, c_2 and ρ are constant for all equations in the system of BIEs. Now, the equations are modified such that the medium parameters are different in each equation in the system of BIEs. By applying this assumption, the parameters do not represent the wave velocities and the density but are mere complex mathematical constants. The further aim is to estimate the optimum values of these parameters such that the misfit of the solution of the system of BIEs and the measured quantity from experimental data is minimized to the desired accuracy. For i^{th} node and j^{th} element pair in the BEM model, Equation 4.7 can be written as:

$$\beta_{ij}^{*} = f(X, p_{ij}) \tag{4.8}$$

Where: $p_{ij} \in \left(c_{1ij}, c_{2ij}, \rho_{ij}\right)$ represent the elastic isotropic parameters for each node pairs ij along the boundary. Though these parameters are derived from wave velocities and the mass density of the homogeneous elastic isotropic medium, now they do not necessarily bear physical meaning. With this assumption, the fundamental solution for a homogeneous elastic isotropic continuum can be modified as follows:

$$u_{ij}^{*}(x, \xi, \omega) = \frac{1}{2\pi\rho_{ij}c_{2ij}^{2}} \left[\psi\, \delta_{ij} - \chi\, r_{,j}\, r_{,i}\right] \tag{4.9}$$

$$\begin{aligned} \tau_{ij}^{*}(x, \xi, \omega) \;=\; & \frac{1}{2\pi} \left[\left(\frac{\delta\psi}{\delta r} - \frac{\chi}{r}\right)\left(\delta_{ij}\frac{\delta r}{\delta n} + r_{,i}\, n_{,j}\right) - 2\frac{\chi}{r}\left(r_{,j}\, n_i - 2r_{,i}\, r_{,j}\frac{\delta r}{\delta n}\right)\right] \\ & - \frac{1}{2\pi}\left[2\frac{\delta\chi}{\delta r}\, r_{,i}\, r_{,j}\frac{\delta r}{\delta n} - \left(\frac{c_{1ij}^{2}}{c_{2ij}^{2}} - 2\right)\left(\frac{\delta\psi}{\delta r} - \frac{\delta\chi}{\delta r} - \frac{\chi}{r}\right) r_{,j}\, n_i\right] \end{aligned} \tag{4.10}$$

Where, the functions ψ and χ are given by:

$$\psi = K_0(z_{2ij}) + \frac{1}{z_{2ij}}\left[K_1(z_{2ij}) - \frac{c_{2ij}}{c_{1ij}}\, K_1(z_{1ij})\right] \tag{4.11}$$

$$\chi = K_2(z_{2ij}) - \frac{c_{1ij}^{2}}{c_{2ij}^{2}}\, K_2(z_{1ij}) \tag{4.12}$$

c_{1ij} and c_{2ij} are the relationship between the field and the source points equivalent to the longitudinal and shear wave velocities of the medium, respectively; ρ_{ij} is the parameter equivalent to the mass density of the medium; i and j are the indices for the collocation node and the field point, respectively; $r = |x - \xi|$ is the distance between collocation (source) point and the integration (field) point along the element; $z_1 = i\omega r/c_{1ij}$, $z_2 = i\omega r/c_{2ij}$, $K_n(z)$ and $K_n(z)$ are the modified Bessel functions of the second type of order n for imaginary argument z, see Bateman (1953). As the parametric replacement of c_1, c_2 and ρ are assumed to be of similar numerical characteristics, the singularity and the asymptotic behavior of these fundamental solutions still behave in a similar manner to that mentioned in Section 2.3.2.

The inversion parameters now are $p = \{c_{1ij}, c_{2ij}, \rho_{ij}\}$. p is a vector of size $3n^2$, where n is the number of boundary nodes in the BEM model.

4.3.3 Particle swarm optimization

Standard PSO algorithm

In PSO algorithm, each particle in the swarm follows an iterative update strategy to improve its position. Consider n number of particles with m number of dimensions. The dimension of the swarm corresponds to the number of parameters in the defined problem. The position and the velocity of the swarm at k^{th} generation are given by $x_{ij}^{(k)}$ and $v_{ij}^{(k)}$, respectively, where $i = \{1, 2, ..., n\}$ and $j = \{1, 2, ..., m\}$. The corresponding update formula for the standard PSO is given by:

$$v_{ij}^{(k+1)} = w\, v_{ij}^{(k)} + c_1\, r_1 \left(pbest_{ij}^{(k)} - x_{ij}^{(k)} \right) + c_2\, r_2 \left(gbest_{ij}^{(k)} - x_{ij}^{(k)} \right) \tag{4.13}$$

$$x_{ij}^{(k+1)} = x_{ij}^{(k)} + v_{ij}^{(k+1)} \tag{4.14}$$

Where: $pbest_i$ is the best position the i^{th} particle has ever found in its search history, and $gbest_i$ is the global best position, i.e., the best position all the particles in the swarm have ever searched; w is a constant referred to as the inertia weight; the constants c_1 and c_2 are the acceleration coefficients. r_1 and r_2 are random numbers in range $[0, 1]$.

PSO parameter selection and enhancement

PSO algorithm is sensitive to the parameters such as inertia weight and acceleration coefficients. Various strategies are found to be developed to solve complex optimization problems. Clerc and Kennedy (2002) studies the PSO convergence by focusing on an individual particle update and proposes the parameter for different conditions from algebraic and analytical

points of view. As a strategy of using variable inertia weight in the PSO update formula, a comparison between chaotic linear descending and chaotic random inertia weights is made in Feng et al. (2007). Dai et al. (2021) uses total variation regularization projection constraints in PSO in GPR inversion studies, in which the acceleration coefficients are chosen based on the studies in Clerc and Kennedy (2002) and chaotic inertia weights studied in Feng et al. (2007). Jaberipour et al. (2011) studies PSO for solving a system of nonlinear equations, where in addition to the standard PSO algorithm, the worst particle in each iterative step is identified, and a random component of the *pbest* position of the particle is updated with a partial differential of the cost function. The addition of gradient terms in the PSO update formula to speed up the convergence of FWI in FDM can be found in Chen and Wang (2017). Adaptive immune PSO for FWI is proposed in Chen et al. (2017), in which the particles are updated by selection, crossover, and mutation operations based on affinity. Considering the highly nonlinear nature of the solution space of the system of BIEs under consideration, the following strategy is adopted in this study.

(i) *Inertia weights and cognitive constants:* The strategy allows the individual particles to explore the random space within the given bounds and be less affected by personal and global best in the initial stage. After exploring the search space with higher inertia weights, the gradual increase in cognitive terms and the decrease in inertia weight guides the particles toward the global minima. For this, the total number of allocated generations is divided into four stages, and the inertia weights and the cognitive constants are chosen as given in Table 4.1.

(ii) *Gradient of the objective function:* In addition to the standard PSO update by Equations (4.13−4.14), the personal best positions of some of the particles are updated with the gradient of the objective function and random step length. The strategy is inspired by the concept of solving the system of nonlinear equations in Jaberipour et al. (2011). This guides the individual particles towards the local minima about the *pbest* position. In the space with a high concentration of local minima, the update of the particle with random step length may overshoot the local minima and hence may increase the misfit of the particle. Thus, to save the particles with better *pbest*, this update is carried only to the 50% of the population with the worst *pbest* values in each iteration. In addition to the standard update by Equations (4.13−4.14), the *pbest* positions of the worst particles in each iteration are modified by Equation (4.15).

Table 4.1 Variation of PSO parameters over generations for particle swarm optimization in BEM

Generations	w	c_1	c_2	c_3
0 - 25%	0.95	0.3	0.1	0.2
25 - 50%	0.8	0.4	0.15	0.2
50 - 75%	0.6	0.8	0.2	0.2
75 - 100%	0.4	0.8	1.2	0.2

$$pbest(p)_{ij}^{(k+1)} = pbest(p)_{ij}^{(k+1)} - \; c_3 \; r_3 \; \nabla_p E \;\; \text{where } p \in \{50\% \text{ of the worst } pbest.\} \tag{4.15}$$

Where, $\nabla_p E$ is the gradient of the objective function defined in Section 4.3.4.

The following algorithm is adopted for particle swarm optimization in this study, see Figure 4.3:

(i) Generate BEM mesh for the boundary where impedance function is desirable.

(ii) Generate the random initial position and velocity. Also, include a homogeneous elastic isotropic model in the initial population.

(iii) Compute the objective function from Equation (4.6) as the cost function for the forward P-SV wavefield problem and determine *pbest* for each particle and *gbest* in the swarm.

(iv) Update the particle velocities using Equation (4.13).

(v) Update the particle positions using Equation (4.14).

(vi) Determine 50% of the particles with worst *pbest* values by comparing the particle best costs and calculate the gradient of the objective function at the *pbest* position using Equation (4.16).

(vii) Update the *pbest* positions of the chosen particles for gradient directions using Equation (4.15).

(viii) Go to step 3 and repeat the process until the desired convergence or the abort criteria are obtained.

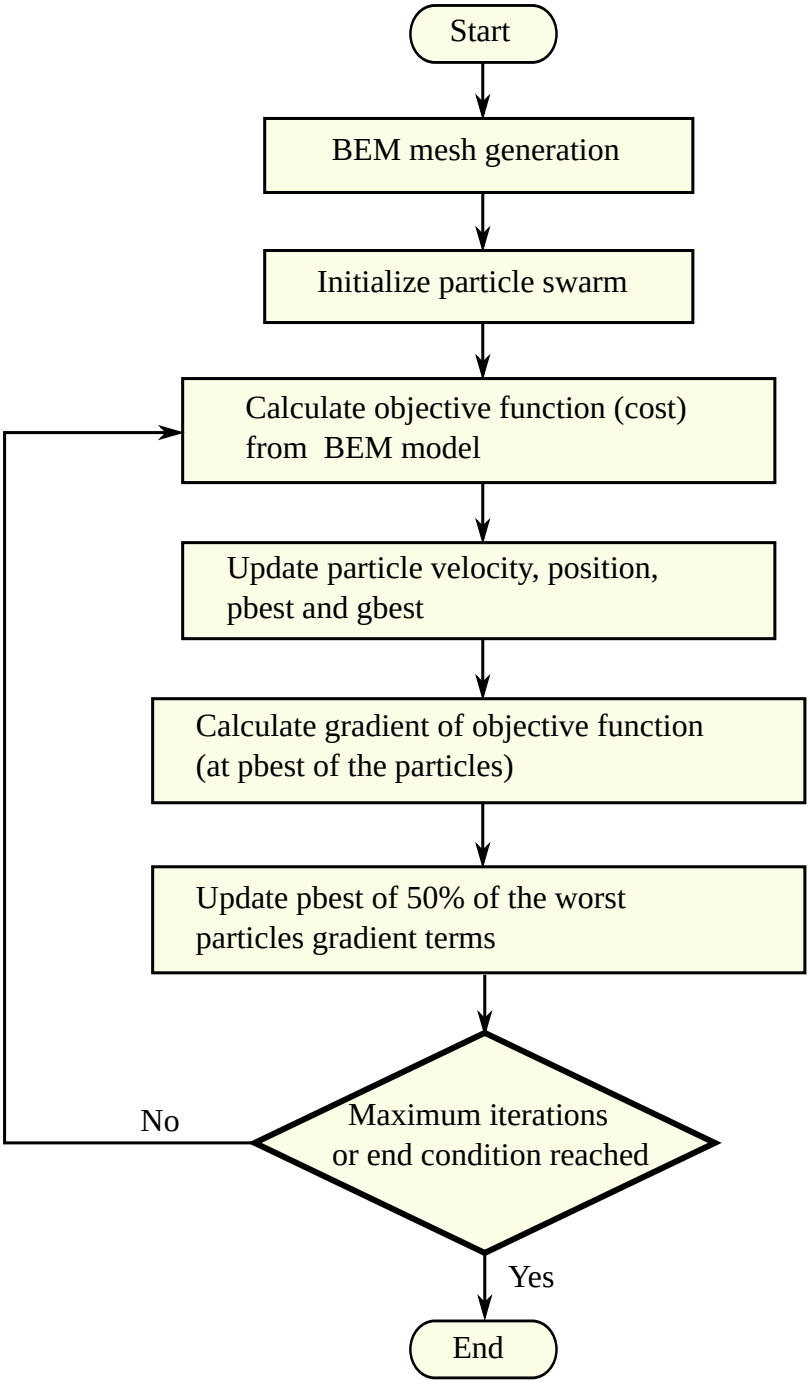

Fig. 4.3 A flowchart for the algorithm of particle swarm optimization in BEM.

4.3.4 Computation of Gradients

The gradient of the objective function can be computed using a similar concept as in Equations (3.11−3.13) in Section 3.5.1. The gradient of the objective function in Equation (4.6) can be expressed as:

$$\begin{aligned} \nabla_p E &= \frac{\partial E}{\partial p} \text{ and} \\ \frac{\partial E}{\partial p_k} &= \mathrm{Re}\left(\left(\frac{\partial u}{\partial p_k} \right)^T \delta d^* \right) \end{aligned} \tag{4.16}$$

Where: $\delta d = u - d$ is the misfit between the model displacement u and the observed displacement in field d; p_k is the inversion parameter, such that $p \in \{c_{1ij}, c_{2ij}, \rho_{ij}\}$.

$\frac{\partial u}{\partial p_k}$ may be referred to as the derivative wave field.Taking partial derivative of Equation (4.2) with respect to the parameter p_k, the following expression is obtained:

$$\frac{\partial (H\, u)}{\partial p_k} = \frac{\partial (G\, t)}{\partial p_k} + \frac{\partial \zeta}{\partial p_k} \tag{4.17}$$

Applying the product rule of derivative and constant traction boundary condition, the partial derivative equation reduces to:

$$\frac{\partial u}{\partial p_k} = H^{-1} \left(t \frac{\partial G}{\partial p_k} + \frac{\partial \zeta}{\partial p_k} - \frac{\partial H}{\partial p_k}\, u \right) \tag{4.18}$$

Taking partial derivatives of (4.3) and (4.5) with respect to parameter p_k and applying Leibniz integral rule, the following partial derivative terms are obtained:

$$\frac{\partial H_{ij}}{\partial p_k} = c_{ij} + \int_{\Gamma_j} \frac{\partial}{\partial p_k} \left(\tau^*_{ij}(p_k, x, \xi, \omega) \right)\, d\xi \tag{4.19}$$

$$\frac{\partial G_{ij}}{\partial p_k} = \int_{\Gamma_j} \frac{\partial}{\partial p_k} \left(u^*_{ij}(p_k, x, \xi, \omega) \right)\, d\xi \tag{4.20}$$

$$\frac{\partial \zeta_j^{(s)}}{\partial p_k} = f_{sj}\, \tilde{g}_s(\omega)\, \frac{\partial}{\partial p_k} \left(u^*_{sj}(p_k, x, x_s, \omega) \right) \tag{4.21}$$

It is observed from Equations (4.19−4.21) that the partial derivative wave field can be computed by the computation of the partial derivatives of the reciprocal displacement and traction. It can be noted from Equations (4.9−4.12) that the equation for the ij^{th} element depends only on ij^{th} parameter in the parameter space. Hence, the partial derivative of the matrices consists of only a single non-zero element. The partial derivatives of the fundamental

solution for homogeneous elastic isotropic medium with modified elastic isotropic parameters c_{1ij}, c_{2ij} and ρ_{ij} in Equations (4.9-4.12) are derived in Appendix D.

4.4 Numerical studies

The proposed concept of BEM optimization using PSO is studied with synthetic examples in a low-frequency regime. The synthetic data are generated using the BEM solution developed in Chapter 2, representing the true field data for P-SV wavefield in frequency domain. The backend module of Pyswarms package (Miranda (2018)) is taken as the basis for the implementation of PSO. The inversion is done by keeping the mass density constant, and the optimization is done on the wave velocity-related parameters.

4.4.1 Numerical study A: Homogeneous half-plane with multiple cavities

Consider a homogeneous elastic isotropic half-plane Ω_0 with elastic medium parameters: Young's modulus of Elasticity $E = 1.5e+9N/m^2$, Poisson's ratio $\nu = 0.3$ and mass density $\rho = 1700kg/m^3$. Let us consider five cavities of radius $a = 2.0m$ arranged as shown in Figure 4.4. The top row of the cavity is located at a depth of $2a$ from the free surface. The cavities are uniformly spaced at $4a$ and $2a$ distances in horizontal and vertical directions, respectively. The region of interest for the computation of impedance is along the free surface in the range of $x_1 \in \pm 7m$. The remaining part of the free surface and the cavities have an influence on the impedance along the boundary of interest. However, the impedance along these boundaries is not of interest to the intended application.

(a) Synthetic data generation by BEM simulation:

Let us consider three seismic sources at depth $0.1m$ and $(x1 = -7.5m, 0.5m, 8.5m)$. 10 seismic receivers are placed along the surface between $x_1 = [-4.5m, 4.5m]$ at a spacing of 1.0m. The physical model in Figure 4.4 is simulated using BEM, where the BEM model is discretized with a total of 370 (40 along the free surface in $x_1 \in \pm 20m$ and 5×66 along the cavities) boundary elements with constant shape function. The displacements computed at the receiver locations of the known model are considered synthetic seismic data for the seismic inverse model in the following section.

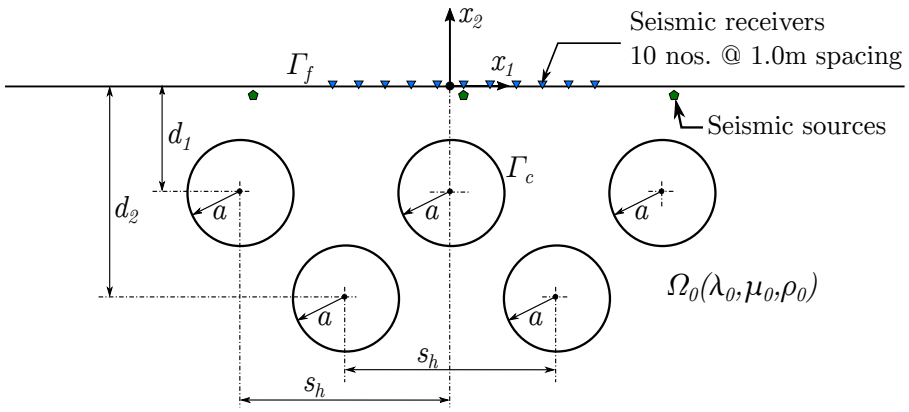

Fig. 4.4 A homogeneous half-plane with multiple circular cavities considered for the generation of synthetic data for PSO application in BEM.

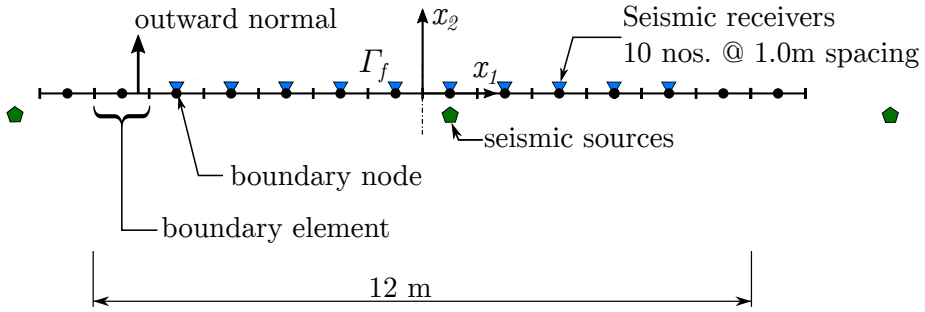

Fig. 4.5 A reduced BEM model of the physical model in Figure 4.4 considered for inverse formulation by PSO.

(b) Seismic inverse model:

The objective of this model is to take only the region of interest and compute the impedance of the system without considering the remaining features. However, the effect of the remaining free surface, the cavities, and the material properties of the domain are accounted for. A BEM model is developed by discretizing the free-surface boundary in $x_1 \in \pm 7m$ with 14 constant boundary elements, see Figure 4.5. The frequency dependent displacements at the receiver locations in the true model are taken as field data. PSO is implemented with 400 particles of dimension 200 over 2000 generations. The computation is done for natural frequencies $5Hz$, $10Hz$, $15Hz$, and $20Hz$. The evolution of the misfit function in the computation is shown in Figure 4.6. It can be observed that the residual error in the optimized model is reduced to around 2.5% at $5Hz$ and increases with the increase in frequency. The misfit is found to be around 8% at $20Hz$ frequency. The distribution of the estimated parameters in

the solution is presented as the factor of homogeneous medium parameters in Figure 4.7. The solution by PSO is used to compute the displacement along the free surface due to a seismic source of unit amplitude at position $x_{s1} = (-2.0m, -0.1m)$. A comparison of the displacement amplitudes along the free surface normalized to the amplitude of the seismic source computed using the optimized model and the synthetic true model is presented in Figure 4.8.

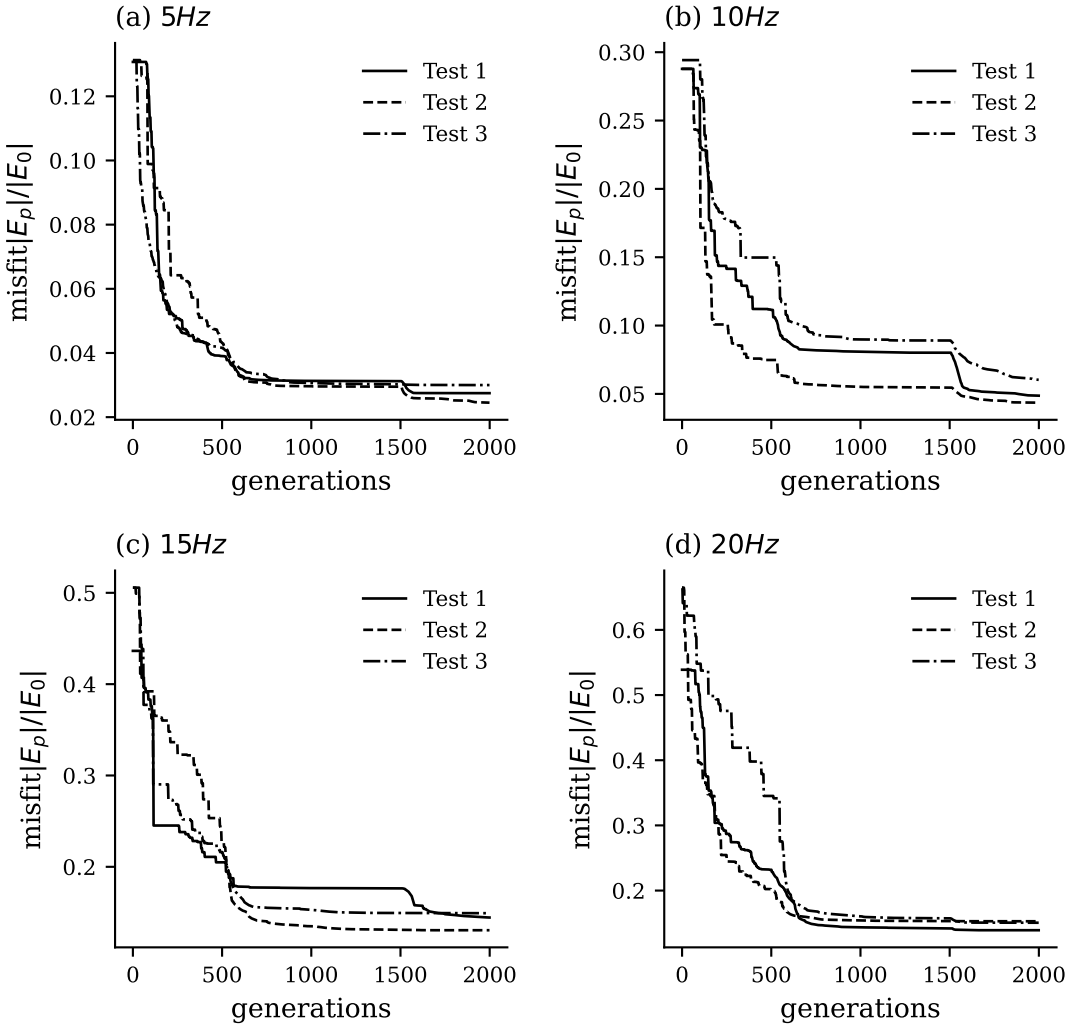

Fig. 4.6 The evolution curves for the misfit functions normalized to the energy in a homogeneous half-plane with multiple circular cavities at different excitation frequencies.

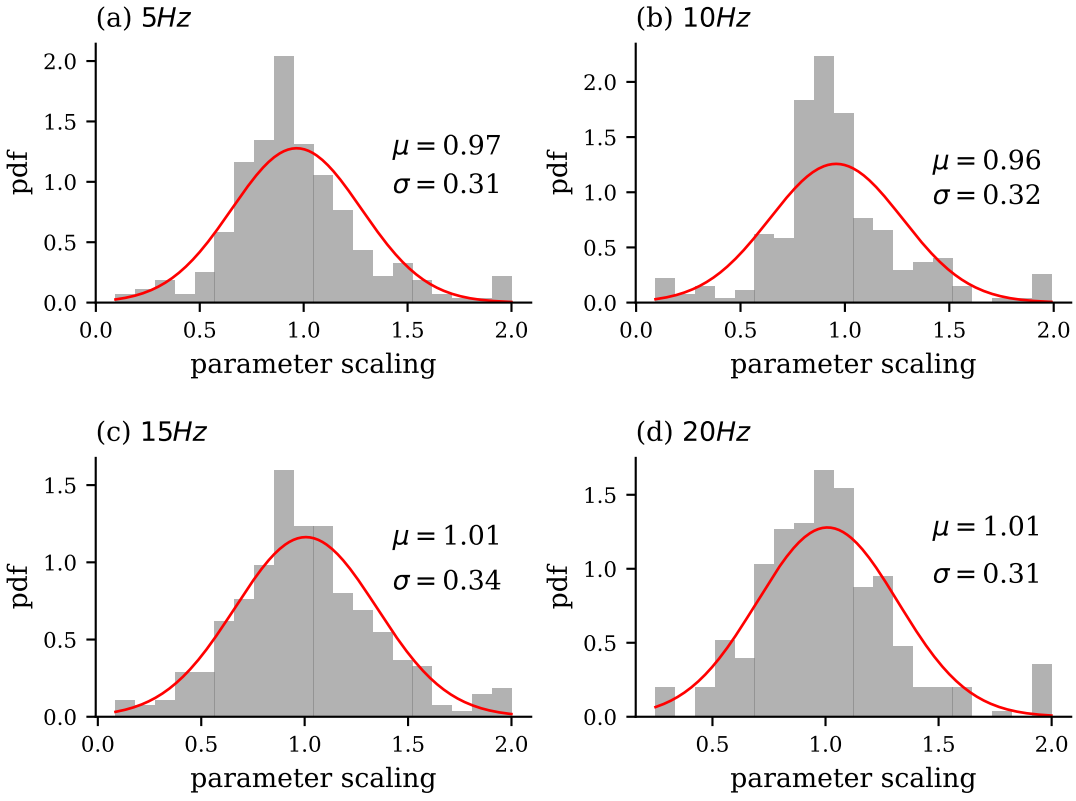

Fig. 4.7 The probability distribution function of the parameters in the optimized model in a homogeneous half-plane with multiple circular cavities.

4.4.2 Numerical study B: A circular cavity embedded in homogeneous half-plane with surface relief

Consider a circular cavity Γ_c of radius $a = 3.0m$ embedded at position $x = (-3a, -2a)$ in a homogeneous elastic isotropic half-plane Ω_0 with elastic medium parameters: Young's modulus of Elasticity $E = 1.5e+9N/m^2$, Poisson's ratio $\nu = 0.3$ and mass density $\rho = 1700kg/m^3$. The geological region consists of a semi-circular canyon Γ_{f0} of radius $2a$. The free surface is given by $\Gamma_0 = \Gamma_{f1} \cup \Gamma_{f0} \cup \Gamma_{f2}$ (see Figure 4.9). The impedance along the wall of the embedded cavity is the region of interest, where the dynamic impedance of the system is to be computed. The free surface, including the topographical irregularity due to the canyon, has an influence on the impedance along the cavity wall. However, the impedance along the free surface is not of interest to the intended application.

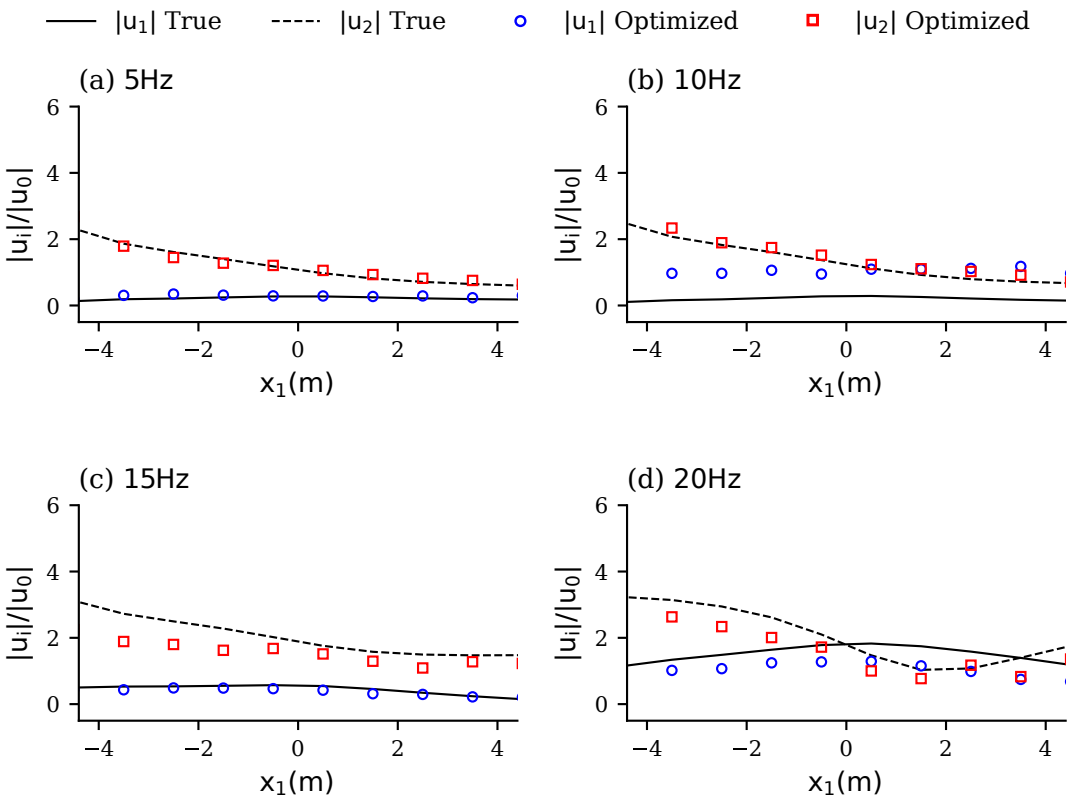

Fig. 4.8 The displacement along the free surface normalized by the seismic source amplitudes in a homogeneous half-plane with multiple circular cavities with the excitation source at $x_1 = -2.5a$ (see Figure 4.5. A comparison of the outputs from the true and the optimized models.

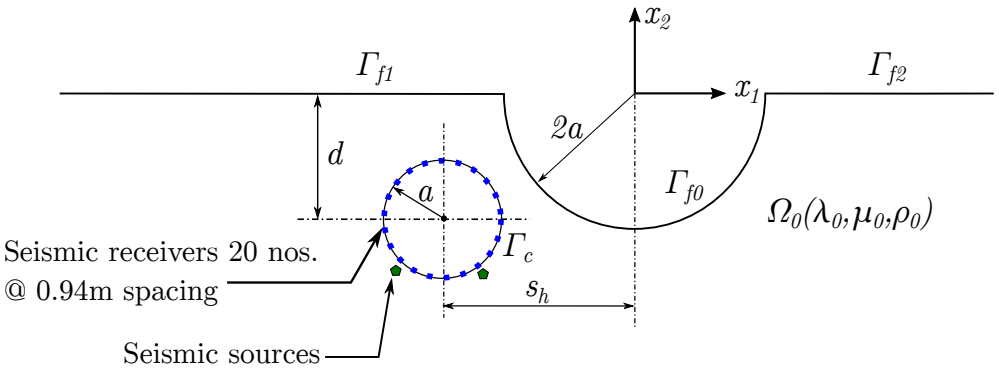

Fig. 4.9 A homogeneous half-plane with a semi-circular canyon and an embedded circular cavity considered for the generation of synthetic data for PSO application in BEM.

(a) Synthetic data generation by BEM simulation:

Let us consider two seismic sources at depth $3a$ and $(x1 = -3.5a, -2.5a)$. 20 seismic receivers are placed along the surface of the embedded cavity. The physical model in Figure

4.9 is simulated using BEM, where the BEM model is discretized with a total of 268 (248 along the free surface relief in $x_1 \in \pm 40a$ and 20 along the cavity) boundary elements with constant shape function. The displacements computed at the receiver locations of the known model are considered synthetic seismic data for the seismic inverse model in the following section.

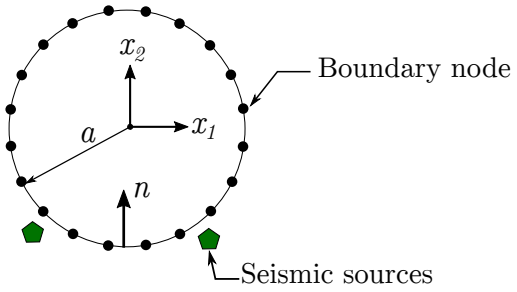

Fig. 4.10 A reduced BEM model of the embedded cavity in Figure 4.9 considered for inverse formulation by PSO.

(b) Seismic inverse model:

The objective of this model is to take only the region of interest and compute the impedance of the system without considering the remaining features. However, the effect of the remaining free surface, the canyon, and the material properties of the domain are accounted for. A BEM model is developed by discretizing only the surface of the embedded cavity with 20 constant boundary elements. The outward normal of each boundary element is towards the center of the cavity (see Figure 4.10). The frequency-dependent displacements at the receiver locations in the true model are taken as field data. PSO is implemented with 600 particles of dimension 400 over 2000 generations. The computation is done for natural frequencies $5Hz$, $10Hz$, $15Hz$, and $20Hz$. The evolution of the misfit function in the computation is shown in Figure 4.11. It can be observed that the residual error in the optimized model is reduced to around 5% at $5Hz$ and increases with the increase in frequency. The misfit is found to be around 15% at $20Hz$ frequency. The distribution of the estimated parameters in the solution is presented as the factor of homogeneous medium parameters in Figure 4.12. The solution by PSO is used to compute the displacement along the free surface due to a seismic source of unit amplitude at position $x_{s1} = (-3.5a, -3.0a)$. A comparison of the displacement amplitudes along the free surface normalized to the amplitude of the seismic source computed using the optimized model and the synthetic true model is presented in Figure 4.13.

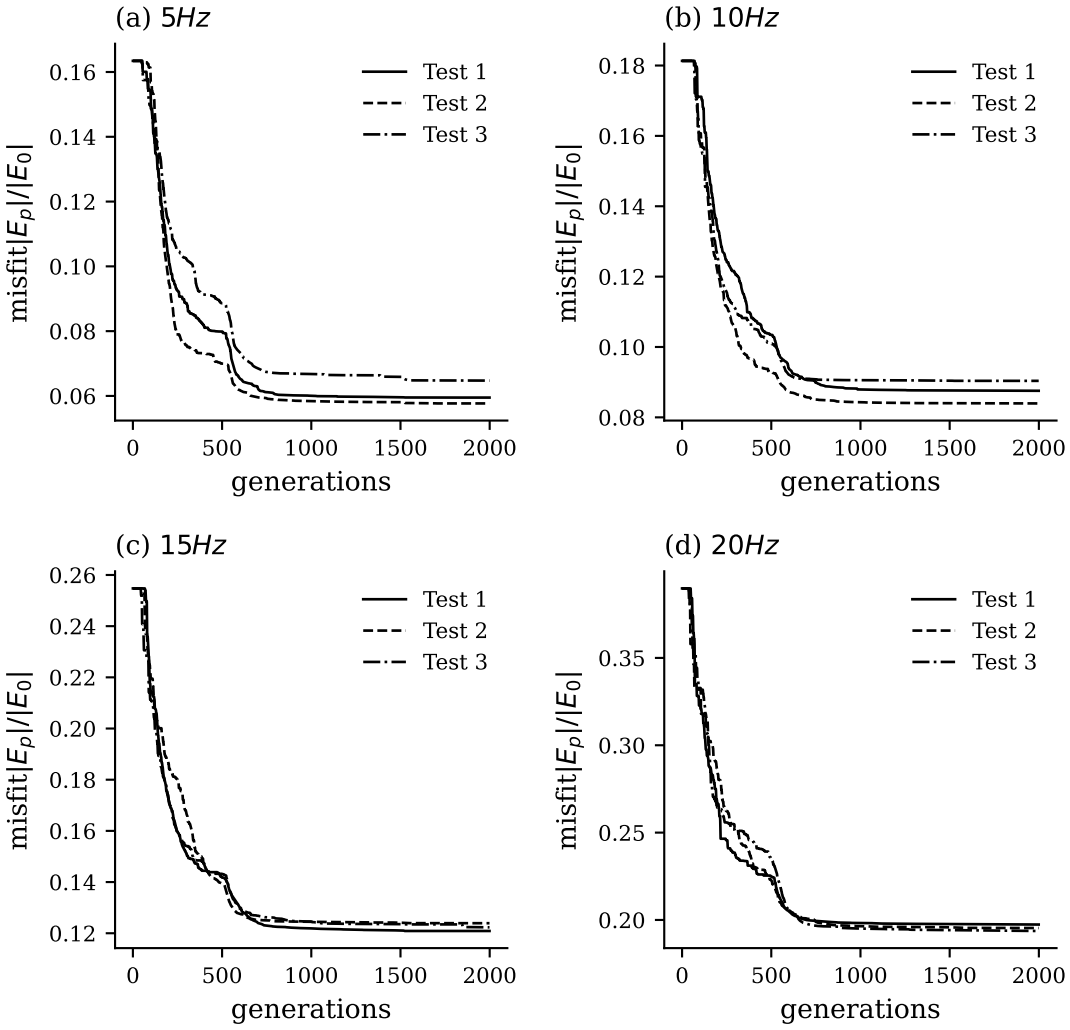

Fig. 4.11 The evolution curves for the misfit functions normalized to the energy in a homogeneous half-plane with an embedded cavity and surface relief at different excitation frequencies.

4.5 Conclusion

Intending to improve the practical applicability of BEM, PSO is implemented in P-SV wave propagation problem to obtain the site-specific impedance function. The fundamental solution for a homogeneous elastic isotropic continuum is considered the basic functional expression in the objective function. The optimization parameters are considered by parametrizing the wave velocities and density over the boundary mesh. The aim is to decrease the misfit between the seismic measurement data and that computed from the numerical model. The standard PSO algorithm is modified by using the gradient terms at the personal best positions and random step lengths to improve the convergence of the method. The output consists of

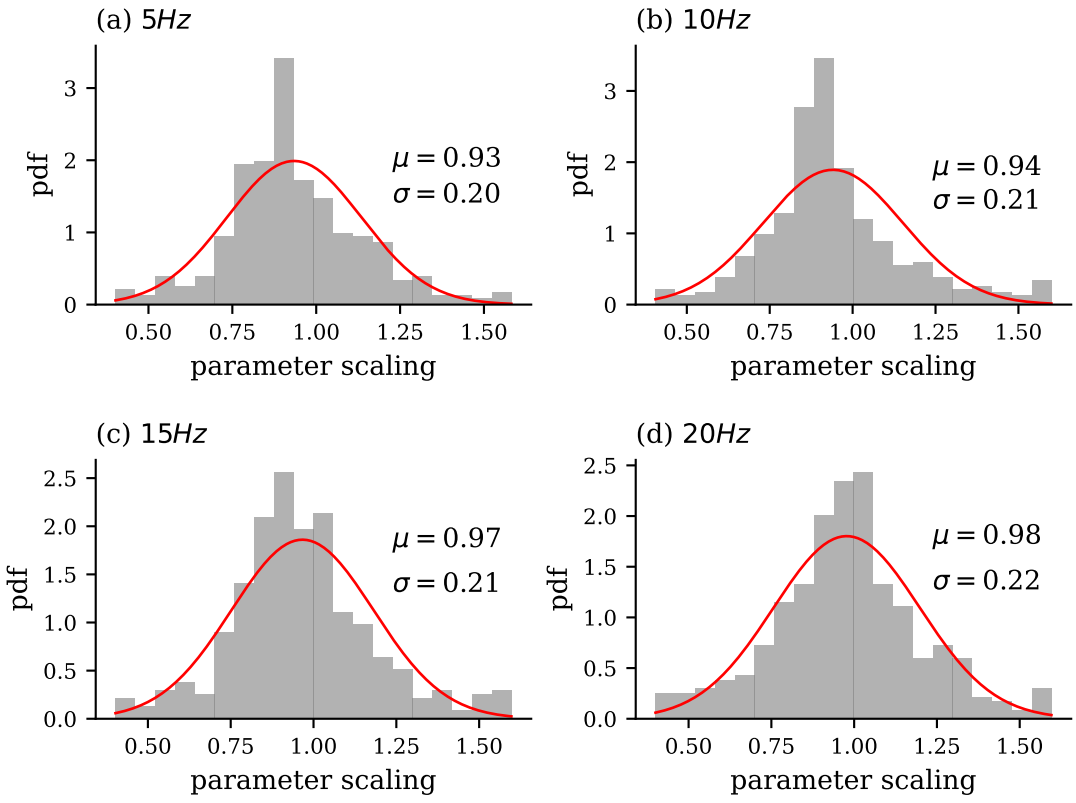

Fig. 4.12 The probability distribution function of the parameters in the optimized model in a homogeneous half-plane with an embedded cavity and surface relief.

the optimum parameters corresponding to the site-specific impedance function for the region under consideration, which can be used for further computation of geomechanical problems by BEM or by coupling the impedance with other domain methods in hybrid form. The method is inserted into the simulation in a Python programming environment. The method's validation and accuracy analysis are performed using synthetic data examples.

It can be concluded from this chapter that particle swarm optimization in BEM with the considered synthetic examples gives a reasonably accurate optimum model for site-specific impedance function. The models in validation tests have shown the outputs with up to 2.5% misfit in the energy norm for $5Hz$ frequency, whereas the accuracy reduces with the increase in frequency, and the results are as low as 15% misfit at $20Hz$ frequency for the chosen examples. Considering the physical domain, the frequency window, and the accuracy desired in geomechanical problems, the results may not indicate the method's direct usability in most practical situations. However, the idea of optimization in BEM in combination with experimental data and stochastic optimization is successfully implemented. The outcome of this chapter can be summarized as follows:

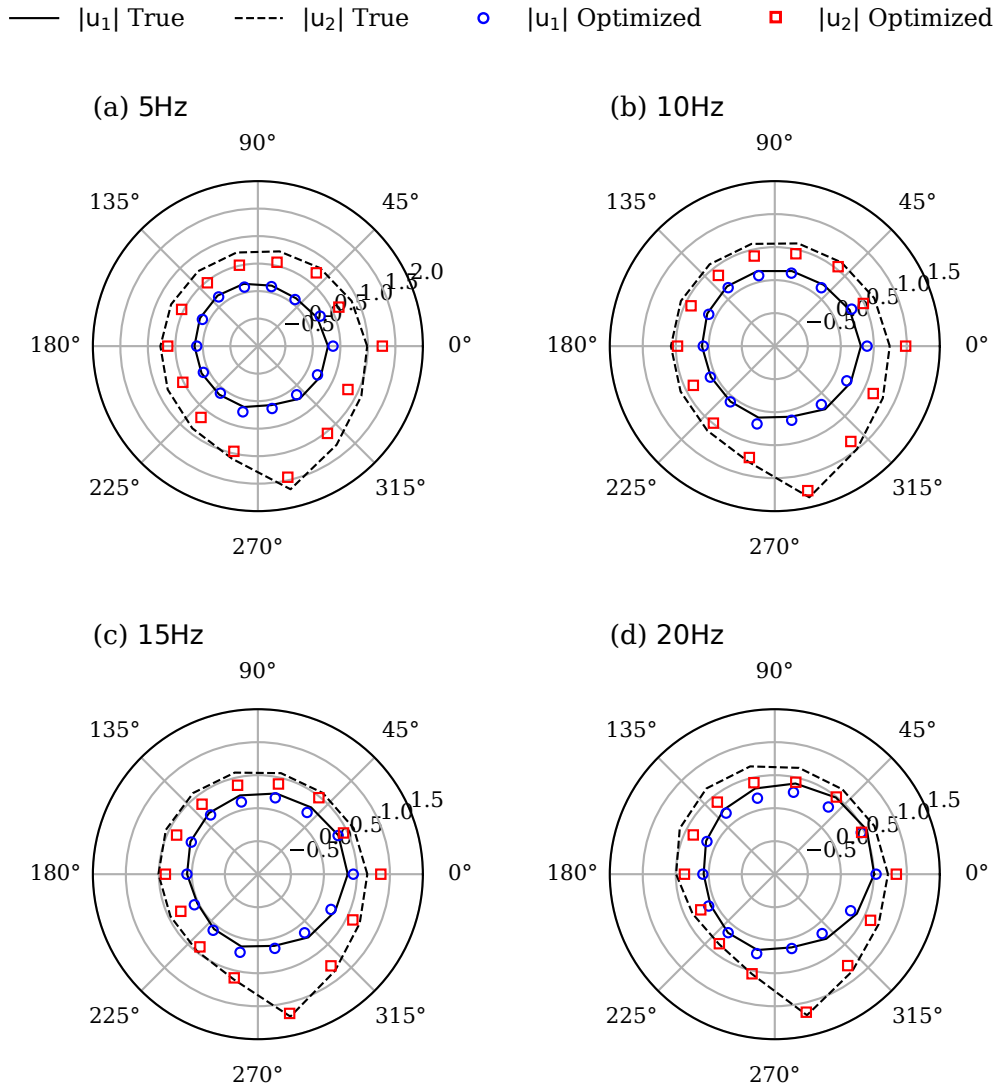

Fig. 4.13 The displacement along the free surface normalized by the seismic source amplitudes in a homogeneous half-plane with an embedded cavity and surface relief with the bottom right excitation source (see Figure 4.10). A comparison of the outputs from the true and the optimized models.

(i) BEM-PSO hybrid experimental-theoretical-numerical approach allows the modeling of an arbitrarily inhomogeneous and heterogeneous media based on the fundamental solution of 2D elastodynamics for homogeneous elastic isotropic continua.

(ii) This approach allows simplifying BEM models significantly. The unimportant features can be removed from the model while their effect is still accounted for in the solution. Such features include the left and right free surface towards infinity and the subsurface

geological features such as layers, cavities, inclusions, etc. This helps to reduce the size of the BEM models.

(iii) The elastodynamic problem is able to be modeled by BEM without the information about subsurface features and topographical details of the surface far away from the site of interest. However, seismic measurement on the surface has to be conducted.

The major limitation of the proposed BEM-PSO approach is that the solutions are mere distributions of mathematical values which are used to compute site-dependent dynamic impedance. Unlike FWI in domain methods such as FDM and FEM, where detailed physical properties of the subsurface are revealed, this method does not give information about the physical parameters, layers, and other underground geological features. The results also indicate that further improvement in the model in various aspects may improve the results and prove the practical applicability of the method. There exist numerous fundamental solutions and Green's functions in elastodynamics that can replace the fundamental solutions for homogeneous elastic isotropic continuum to obtain a better search space. The parameters can be chosen from a different perspective, and the search algorithm can be improved for those spaces. Additionally, to implement the impedance function in BEM for real-world problems, this can be coupled to widely used FEM as BEM-FEM hybrid methods.

Chapter 5

Wave propagation through poroelastic soil with underground structures via hybrid BEM-FEM

The BEM-PSO optimized models for seismic wave propagation in arbitrarily inhomogeneous and heterogeneous elastic isotropic half-plane are great tools for dynamic analysis in naturally occurring geological media. However, the models are not able to explain many near-field inelastic behaviors. A hybrid BEM-FEM computational technique is studied with the intent to solve such problems while exploiting the advantages of BEM too. A hybrid BEM-FEM model for the evaluation of the seismic response of a complex poroelastic soil region containing underground structures is developed in this chapter. The model is based on an efficient computational technique unifying the benefits of both BEM and FEM. The mechanical model takes the whole seismic wave path from the seismic source, through the heterogeneous geological saturated deposits, till the local site with underground structure into consideration. The seismic load comprises time-harmonic or transient P- and SV-wave, and follows the plane strain case. A viscoelastic isomorphism of Biot's equations of dynamic poroelasticity presented by Bardet's model is used. The direct BEM is applied for the modeling of unbounded part of the geological region, while the FEM is used for the modeling of local finite geological profile containing an underground structure. The BEM model is inserted as a macro-finite-element in the commercial program ABAQUS, where the final solution of the entire problem is obtained. The simulation results reveal that the seismic response is sensitive to the site conditions, such as the existence of surface relief and layers, soil inhomogeneity and poroelasticity, and most importantly, the soil-underground structure interaction. The main advantage of the hybrid model is that it can be extended to incorporate many near-field nonlinear behaviors in the region modeled by FEM while satisfying Sommerfeld's radia-

tion condition at infinity in the region modeled by BEM. Parts of this chapter are published as:

Basnet, M. B., Aji, H. D., Wuttke, F., and Dineva, P. (2018). Wave propagation through poroelastic soil with underground structures via hybrid BEM-FEM, *ZAMM-Journal of Applied Mathematics and Mechanics/Zeitschrift für Angewandte Mathematik und Mechanik*, 98(8) 1390-1411.

5.1 Introduction

Historically, underground facilities have experienced a lower rate of damage than the surface structures. Nevertheless, some underground structures registered significant damages in recent large earthquakes, for example Baladeh, Iran (Pakbaz and Yareevand, 2005), and Mid-Niigata, Japan (Konagai et al., 2009). These facts emphasize the importance of the seismic design of underground structures. One distinct aspect of the seismic design is the higher correlation of the underground structure's response to the surrounding ground response instead of its own inertia (Hashash et al., 2001). This surely highlighted the paramount role of the wave propagated through the surrounding media. It is well-known fact that rock and soil are commonly fluid-saturated, especially under the ground water table or in coastal regions. In the following paragraphs, we present a brief state-of-the-art of the available computational tools evaluating the seismic response of underground structures in saturated soils via the most frequently employed Biot's model (Biot, 1956).

A detailed review of this subject can be found in (Manolis and Dineva, 2015, Manolis et al., 2017, Schanz, 2009). The available results are mainly limited to: (a) poroelastic full space with a different types of heterogeneities, such as a circular (Kattis et al., 2003, Mei et al., 1984) or a spherical cavity (Zimmerman and Stern, 1993), double cavities (Wang et al., 2005), piecewise circular tunnel (Lu et al., 2007), a circular lined tunnel (Hasheminejad and Kazemirad, 2008, Li and Zhang, 2013), twin parallel elliptic tunnels (Zhou et al., 2009); (b) poroelastic half-space with underground structures, see (Ding et al., 2008, Jiang et al., 2009, Li and Zhao, 2008, Liang and Liu, 2009, Liu et al., 2017, 2015, 2016).

The computational tools available in the literature can be categorized into analytical, numerical, and hybrid. Analytical methods mainly refer to wave function expansion methods, see (Hasheminejad and Avazmohammadi, 2007, Hasheminejad and Kazemirad, 2008, Hu et al., 1998, Jiang et al., 2009, Kattis et al., 2003, Li and Zhao, 2008, Liang et al., 2006, Zimmerman and Stern, 1993). As a whole, the analytical methods are restricted to inhomogeneous media with simple geometry (parallel, horizontal layers in the half-space) and heterogeneities with dimensions considerably larger than the prevailing wavelengths and

therefore they are only limited to zoning studies. The numerical approach is often favored for cases of complex geometry. The numerical tools can be further classified into (a) finite difference method (FDM), see (Blanc et al., 2013, Dai et al., 1995, Itzá et al., 2016, Masson and Pride, 2010, Wenzlau and Müller, 2009, Zeng and Liu, 2001); (b) finite element method (FEM), see (Dupuy et al., 2011, Shi et al., 2016, Turek et al., 2013); (c) boundary element method (BEM), see (Bo-yang and Jia-qi, 2015, Liu et al., 2016, Manolis and Dineva, 2015, Manolis et al., 2017, 2015, Saitoh et al., 2014, Schanz, 2001, 2009); (d) spectral element method, see (Morency and Tromp, 2008); (e) method of fundamental solutions (MFS), see (Liang and Liu, 2009, Liu et al., 2017, Rajapakse and Senjuntichai, 1995). In each case, the unbounded domain is necessary to be incorporated into the model for compliance with Sommerfeld's condition.

Each one of these methods has its advantages and drawbacks, thus, hybrid methods are developed to gain advantages of the comprising methods and overcome their shortcomings. Hybrid techniques include analytical and numerical methods (Dineva et al., 2012, Panza et al., 2009, Wuttke et al., 2011) or combining two or more numerical methods as FEM-BEM (Jean, 2015, Romero et al., 2013, Vasilev et al., 2015), FEM-scaled boundary finite element method (Borsutzky, 1984) and FDM-BEM (Manolis et al., 2015). Coupled FE-BE methods bring forward the advantages of finite elements in dealing with complex geometries, inhomogeneity and non-linearity, and the ability of the boundary element technique to simulate the unbounded region. The advantages of BEM are well-known in the literature (Manolis et al., 2017), a short discussion of which is included in this chapter as follows:

The main advantages of BEM in treating seismic wave propagation are: (a) Reduction in the size of the problem dimensionality and in the size of the resulting algebraic system, in contrast to other numerical domain methods; (b) Possibility to model lateral inhomogeneity in contrast to analytical methods; (c) Solution at each internal point in the domain is expressed in terms of boundary values without recourse to domain discretization, and this facility is very important when wave propagation problems are being solved in multilayered solids; (d) Flexibility to model relief peculiarities, in contrast to analytical methods and finite difference methods which encounter problems with implementing conditions on boundaries of complex geometric shapes; (e) The semi-analytical character of the method is important for accuracy reasons insofar as it is based on the fundamental solution of the governing equation; (f) High level of accuracy is achieved since numerical quadrature techniques are directly applied to the boundary integral equations, which is an exact solution to the problem at hand; (g) BEM has proven to be a powerful tool for solving exterior boundary-value problems. The fundamental solution used in the construction of the boundary integral equations obeys the radiation condition, and thus, infinitely extended boundaries are automatically incorporated,

in contrast to other numerical methods where the special transmitting and/or non-reflecting viscous boundaries have to be used. (h) High accuracy in computation of Shell Correction Factor (SCF) near cavities, since the solution at points close to cavity boundary is expressed in terms of boundary values without recourse to domain discretization. The hybrid BEM-FEM, in combination with the used viscoelastic isomorphism of Biot's dynamic poroelasticity, has an additional advantage. Thanks to its mechanical (one-phase instead of two-phase material) and mathematical simplicity (the wave equation and the fundamental solutions are much simpler than that in the case of Biot's model).

The available coupling techniques can be categorized into direct coupling method (Von Estorff and Hagen, 2005), FEM-hosted, BEM-hosted, staggered method and iterative method. In BEM-hosted, the FEM sub-domain is treated as an equivalent BEM sub-region. Reversely, in FEM-hosted approach, the BEM reciprocal matrix is transformed into displacement-based stiffness matrix which is then super-positioned into the stiffness matrix of the FEM domain on its proper degrees-of-freedom designation.

it can be concluded from the evaluation of the state-of-the-art that there is a lack of high-performance methodology and corresponding software accounting for all components along the seismic path: (a) seismic source; (b) laterally inhomogeneous, poroelastic and heterogeneous wave path; (c) local geological region with its specific geometrical and mechanical properties, containing underground structures. This motivates the authors to develop a 2D hybrid FEM-hosted technique based on BEM via commercial software ABAQUS and a viscoelastic isomorphism to Biot's equations of dynamic poroelasticity for evaluation of the seismic response of saturated soil-underground structure system. This chapter is organized as follows: Section 5.2 formulates the mechanical problem under consideration, while the hybrid BEM-FEM is described and discussed in Section 5.3. Benchmark examples for verification purposes are presented in Section 5.4 and detailed numerical simulations are carried out in Section 5.5. Finally, some concluding remarks are given in Section 5.6.

5.2 Formulation of the mechanical problem

In a Cartesian coordinate system $O_{x_1x_2x_3}$ consider a finite geological region Ω_b containing an embedded underground structure Ω_c and free-surface relief with arbitrary geometry. The boundary of the bounded finite domain Ω_b is $\Gamma_{\Omega_b} = \Gamma_b \cup \Gamma_{int}$, where Γ_b is the free surface boundary and Γ_{int} is the interface boundary between the finite region Ω_b and the unbounded part Ω_a of the half-space with free surface $\Gamma_a = \Gamma_{a_l} \cup \Gamma_{a_r}$. The boundary of the region Ω_a is $\Gamma_{\Omega_a} = \Gamma_a \cup \Gamma_{int}$, while the boundary of the underground structure is Γ_c, see Figure 5.1. All boundaries are with arbitrary geometry. The described system is subjected to an in-plane

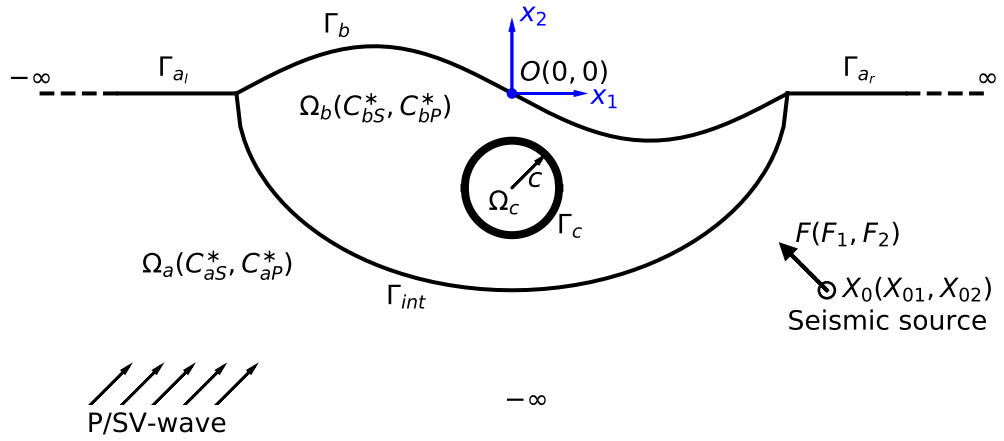

Fig. 5.1 The problem geometry.

dynamic load that comprises either (i) an incident time-harmonic or transient plane P- or SV-wave tracing a prescribed incident angle with respect to axis O_{x_1} or (ii) wave radiated by time-harmonic or transient line seismic source with a prescribed magnitude $F_i, i = 1,2$ embedded at point $X_0(X_{01}, X_{02}) \in \Omega_a$, i.e., a concentrated seismic force $F_i g(t)\delta(x - X_0)$ is applied, where $g(t)$ is the time function of the seismic signal and δ is the Dirac delta function. The underground structure Ω_c is assumed to be an unlined tunnel. The geological regions Ω_a and Ω_b are with saturated soils with mechanical properties described by Bardet's model (Bardet, 1992) which is a viscoelastic isomorphism of Kelvin-Voigt type to Biot's equations (Biot, 1956) of dynamic poroelasticity. In the frame of the viscoelastic model of Kelvin-Voigt the complex-valued frequency-dependent phase velocities of shear SV-wave $C_S^{*2} = {C_S}^2(1 - i\omega\xi_S)$ and longitudinal P-wave $C_P^{*2} = {C_P}^2(1 - i\omega\xi_P)$ are considered. Here: ${C_S}^2 = \frac{\mu}{\rho}$ and ${C_P}^2 = \frac{\lambda+2\mu}{\rho}$ are their real parts, $\omega(sec^{-1})$ is the angular frequency, ξ_S and ξ_P are the corresponding attenuation coefficients that represent the small hysteretic damping ratios, λ and μ are the real parts of the complex-valued Lame constants, ρ is the mass density. The following notations are used for the material properties of ranges Ω_a and Ω_b: λ_a, μ_a, ρ_a and λ_b, μ_b, ρ_b correspondingly. Plane strain state and respectively in-plane wave motion in the plane $x_3 = 0$ is assumed, see Figure 5.1. The only non-zero field quantities are displacement components u_1, u_2 and stresses $\sigma_{11}, \sigma_{22}, \sigma_{12}$ dependent on the coordinates $x(x_1, x_2)$ and on the time t.

What follows is to formulate an initial boundary-value problem (IBVP) that takes into account the entire wave path from the seismic source in the geological range Ω_a through the geological deposits and all the way up to the local geological site Ω_b under consideration.

The dynamic equilibrium equation is:

$$\sigma_{ij,j}(x,t)+\Psi F_i(x,t)=\rho\frac{\partial^2 u_i(x,t)}{\partial t^2}\quad for\ x\in\Omega_a\cup\Omega_b \tag{5.1}$$

Where at $\Psi=0$ we consider the case of incident plane seismic wave, while at $\Psi=1$ the embedded seismic source is taken into account, comma subscripts denote partial differentiation with respect to the spatial coordinates, while the summation convention over repeated indices is implied.

In order to formulate the initial boundary value problem we should add the initial and boundary conditions. Note that the continuum is assumed to be in rest before time $t=0$, so zero initial conditions $u_i=0;\ \frac{\partial u_i}{\partial t}=0,\ t<0$ hold. The compatibility and dynamic equilibrium boundary conditions are satisfied for displacement and traction along the interface boundary Γ_{int} and traction-free boundary conditions are satisfied along boundaries $\Gamma_a\cup\Gamma_b\cup\Gamma_c$. At infinity Sommerfeld's radiation conditions are satisfied for the scattered wave field.

As far as the initial boundary-value problems described in the time-domain should deal with solution of hyperbolic partial differential equation (5.1) which in many cases is not easy to solve, very often integral transforms such as Fourier or Laplace are applied in order to work with elliptic partial differential equation (5.2). The solution of the problem for transient waves is solved by the use of the following well-known numerical procedure, see (Chaillat et al., 2009): *(a)* direct Fourier transform (FT) is applied to the governing equation (5.1) and the corresponding boundary-value problem in frequency domain with governing equation (5.2) is solved; *(b)* the inverse FFT is applied to the solutions in frequency domain and finally, the solutions in time-domain are determined.

$$\begin{aligned}
&\left(\frac{k_S^2}{k_P^2}-1\right)(u_{2,12}+u_{1,11})+u_{1,11}+u_{1,22}=-k_P^2u_1+\Psi F_1\hat{g}(\omega)\delta(x-X_0);\\
&\left(\frac{k_S^2}{k_P^2}-1\right)(u_{1,12}+u_{2,22})+u_{2,11}+u_{2,22}=-k_S^2u_2+\Psi F_2\hat{g}(\omega)\delta(x-X_0)\\
&\qquad\qquad x\in\Omega_a\cup\Omega_b
\end{aligned} \tag{5.2}$$

Here: $\hat{g}(\omega)$ is the Fourier transform (FT) of the time function $g(t)$; for simplicity of notations the same notation for displacement $u_i(x,t)$ and it's FT $\hat{u}_i\equiv u_i(x,\omega)$ is used, k_P and k_S are the complex-valued wave numbers, which in the case of the linear Kelvin-Voigt viscoelastic model are expressed by the following formulas:

$$
\begin{aligned}
k_P^2 = \frac{\omega^2}{C_P^{*2}} = \frac{\omega^2}{C_P^2\,(1-i\omega\xi_P)} \underset{\omega\xi_P<<1}{\approx} \left(\frac{\omega}{C_P}\right)^2 \left(1+\frac{i}{2}\omega\xi_P\right)^2; \\
k_S^2 = \frac{\omega^2}{C_S^{*2}} = \frac{\omega^2}{C_S^2\,(1-i\omega\xi_S)} \underset{\omega\xi_S<<1}{\approx} \left(\frac{\omega}{C_S}\right)^2 \left(1+\frac{i}{2}\omega\xi_S\right)^2
\end{aligned}
\tag{5.3}
$$

Bardet (Bardet, 1992) introduced the poroelastic-viscoelastic similarity by equating the wave numbers in Biot's poroelastic model (Biot, 1956) with the viscoelastic ones presented by equation (5.3). The result is a manifestation of equivalence between Biot's poroelastic model and linear Kelvin-Voigt viscoelastic material with the longitudinal and shear wave velocities and attenuations related to the poroelastic parameters of Biot's model as follows:

$$
C_P = \sqrt{\frac{(P+2Q+R)}{\rho_{sat}}};\; C_S = \sqrt{\frac{\mu}{\rho_{sat}}} \tag{5.4}
$$

$$
\xi_P = \frac{\rho_{sat}}{b}\left(\frac{(Q+R}{P+2Q+R}\cdot\frac{n\rho_f}{\rho_{sat}}\right);\; \xi_S = \frac{\rho_{sat}}{b}\left(\frac{n\rho_f}{\rho_{sat}}\right);\; b = n^2 g\frac{\rho_f}{\hat{k}} \tag{5.5}
$$

$$
\lambda_{sat} = \lambda_{dry} + \frac{Q^2}{R} = \frac{3\nu_{dry}}{1+\nu_{dry}}K_{dry} + \frac{Q^2}{R};\; \mu_{sat} = \mu_{dry} = \mu \tag{5.6}
$$

$$
Q = \frac{nK_g\left(1-n-\frac{K_{dry}}{K_g}\right)}{\left(1-n-\frac{K_{dry}}{K_g}+n\frac{K_g}{K_f}\right)};\; R = \frac{K_g n^2}{\left(1-n-\frac{K_{dry}}{K_g}+n\frac{K_g}{K_f}\right)};\; P = \frac{3\left(1-\nu_{dry}\right)}{1+\nu_{dry}}K_{dry} + \frac{Q^2}{R} \tag{5.7}
$$

Here g is the acceleration due to gravity, $\hat{k}$ is the hydraulic conductivity, P, Q and R are the material constants in Biot's model. The representative elementary volume V of a solid-fluid system consisting of an isotropic elastic porous skeleton with porosity $n = V_{pore}/V$, where V_{pore} is the existing pore volume, which is described by the following key parameters: *(a)* solid grain (material build up the matrix) with elastic bulk module K_g and density of solid grain ρ_g; *(b)* fluid with elastic bulk module K_f and density ρ_f; *(c)* dry rock (all pores are with air) with elastic bulk module K_{dry} and density: $\rho_{dry} = (1-n)\rho_g$. The solid-fluid system density is $\rho_{sat} = \rho_{dry} + n\rho_f = (1-n)\rho_g + n\rho_f$. In Biot's model, only the hydro-mechanical coupling is working and the pore pressure induces only volume dilatational changes in the soil. Thus the shear strength of the porous material is provided by the solid frame and it is not affected by the fluid, i.e. both dry and saturated soils are described by the same shear modulus $\mu = \mu_{sat} = \mu_{dry}$. The key characteristics in Bardet's model are $n, K_f, \rho_f, \rho_g, K_g, K_{dry}, \mu, \hat{k}$.

Expressions (5.4) - (5.7) are derived in the case that $\omega\rho_{sat}/b << 1$, $\omega\xi_S << 1$ and $\omega\xi_P << 1$. Due to the fact that the hydraulic conductivity $\hat{k}$ for soils has small values (for example, for sand $\hat{k} = 10^{-6} - 10^{-4}$), these conditions are fulfilled for the relatively lower frequencies typical for earthquake-type events. The limitation of Bardet's model discussed above is not restrictive to the type of problems we consider here. Indeed, for soil with porosity $n = 0.3$ and permeability $\hat{k} = 10^{-5} m/s$, the value of coefficient b is approximately 10^8 and this means that the frequencies of the excitation match in all cases of the earthquake-type events. The advantage of Bardet's model is that it reduces the complex two-phase poroelastic model to the simpler viscoelastic one and can be applied for seismic wave propagation in more complex fluid-saturated geological regions, see (Manolis et al., 2017). The model has been verified by the solution of the problem for the scattering of plane compression waves by a spherical poroelastic inhomogeneity in Bardet's model (Bardet, 1992), where it is shown that the viscoelastic isomorphism solutions accord identical to the original poroelastic problem solution within the specific range of parameters examined. In the case of an incident plane wave, $(\Psi = 0)$ the boundary conditions along the interface Γ_{int} need to be discussed. The total wave field $u_i(x \in \Gamma_{\Omega_a}, \omega)$, $t_i(x \in \Gamma_{\Omega_a}, \omega)$ outside the bounded region Ω_b can be presented as a superposition of the free-field motion $u_i^{ff,a}(x,\omega)$, $t_i^{ff,a}(x,\omega)$, $x \in \Gamma_{\Omega_a}$ and scattered wavefield $u_i^{sc,a}(x,\omega)$, $t_i^{sc,a}(x,\omega)$, $x \in \Gamma_{\Omega_a}$ due to wave scattering by the existing boundaries, i.e.

$$\begin{aligned} u_i(x,\omega) &= u_i^{ff,a}(x,\omega) + u_i^{sc,a}(x,\omega),\ x \in \Gamma_{\Omega_a}; \\ t_i(x,\omega) &= t_i^{ff,a}(x,\omega) + t_i^{sc,a}(x,\omega),\ x \in \Gamma_{\Omega_a} \end{aligned} \tag{5.8}$$

Here, tractions $t_i = \sigma_{ij} n_j$, n_j are the components of the outward normal vector. The free-field motion is the wave field in a homogeneous half-plane with material constants λ_a, μ_a, ρ_a having flat free surface and without any type of heterogeneities. The total wave field $u_i^b(x,\omega)$, $t_i^b(x,\omega)$ inside the bounded region Ω_b is equal to that scattered by its existing boundaries $u_i^{sc,b}(x,\omega)$, $t_i^{sc,b}(x,\omega)$. So, having all this in mind, the following boundary conditions hold along the interface boundary Γ_{int}:

$$\begin{aligned} u_i^{sc,b}(x,\omega) &= u_i(x,\omega) - u_i^{ff,a}(x,\omega),\ x \in \Gamma_{int}; \\ t_i^{sc,b}(x,\omega) &= -\left(t_i(x,\omega) - u_i^{ff,a}(x,\omega) \right),\ x \in \Gamma_{int} \end{aligned} \tag{5.9}$$

The solutions for the free field motion $\left(u_i^{ff,a}(x,\omega),\ t_i^{ff,a}(x,\omega) \right)$ in frequency domain are given in (Dineva et al., 2014).

Finally, the BVP is defined in frequency domain by the governing equation (5.2) and the above-discussed boundary conditions along the boundaries $\Gamma_a \cup \Gamma_b \cup \Gamma_{int} \cup \Gamma_c$. The synthetic seismic signals will depend on the type and properties of the seismic load and on the material and geometric characteristics of the whole wave path starting from the seismic source till the observer point.

5.3 Hybrid BEM-FEM approach

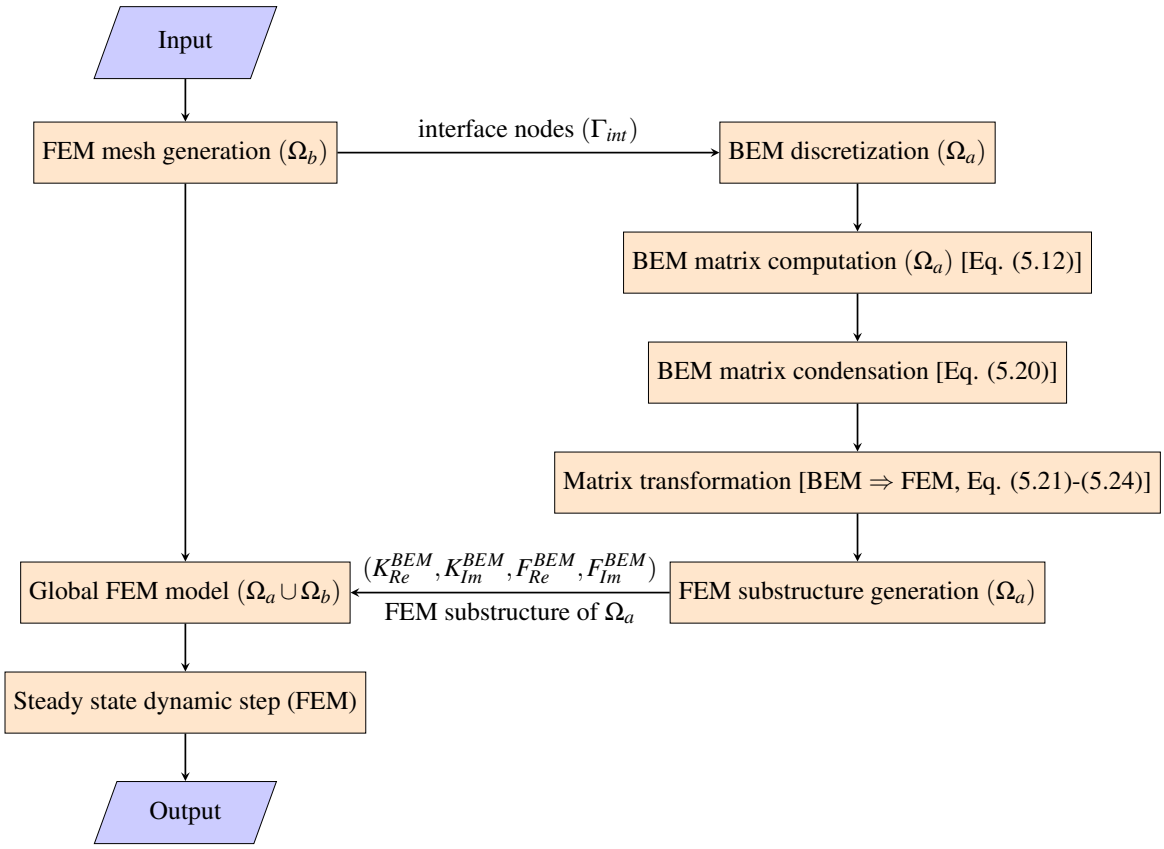

Fig. 5.2 A flowchart of the hybrid BEM-FEM direct coupling technique in frequency domain.

A 2D FEM-hosted hybrid approach using commercial software is presented. ABAQUS, currently one of the most powerful finite element software in the industry due to its broad material library, ease of use, powerful solver and user subroutines procedure, is chosen. The boundary element formulation is employed to model the unbounded poroelastic region Ω_a. The resulting stiffness and damping matrices are then exported into the generation of a substructure in the FEM environment. The force matrix is presented as input in the dynamic analysis step of ABAQUS. The FEM is used to simulate the near-field wave propagation

and the saturated soil-underground structure interaction. The hybrid approach is realized in frequency domain, while inverse FFT is applied to have solutions in time domain. The essence of coupling these numerical methods is to best exploit the features of the constituent parts. Each of the two techniques here is applied in that part of the whole model where it works more efficiently: *(a)* the BEM formulation of the elastodynamic problem is mathematically equivalent to the original formulation via partial differential equations and the fact that it is based on the fundamental solution of this governing equation, guarantees a high level of solution accuracy. Additionally, the BEM numerical scheme fits well to the external problems, because the fundamental solution obeys Sommerfeld's radiation condition, and thus infinitely extended boundaries are automatically accounted for without resorting to special types of viscous boundaries as is in FEM; *(b)* the major strength of FEM is its versatility in handling various classes of problems, including nonlinearity, anisotropy and nonhomogeneity and an important fact also is that there exist commercial FEM codes that can be used successfully in mechanical modeling of complex engineering structures.

The developed hybrid numerical scheme consists of the following steps: (i) direct BEM is developed for the unbounded geological region Ω_a; (ii) conventional FEM is used for the near soil region Ω_b with the underground structure; (iii) insertion of the BEM model of the seismically active far-field soil region as a macro-finite-element in ABAQUS and the solution of the entire BVP in the frequency domain; (iv) inverse FFT is applied to the solutions in frequency domain and finally, the solution in time-domain is obtained.

5.3.1 BEM for the unbounded geological region

The model in the semi-infinite region Ω_a is described via boundary integral equation (BIE) along the boundary $\Gamma_{\Omega_a} = \Gamma_a \cup \Gamma_{int}$ as follows, see (Manolis et al., 2017):

The case when the seismic load is an incident plane P- or SV-wave. The BIE is with respect to the scattered wave field quantities.

$$\begin{aligned} & c_{lk}\left(u_k^{(\Omega_a)}(x,\omega) - u_k^{ff(\Omega_a)}(x,\omega)\hat{g}(\omega)\right) \\ & \quad = \int_{\Gamma_{\Omega_a}} U_{lk}^{(\Omega_a)}(x,\xi,\omega)\left[t_k^{(\Omega_a)}(\xi,\omega) - t_k^{ff(\Omega_a)}(\xi,\omega)\hat{g}(\omega)\right] d\Gamma \\ & \quad - \int_{\Gamma_{\Omega_a}} P_{lk}^{(\Omega_a)}(x,\xi,\omega)\left[u_k^{(\Omega_a)}(\xi,\omega) - u_k^{ff(\Omega_a)}(\xi,\omega)\hat{g}(\omega)\right] d\Gamma \end{aligned} \tag{5.10}$$

The case when the seismic load is the wave radiated by a seismic source embedded at point X_0. The BIE is with respect to the total wave field quantities.

$$c_{lk}u_k^{(\Omega_a)}(x,\omega) = \int_{\Gamma_{\Omega_a}} U_{lk}^{(\Omega_a)}(x,\xi,\omega)t_k^{(\Omega_a)}(\xi,\omega)d\Gamma - \int_{\Gamma_{\Omega_a}} P_{lk}^{(\Omega_a)}(x,\xi,\omega)u_k^{(\Omega_a)}(\xi,\omega)d\Gamma + F_k\hat{g}(\omega)U_{lk}^{(\Omega_a)}(x,X_0,\omega) \tag{5.11}$$

Here: c_{lk} is the jump term depending on the local geometry at the collocation point x; (x,ξ) are the position vectors of the source and the field points; U_{lk} is the displacement fundamental solution of Eq. (5.2), see (Dominguez, 1993); $P_{ij} = C_{iqsl}U_{sj,l}n_q$ is its corresponding traction; the free-field wave motion quantities $u_k^{ff(\Omega_a)}$ and $t_k^{ff(\Omega_a)}$ are given in (Dineva et al., 2014).

BIE (5.10), traction free boundary condition along Γ_a, boundary conditions in expression (5.9) along Γ_{int} and Sommerfeld's radiation condition at infinity describe the case of incident wave. BIE (5.11), traction-free boundary condition along the boundary Γ_a, compatibility and dynamic equilibrium boundary conditions for the total displacements and tractions along Γ_{int} and Sommerfeld's radiation condition at infinity describe the case of the wave radiated from a seismic source located at point X_0.

A standard numerical technique based on the discretization of the BIEs by isoparametric quadratic boundary elements and the collocation procedure is applied, see (Manolis et al., 2017). By keeping in mind the asymptotic behavior of the frequency-dependent fundamental solution for small arguments, two types of singular integrals appear: (a) Integral with a weak singularity of order $O(\ln r)$, i.e. $\int_{\Gamma_{\Omega_a}} U_{lk}(x,\xi,\omega)t_k(\xi,\omega)d\Gamma$ and (b) Integral with a strong singularity of order$O(1/r)$, i.e. $\int_{\Gamma_{\Omega_a}} P_{lk}(x,\xi,\omega)u_k(\xi,\omega)d\Gamma$, where r is the distance between the source and field points. The weakly singular displacement kernel can be numerically integrated by special-purpose Gaussian quadrature, supplemented by a breakdown of the singular boundary element into sub-elements for better accuracy, and the strongly singular traction kernel is integrated indirectly by applying the rigid-body motion concept. The BIE (5.10) transforms into the following matrix equation after discretization and collocation numerical procedure:

$$Gt - Hu = Hu^{ff} - Gt^{ff} = \Phi \tag{5.12}$$

Here: H and G are matrices of size $2N \times 2N$, N is the total number of nodes, u and t are displacement and traction vectors at the nodes, u^{ff} and t^{ff} are the free field nodal displace-

ments and tractions, and right-hand side $Hu^{ff} - Gt^{ff} = \Phi$ of equation (5.12) describes the applied seismic load. The analogous matrix equation is obtained after discretization of BIE (5.11) with the only difference in the vector Φ, which now is derived through the contribution of the term $F_k \hat{g}(\omega) U_{lk}(x, X_0, \omega)$.

5.3.2 FEM for the bounded geological region

The elastodynamic equation in frequency domain in the frame of FEM is presented by the following system of linear algebraic equations:

$$\left[-\omega^2 M + i\omega C + K\right] u = F \tag{5.13}$$

Where M, C, K are the mass, damping and static stiffness matrices, $i = \sqrt{-1}$, u and F are nodal displacement and force vector. When the structural damping is taken into consideration, the equation of motion becomes:

$$\left[-\omega^2 M + i\omega C + (K + iK_s)\right] u = F \tag{5.14}$$

where K_s is the structural damping matrix.

5.3.3 Coupling of BEM and FEM along the interface Γ_{int} between unbounded and bounded regions

Condensation of the boundary element model's degrees of freedom

The condensation is performed similarly to those proposed in (Vasilev et al., 2015). Let us refer the interface boundary Γ_{int} to index 1 while the boundary Γ_a is referred to index 2. Then Eq. (5.12) can be rewritten as follows:

$$\begin{bmatrix} G_{11} & G_{12} \\ G_{21} & G_{22} \end{bmatrix} \begin{bmatrix} t_1 \\ t_2 \end{bmatrix} - \begin{bmatrix} H_{11} & H_{12} \\ H_{21} & H_{22} \end{bmatrix} \begin{bmatrix} u_1 \\ u_2 \end{bmatrix} = \begin{bmatrix} \Phi_1 \\ \Phi_2 \end{bmatrix} \tag{5.15}$$

The matrix equation (5.15) can be expanded into two equations (5.16) and (5.17) representing the first and the second rows of equation (5.15), respectively:

$$[G_{11}][t_1] + [G_{12}][t_2] - [H_{11}][u_1] - [H_{12}][u_2] = [\Phi_1] \tag{5.16}$$

$$[G_{21}][t_1]+[G_{22}][t_2]-[H_{21}][u_1]-[H_{22}][u_2]=[\Phi_2] \tag{5.17}$$

solving equation (5.17) for the vector $[u_2]$ the following relation is derived:

$$u_2 = A_t t_1 + A_u u_1 + \Theta \tag{5.18}$$

Where: $\Theta = [H_{22}]^{-1}(G_{22}t_2 - \Phi_2)$; $A_t = [H_{22}]^{-1}[G_{21}]$; $A_u = -[H_{22}]^{-1}[H_{21}]$.
After inserting the expression of $[u_2]$ from equation (5.18) in the first row of equation (5.15), we obtain:

$$(G_{11} - H_{12}A_t)\,t_1 = (H_{12}A_u + H_{11})\,u_1 + H_{12}\Theta - G_{12}t_2 + \Phi_1 \tag{5.19}$$

Having in mind that $t_2(x \in \Gamma_a, \omega) = 0$, the following compact relation between traction t_1 and displacement u_1 along the contact interface zone Γ_{int} can be written:

$$t_1 = Bu_1 + P \tag{5.20}$$

Here: $B = [G_{11} - H_{12}A_t]^{-1}(H_{12}A_u + H_{11})$ and $P = [G_{11} - H_{12}A_t]^{-1}(H_{12}\Theta + \Phi_1)$

It can be seen from Eq. (5.20) that the relation between traction and displacement along the contact zone Γ_{int} depends on the material properties of the unbounded range Ω_a, the geometry of the boundary Γ_{int}, and the seismic load presented by the vector Φ.

Representation of the BEM model as a MFE

FEM-hosted coupling method is used. To ensure the compatibility and equilibrium of traction along the interface, the BEM model needs to be converted into a macro-finite-element of nodal-based forces. In FEM, the nodal force vector due to traction along a surface Γ_e of the $e-th$ boundary element is defined via quadratic shape functions $N_i, i = 1,2,3,...$ as:

$$F^e = \int_{\Gamma_e} [N]^T t_{\Gamma_e} d\Gamma \tag{5.21}$$

At the same time the traction t_{Γ_e} along the boundary element can be expressed by the usage of quadratic shape functions and the nodal tractions in the following form $t_{\Gamma_e} = N_j t^j_{\Gamma_e}$. Then Eq. (5.21) becomes:

$$F^e = \int_{\Gamma_e} [N]^T [N] \, d\Gamma \, t^e = [\Lambda^e] t^e \tag{5.22}$$

Where $[\Lambda^e] = \int_{\Gamma_e} [N]^T [N] \, d\Gamma$ can be computed for each single $e-th$ boundary element. Application of expression (5.22) for all boundary elements along the contact interface boundary Γ_{int} leads to the global matrix $[M^*] = \sum_e [\Lambda^e]$ and for the nodal force vector $F(x \in \Gamma_{int}, \omega)$ along the interface Γ_{int} one can read:

$$F(x \in \Gamma_{int}, \omega) = [M^*] t_1 \tag{5.23}$$

Where the nodal traction vector t_1 is given by expression (5.20). After inserting Eq. (5.23) into (5.12), the following expression is obtained:

$$\left[G_f\right] F - [H] u = \Phi; \;\; \left[G_f\right] = [G] [M^*]^{-1} \;\; \Rightarrow \;\; F = \underbrace{\left[G_f\right]^{-1} [H]}_{K} u + \underbrace{\left[G_f\right]^{-1} \Phi}_{R} \tag{5.24}$$

Finally, the nodal force vector $F(x \in \Gamma_{int}, \omega)$ along the interface Γ_{int} is expressed via the stiffness matrix $K = \left[G_f\right]^{-1} [H]$ and the free term vector $R = \left[G_f\right]^{-1} \Phi$.

5.3.4 Implementation of the macro-finite-element in ABAQUS software

The method used to couple the BEM into the FEM environment of ABAQUS is based on the *substructure generation procedure* in which a substructure of the BEM domain Ω_a is created and attached to the FEM model of the bounded domain via prescribed common nodes where compatibility and equilibrium conditions are satisfied. Sub-structuring is a common method in FEM simulation where a portion of the degrees-of-freedom from the global equation is pre-analyzed and later condensed into a few representative ones, thus, reducing the size of the main computation.

As described above, the computation of the BEM step will result in the complex-valued governing equation (5.25) with complex-valued stiffness matrix, displacement and free-term vector presenting the seismic load:

$$F = Ku + R; \;\; K = K_{Re} + iK_{Im}; \;\; u = u_{Re} + iu_{Im}; \;\; R = R_{Re} + iR_{Im}; \tag{5.25}$$

Here the K matrix and the load vector R are generated by the author's BEM software program, developed in *Python* programming language (Van Rossum and others, 2007).

The elastodynamic matrix equation in the frame of FEM via ABAQUS is presented by Eq. (5.14). After fitting Eq. (5.14) and Eq. (5.25) and introducing superscript BEM and FEM for regions Ω_a and Ω_b correspondingly, the global stiffness matrix becomes $K^{global} = K^{FEM} + K^{BEM}_{Re}$. The damping can be introduced as viscous damping matrix $C^{global} = C^{FEM} + K^{BEM}_{Im}/\omega$ or structural damping matrix $K^{global}_s = K^{FEM}_s + K^{BEM}_{Im}$.

The resulting global system of linear equations is no more symmetric, and the sparcity of the matrix is highly reduced by the addition of dense matrix from BEM. Thus, traditional symmetric and sparse matrix solvers cannot be used to solve the system. Instead, unsymmetric solvers like PLU decomposition have to be used to solve the system of linear equations. A built-in unsymmetric solver from ABAQUS is used to avoid numerical errors.

5.4 Numerical Verification Scheme

The aim of the verification study is to establish the error bounds of the proposed hybrid tool and to evaluate its accuracy and convergence on the base of solutions of several benchmark examples. The solutions obtained by the hybrid BEM-FEM are compared with those solved by pure analytical technique or pure BEM. The reference poroelastic geomaterial is sandstone with the following mechanical properties (Lin et al., 2005): bulk modulus $(K_g) = 36000.00MPa$, Poisson's ratio $(\nu) = 0.3$, density of solid $(\rho_g) = 2650.00Kg/m^3$, bulk modulus of fluid $(K_f) = 2000.00MPa$, fluid density $(\rho_f) = 1000kg/m^3$ and hydraulic conductivity $(\hat{k}) = 10^{-6}$. The dry bulk modulus is calculated by the expression $K_{dry} = K_{cr} + (1 - n/n_{cr})(K_g - K_{cr})$ based on experimental data, where the field variable critical bulk modulus is $K_{cr} = 200.00MPa$ at critical porosity $n_{cr} = 0.36$. The sandstone is frame-supported for the porosity less than n_{cr} and becomes loose sand beyond n_{cr}, see (Nur et al., 1998). The same poroelastic material with varying porosity is used in Sections 5.4 and 5.5.

5.4.1 Test example 1

A finite elastic range Ω_b with the geometry of semi-ellipse rests in an elastic half-plane subjected to normal time-harmonic P/SV-wave. Comparison with the analytical solution for free-field motion in homogeneous elastic half-plane.

Consider a finite local geological region Ω_b with semi-elliptical geometry with radii $R = 70m$ and $r = 35m$, which is elastic isotropic with density ρ_b and Lame constants λ_b and μ_b (Figure 5.3). It is situated in an elastic isotropic homogeneous half-plane Ω_a with

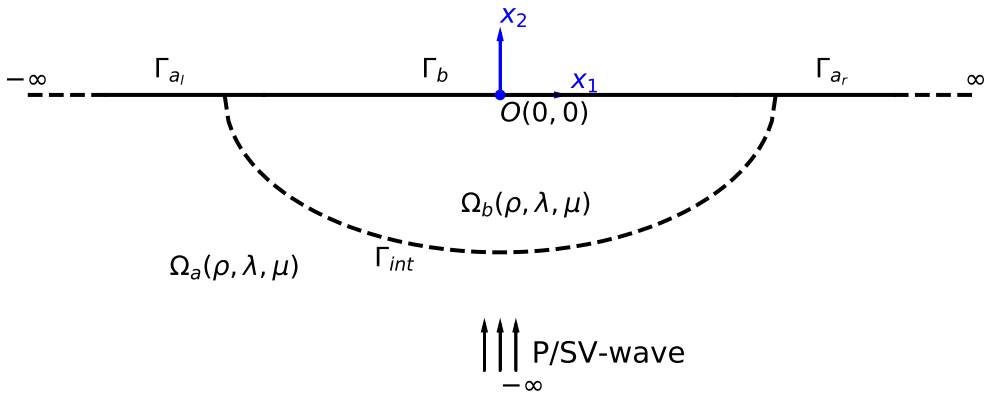

Fig. 5.3 The problem geometry of Test Example 1.

density ρ_a and Lame constants λ_a and μ_a. An incident normal time-harmonic P- or SV-wave with frequency ω impinges on the finite region. In the case $\rho_b = \rho_a = \rho$, $\lambda_b = \lambda_a = \lambda$ and $\mu_b = \mu_a = \mu$, the interface boundary Γ_{int} is not the real boundary but the hypothetic one in the hybrid numerical model proposed here. In this case, the solutions obtained by the hybrid technique should recover the analytical ones for the free field motion presented in (Dineva et al., 2014). The material properties are as follows: Density $\rho = 2000kg/m^3$, Poisson's ratio $\nu = 0.33$, Young's modulus $E = 266.0MPa$. The length of each boundary element does not exceed $\lambda_S/15$, where λ_S is the shear wavelength. The BEM mesh used in the unbounded region Ω_a consists of 72 quadratic boundary elements along the interface boundary Γ_{int} and 378 along the free surface boundary Γ_a. The length L of the discretized part of the boundary Γ_a is $L = \pm 10R$. The FEM mesh used for the finite region Ω_b consists of 2709 quadratic plane strain elements. Figure 5.4 shows a comparison between the normalized displacement amplitudes along the free surface obtained by the hybrid techniques and by the analytical solution at a fixed frequency. Both of the solutions are very close; the difference is not more than 7%. Note that if the reference poroelastic soil material is considered at porosities $n = 0$ (pure elastic material) and $n \in [0.05, 0.2]$, the solutions obtained by the hybrid BEM-FEM are almost identical for the different porosities. The elastic bulk module K_{dry} is much greater than fluid bulk module K_f ($K_{dry} >> K_f$) at low porosities. Such a material is close to the elastic solid-dominated case where the dry frame strength is high and there is no remarkable influence of the fluid on the solid-fluid system's behavior.

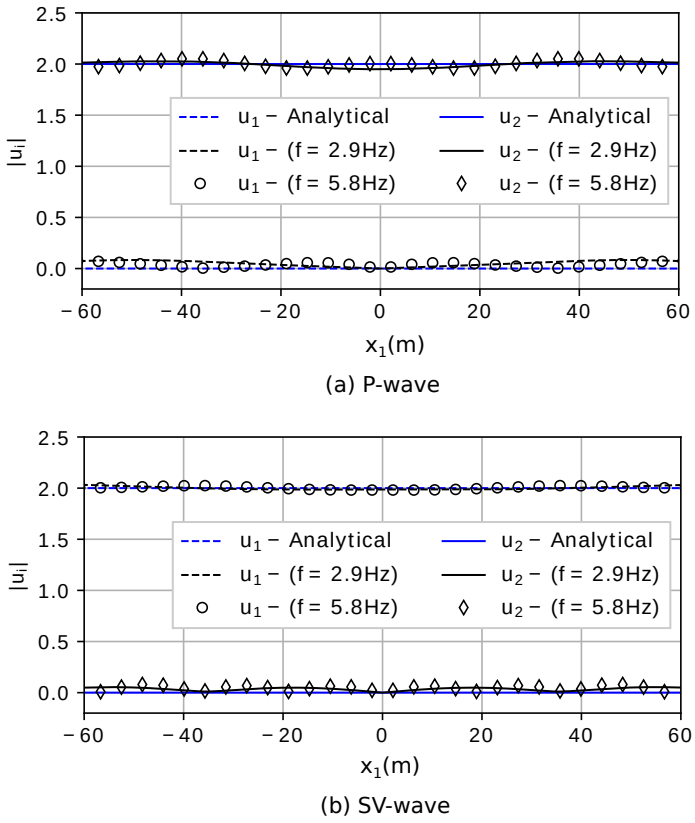

Fig. 5.4 Normalized displacement amplitudes along the free surface of an elastic homogeneous half-plane subjected to normal incident *(a)* P-wave *(b)* and SV-wave with frequency f.

5.4.2 Test example 2

A semi-circular canyon in an elastic half-plane under normal time-harmonic P/SV-wave. Comparison with pure BEM model.

Consider a finite local geological region Ω_b with the geometry of semi-ellipse of radii $R = 70m, r = 35m$, which is elastic isotropic with density ρ_b and Lame constants λ_b and μ_b containing a semi-circular canyon with radius $c = 10m$ along its free surface (Figure 5.5). The finite geological region is situated in an elastic isotropic homogeneous half-plane Ω_a with density ρ_a and Lame constants λ_a and μ_a. An incident normal time-harmonic P- or SV-wave with frequency ω is the seismic load. In the case $\rho_b = \rho_a = \rho = 2000kg/m^3$, $\lambda_b = \lambda_a = \lambda$ and $\mu_b = \mu_a = \mu$, the interface boundary Γ_{int} is not the real boundary. The Poisson's ratio is $\nu = 1/3$ and $C_S = 233.33m/s$. In this case, the solutions obtained by hybrid BEM-FEM should recover the numerical solution obtained by pure BEM for an elastic half-plane with a semi-circle canyon on its surface. This test example has been solved in (Wong, 1982) by applying a generalized inversion technique, in (Sanchez-Sesma and Campillo, 1991) by

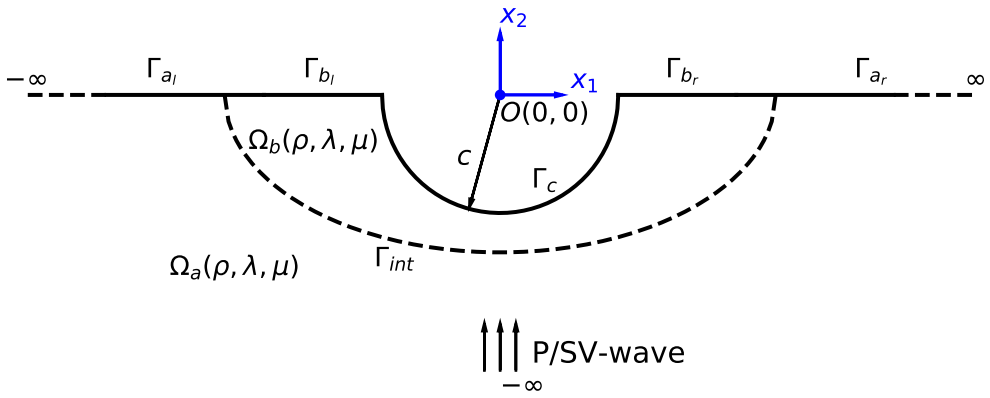

Fig. 5.5 The problem geometry of Test Example 2.

indirect BEM, in (Álvarez Rubio et al., 2004) by direct BEM and in (Parvanova et al., 2014) by direct BEM based on sub-structure technique. In Figure 5.6 a comparison between the solutions obtained by the authors using pure BEM and hybrid BEM-FEM for displacement amplitudes along the free surface at a fixed non-dimensional frequency $\eta = (\omega c/\pi C_S) = 1$ in the case of incident normal P- and SV-wave is presented. Physically, parameter η equals the number of wavelengths contained in a length equal to the size of the heterogeneity. Additionally, the authors' solutions are compared with those obtained in (Álvarez Rubio et al., 2004). Note, that points $x_1/c = \pm 1$ correspond to the right and left edges of the canyon, while the point $x_1/c = 0$ corresponds to its bottom. When the reference poroelastic soil material is considered for this test example at porosities $n \in [0.0, 0.2]$, the solutions obtained by the hybrid FE-BEM are almost identical for all the different porosities in the considered interval. So, the hybrid technique gives accurate solutions not only for the pure elastic but also for the poroelastic case.

5.4.3 Test example 3

A circular cavity embedded in poroelastic half-plane Ω_a under normal time-harmonic plane P/SV-wave. Comparison with pure BEM model.

Consider a finite local poroelastic region Ω_b with semi-elliptical geometry with radii $R = 70m$ and $r = 35m$, which contains a circular cavity with radius $c = 6m$ embedded at depth $h = 1.5c$ (Figure 5.7). The finite geological region is situated in poroelastic half-plane Ω_a with the same material properties as those of the finite range Ω_b and as those of the reference poroelastic geomaterial prescribed above. An incident normal time-harmonic P- or

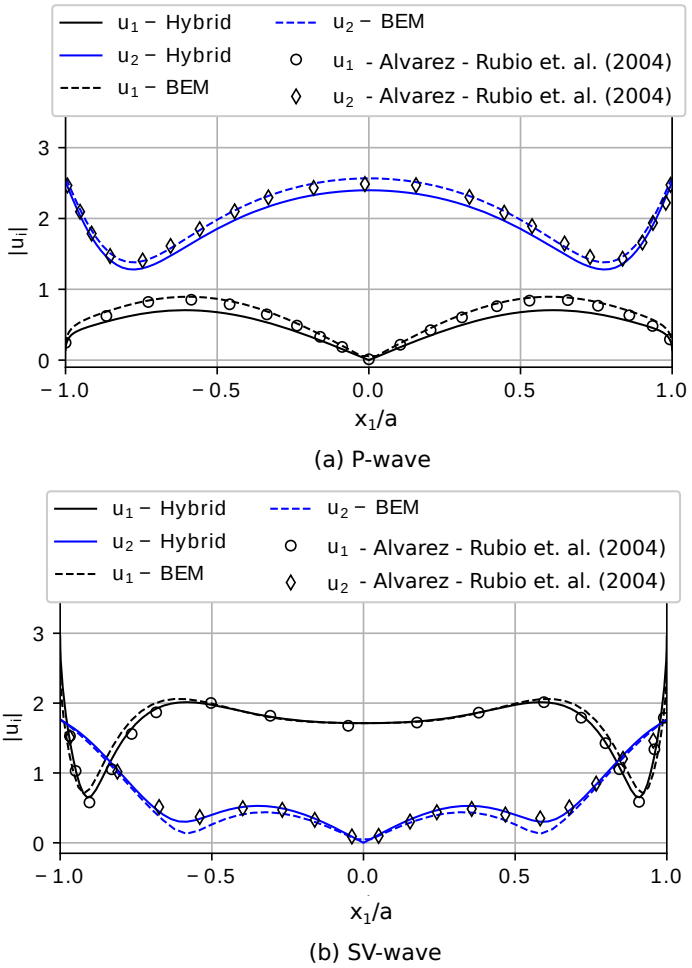

Fig. 5.6 Normalized displacement amplitudes along the canyon in elastic half-plane subjected to normal incident *(a)* P-wave *(b)* and SV-wave with normalized frequency $\eta = 1$.

SV-wave with frequency ω impinges on the finite region with the circular cavity. In the case considered here, the interface boundary Γ_{int} is not the real boundary but the hypothetic one in the hybrid numerical model. In this case, the solutions obtained by the hybrid technique BEM-FEM should recover the numerical solution obtained by pure BEM for a circular cavity in a homogeneous poroelastic half-plane. The porosity is $n = 0$ and $n = 0.1$. Figure 5.8 present normalized displacement amplitudes along the free surface of the poroelastic half-plane under normal incident (a) P-wave and (b) SV-wave with normalized frequency $\eta = (\omega c/\pi C_S) = 0.5$. The shown solutions are obtained by pure BEM and by hybrid model for elastic case $n = 0$ and for poroelastic one at porosity $n = 0.1$. All solutions recover the results in (Luco and de Barros, 1994) for elastic soil.

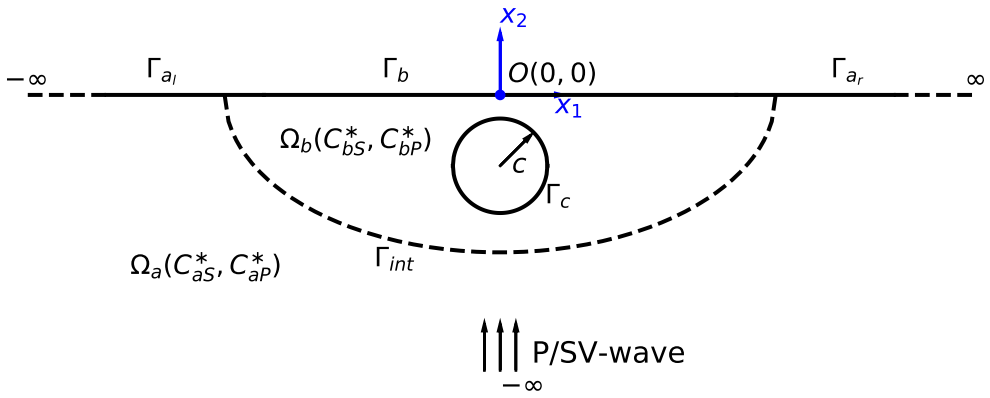

Fig. 5.7 The problem geometry of Test Example 3.

5.5 Simulations and parametric analysis

The aim of this section is to reveal the potential of the proposed hybrid BE-FE computational technique for the synthesis of theoretical seismograms in a complex poroelastic geological region with underground structures. For this purpose, we consider an illustrative example with the geometry shown in Figure 5.9. Consider a finite poroelastic geological range Ω_b with free-surface relief represented by two semi-elliptical hills with centers at $(\pm 20m; 0)$, the major (vertical) axis of $20m$, and minor (horizontal) axis of $15m$. The finite region contains two embedded circular unlined tunnels of radius $c = 10m$ at depth $h = 10m$ and the distance between them is $2d = 40m$. The finite geological region Ω_b is interfaced to semi-infinite poroelastic geological region Ω_a by a semi-elliptical interface boundary Γ_{int} with the major (horizontal) axis of $70m$, and minor (vertical) axis of $35m$. The FEM mesh used for the finite domain Ω_b consists of 2765 quadratic plane strain elements (CPE8R) in ABAQUS, while the BEM mesh in the semi-infinite range Ω_a is presented by 396 quadratic boundary elements (110 along Γ_{int} and 286 along Γ_a in the interval $x_1 \in [0, \pm 200m]$). The simulations are done for both dry and saturated conditions and both the domains are considered to have the same degree of saturation for each simulation, i.e. both dry or both saturated.

Displacement component amplitudes along the free surface of the finite poroelastic region Ω_b (Figure 5.9) with porosities $n_b = 0.1$, $n_b = 0.22$ and $n_b = 0.34$ for dry and saturated soils in the case of vertical incident P-wave with a fixed frequency of $5Hz$ is plotted in Figure 5.10. Figures 5.10*a, b* show the horizontal and vertical displacement amplitudes when the soil porosity in the semi-infinite range Ω_a is $n_a = 0.1$, while Figures 5.10*c, d* are for horizontal and vertical displacement amplitudes at porosity $n_a = 0.34$. Analogous results are given in

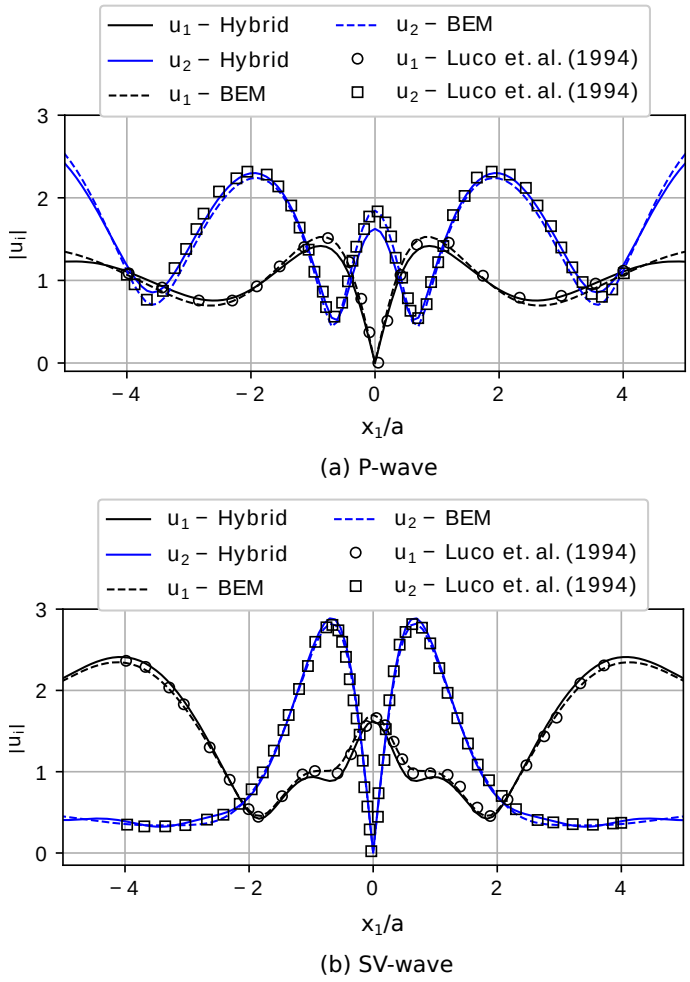

Fig. 5.8 Normalized displacement amplitudes along the free surface in poroelastic half-plane with embedded cavity subjected to normal incident *(a)* P-wave *(b)* and SV-wave with normalized frequency $\eta = 0.5$.

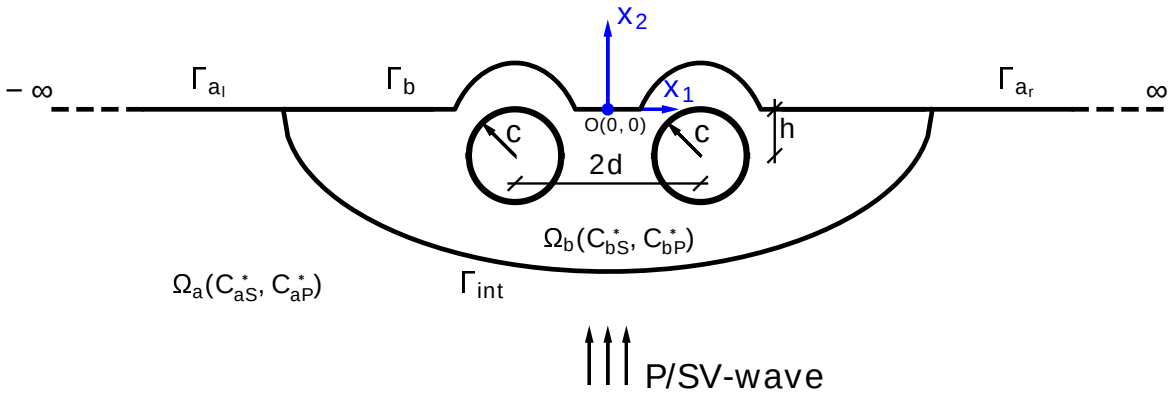

Fig. 5.9 The geometry of the illustrative example.

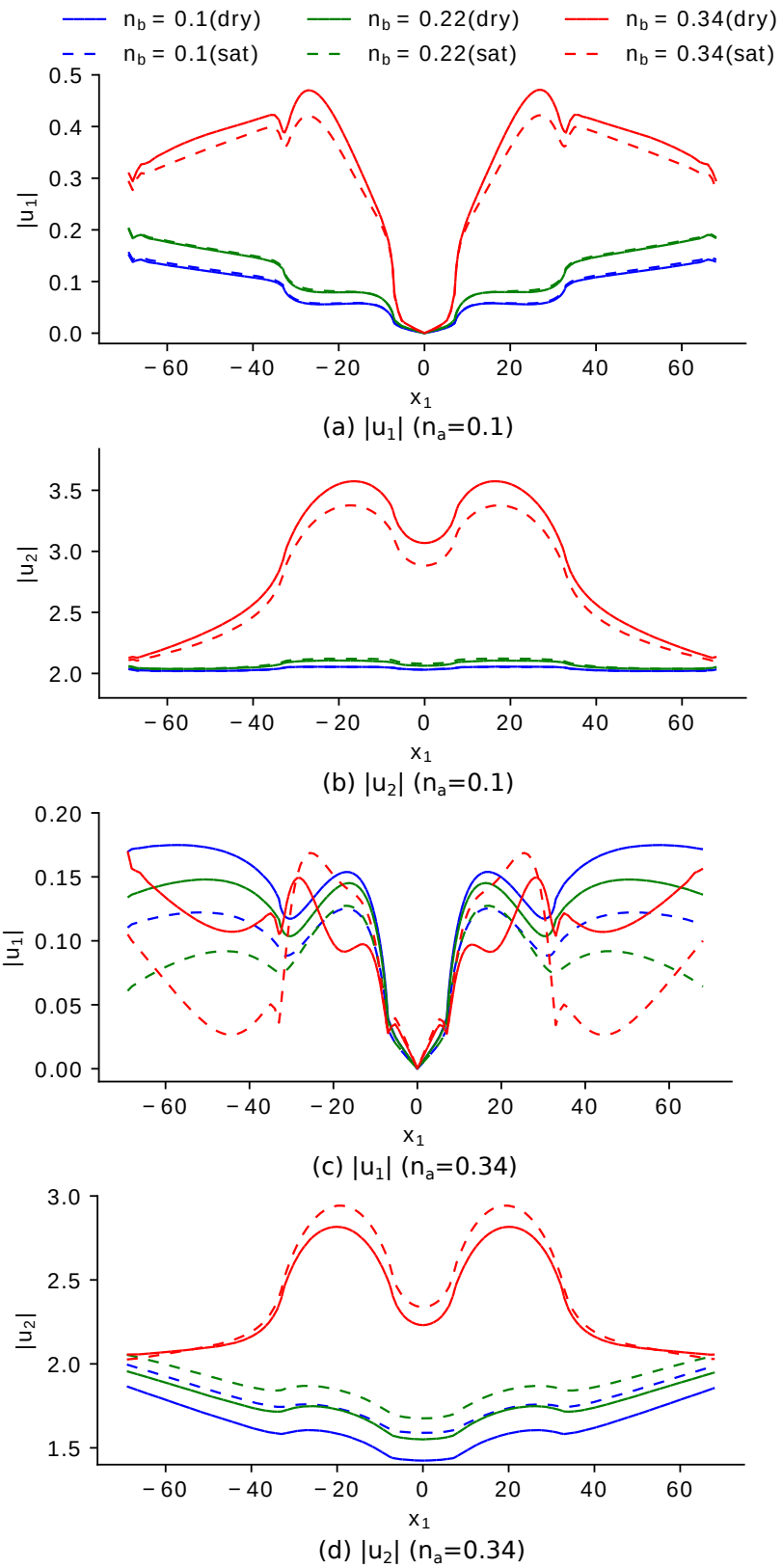

Fig. 5.10 Displacement component amplitudes along the free surface in case of vertical incident P-wave with frequency of $5Hz$.

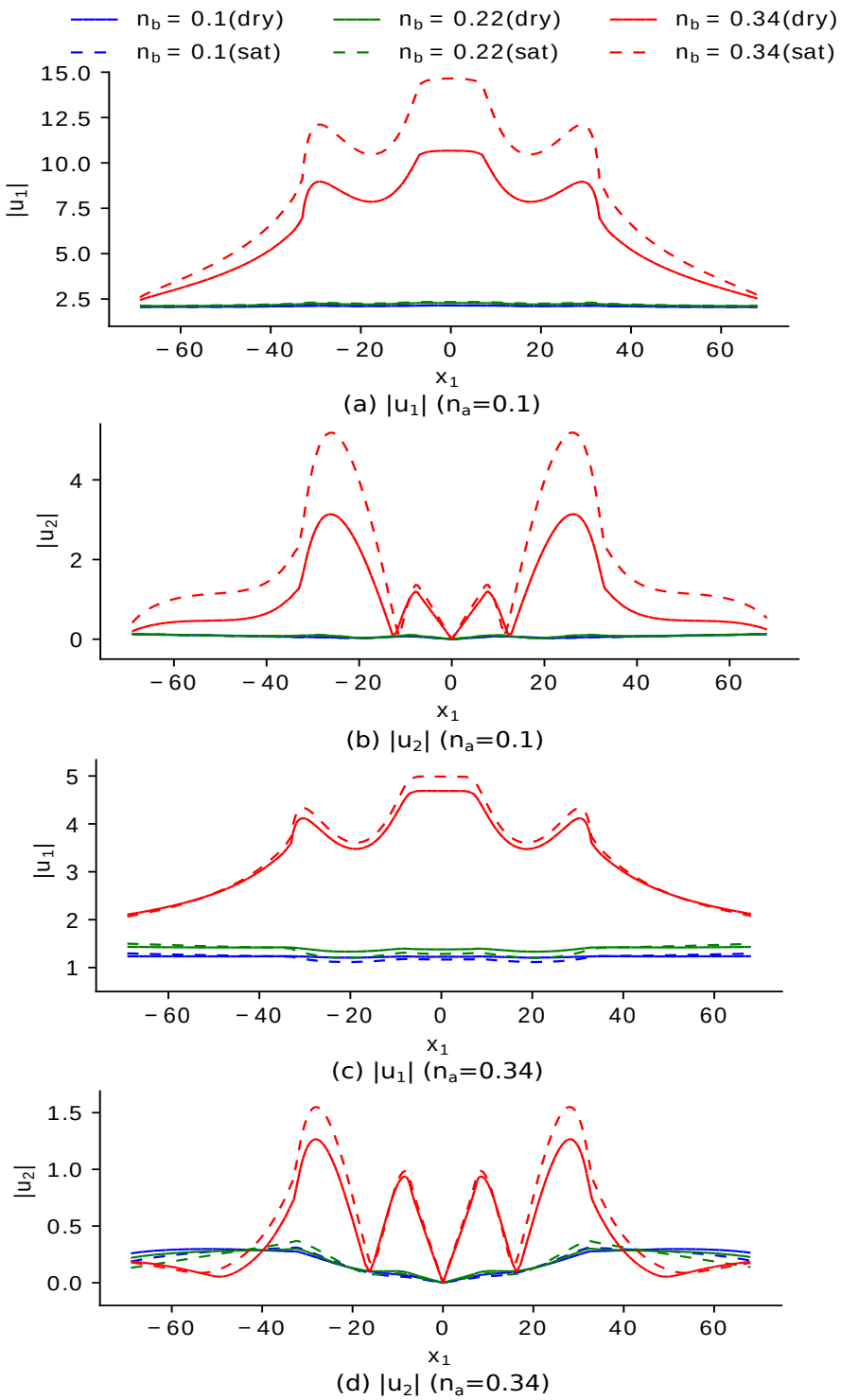

Fig. 5.11 Displacement component amplitudes along the free surface in case of vertical incident SV-wave with frequency of $5Hz$.

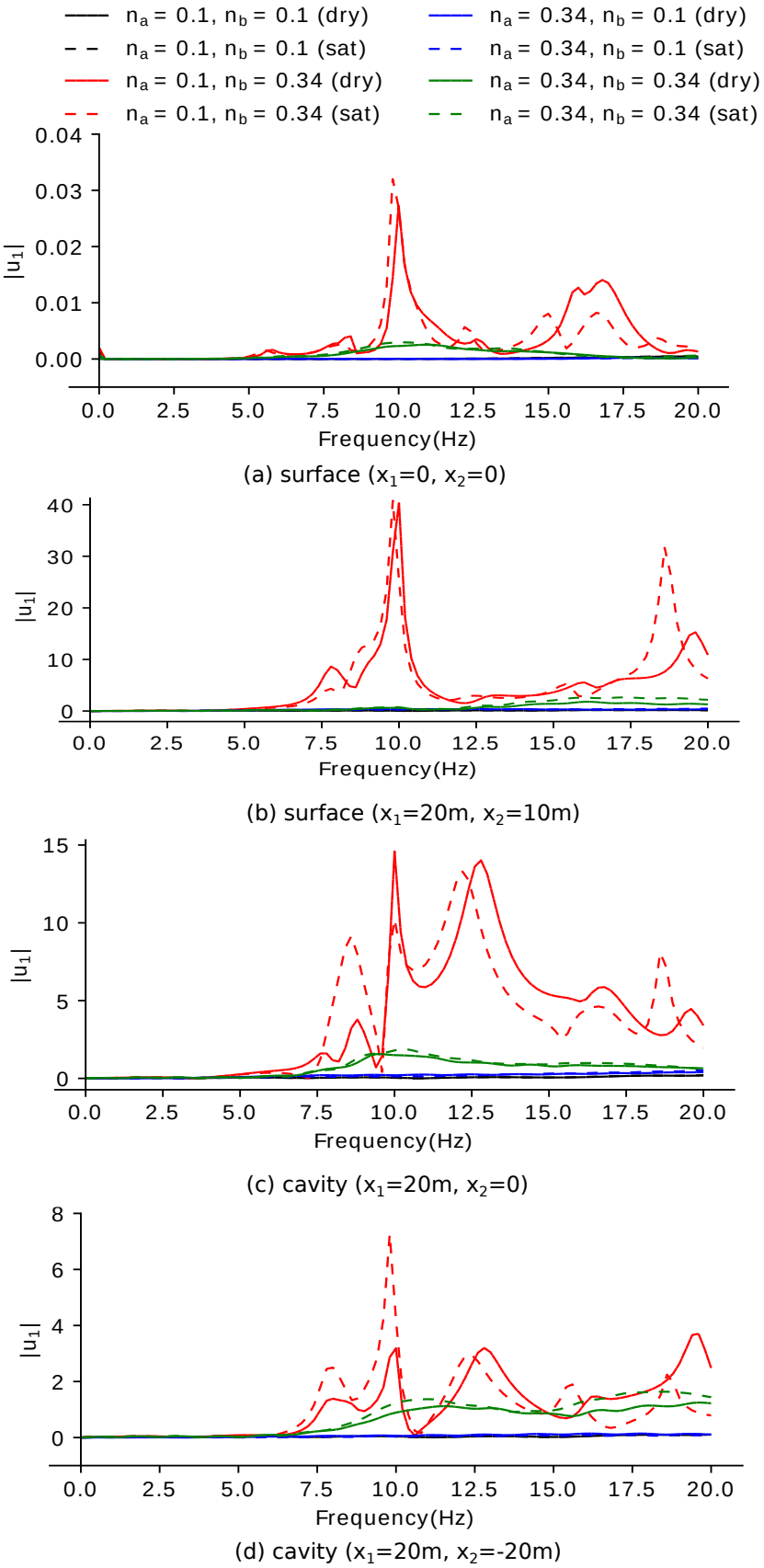

Fig. 5.12 Horizontal displacement amplitude versus frequency of vertical incident P-wave at different observer points for different porosities n_a and n_b of the soil in the regions Ω_a and Ω_b.

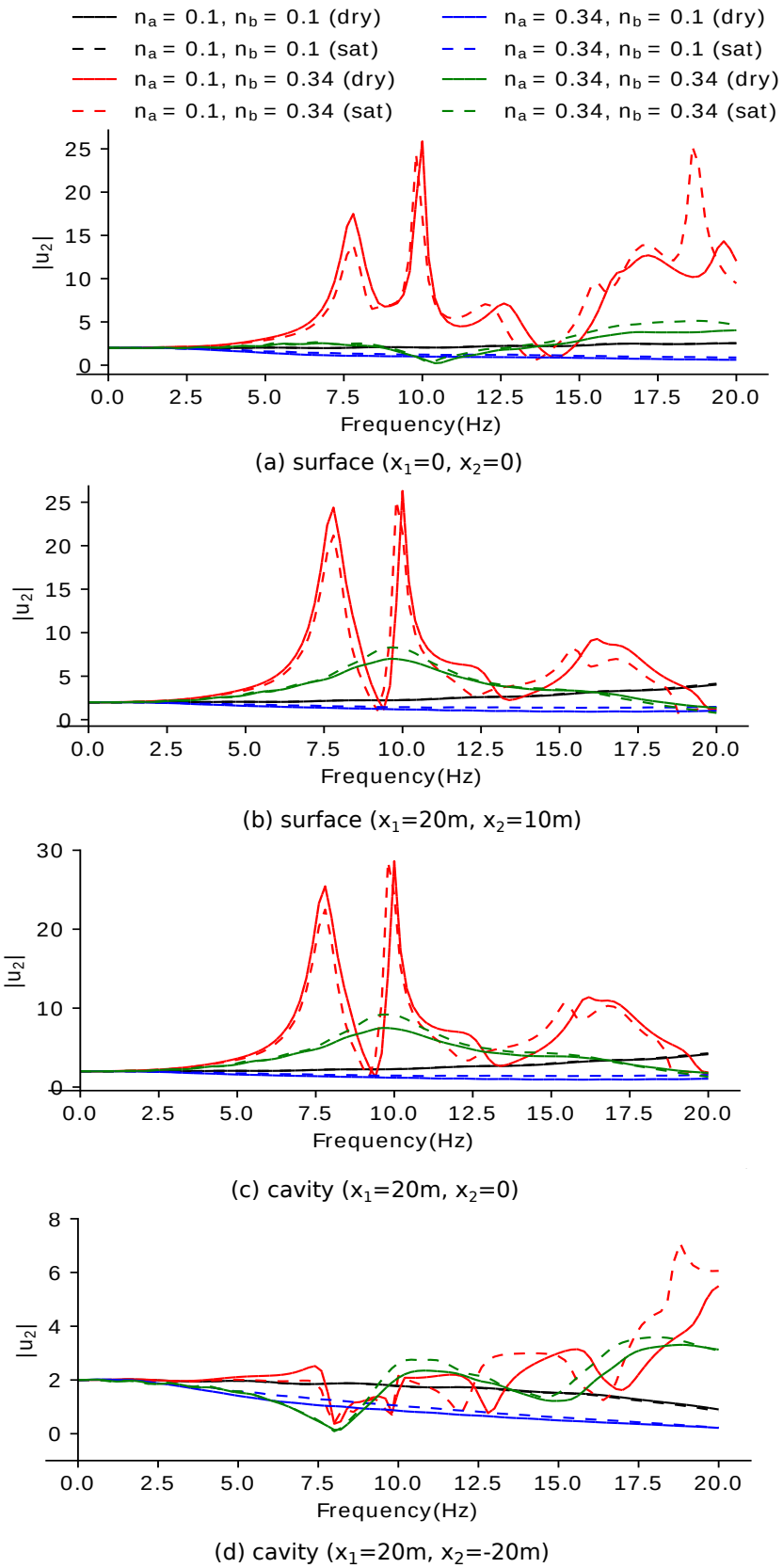

Fig. 5.13 Vertical displacement amplitude versus frequency of vertical incident P-wave at different observer points for different porosities n_a and n_b of the soil in the regions Ω_a and Ω_b.

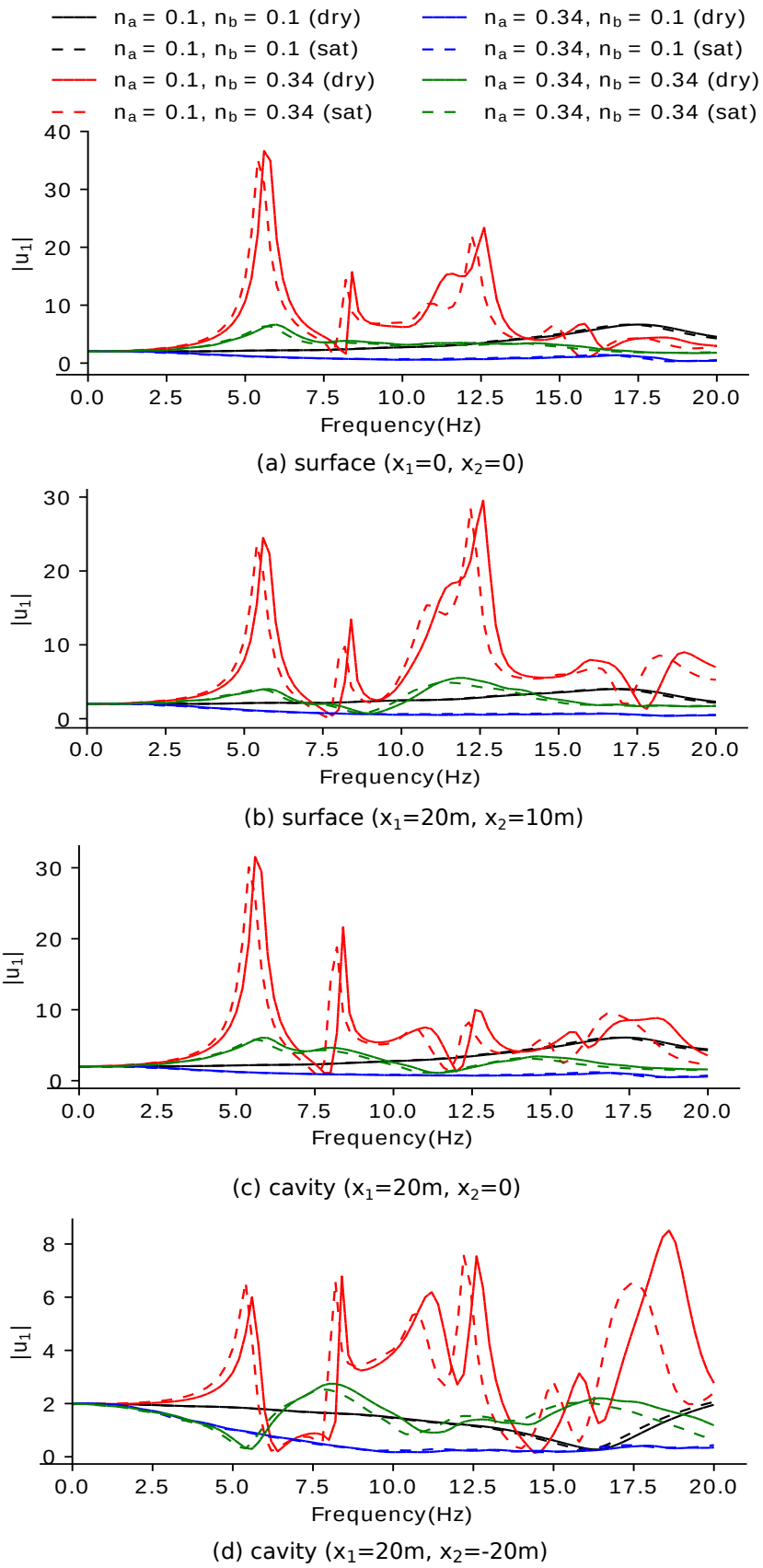

Fig. 5.14 Horizontal displacement amplitude versus frequency of vertical incident SV-wave at different observer points for different porosities n_a and n_b of the soil in the regions Ω_a and Ω_b.

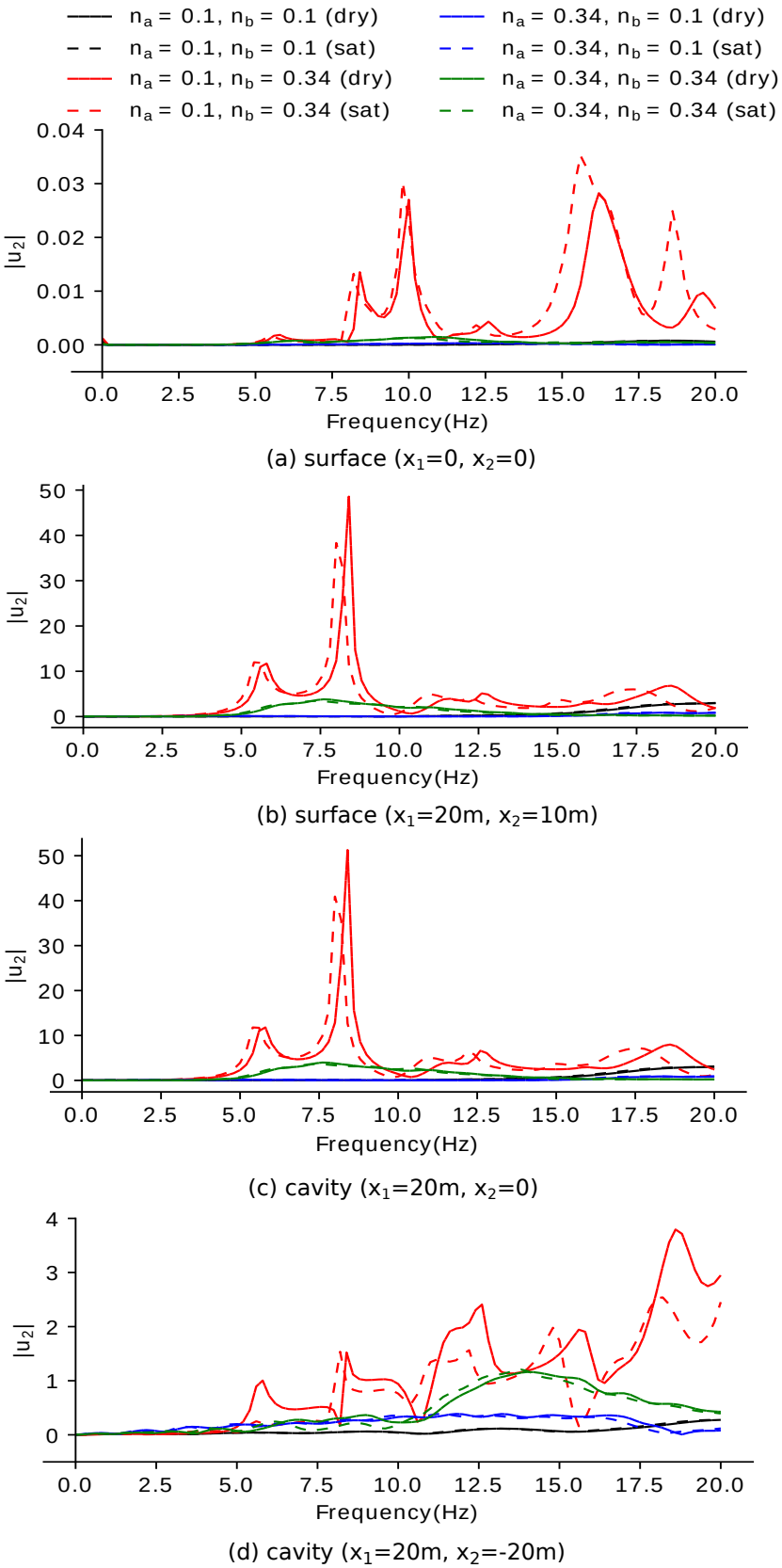

Fig. 5.15 Vertical displacement amplitude versus frequency of vertical incident SV-wave at different observer points for different porosities n_a and n_b of the soil in the regions Ω_a and Ω_b.

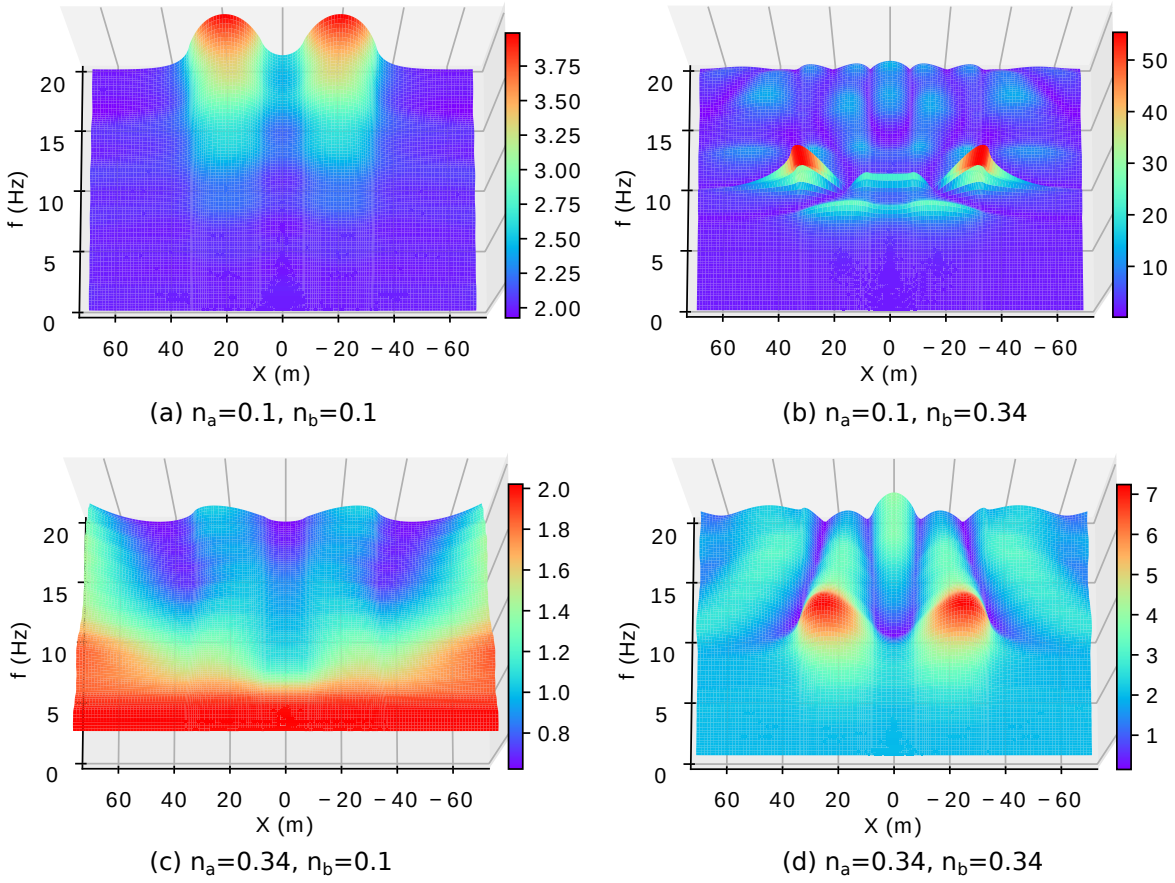

Fig. 5.16 Vertical displacement amplitude along the free surface versus frequency of vertical incident P-wave for different porosities n_a and n_b of the dry soil in the regions Ω_a and Ω_b.

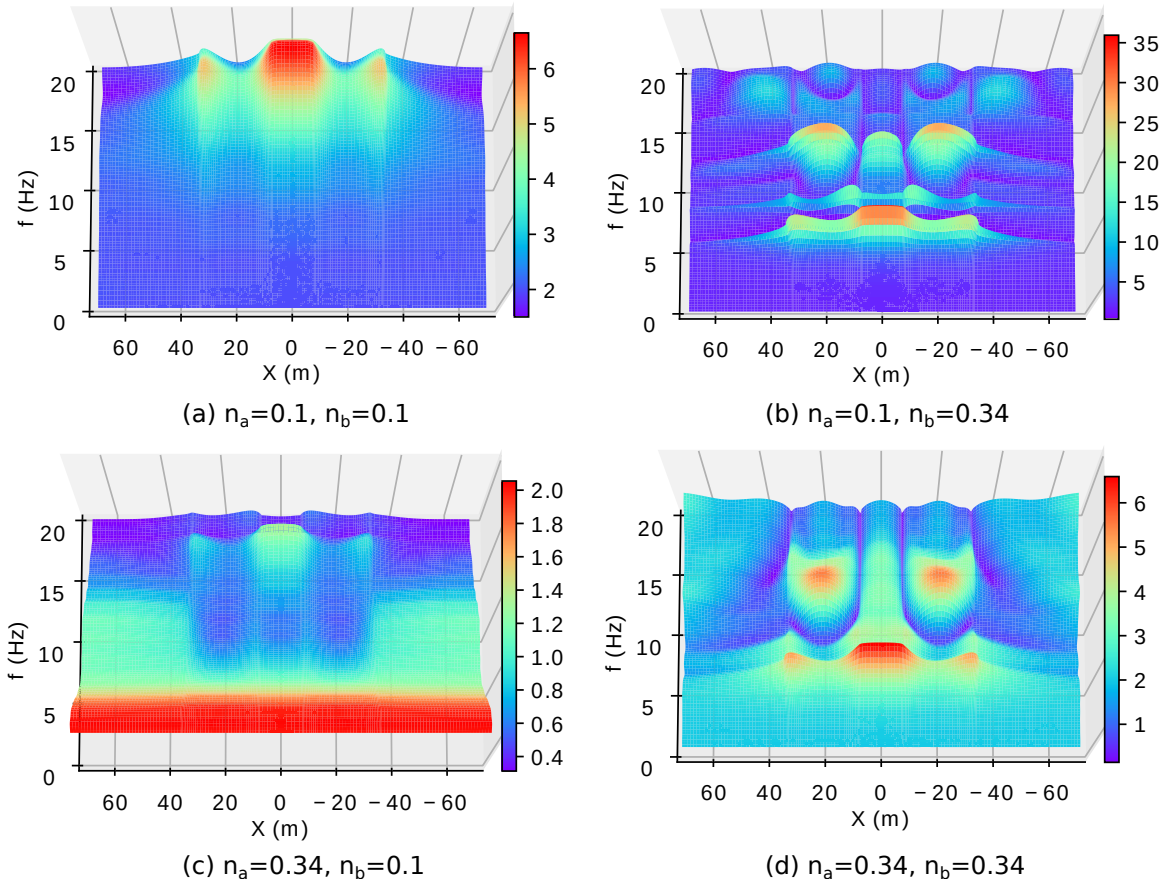

Fig. 5.17 Horizontal displacement amplitude along the free surface versus frequency of vertical incident SV-wave for different porosities n_a and n_b of the dry soil in the regions Ω_a and Ω_b.

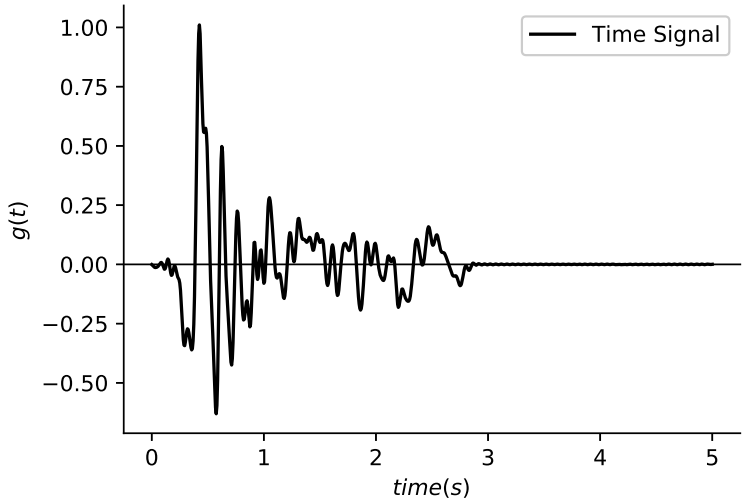

(a) Time History

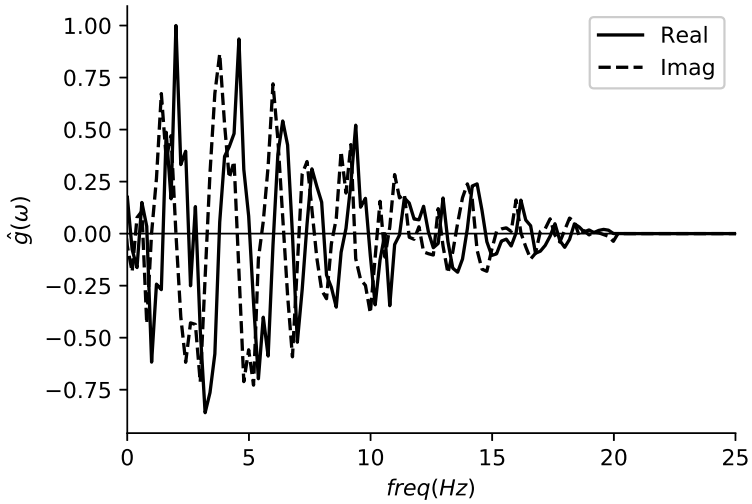

(b) Normalized frequency content

Fig. 5.18 Normalized time history signal used for simulation.

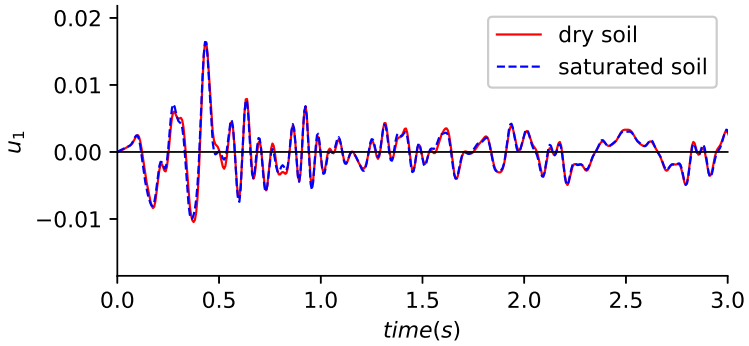

(a) u_1 $(n_a = 0.1, n_b = 0.1)$

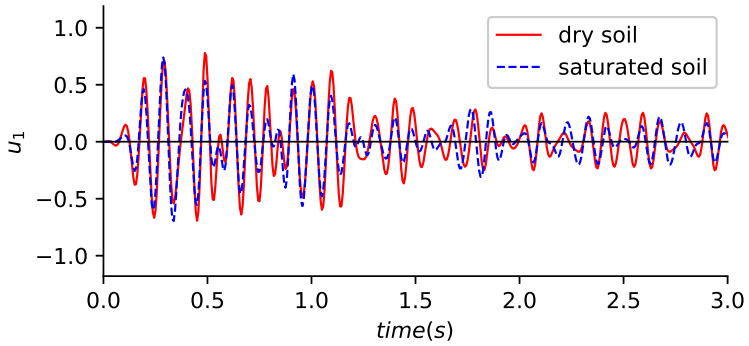

(b) u_1 $(n_a = 0.1, n_b = 0.34)$

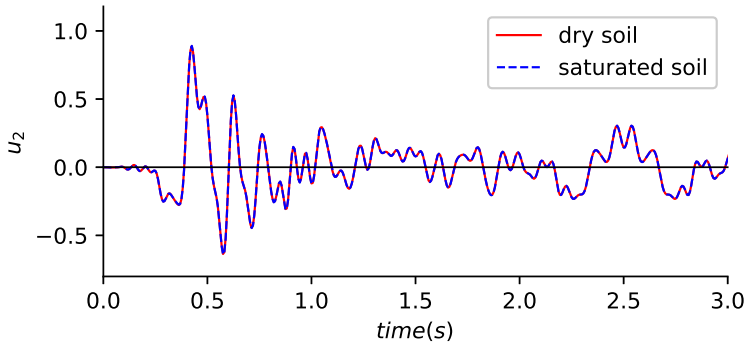

(c) u_2 $(n_a = 0.1, n_b = 0.1)$

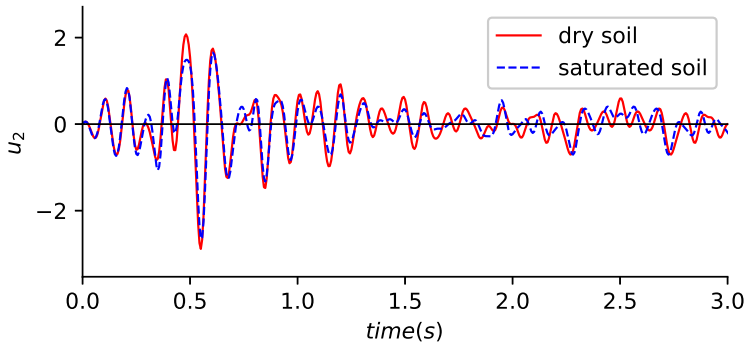

(d) u_2 $(n_a = 0.1, n_b = 0.34)$

Fig. 5.19 Displacement components at a fixed observer point with coordinates $(x_1 = 20m, x_2 = 10m)$ versus time in case of vertical incident P-wave: *(a, c)* horizontal and vertical components for $n_a = 0.1, n_b = 0.1$ and *(b, d)* horizontal and vertical components for $n_a = 0.1, n_b = 0.34$.

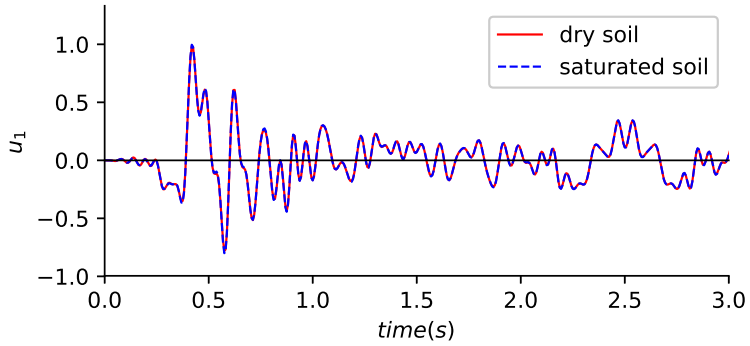

(a) u_1 $(n_a = 0.1, n_b = 0.1)$

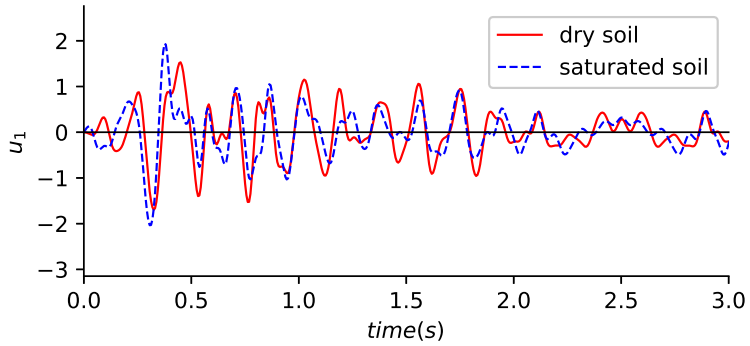

(b) u_1 $(n_a = 0.1, n_b = 0.34)$

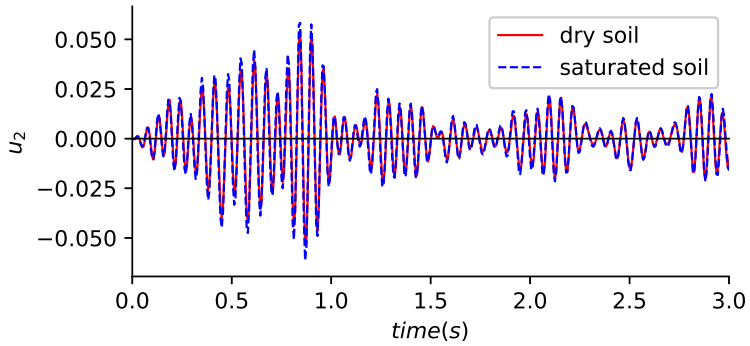

(c) u_2 $(n_a = 0.1, n_b = 0.1)$

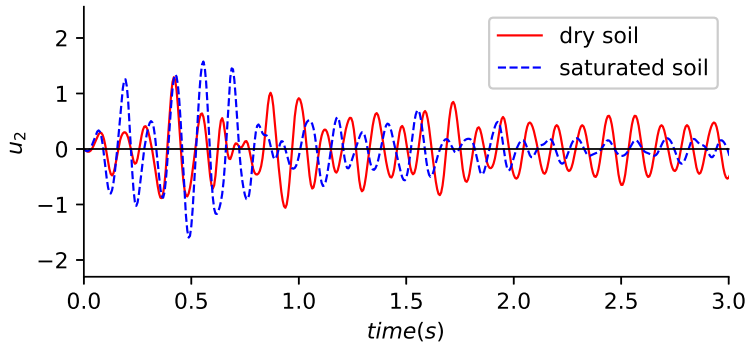

(d) u_2 $(n_a = 0.1, n_b = 0.34)$

Fig. 5.20 Displacement components at a fixed observer point with coordinates $(x_1 = 20m, x_2 = 10m)$ versus time in case of vertical incident SV-wave: *(a, c)* horizontal and vertical components for $n_a = 0.1, n_b = 0.1$ and *(b, d)* horizontal and vertical components for $n_a = 0.1, n_b = 0.34$.

Figures 5.11*a, b, c, d* in the case the seismic load is a normal shear SV-wave. The surface displacement amplitudes are normalized by the amplitude of the incident wave. Figures 5.10 and 5.11 clearly demonstrate the seismic site effects and their sensitivity to the type of dynamic load, the existence of free surface relief and embedded underground structures, the type of the soil and the porosity of the finite-size geological region and the half-plane where it is situated. The components of the displacement field delineate quite precisely the complex geometry of the considered geological region. Numerical results show that there is amplification/deamplification of the seismic signal at the free surface of the finite local region and this is due to the existence of domains with different porosities and especially due to the layer with the higher porosity (yielding a lower wave velocity compared to the bedrock). The elastic bulk module K_{dry} is much greater than the fluid bulk module K_f $(K_{dry} >> K_f)$ at low porosities. Such a material with the high dry frame strength is close to the elastic solid and there is no remarkable influence of the fluid on the solid-fluid system behavior, see results for porosities $n_b = 0.1$ and $n_b = 0.22$. More specifically, a poroelastic medium with high stiffness in the dry skeleton behaves like a purely elastic medium. The greater influence of porosity (respective to the fluid phase) can be observed at higher porosities where $K_{dry} \approx K_f$, see the results for $n_b = 0.34$. Thus, the results of this particular illustrative example, in both qualitative and quantitative terms, evince the importance of considering the local geological details regarding the overall site properties. Bardet's viscoelastic material has the capacity to account for the increase in the stiffness of the porous skeleton due to the pore water pressure increase induced by the seismic load. This can be seen in expressions (5.7), and also from the increased value of λ_{sat} (followed by an increase in P-wave phase velocity) in comparison with the value of λ_{dry}. Specifically, the pore water seems to stiffen the geological material because the seismic wave excitation increases the pore water pressure. In particular, the P-wave characteristics are modified significantly by the change from dry to saturated condition of the geomaterial. This effect of the saturated soil is not clearly visible when considering complex layered geological media with surface relief and underground structures where other key factors such as wave reflection influence together with the effect of porosity.

The frequency content effect can be seen in Figures 5.12-5.17. Horizontal and vertical displacement amplitudes versus frequency of incident normal P- and SV-wave at different observer points $x_1 = 0;\ 20m$ along the free surface and at the top and the bottom of the cavity inside the geological region under consideration are shown in Figures 5.12-5.15. The results are for different combinations of the soil porosities n_a and n_b of both sub-domains Ω_a and Ω_b. The maximal resonance peak of the horizontal displacement amplitudes in Figure 5.12 (incident normal P-wave) occurs at $10Hz$ for $n_a = 0.1,\ n_b = 0.34$. The resonance

peak at the observer point $x_1 = 0.0$ is about 0.035, while that at $x_1 = 20m$ is about 40.0. The maximal amplification at the cavity's top occurs at frequency $10Hz$ and for $n_b = 0.34$ (saturated soil), while that for the cavity's bottom occurs at frequency $10Hz$ and for $n_b = 0.34$ (dry soil), see Figure 5.12*c,d*. The analogous picture for incident SV-wave in Figure 5.14 ($n_a = 0.1,\ n_b = 0.34$) looks different and the maximal amplifications are at observer points $x_1 = 0.0$ and $x_1 = 20$. The first resonance peak of the horizontal displacement amplitudes for SV-wave is shifted to a lower frequency (Figure 5.14) in comparison with analogous ones in the case of P-wave (Figure 5.12). The maximal amplification of the vertical displacement amplitude occurs in the case of incident SV-wave for porosities of near and far-field zones as follows $n_a = 0.1,\ n_b = 0.34$, see Figure 5.15. The maximal amplifications at the observer point $x_1 = 20m$ for porosities $n_a = 0.1,\ n_b = 0.34$ occur at the frequencies: *(a)* $10.0Hz$ and $7.5Hz$ in the case of incident P-wave for the horizontal (Figure 5.12) and vertical (Figure 5.13) displacement amplitude, correspondingly; *(b)* $12.5Hz$ and $8.5Hz$ in the case of incident SV-wave for the horizontal (Figure 5.14) and vertical (Figure 5.15) displacement amplitude, correspondingly.

Figures 5.12-5.17 illustrate the following effects: (i) as the incident wave frequency increases, the displacement amplitudes show different zones of amplification and deamplification, depending also on the type of the incident wave. Large values in the frequency of the incoming wave yield a complicated displacement picture with high signal amplifcation, and serves as a strong indicator of the presence of a complex inhomogeneous and heterogeneous geological region; (ii) the resonance frequencies are shifted to the lower ones for the saturated soils in comparison with the dry ones; (iii) the maximal values of the displacement amplitudes occur at the observer point $x_1 = 20m$ where the peak of the hill is located; (iv) existence of the free surface relief and underground structures have strong influence on the wave picture in the vicinity of relief zone and tunnels and in this aspect the anti-seismic design of the buildings near such a region should improve the input level of earthquake ground motion to some extent; (v) the spectral characteristics strongly depend on the porosities of the near- and far- field zones and amplification increases with the increase of the porosity in the near-field zone; (vi) Figures 5.16$-$5.17 demonstrate visually how the wave scattering and diffraction fields change strongly in the near-field zone of the hills and tunnels.

The displacement seismic response at a fixed observer point with coordinates $(x_1 = 20m; x_2 = 10m)$ due to a transient incident normal P- and SV-wave is presented in Figure 5.19 and Figure 5.20 correspondingly. Two types of combinations for porosities are used for dry and saturated soils: *(a)* $n_a = 0.1;\ n_b = 0.1$, *(b)* $n_a = 0.1;\ n_b = 0.34$. The input seismic signal is a portion of a real record of an earthquake that happened in Panagyurishte, Bulgaria ($M = 3.0$, depth is $15km$) with a time history presented in Figure 5.18. The displacement

components are normalized by the maximal value of the displacement in the input seismic signal.

The following conclusions can be done from the results in Figures 5.19-5.20: (i) in the case of low porosities $n_a = 0.1;\ n_b = 0.34$, there is no difference between solutions for dry and saturated soils, see Figure 5.19*a,c* and Figure 5.20*a,c*; (ii) in the case of incident P-wave for the following combination of soil porosities $n_a = 0.1;\ n_b = 0.34$, the seismic response for the saturated soil is lower than that for the dry one, see Figure 5.19*b,d*; (iii) in the case of incident SV-wave for $n_a = 0.1;\ n_b = 0.34$, the seismic response for the saturated soil is lower than that for dry one after the time $t = 1s$, see Figure 5.20*b,d*.

5.6 Concluding remarks

An efficient hybrid technique comprising FEM through commercial ABAQUS software and the BEM application from the authors is developed for the solution of 2D seismic problems for saturated geological regions with underground structures. The hybrid numerical scheme is based on the following computational steps: (a) direct BEM for the unbounded part of the geological region; (b) conventional FEM for the near-field soil profile together with the underground structures; (c) the BEM model is inserted as a macro-finite-element in the FEM commercial software ABAQUS which solves the entire problem in the frequency domain; (d) finally, inverse FFT is applied to recover finally solution in time domain. The verification study of the numerical scheme is presented.

The simulations reveal the complex character of the seismic field in a saturated geological region containing relief peculiarities, layers and underground structures. The main contribution of this model is the capability to describe the entire wave path starting from the seismic source to the local site under consideration in one model. The obtained results allow for the integration of BEM modules into a commercial software ABAQUS so that it can realistically model the semi-infinite, far-field geological region through which seismic waves travel by the usage of a macro-finite-element. More specifically, it is possible to create a library of macro-finite-elements presenting different BEM models with more complex mechanical properties of the unbounded far-field zone. The proposed hybrid model has the potential to be developed further for 2D and 3D soil-structure interaction problems, accounting for the key factors such as anisotropy, continuous inhomogeneity and poroelasticity of the far-field semi-infinite BEM zone, the physical and geometrical non-linearity of the bounded FEM local region containing underground and/or overground structures.

The hybrid BEM-FEM technique proves a valuable tool for numerical analysis in soil-structure interaction problems involved in earthquake engineering and structural dynamics.

Any nonlinear behaviors at the soil-structure interface or in the structures can be incorporated into the FEM region.

Chapter 6

Enhancement of in-plane seismic full waveform inversion by CPU and GPU parallelization

FWI is regarded as one of the important tools in exploration geophysics. It is widely used to produce a high quality image of subsurface of the earth, based on the seismic measurements on the surface. Seismic FWI by FDM and inverse modeling by BEM using PSO, studied in previous chapters, show its applicability to model seismic wave propagation in inhomogeneous and heterogeneous half-plane. However, due to the amount of data, model size and iterative procedures, the numerical computation of FWI are computationally intensive and time-consuming. This chapter addresses the parallel computation of seismic FWI in CPU and GPU. The stress velocity formulation of P-SV wave equation is considered in time domain. A four node staggered grid finite-difference method is applied to solve the equation, where PML is used along the external boundaries to satisfy Sommerfeld's radiation condition at infinity. Conjugate gradient method is used as a local search algorithm for adjoined modeling in FWI. The host code is in C++, and parallel computation codes are in CUDA C. The computational time and performance gained from CUDA C and OpenMP parallel computation of FWI in different hardware are compared to the serial code. Parts of this chapter are published as:

Basnet, M. B., Anas, M., Rizvi, Z. H., Ali, A. H., Zain, M., Cascante, G., and Wuttke, F. (2022). Enhancement of In-Plane Seismic Full Waveform Inversion with CPU and GPU Parallelization. *Applied Sciences,* 12(17), 8844.

6.1 Introduction

The physical properties of the Earth's subsurface have always been of interest to humankind. Ranging from scientific development to industrial use, such as oil and gas industries and engineering applications, determining or approximating the physical properties is essential. Exploration geophysics is the branch of geophysics that uses physical methods such as seismic, acoustic, electromagnetic, or electric measurements to extract information about the Earth's subsurface without physical disturbances. FWI is a wave inversion procedure where the high-quality estimate of the subsurface parameters is obtained by minimizing the misfit between the observed and modeled data. Seismic and acoustic waveform inversion is widely in practice. Seismic or acoustic signals are applied at the surface, which gets propagated through the subsurface of interest, and the output signals are obtained at receiver points (see Figure 6.1). The wave phenomenon is modeled using an appropriate numerical technique, and the output is compared to that obtained from the field test. The model is updated with a mathematically calculated approximation function until we get a desired minimum value of the misfit to get a high-quality approximation of the subsurface properties (Guasch et al., 2020). This chapter deals mainly with time-domain seismic wave inversion in a two-dimensional system using FDM.

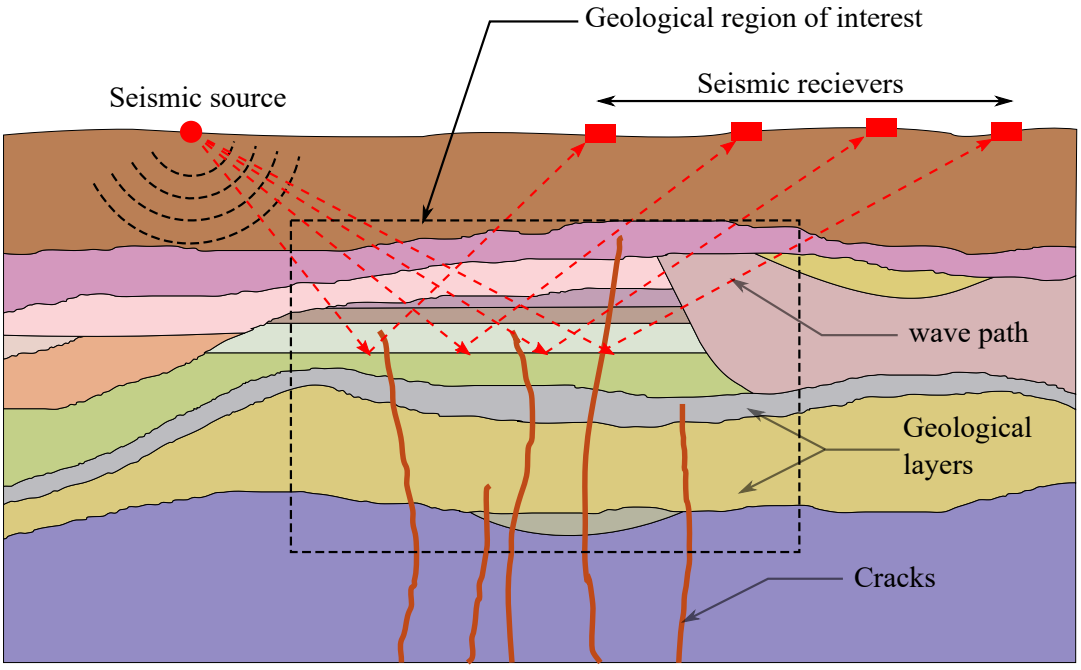

Fig. 6.1 A schematic representation of geophysical investigation using seismic waveform inversion of a subsurface geological region with multiple layers.

6.1.1 Seismic full waveform inversion

The first introduction and numerical implementation of FWI is found to be developed in the 1980s (Tarantola, 1984a,b, 1988, Gauthier et al., 1986, Mora, 1987, Pica et al., 1990). Since its first implementation, many authors have implemented and modified it for different purposes and methods. The time domain FWI approach is applied in frequency domain approach in (Pratt, 1990b, Pratt and Worthington, 1990). The performance of frequency domain approach of FWI is optimized with parallelization by (Sourbier et al., 2009a,b). FWI is widely used for inversion of: (a) acoustic waves, e.g., (Yang et al., 2018, Wei et al., 2014, Köhn, 2011) (b) seismic waves, e.g. (Fabien-Ouellet et al., 2017, Charara et al., 2000, Pan et al., 2020, Köhn, 2011). With the advancement in modern-day computers and parallel processing capabilities, FWI is gaining its popularity in exploration geophysics.

FDM is one of the most widely used inversion methods in the numerical implementation of FWI. Conventional FDM is based on the straightforward numerical implementation of PDEs for the given BVP. The partial differential terms are substituted with algebraic differences for a small argument x, such that $x \to 0$, which makes it easy to implement and understand (refer Equations (6.6)–(6.7)). The finite difference formulation for seismic waves can be found in: *(a)* (Moczo, 1998, Moczo et al., 2007, Chen and Cao, 2016) for forward wave propagation problems and *(b)* (Fang et al., 2020, Köhn, 2011, Li et al., 2016, Abubakar et al., 2011) for FWI problems. To satisfy Sommerfeld's radiation condition at infinity (i.e., the wave radiating towards infinity should not come back unless there are reflecting boundaries), absorbing boundaries or PML is used, see (Köhn, 2011). PML damps the outgoing wave field over a distance (number of grids in discrete form), making it more efficient and accurate than a normal absorbing boundary. Details about PML can be found in (Komatitsch and Martin, 2007, Martin et al., 2008, Martin and Komatitsch, 2009).

6.1.2 Parallel computation

The finite difference for FWI is computationally intensive. In each iteration step of FWI, the forward wave propagation model has to be computed several times and is both time and resource-consuming. Therefore, reducing the computation costs of FWI has been an important area of research for geophysical researchers. Parallel processing can efficiently perform seismic wave propagation and FWI computations at a large scale. To maximize the potential of parallel machines, the research challenge is to reframe the problem, develop parallel algorithms, and devise new computational strategies. Processing speeds on a single thread in CPUs have stagnated in the past two decades. However, computer hardware and software advances have made parallel processing a realistic and appealing technology.

GPUs are now among the most popular computing resources for parallel computation because of their high processing rates and low cost. Their capabilities have evolved from simple peripherals to powerful, programmable, and sophisticated processors in their own right. The potential of using inexpensive graphics technology for general-purpose computing has sparked great interest.

Since the early 2000s, seismic forward modeling has used parallelization strategies based on software enhancements utilizing APIs such as OpenMP and hardware improvements by porting codes to GPUs Li et al. (2020). Jiang and Zhu (2018) discusses the implementation of GPU-based 2D elastic FWI in the time domain on a single GPU card. The authors utilized a boundary-saving strategy to reconstruct forward wave fields to reduce the significant RAM utilization. The work demonstrates that using shared memory can reduce the modeling time by about a third. Wang et al. (2011) describes the development of a parallel scheme to speed up FWI on GPUs with Compute Unified Device Architecture (CUDA). Using the GTX480 GPU, the authors could speed up the FWI 80 times compared to the CPU implementation. The acceleration of a 3-D finite difference in time domain wave propagation code on NVIDIA GPU graphics cards and CUDA programming language is discussed in (Michéa and Komatitsch, 2010). The authors also used Message Passing Interface (MPI) to use multiple GPUs in parallel. The authors report the acceleration of the wave propagation code by a factor between 20 to 60 compared to a serial implementation.

It can be concluded from the literature review that the parallel programming of FWI in GPU has significantly improved the computational speed. However, the different physical methods have to be tested, and the computational efficiency needs to be further enhanced to adopt it for practical applicability. In this chapter, the numerical models of seismic forward and FWI models for P/SV wave field in GPU are implemented and tested against the serial and CPU parallel codes. As mentioned earlier, the work investigates the parallelization of the method using the OpenMP and CUDA Application Programming Interface (API) on the CPU and GPU, respectively.

6.1.3 Importance, scope and limitations of the study

FWI is a handy non-destructive method to obtain accurate information about the subsurface parameters of the earth, and its importance is still increasing. However, FWI primarily has two significant scopes for improvement to find widespread applicability in exploration geophysics and engineering. They are: *(a)* the improvement of the optimization and parameter search algorithms, which is not the scope of this study, and *(b)* the improvement in computational efficiency. FWI is an iterative algorithm that demands high computational costs and high

memory, which is generally out of the scope of general computers. The computation for the given hardware often takes days or months, which makes it practically inefficient.

The present study mainly focuses on enhancing in-plane seismic FWI with CPU and GPU parallelization. The existing numerical algorithms are implemented in serial and parallel codes, and the computational efficiency achieved by parallelization is studied. Thus, the computational enhancement by parallelization is limited to the specific algorithm used in the programming. The study is conducted about in-plane elastic waves in time domain, and FWI is conducted using the step-gradient method (Köhn et al., 2014). Other advanced algorithms, where faster and more robust search methods enhance the FWI algorithms, are not within the scope of this study. Additionally, the test and validation are conducted for the limited number of hardware available. The performance boost due to CPU and GPU parallelization may vary depending upon the hardware configuration.

6.2 Mathematical model

6.2.1 Stress velocity formulation of 2D elastic wave equation

The stress velocity formulation of the elastodynamic equation, as given by (Köhn, 2011), and substituted in two-dimensional in-plane wave motion equation (P-SV wave field), can be written as in Equations (6.1)–(6.5).

$$\rho \frac{\partial v_x}{\partial t} = \frac{\partial \sigma_{xx}}{\partial x} + \frac{\partial \sigma_{xy}}{\partial y} + f_x, \tag{6.1}$$

$$\rho \frac{\partial v_y}{\partial t} = \frac{\partial \sigma_{xy}}{\partial x} + \frac{\partial \sigma_{yy}}{\partial y} + f_y, \tag{6.2}$$

$$\frac{\partial \sigma_{xx}}{\partial t} = (\lambda + 2\mu)\frac{\partial v_x}{\partial x} + \lambda \frac{\partial v_y}{\partial y} + \frac{\partial \sigma_{xx0}}{\partial t}, \tag{6.3}$$

$$\frac{\partial \sigma_{yy}}{\partial t} = \lambda \frac{\partial v_x}{\partial x} + (\lambda + 2\mu)\frac{\partial v_y}{\partial y} + \frac{\partial \sigma_{yy0}}{\partial t}, \tag{6.4}$$

$$\frac{\partial \sigma_{xy}}{\partial t} = \frac{1}{2}\left(\frac{\partial v_x}{\partial y} + \frac{\partial v_y}{\partial x}\right) + \frac{\partial \sigma_{xy0}}{\partial t} \tag{6.5}$$

where x and y are two-dimensional space variables, t is time variable, v_x and v_y are particle velocities along x and y directions, $\partial\sigma_{xx}$, $\partial\sigma_{yy}$ $\partial\sigma_{xy}$, are principle and shear stress variables, $\partial\sigma_{xx0}$, $\partial\sigma_{yy0}$ $\partial\sigma_{xy0}$, are body stresses and, $\frac{\partial}{\partial t}$, $\frac{\partial}{\partial x}$ and $\frac{\partial}{\partial y}$ are partial differential operators to the respective variables.

6.2.2 Numerical implementation in FDM

For the numerical implementation of elastodynamic wave equations (6.1)–(6.5), they are discretized in finite time and space over a two-dimensional grid. The finite-difference operators are based on simple differences over a small interval of space and time as given in Equations (6.6) and (6.7).

$$\frac{\partial P^{+}}{\partial x} \approx \frac{P[i+1]-P[i]}{dh} \quad \text{Forward operator.} \tag{6.6}$$

$$\frac{\partial P^{-}}{\partial x} \approx \frac{P[i]-P[i-1]}{dh} \quad \text{Backward operator} \tag{6.7}$$

Where, P is the given function, i is the grid index, and dh is a small increment in the space or time variable x. A combination of forward and backward operators is also possible.

A standard staggered grid (SSG), suggested by (Virieux, 1986, Levander, 1988), is widely implemented by other researchers for computation of two-dimensional seismic wave propagation problems. The standard staggered grid, as implemented in (Köhn, 2011) and shown in Figure 6.2, is used for numerical implementation in this Chapter. An arithmetic mean is used to obtain density ρ, and a harmonic mean is used to obtain Lame constant parameter μ at the half grid points in the staggered grid. A detail of finite difference discretization of seismic FWI problem and computational implementation can be found in (Köhn, 2011, Köhn et al., 2014).

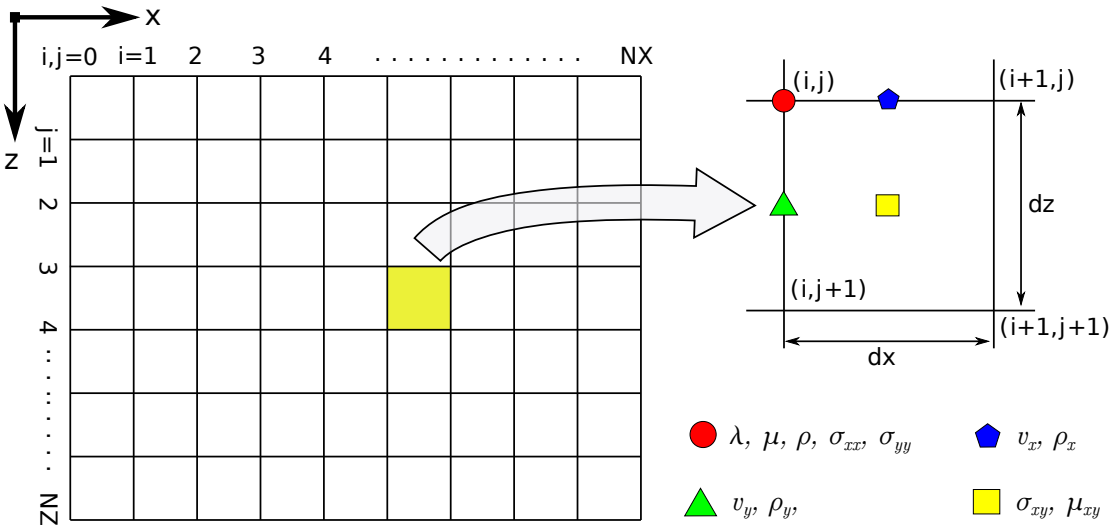

Fig. 6.2 A staggered grid configuration for use in seismic finite difference modeling following (Köhn, 2011, Köhn et al., 2014, Virieux, 1986, Levander, 1988).

PML, as implemented in Köhn et al. (2014), is used along the boundary. The perfectly matched layer frame is added to the finite difference grid, where the wave equation is solved in the frequency domain with coordinate stretching in this region (see Figure 6.3). The arrangement absorbs the outgoing waves and creates a reflectionless boundary frame (Komatitsch and Martin, 2007) and the Sommerfeld's radiation condition is numerically implemented.

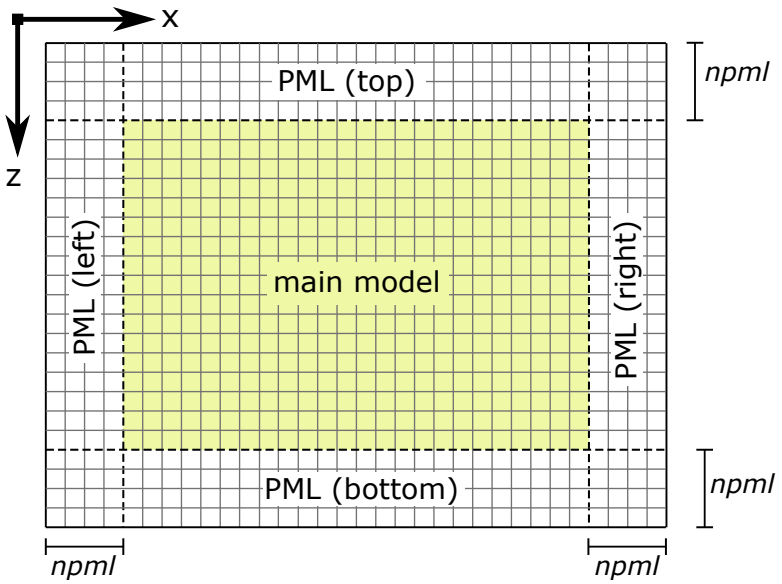

Fig. 6.3 Perfectly matched layers in finite difference grid (*npml* = Number of grids in perfectly matched layers).

For FWI, a start model has to be initialized in the first step. A start model could be a informed guesswork with the information available about the ground. The mathematical model is solved for the given seismic source, and the output signals are recorded at the receiver locations. This part is called the forward model, and the modeled output at the receivers is called modeled data (u^{mod}). The seismic recordings, that we have from the field recordings, are referred to as observed data (u^{obs}). The difference between them is referred to as residual data and can be measured using vector norm. For this case, L_2 norm, given by Equation (6.8) is used. The gradient-based method given in Köhn (2011) is implemented in parallel FWI computation in this chapter.

$$\mid L \mid_2 = \left(\sum_{i=1}^{n} \mid u^{mod} - u^{obs} \mid^2 \right)^{1/2} \tag{6.8}$$

where, n is the number of receivers. L_2 norm is related to energy, which is used to calculate the energy gradients, and with proper step length, the misfit is gradually minimized in each iteration; see Köhn et al. (2014).

6.3 Parallel computational model

In terms of CPU clock speed, current generation computing has reached saturation, primarily due to the enormous increase in cost and power requirement for increasing clock frequency further from current standards (Ross, 2008). Until 2004 Moore's law was in full force, with chip densities doubling every two years. It also increased clock speed as the chip dimension decreased due to Dennard scaling. According to this principle, the power needed to run transistors in a given volume remains constant regardless of the number of transistors. As the transistors do not scale with size, the power density increases as transistors get smaller. Increasing clock speeds also implies a higher voltage, which increases power consumption. With a smaller transistor, the static power named leakage begins to dominate. In addition, more heat is generated with increasing clock speeds, requiring more robust cooling solutions.

The processor shifted from a single-core to a multicore to combat the above mentioned issue. Power and frequency are fundamentally linked in multicore processors. By incorporating multiple cores, the frequency of each core can be lowered, which allows the power generally given to a single core to be distributed among multiple cores. Thus, a multicore processor produces significantly higher performance and results in parallel processing (Ramanathan, 2006). By focusing more on increasing the core count rather than the clock speed, parallel computing is one of the most optimal methods of achieving high performance from a CPU (Robey and Zamora, 2021). The comparison between OpenMP and CUDA is given in Table 6.1.

6.3.1 OpenMP

OpenMP is a parallel programming model for shared memory and distributed shared memory multiprocessors. The OpenMP API supports multi-platform shared-memory parallel programming in C/C++ and Fortran. The OpenMP API defines a portable, scalable model with a simple and flexible interface for developing parallel applications on platforms from the desktop to the supercomputer. OpenMP supports the parallelization of small portions of a program at a time rather than all at once, a method also known as incremental parallelization. As a result, it is possible to observe the impact of the parallelization of individual functions on the application (Chandra et al., 2001). Through OpenMP, the compiler guides the paral-

Table 6.1 Major features of OpenMP and CUDA (Memeti et al., 2017)

	OpenMP	**CUDA**
Parallelism	- Data Parallelism - Asynchronous task parallelism - Host and device	- Data Parallelism - Asynchronous task parallelism - Device only
Architecture abstraction	- Memory hierarchy - Data and computation binding - Explicit data mapping and movement	-Memory hierarchy - Explicit data mapping and movement
Synchronisation	- Barrier - Reduction - Joint	- Barrier
Framework Implementation	- Compiler directives for C/C++ and Fortran	C/C++ extensions

lelization of code through directives, easing the burden on programmers of doing it manually (Gimenes et al., 2018). The steps to parallelize the given code using OpenMP have been elaborated in Figure 6.4. An important aspect in OpenMP is identifying which functions take the longest to execute. The second step involves identifying the code blocks in the function that could be parallelized. This is conducted by ensuring that operations in parallel are not accessed in the middle of their execution and that each result is calculated independently of the others in parallel. After declaring sections as parallel, the variables are defined as each thread may require a variable only accessible to them. Finally, several test cases must be run to check that the results are identical to sequential code and that there is no race condition.

6.3.2 GPU

GPUs are programmable processors among the most powerful computing devices available in terms of performance and price. GPUs are high-density processors known to accelerate graphics applications compared to CPUs due to their multi-core design and high memory bandwidth. Because of the GPU's parallel architecture, it has sustained a steady performance boost. A current-generation high-end GPU exceeds a high-end general-purpose CPU in terms of processing power. On a GPU, a shared memory pool available to all threads in the block performs substantially better than a global memory pool, see Figure 6.5. The programming model is based on the hierarchy of hardware parallelism. The GPU kernel divides all threads into equal-sized static workgroups of several hundred. Workgroups effectively exchange their state and synchronize, allowing for coordinated data processing. A workgroup's threads are all scheduled to run on a single core simultaneously. Serial execution of the code takes

place on the CPU. On the GPU, parallelism is represented via a kernel function that runs many threads simultaneously.

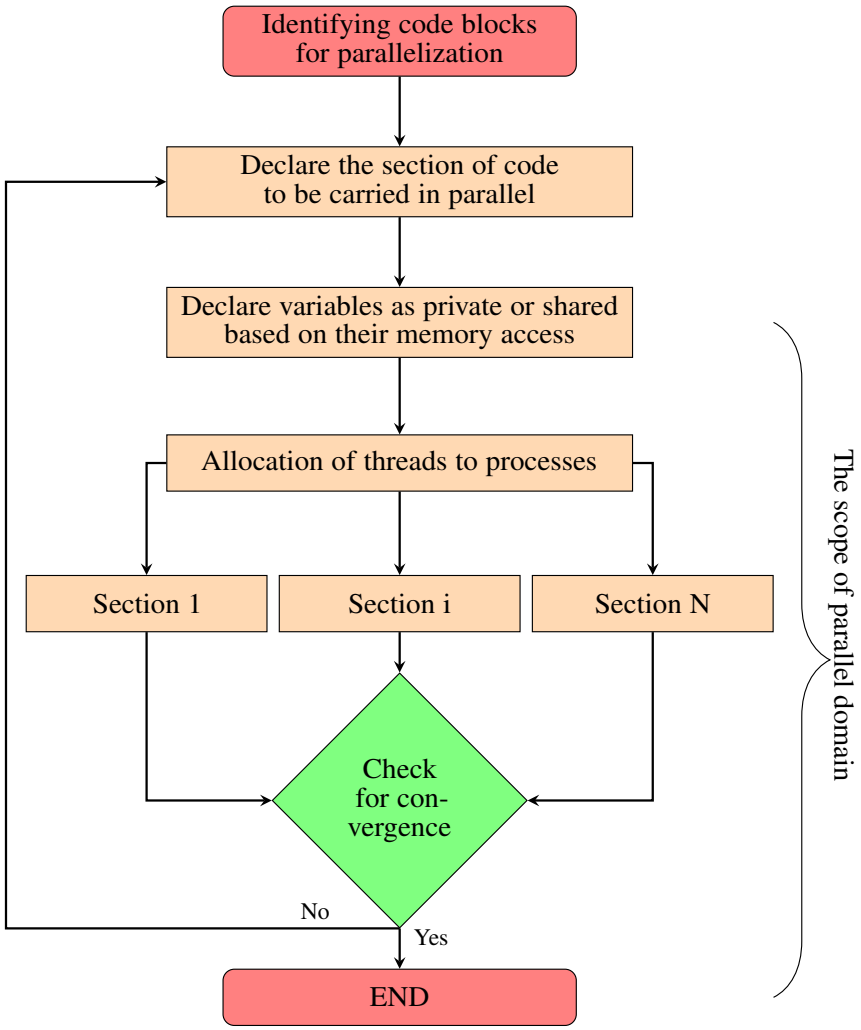

Fig. 6.4 A flowchart of parallel computation using OpenMP.

Compute Unified Device Architecture (CUDA)

The introduction of NVIDIA's CUDA allowed it to be used to accelerate non-graphical applications. CUDA programming on GPUs has drastically increased computing performance, making it a popular parallelism option. CUDA is a C-based language designed to use GPUs' massive parallelism. Nvidia's CUDA framework comprises an expanded C/C++ programming language and optimized libraries (cuBLAS, cuFFT) for common mathematical tasks. CUDA provides a basic abstract programming model that may be used on several GPU generations in the future.

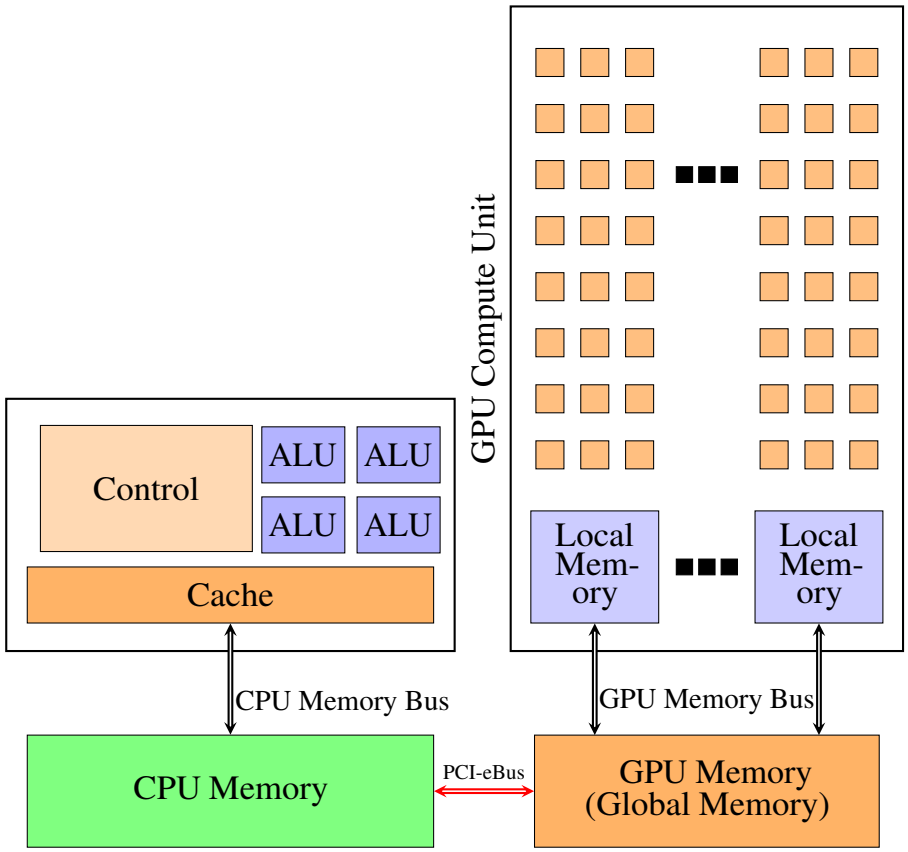

Fig. 6.5 CPU and GPU Architecture

The steps to parallelize the code using CUDA on GPU in this study is elaborated in Figure 6.6. The prepossessing is conducted on CPU using Python programming language and is saved as binary files. The files are read in C++ host code, from which the necessary variables are transferred to the GPU device for the parallel computation of forward and FWI simulations. The GPU is used for the rest of the calculation. The forward simulations are run over the initial input parameters. Then the output from the forward simulations is compared with the field measurement records to calculate the data misfit. If the data misfit is less than the minimum, the parameters (Lame constants: λ, μ, and density: ρ) are estimated to the desired accuracy. Suppose the data misfit is more than the minimum; the simulation is forwarded to an adjoint simulation where the gradients of the parameters are calculated. The computed gradients are then smoothed and optimized, and the best-fitting step length is calculated using a parabolic line search algorithm. With the gradients and the step length the medium parameters are updated as $m_{i+1} = l\ \partial m + m_i$, where i is the iteration step, m_i is the medium parameters at i^{th} iteration step, ∂m the gradient of the parameter and l the computed step length. The forward simulation is run in the next iteration with the updated medium parameters. The loop runs until the misfit is obtained within the desired limits. After the

desired misfits are obtained, the latest obtained medium parameters are copied to the host CPU as binary files, where the post-processing of the results continues in Python.

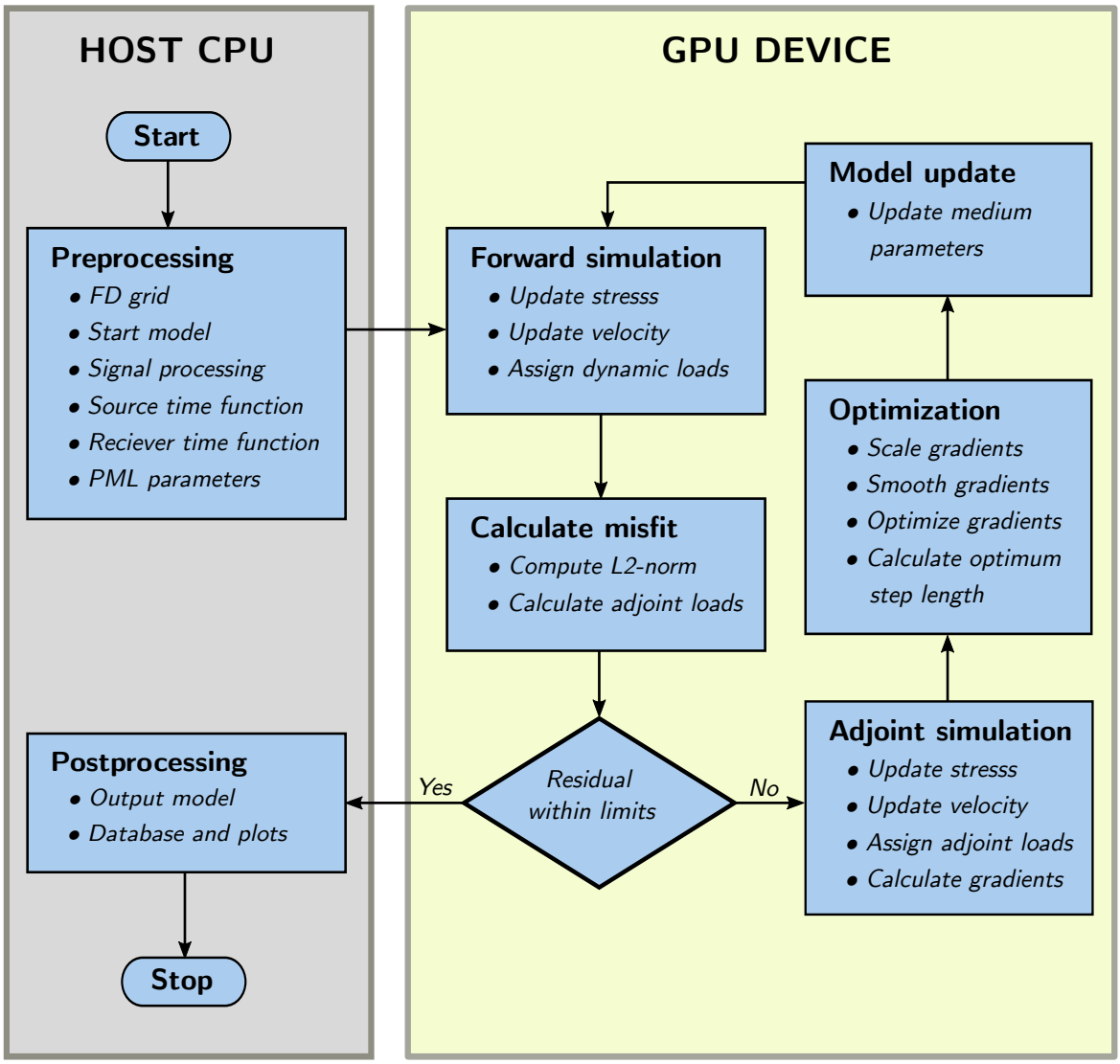

Fig. 6.6 A flowchart of parallel computation of seismic FWI in GPU.

6.4 Numerical simulations

This section presents the implementation of seismic Forward and FWI simulations in parallel computation based on GPU and compares the performance to that of parallel computation in CPU described in Section 6.3. The hardware used for computation is as shown in Table 6.2. Two different simulations are considered to study the efficiency of parallel computation in GPU. To study the computational efficiency of the forward-only model, a scenario of seismic

wave propagation in a water reservoir dam is presented in Section 6.4.1. For the seismic FWI, a spherical inclusion in full space is shown in Section 6.4.2.

Table 6.2 CPU and GPU hardware used for computation in this study.

Hardware	**CPU/GPU**	**Memory**	**OS**
CPU1	11th Gen Intel(R) Core(TM) i5-1135G7 @ 2.40 GHz	8 GB	Ubuntu 20.04
CPU2	AMD Ryzen Threadripper 3970X(2.9 GHz)	64 GB	Ubuntu 20.04
GPU1	Nvidia GeForce GTX 1650	4 GB	Ubuntu 20.04
GPU2	Nvidia GeForce GTX 2080 Ti	8 GB	Ubuntu 20.04

6.4.1 Seismic forward model

For the numerical simulation of the forward wave propagation problem, an earthen water reservoir dam with the dimensions as shown in Figure 6.7 is considered. The depth of the water on the upstream slope of the dam is 3.0 m. A line crack (5.6 cm wide and 10 m long) starts at 1.5 m below the center of the free surface of the dam and extends towards the far field at an angle of 45 degree to the vertical. The crack is filled with extremely soft saturated soil. The water table inside the dam is represented by the draw-down curve, as shown in the figure. A realistic range of wave propagation is considered by adopting the elastic medium parameters as suggested in Santamarina et al. (2005). The medium parameters for the model are shown in Table 6.3 and the effect of the air-water and the air-solid interface is considered a free surface. A synthetic time signal (Ricker wavelet) of unit amplitude and center frequency of 0.8 kHz acting vertically is considered. The seismic source are fired at the top of the upstream slope of the dam. Twenty-five seismic receivers are positioned along the dam's upstream and downstream slope with a spacing of 0.53 m ($dx = 0.5$ m, $dz = 0.17$ m). A source function of unit amplitude is considered; thus, the seismograms recorded at the receivers are the unitless values normalized by the excitation function. The dam is initially (at $t = 0$) considered at rest.

The model is discretized with $nx = 1493$, $nz = 393$ grid points along the respective directions with a grid spacing $dx = dz = 0.02$ m. Twenty perfectly matched layers are used in all four directions. The particle velocities normalized to their peak amplitudes at different receiver positions are shown in Figure 6.8. The output corresponds to the input Ricker wavelet signals of 0.8kHz central frequency as shown in Figure 6.9. The particle velocities v_z and v_x in the dam are shown in Figure 6.10 - 6.11, respectively.

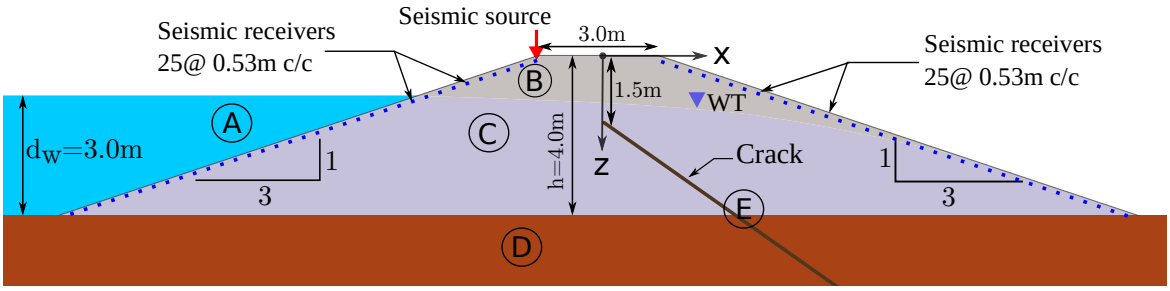

Fig. 6.7 A physical model of a dam including a crack and soil-water interface to perform forward seismic wave simulation. The material parameters are as given in Table 6.3 and 55 seismic receivers are located along the dam surface with a spacing of 0.53 m.

Table 6.3 Medium parameters for forward seismic modeling.

Medium	**Code**	**P-Wave Velocity** (c_1)	**S-Wave Velocity** (c_2)	**Density** (ρ)
Water	A	1482 m/s	0.0	1000 kg/m^3
Unsaturated soil in the dam	B	800 m/s	400 m/s	1700 kg/m^3
Saturated soil in the dam	C	1450 m/s	400 m/s	1950 kg/m^3
Subsurface layers	D	1900 m/s	700 m/s	2100 kg/m^3
Crack filler	E	1600 m/s	100 m/s	1000 kg/m^3

6.4.2 Seismic FWI model

For FWI simulations, a simple spherical inclusion model, as used by (Köhn, 2011) for acoustic FWI is considered. A rectangular homogeneous elastic region in range $x = (0, 15\text{m})$ m and $z = (0, 30\text{m})$ in a homogeneous full-plane with density $\rho = 1500$ kg/m^3 and wave velocities $c_1 = 500$ m/s, $c_2 = 300$ m/s with a circular inclusion of radius $r = 3$ m at the center of the grid with density $\rho = 1700$ kg/m^3 and wave velocities c_1 =800 m/s, $c_2 = 400$ m/s is considered (Figure 6.12). Three seismic sources are used at coordinates $x = 1$ m and z =7.5 m, 15 m, 22.5 m. Fifty-five receivers are used at $x = 14$ m and between $y = 1.5$ m to $y = 28.5$ m in an interval of 0.5 m, as shown in Figure 6.12. The model is discretized with $nx = 301$ and $nz = 601$ number of grids in x- and z-directions, respectively, with a grid spacing $dx = dz = 0.05$ m. 10 convolutional PML layers are used in all four boundaries.

A synthetic data set is considered as observed seismic records. A Ricker wavelet with peak frequency 2.50 kHz and amplitude 1.0 as shown in Figure 6.13, are fired simultaneously as input velocities in the z-direction, and the observed data is generated by the forward modeling of the true model. A seismic FWI simulation is performed with the developed parallel codes. The start model is a homogeneous full plane with the same material properties as the true model without spherical inclusion. The material updates in different iteration

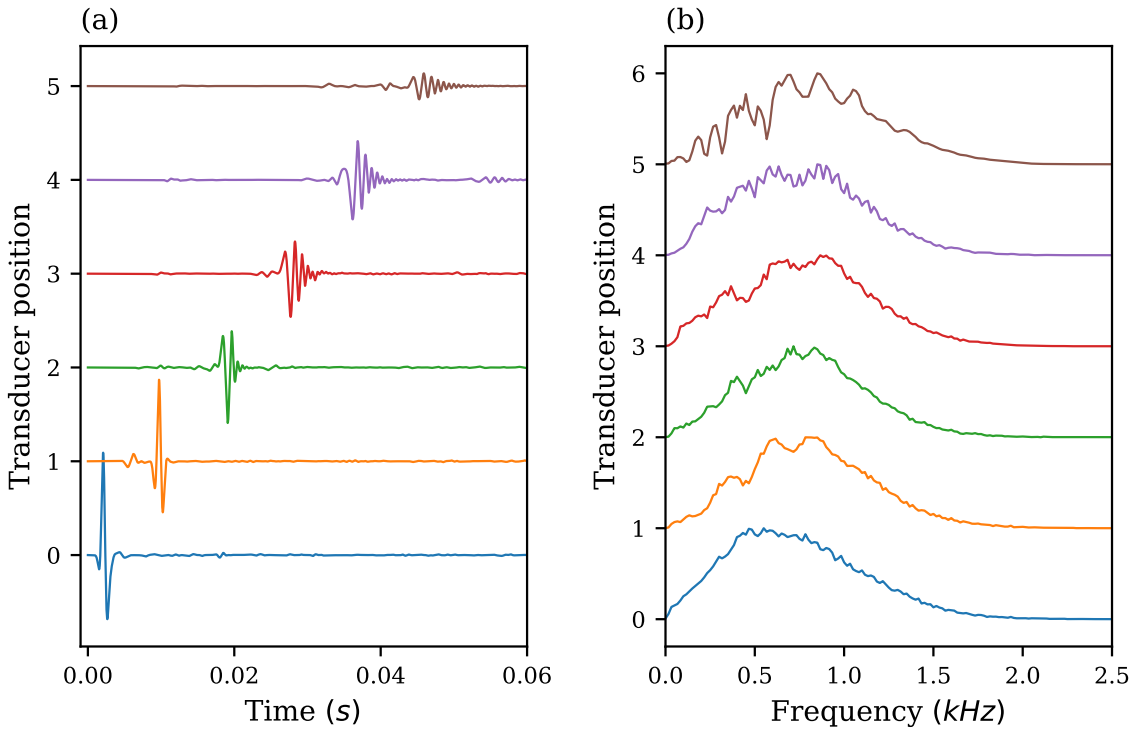

Fig. 6.8 Vertical components of particle velocity, normalized by the peak amplitude of the input signal, recorded in the receivers located at the surface of the dam at different the transducer locations $x = [-1.5\text{ m},\ 1.5\text{ m}, 4.5\text{ m}, 7.5\text{ m}, 10.5\text{ m}, 13.5\text{ m}]$: (**a**) Time signal, (**b**) The frequency amplitudes normalized to the peak amplitude of the same signal. (The source is located at $x = -1.5$ m).

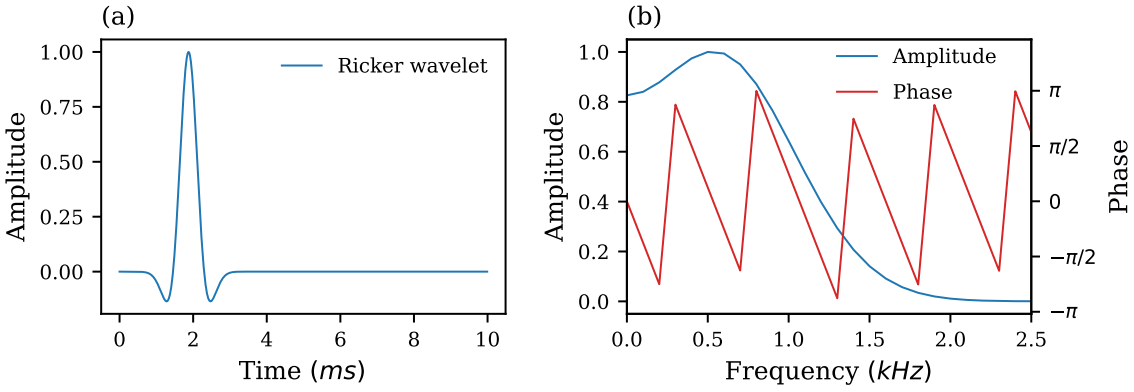

Fig. 6.9 Ricker wavelet of unit amplitude with center frequency 0.8 kHz used as velocity source for the excitation in forward seismic simulation model: (**a**) normalized amplitude in time domain, (**b**) normalized amplitudes in frequency domain.

steps are shown in Figures 6.14 and 6.15 for longitudinal and shear wave velocity models, respectively. The convergence of the inversion model is represented by the change in L2-norm

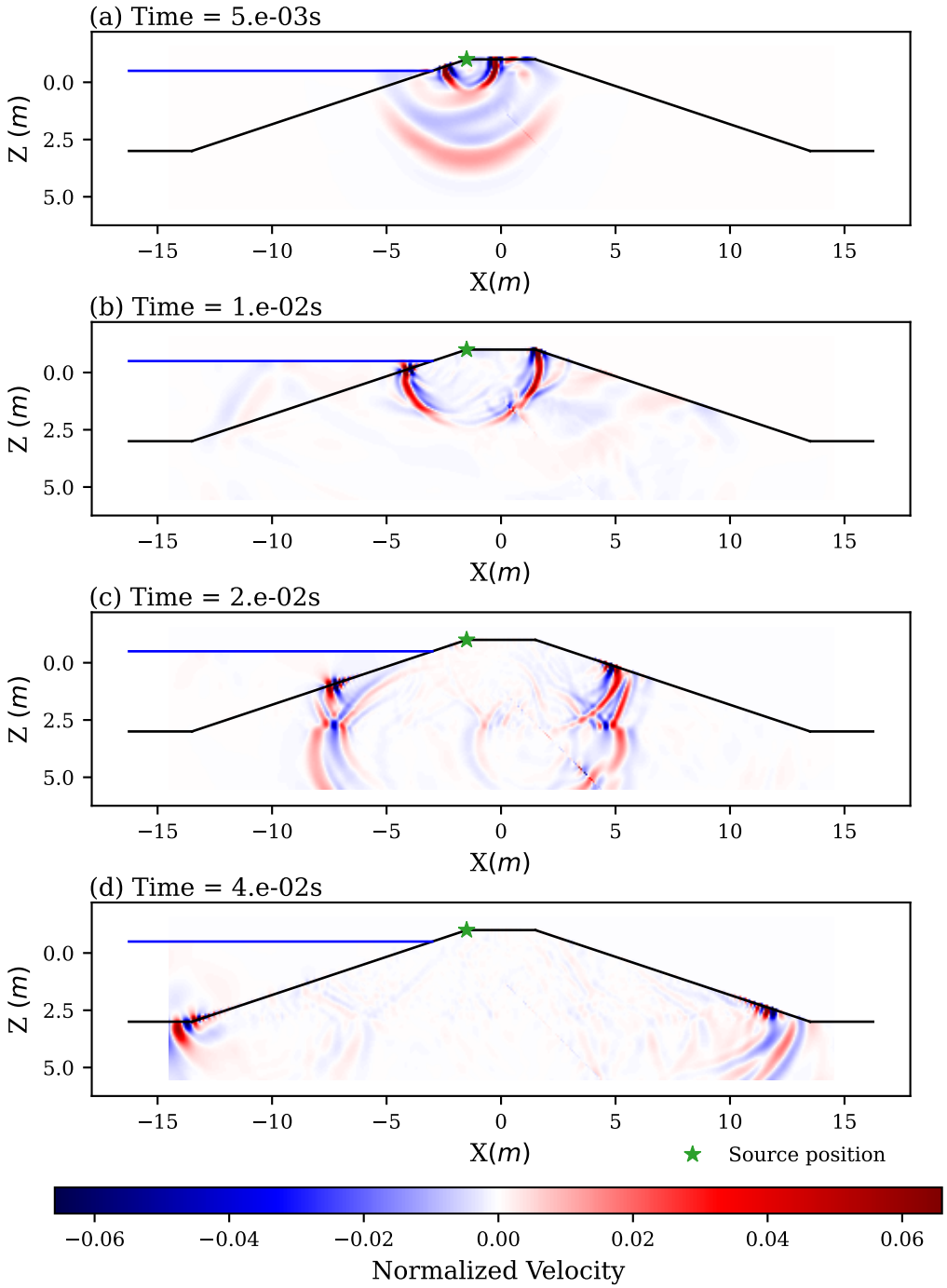

Fig. 6.10 Vertical component of particle velocity (v_z), normalized to the velocity wavelet at the excitation point, in the forward seismic model.

over the iteration steps, shown in Figure 6.16. The obtained results show a fair inversion of the given true model.

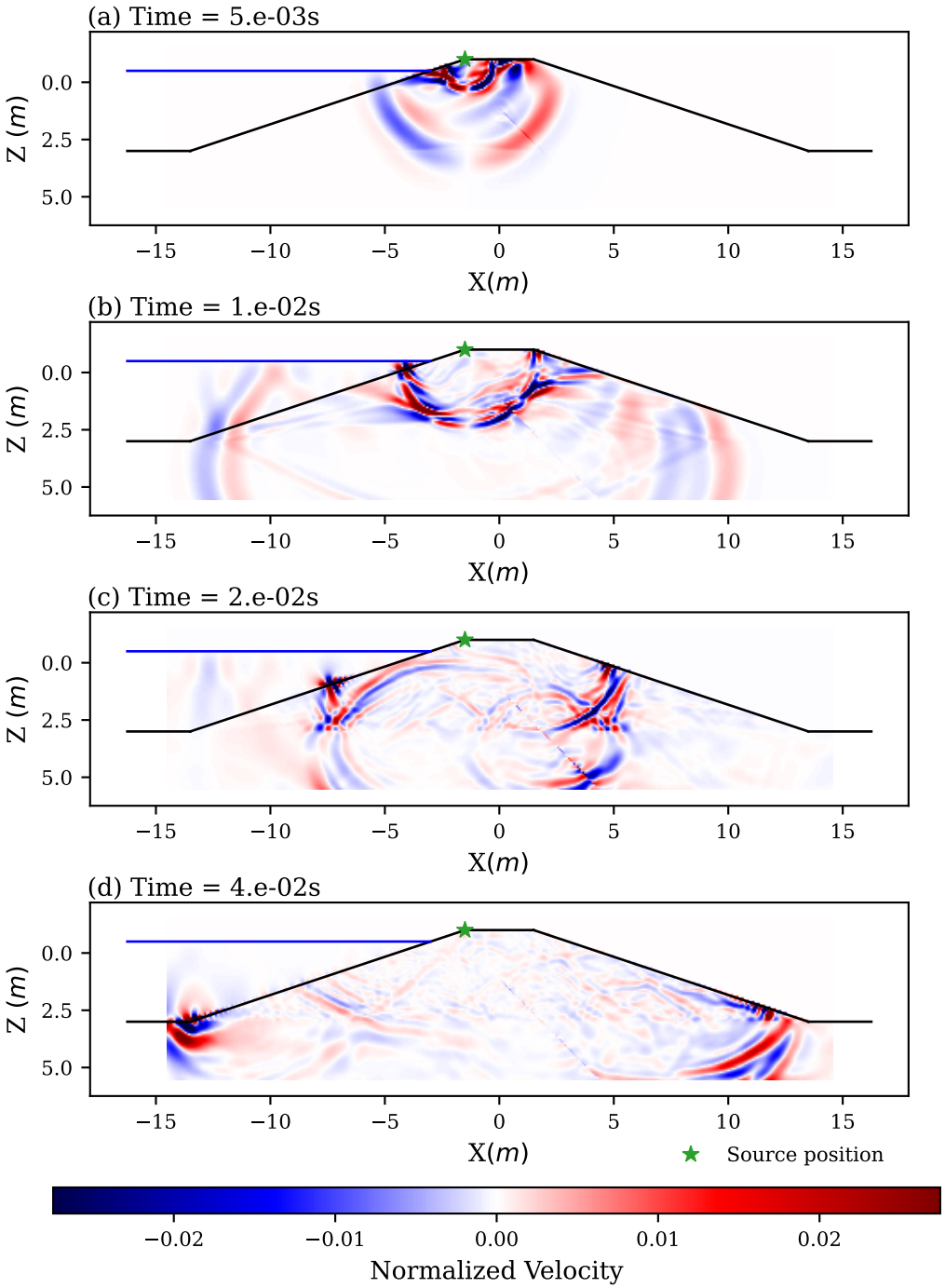

Fig. 6.11 Horizontal component of particle velocity (v_x), normalized to the velocity wavelet at the excitation point, in the forward seismic model.

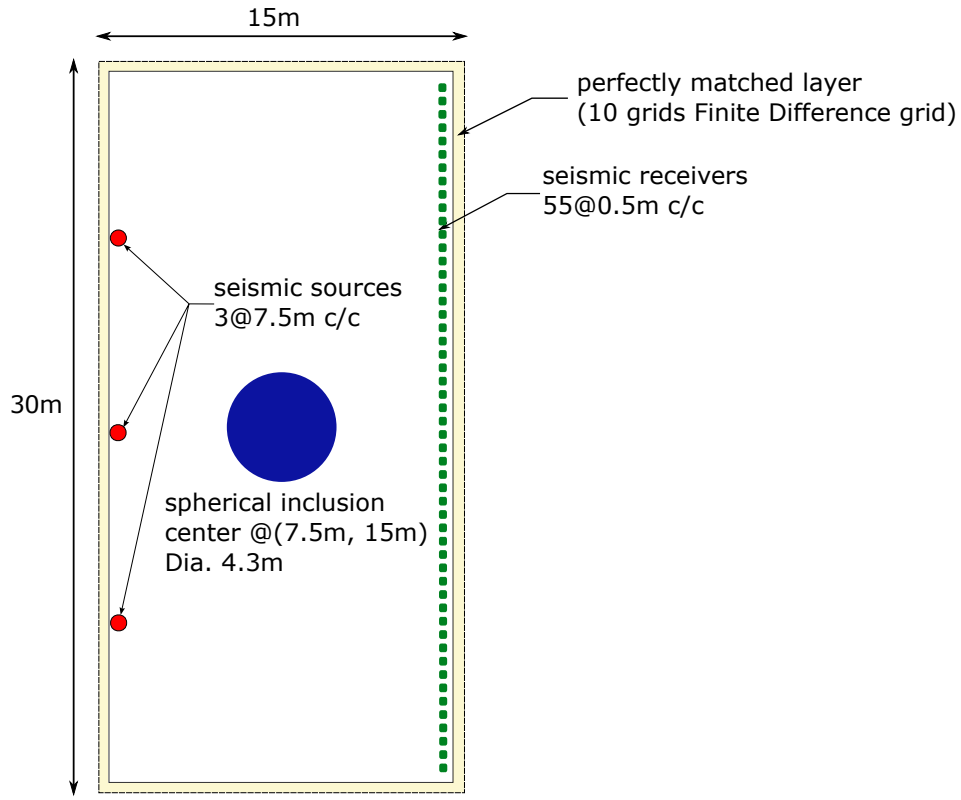

Fig. 6.12 A spherical inclusion in a rectangular finite difference grid considered for FWI simulation.

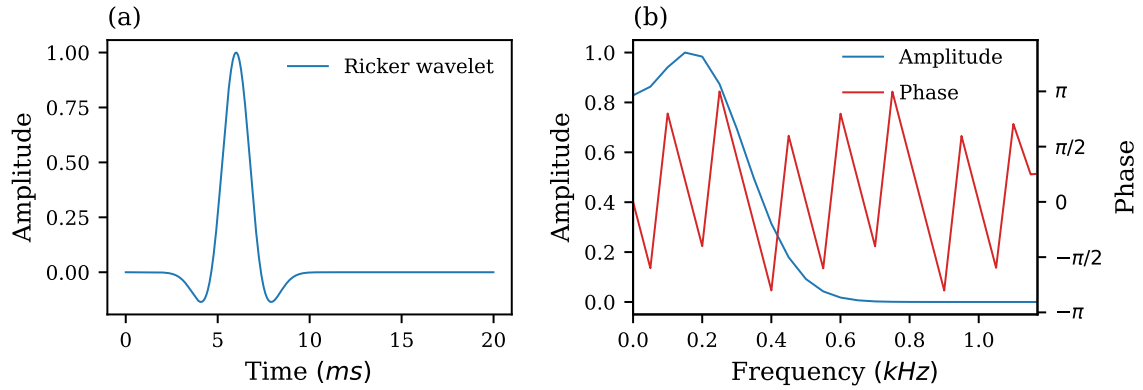

Fig. 6.13 Ricker wavelet of unit amplitude with center frequency $250Hz$ used as velocity source for the excitation in FWI model: (**a**) normalized amplitude in time domain, (**b**) normalized amplitudes in frequency domain.

6.5 Results and discussion

A series of studies are performed to show the enhancement of in-plane seismic full waveform inversion using CPU and GPU parallelization. Initially, the forward model is studied with

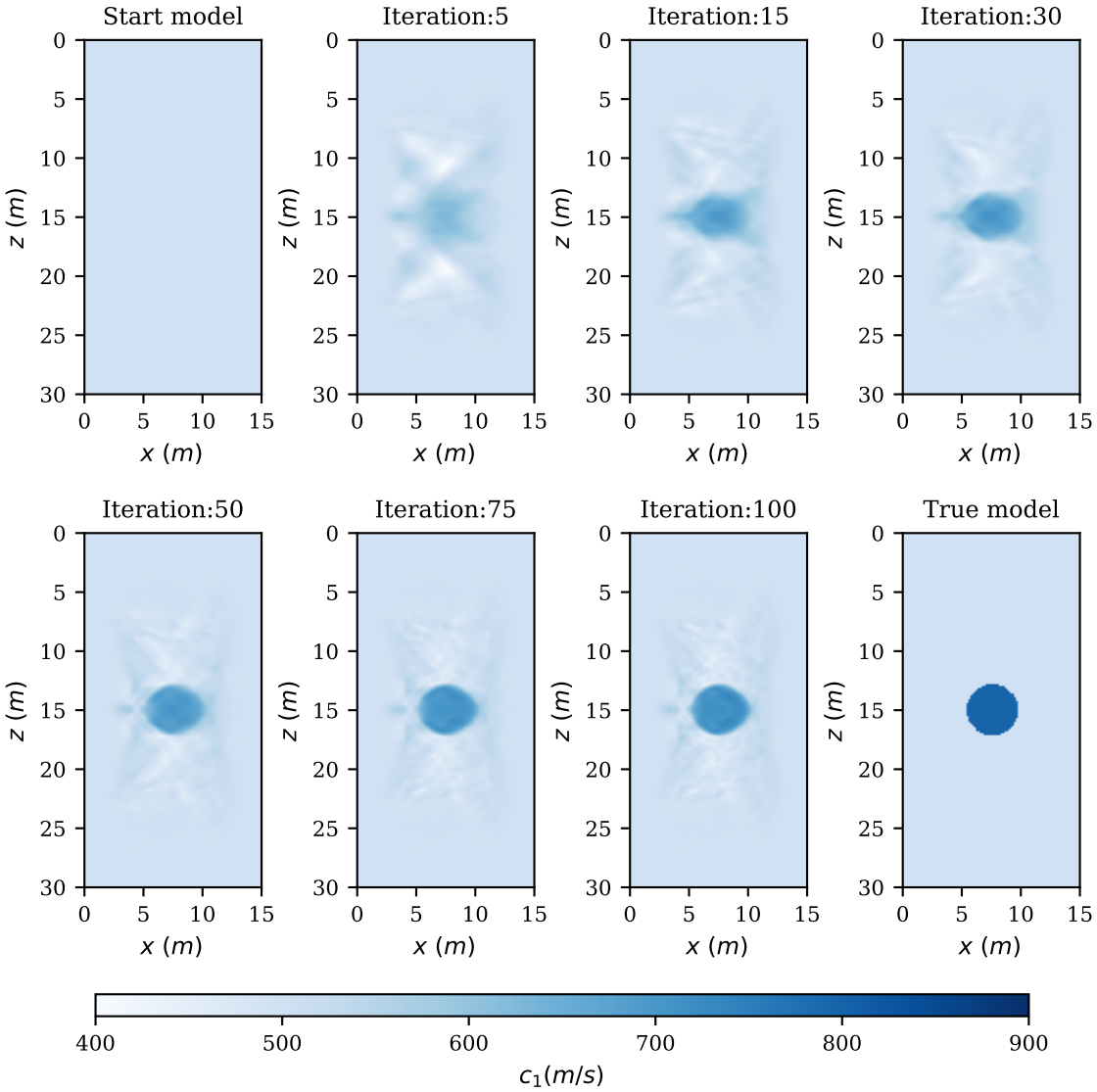

Fig. 6.14 Longitudinal wave velocity inversion at different iteration steps in seismic FWI of a spherical inclusion in full-plane.

an example of wave propagation in a dam in Section 6.4.1. The validated forward model is further developed into the full waveform inversion model in Section 6.4.2 using low-frequency anomaly for a circular inclusion in full space. The developed FWI codes are programmed for serial computation in CPU, parallel computation in CPU using openMP parallel modules and parallel computation in GPU using CUDA C programming languages. The same physical parameters and mathematical models, with a variation in time and space grids, are used for comparative performance analysis of the developed codes over the available hardware.

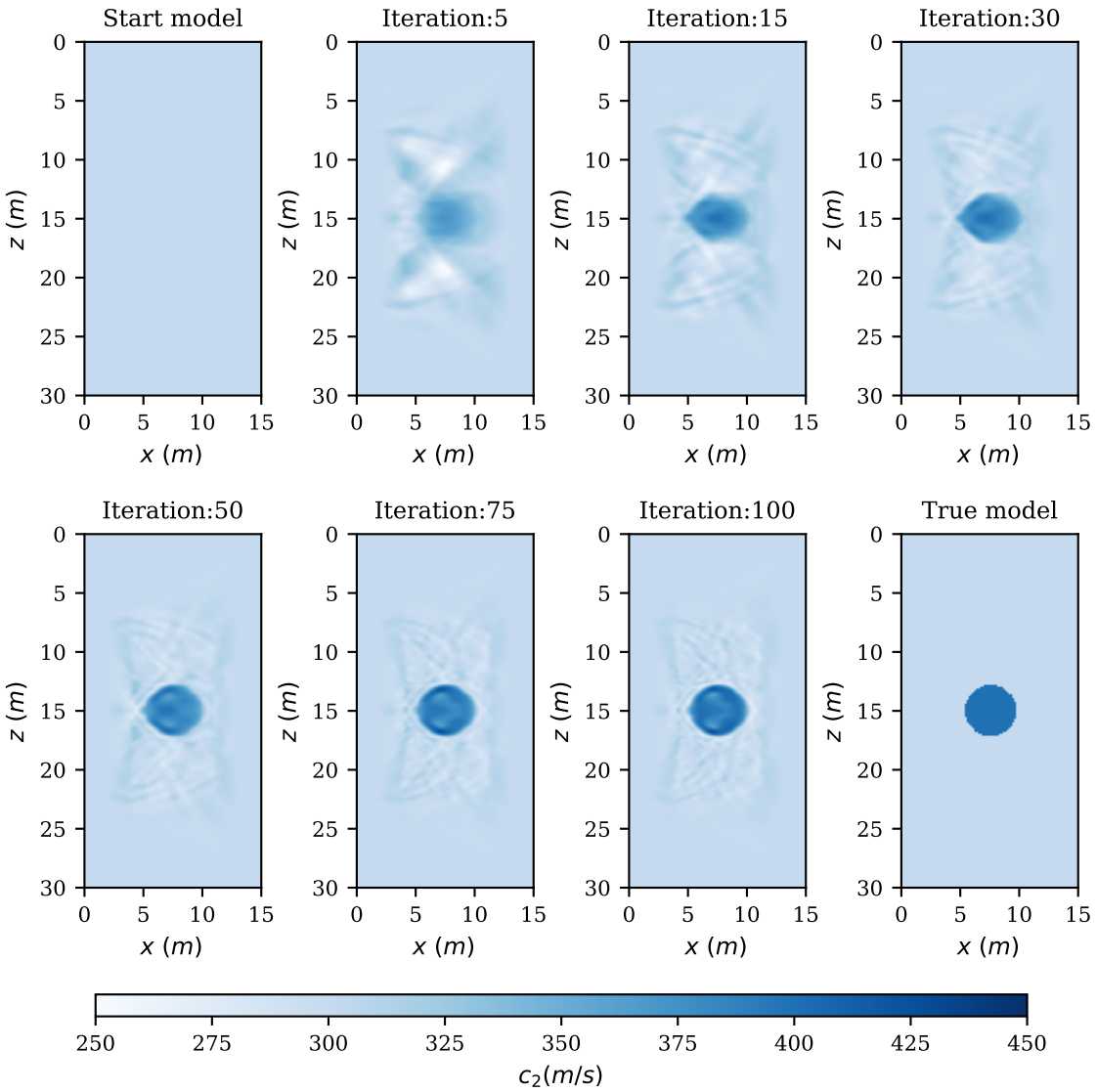

Fig. 6.15 Shear wave velocity inversion at different iteration steps in seismic FWI of a spherical inclusion in full-plane.

The seismic wave propagation in the dam shows that the presence of cracks in the dam significantly alters the propagation of elastic waves (Figures 6.10 and 6.11). Similarly, a minor disturbance can also be observed due to the presence of a water table. The effective wavelength of P and SV waves in saturated soil inside the dam is measured in Figures 6.10 and 6.11 to be approximately 2.0 m and 0.7 m, respectively. The measured wavelengths correspond to the medium parameters and the central frequency of the input signal, which validates the seismic simulation codes in CPU and GPU. It can also be observed from Figure 6.8b that the peak frequency response shifts to slightly higher frequencies with the

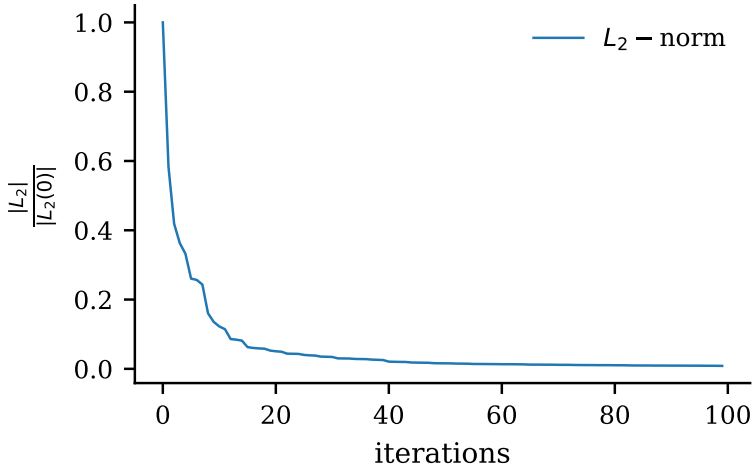

Fig. 6.16 L_2 norm in the first 40 steps, normalized to the L_2 norm in the first step, in Seismic FWI a spherical inclusion in full-plane.

distance of wave propagation. From the perspective of computational efficiency, similar results are obtained from serial computation, parallel computation using openMP and parallel computation in GPU. Figures 6.17–6.19 show the computational time and performance boost in forward simulations. It can be seen that the performance in the most capable GPU that we used is 60 to 80 times that compared to the sequential code. The CPU parallel computation using OpenMP with 16 threads only shows an improvement of performance by 2 to 4 times. For the GPU1, the simulation was out of memory after 3800-time steps for the given spatial grid; see Figure 6.17.

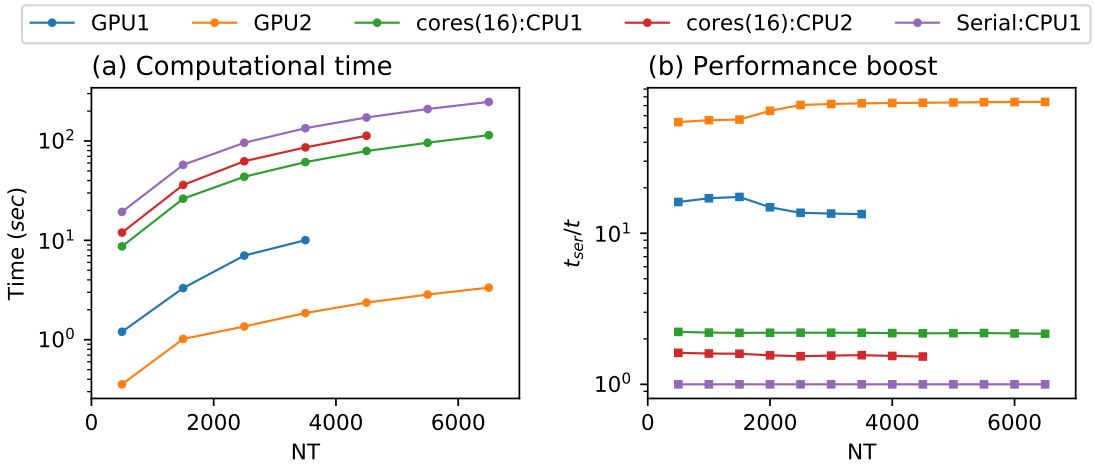

Fig. 6.17 Comparison of computational time and performance for variation of temporal grid size NT keeping spatial grid size constant ($NX = 201$, $NZ = 401$) in forward simulations.

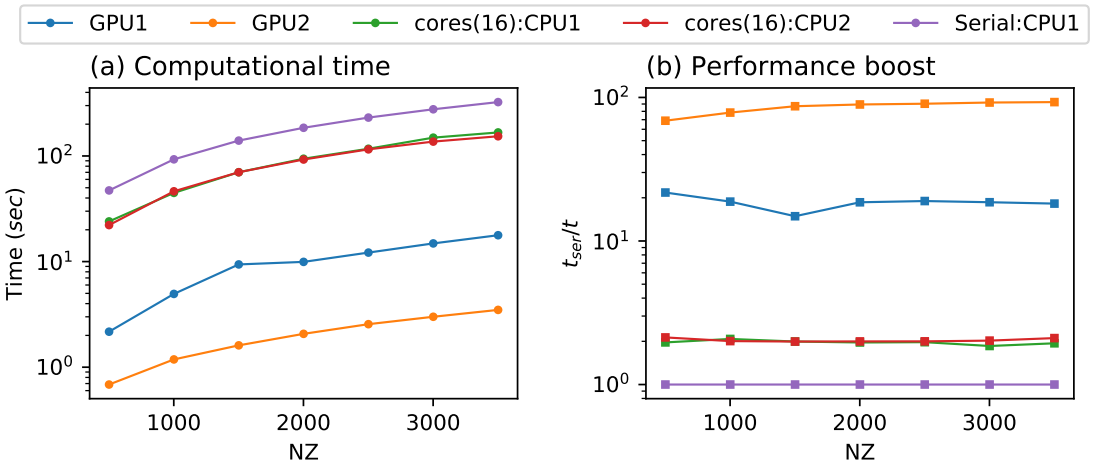

Fig. 6.18 Comparison of computational time and performance for variation of spatial grid size along Z direction NZ keeping spatial grid size along X direction and temporal grid constant ($NX = 201$, $NT = 1000$) in forward simulations.

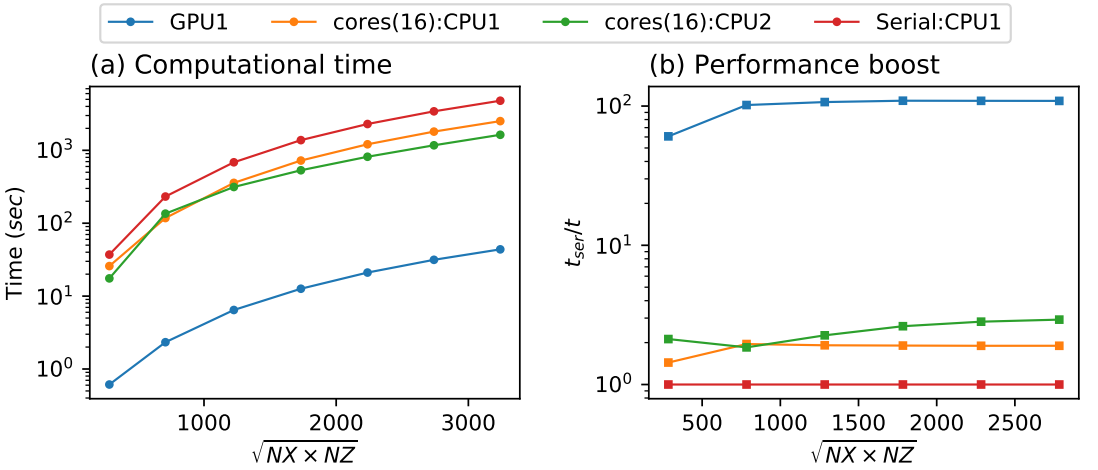

Fig. 6.19 Comparison of computational time and performance for variation of spatial grid $NX \times NZ$ keeping temporal grid size constant ($NT = 1000$) in forward simulations.

It is observed from the FWI models that the higher wavelength band of the wave field gives the general outline and the layers in the model, guiding the convergence towards the global minima. In contrast, the lower wavelength band adds more detailing and sharper images. Thus, it can be interpreted that the low-frequency signals give less detailed or more blurred results near the true model, whereas high-frequency signals give more detailed and accurate inversion results. However, computation in the high-frequency range has higher possibilities that the model may converge to the local minima. It is also observed for the spherical inclusion model that the higher the impedance ratio between the main body and the

inclusion, the sharper inversion results and faster convergence are achieved. For the parallel computation of Full Waveform Inversion, the whole computation process is conducted in GPU, except the pre-processing and post-processing. It can be seen from Figure 6.6 that the whole iteration of full-waveform inversion is performed in GPU. The strategy is implemented to reduce the overload due to the memory copying from the host to the device and vice versa. The major limitation of this approach is that multiple GPUs can not be used and that the model's size depends upon the memory available in a single GPU. Similarly, Figures 6.20 and 6.21 show the computational time and performance boost in FWI simulations. The results show a similar improvement to that of forward simulations. The performance boost in the most capable GPU we used is about 50 to 90 times that of a serial computation. In the case of FWI simulations, the parallel computation in CPU using OpenMP with 16 threads has given a performance boost of up to 11 times compared to the serial computation.

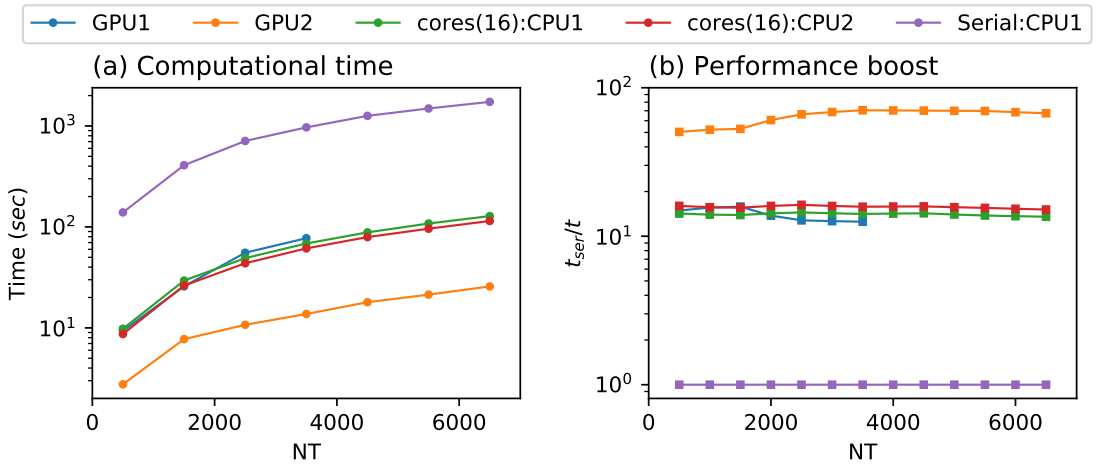

Fig. 6.20 Comparison of computational time for 20 iterations and performance for variation of temporal grid size NT keeping spatial grid size constant ($NX = 201$, $NZ = 401$) in FWI simulations.

Overall, an average performance boost of about 80 times is observed in all the different modeling cases. It may not be significant for forward seismic models computed within minutes. However, for full-waveform inversion models, which may take hours and days for the whole iterations to compute, this may bring the computation of days to hours and hours to some minutes. This enhancement is based mainly on faster computation using parallelization. A further enhancement can be made by using a more robust optimization algorithm and machine learning methods for regression and optimization studies (Wuttke et al., 2021, Rizvi et al., 2020).

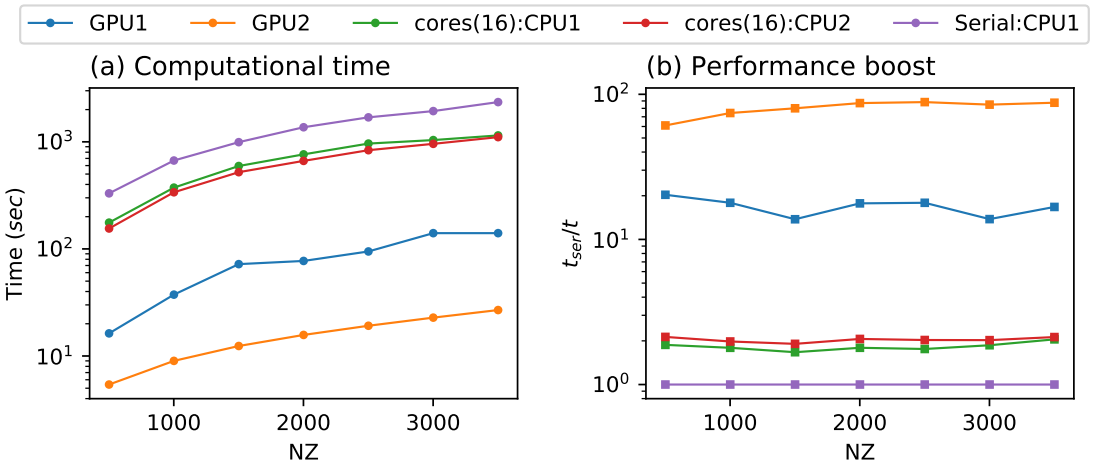

Fig. 6.21 Comparison of computational for 20 iterations time and performance for variation of spatial grid size along Z direction NZ keeping spatial grid size along X direction and temporal grid constant ($NX = 201$, $NT = 1000$) in FWI simulations.

6.6 Conclusions

Parallel programming in GPU using CUDA C is implemented for in-plane seismic full waveform inversion, and the computational efficiency is compared to the serial and openMP parallel codes. The forward seismic wave propagation is studied for an earthen water reservoir dam with a crack and water table in the first step. It is important to study the forward model, as the FWI is based on an iterative computation of several forward models with a gradual improvement of the model model and minimization of the misfit. The influence of the crack and water table is visible in the results. In the next step, the full waveform inversion model is programmed in CUDA C, and a study is conducted for a spherical inclusion in full space.

The computational efficiency of GPU parallelization for the forward and full-waveform inversion models is studied compared to serial and CPU parallel codes. Comparing the computed results on different hardware and programming environments shows a significant reduction in computation time. The comparison is made for the change in the model size in time and space, which in the Finite Difference Method are grid sizes in Cartesian direction (NX, NZ) and the number of time steps (NT). For all the cases, the improvement in performance increases with an increase in the model dimension and remains constant after a certain threshold. The GPU parallel computation has shown a speed enhancement of about 60 to 100 times, whereas that of CPU parallelization in openMP (16 threads) is between 5 to 11 times that of the serial code. It can be concluded that GPU computation can significantly enhance the performance of in-plane seismic full waveform inversion. With the advancement of modern GPU, the FWI computation can be implemented into practical

applications by bringing the calculation of the days into hours. It also provides further opportunities to implement robust optimization and machine learning algorithms to enhance FWI computations. The advantage gained in computational time by parallel computation in GPU shows that the advanced mathematical formulations in elastodynamics, which require computationally intensive direct or iterative solvers, can be applied for practical modeling in earthquake engineering and soil-structure interaction problems.

Chapter 7

General conclusion and outlook

7.1 Conclusion

This dissertation focuses on improving the applicability of BEM for dynamic analysis in earthquake engineering and geotechnical engineering. The major drawbacks of conventional BEM are addressed by incorporating the advantage of other methods. One of the major drawbacks of BEM is that the solutions are available primarily for a homogeneous medium. To improve the applicability of the solutions in an arbitrarily inhomogeneous and heterogeneous medium, the inverse modeling concept in FWI is inherited into BEM. Primarily, a modified PSO based on the site-specific seismic measurement is implemented in BEM. The solution of the inverse formulation is obtained as site-specific impedance dependent on the BEM mesh. The obtained impedance functions represent the impedance due to the infinite or semi-infinite geological region. However, the optimized impedance alone cannot describe the detailed stress-strain behavior over the whole structural domain and soil-structure interaction. A hybrid modeling concept by BEM-FEM coupling is studied to address this issue. In such hybrid models, the near-field geological region including structures is modeled and computed by FEM. The wavefield solution in infinite or semi-infinite region is calculated by BEM and introduced into the FEM model by direct coupling as a macro-finite element. P-SV wavefield is considered for mathematical development and numerical implementation throughout this thesis. In addition to the numerical development, a study for enhancement of the computational efficiency of FWI is performed using parallel computation in CPU and GPU.

Inverse formulation of the integral equations in BIEM in analytical or numerical expression is a mathematically complex problem. It is equally challenging to get a numerical solution by local optimization based on a line search algorithm. To overcome this, PSO is implemented in BEM for P-SV wave propagation resulting in reasonably accurate results. A

modified form of the frequency-dependent fundamental solution for a homogeneous elastic isotropic medium is considered the basic functional expression. The optimization parameters are defined by parametrizing the wave velocities and density over the boundary mesh. For the numerical test examples considered in this study, a misfit of as low as 2.5% is obtained. It is shown that, with further improvement, this method can be a valuable tool to model the effect of the infinite domains for realistic geomechanical problems.

A case of underground structures in poroelastic half-space is considered by BEM-FEM coupled models. The BEM model is developed as the author's in-house simulation tool, while commercial ABAQUS software is used for FEM models. The numerical models are verified, and a parametric study is performed using synthetic examples for the variation of porosity for dry and saturated cases. The models can describe the entire wave path from the seismic source to the local site conditions in a single hybrid model. The site effects due to the variation of poroelastic material properties in near and far-field regions of a half-plane with surface topography and subsurface infrastructures are evaluated numerically. This proves the hybrid BEM-FEM models can be valuable for dynamic analysis of geotechnical problems involving both the effect of wave propagation in the semi-infinite far-field media and the dynamic behavior of the engineering structures located in the near-field local regions.

It is shown that FWI in BEM and using BEM-FEM coupled hybrid models can provide an integrated solution that involves wave propagation in an infinite heterogeneous geological region with local site effects near the important infrastructure. However, such models are computationally expensive and require a lot of CPU and memory requirements in the computers. The massive size of the model, involvement of fully populated complex matrices, non-linear iterative procedures, and the requirement of a large number of particles in the PSO algorithm make the computation time-consuming and demand a considerably large memory. However, modern-day computers can perform parallel computation in CPU and GPU. To study the efficiency of parallel computation in inverse formulation, the stress-velocity formulation in time domain is implemented in parallel computation code in GPU and CPU. In this study, the serial and CPU parallel codes are programmed in C++ programming language, and the GPU parallel codes are developed in CUDA C environment. The computational core is wrapped into a Python interface. A performance gain of up to 90 times compared to the serial code is obtained by GPU computation in CUDA C programming environment. The results show that parallel computation in GPU can be used to reduce the computational time of inverse models in dynamic modeling so that they can be performed in a practically feasible time frame.

7.2 Outlooks and future works

The major outcome of this study is that the applicability of BEM for dynamic analysis of heterogeneous and inhomogeneous infinite and semi-infinite media can be enhanced by numerical optimization and by coupling with FEM. It can also be deducted that the computational efficiency for such models can be improved by using parallel computation in CPU and GPU. However, this research's outcome alone is insufficient for solving the problems that arise in the dynamic modeling of heterogeneous and inhomogeneous semi-infinite geological domains. Based on the development in this thesis, the following works are recommended for future research:

(i) *Numerical optimization in BEM:* The optimization strategy presented in this thesis shows a lot of possibilities for improvement. The major research area in this direction can be replacing the fundamental solution for homogeneous elastic isotropic medium in the objective function by other existing fundamental solutions and half-space Green's function (see Appendix C). The convergence and accuracy of the optimization may be improved by using the other type of solutions.

(ii) *FWI in hybrid FEM-BEM models:* The inverse computation in this study is implemented in pure BEM models. The developed FEM-BEM coupled methodology is applied as forward simulation model. Inverse formulation and numerical simulations in FEM-BEM coupled models can be the next step in estimating the site-specific impedance functions in heterogeneous geological domains.

(iii) *Numerical optimization and intelligent algorithms*: This study presents the outcome of particle swarm optimization in BEM. The use of state-of-the-art machine learning and artificial intelligence algorithms may further enhance the convergence, accuracy, and computational efficiency of the optimization problem in BEM for dynamic analysis of heterogeneous and inhomogeneous infinite media.

References

Abubakar, A., Pan, G., Li, M., Zhang, L., Habashy, T. M., and Van Den Berg, P. M. (2011). Three-dimensional seismic full-waveform inversion using the finite-difference contrast source inversion method. *Geophysical Prospecting*, 59(Modelling Methods for Geophysical Imaging: Trends and Perspectives):874–888. Publisher: European Association of Geoscientists & Engineers.

Achenbach, J. D., Lauwerier, H. A., and Koiter, W. T. (1973). *Applied mathematics and mechanics*.

Alielahi, H., Kamalian, M., Marnani, J. A., Jafari, M. K., and Panji, M. (2013). Applying a time-domain boundary element method for study of seismic ground response in the vicinity of embedded cylindrical cavity. *International Journal of Civil Engineering*, 11(1):10.

Antes, H. (1985). A boundary element procedure for transient wave propagations in two-dimensional isotropic elastic media. *Finite Elements in Analysis and Design*, 1(4):313–322. Publisher: Elsevier.

Antes, H. and Von Estorff, O. (1989). Dynamic response analysis of rigid foundations and of elastic structures by boundary element procedures. *Soil Dynamics and Earthquake Engineering*, 8(2):68–74. Publisher: Elsevier.

Apsel, R. J. and Luco, J. E. (1983). On the Green's functions for a layered half-space. Part II. *Bulletin of the seismological society of America*, 73(4):931–951. Publisher: The Seismological Society of America.

Banaugh, R. and Goldsmith, W. (1963a). Diffraction of Steady Elastic Waves by Surfaces of Arbitrary Shape. *The Journal of the Acoustical Society of America*, 35:1590.

Banaugh, R. P. and Goldsmith, W. (1963b). Diffraction of steady acoustic waves by surfaces of arbitrary shape. *The Journal of the Acoustical Society of America*, 35(10):1590–1601. Publisher: Acoustical Society of America.

Banerjee, P. K., Ahmad, S., and Manolis, G. D. (1986). Transient elastodynamic analysis of three-dimensional problems by boundary element method. *Earthquake Engineering & Structural Dynamics*, 14(6):933–949.

Banerjee, P. K. and Mamoon, S. M. (1990). A fundamental solution due to a periodic point force in the interior of an elastic half-space. *Earthquake engineering & structural dynamics*, 19(1):91–105. Publisher: Wiley Online Library.

Bardet, J.-P. (1992). A viscoelastic model for the dynamic behavior of saturated poroelastic soils.

Barra, L. P. and Telles, J. C. (1999). A hyper-singular numerical Green's function generation for BEM applied to dynamic SIF problems. *Engineering Analysis with Boundary Elements*, 23:77–87.

Bateman, H. (1953). *Higher transcendental functions [volumes i-iii]*, volume 1. McGraw-Hill Book Company.

Ben-Hadj-Ali, H., Operto, S., and Virieux, J. (2008). Velocity model building by 3D frequency-domain, full-waveform inversion of wide-aperture seismic data. *Geophysics*, 73(5):VE101–VE117. Publisher: Society of Exploration Geophysicists.

Berenger, J.-P. (1994). A perfectly matched layer for the absorption of electromagnetic waves. *Journal of Computational Physics*, 114(2):185–200.

Beskos, D. (1987a). BEM in Mechanics.

Beskos, D. E. (1987b). Boundary element methods in dynamic analysis.

Beskos, D. E. (1997). Boundary element methods in dynamic analysis: Part II (1986-1996).

Biot, M. A. (1956). Theory of propagation of elastic waves in a fluid-saturated porous solid. I. Low-frequency range. *The Journal of the Acoustical Society of America*, 28(2):168–178. Publisher: ASA.

Blanc, E., Chiavassa, G., and Lombard, B. (2013). A time-domain numerical modeling of two-dimensional wave propagation in porous media with frequency-dependent dynamic permeability. *The Journal of the Acoustical Society of America*, 134(6):4610–4623. Publisher: ASA.

Bo-yang, D. and Jia-qi, J. (2015). Time-domain BEM calculation for porodynamics. *Applied Mathematics & Mechanics (1000-0887)*, 36(1):31–47.

Borsutzky, R. (1984). *Seismic Risk Analysis of Buried Lifelines*. PhD Thesis.

Brebbia, C. A. (1978). *The boundary element method for engineers*. Pentech Press Ltd. Plymouth.

Brossier, R. (2011). Two-dimensional frequency-domain visco-elastic full waveform inversion: Parallel algorithms, optimization and performance. *Computers & Geosciences*, 37(4):444–455. Publisher: Elsevier.

Brossier, R., Operto, S., and Virieux, J. (2009). Seismic imaging of complex onshore structures by 2D elastic frequency-domain full-waveform inversion. *Geophysics*, 74(6):WCC105–WCC118. Publisher: Society of Exploration Geophysicists.

Brossier, R., Operto, S., and Virieux, J. (2010). Which data residual norm for robust elastic frequency-domain full waveform inversion? *Geophysics*, 75(3):R37–R46. Publisher: Society of Exploration Geophysicists.

Bunks, C., Saleck, F. M., Zaleski, S., and Chavent, G. (1995). Multiscale seismic waveform inversion. *GEOPHYSICS*, 60(5):1457–1473.

Castellanos, C., Métivier, L., Operto, S., Brossier, R., and Virieux, J. (2015). Fast full waveform inversion with source encoding and second-order optimization methods. *Geophysical Journal International*, 200(2):720–744.

Chaillat, S., Bonnet, M., and Semblat, J. F. (2009). A new fast multi-domain BEM to model seismic wave propagation and amplification in 3-D geological structures. *Geophysical Journal International*, 177(2):509–531.

Chandra, R., Dagum, L., Kohr, D., Menon, R., Maydan, D., and McDonald, J. (2001). *Parallel programming in OpenMP*. Morgan kaufmann.

Charara, M., Barnes, C., and Tarantola, A. (2000). Full waveform inversion of seismic data for a viscoelastic medium. *Methods and applications of inversion*, pages 68–81. Publisher: Springer.

Chen, G. and Wang, Z. (2017). Robust full-waveform inversion based on particle swarm optimization. *th Annual Meeting*, page 5.

Chen, G., Wang, Z., and Wang, Y. (2017). A study of full-waveform inversion based on adaptive immune particle swarm optimization. In *SEG 2017 Workshop: Full-waveform Inversion and Beyond, Beijing, China, 20-22 November 2017*, pages 31–35, Beijing, China. Society of Exploration Geophysicists.

Chen, J.-B. and Cao, J. (2016). Modeling of frequency-domain elastic-wave equation with an average-derivative optimal method. *Geophysics*, 81(6):T339–T356. Publisher: Society of Exploration Geophysicists.

Clerc, M. and Kennedy, J. (2002). The particle swarm - explosion, stability, and convergence in a multidimensional complex space. *IEEE Transactions on Evolutionary Computation*, 6(1):58–73.

Cole, D. M., Kosloff, D. D., and Minster, J. B. (1978). A numerical boundary integral equation method for elastodynamics. I. *Bulletin of the seismological society of America*, 68(5):1331–1357. Publisher: The Seismological Society of America.

Cruse, T. A. and Rizzo, F. J. (1968). A direct formulation and numerical solution of the general transient elastodynamic problem. I. *Journal of Mathematical Analysis and Applications*, 22(1):244–259. Publisher: Academic Press.

Dai, N., Vafidis, A., and Kanasewich, E. (1995). Wave propagation in heterogeneous, porous media: A velocity-stress, finite-difference method. *Geophysics*, 60(2):327–340. Publisher: Society of Exploration Geophysicists.

Dai, Q., Zhang, H., and Zhang, B. (2021). An Improved Particle Swarm Optimization Based on Total Variation Regularization and Projection Constraint with Applications in Ground-Penetrating Radar Inversion: A Model Simulation Study. *Remote Sensing*, 13(13):2514.

Daros, C. (2009). A time-harmonic fundamental solution for a class of inhomogeneous transversely isotropic media. *Wave motion*, 46(4):269–279. Publisher: Elsevier.

Daros, C. (2013). Green's function for SH-waves in inhomogeneous anisotropic elastic solid with power-function velocity variation. *Wave Motion*, 50(2):101–110. Publisher: Elsevier.

Daros, C. and Mesquita, E. (2006). A time domain harmonic BEM implementation for non-homogeneous 3D solids. *Engineering analysis with boundary elements*, 30(7):531–538. Publisher: Elsevier.

Daros, C. H. (2008). A fundamental solution for SH-waves in a class of inhomogeneous anisotropic media. *International Journal of Engineering Science*, 46(8):809–817. Publisher: Elsevier.

Daros, C. H. (2010). On modelling SH-waves in a class of inhomogeneous anisotropic media via the Boundary Element Method. *ZAMM-Journal of Applied Mathematics and Mechanics/Zeitschrift für Angewandte Mathematik und Mechanik: Applied Mathematics and Mechanics*, 90(2):113–121. Publisher: Wiley Online Library.

Dineva, P., Manolis, G., and Rangelov, T. (2006). Sub-surface crack in an inhomogeneous half-plane: Wave scattering phenomena by BEM. *Engineering analysis with boundary elements*, 30(5):350–362. Publisher: Elsevier.

Dineva, P., Parvanova, S., Vasilev, G., and Wuttke, F. (2014). Seismic Soil-Tunnels Interaction via BEM Part I. Mechanical Model. *Journal of Theoretical and Applied Mechanics*, 44(3):31–48.

Dineva, P., Rangelov, T., and Manolis, G. (2007). Elastic wave propagation in a class of cracked, functionally graded materials by BIEM. *Computational Mechanics*, 39(3):293–308. Publisher: Springer.

Dineva, P. S., Manolis, G. D., and Rangelov, T. V. (2008). Site effects due to wave path inhomogeneity by BEM. *Engineering analysis with boundary elements*, 32(12):1025–1036. Publisher: Elsevier.

Dineva, P. S., Wuttke, F., and Manolis, G. D. (2012). Elastic wave scattering and stress concentration effects in non-homogeneous poroelastic geological media with discontinuities. *Soil Dynamics and Earthquake Engineering*, 41:102–118.

Ding, G.-y., Cai, Y.-q., and xu, C.-j. (2008). Scattering of P waves by a cylindrical shell in a saturated half-space. *Engineering Mechanics*, 25(12):35–41.

Dominguez, J. (1993). *Boundary elements in dynamics*. Wit Press.

Dominguez, J. and Roesset, J. M. (1978a). Dynamic stiffness of rectangular foundations. *Nasa Sti/recon Technical Report N*, 79:16152.

Dominguez, J. and Roesset, J. M. (1978b). *Response of embedded foundations to travelling waves*. Massachusetts Institute of Technology, Department of Civil Engineering, Constructed Facilities Division.

Doyle, J. M. (1966). Integration of the Laplace transformed equations of classical elastokinetics. *Journal of Mathematical Analysis and Applications*, 13(1):118–131. Publisher: Academic Press.

Dupuy, B., De Barros, L., Garambois, S., and Virieux, J. (2011). Wave propagation in heterogeneous porous media formulated in the frequency-space domain using a discontinuous Galerkin method. *Geophysics*, 76(4):N13–N28. Publisher: Society of Exploration Geophysicists.

Eason, G., Fulton, J., and Sneddon, I. N. (1956). The generation of waves in an infinite elastic solid by variable body forces. *Philosophical Transactions of the Royal Society of London. Series A, Mathematical and Physical Sciences*, 248(955):575–607. Publisher: The Royal Society London.

Eringen, A. C. and Suhubi, E. S. (1975). Elastodynamics. *Academic Press: New York*, pages 614–626.

Fabien-Ouellet, G., Gloaguen, E., and Giroux, B. (2017). Time domain viscoelastic full waveform inversion. *Geophysical Journal International*, 209(3):1718–1734. Publisher: Oxford University Press.

Fang, J., Chen, H., Zhou, H., Rao, Y., Sun, P., and Zhang, J. (2020). Elastic full-waveform inversion based on GPU accelerated temporal fourth-order finite-difference approximation. *Computers & Geosciences*, 135:104381. Publisher: Elsevier.

Feng, Y., Yao, Y.-M., and Wang, A.-X. (2007). Comparing with Chaotic Inertia Weights in Particle Swarm Optimization. In *2007 International Conference on Machine Learning and Cybernetics*, pages 329–333, Hong Kong, China. IEEE.

Fichtner, A., Kennett, B., Igel, H., and Bunge, H.-p. (2010). Full waveform tomography for radially anisotropic structure: New insights into present and past states of the Australasian upper mantle. *Earth and Planetary Science Letters*, 290:270–280.

Fontara, I., Parvanova, S., Wuttke, F., Rangelov, T., and Dineva, P. (2014a). BEM for seismic wave propagation in inhomogeneous in depth half-plane. In *9th International Conference on Structural Dynamics, EURODYN*.

Fontara, I.-K. (2015). *Simulation of seismic wave fields in inhomogeneous half-plane by non-conventional BEM*. PhD Thesis, Christian-Albrechts Universität Kiel.

Fontara, I. K., Parvanova, S., Dineva, P., Rangelov, T. V., and Wuttke, F. (2014b). Seismic signals synthesis for laterally inhomogeneous geological media via BIEM. In *Proceedings of 37th International Conference on Boundary Elements and other Mesh Reduction Methods*, pages 8–10.

Fontara, I. K., Wuttke, F., Rangelov, T., and Dineva, P. (2014c). A non-conventional BEM for seismic wave propagation in continuously inhomogeneous half-plane.

Fredholm, I. (1903). Sur une classe d'équations fonctionnelles. *Acta mathematica*, 27:365–390. Publisher: Institut Mittag-Leffler.

Friedman, M. B. and Shaw, R. (1962). Diffraction of pulses by cylindrical obstacles of arbitrary cross section.

Furukawa, A., Saitoh, T., and Hirose, S. (2014). Convolution quadrature time-domain boundary element method for 2-D and 3-D elastodynamic analyses in general anisotropic elastic solids. *Engineering Analysis with Boundary Elements*, 39:64–74. Publisher: Elsevier.

García-Sánchez, F. and Zhang, C. (2007). A comparative study of three BEM for transient dynamic crack analysis of 2-D anisotropic solids. *Computational Mechanics*, 40(4):753–769. Publisher: Springer.

Gauthier, O., Virieux, J., and Tarantola, A. (1986). Two-dimensional nonlinear inversion of seismic waveforms: Numerical results. *Geophysics*, 51(7):1387–1403. Publisher: Society of Exploration Geophysicists.

Ge, Z. (2010). Simulation of the seismic response of sedimentary basins with constant-gradient velocity along arbitrary direction using boundary element method: SH case. *Earthquake Science*, 23(2):149–155. Publisher: Springer.

Gimenes, T. L., Pisani, F., and Borin, E. (2018). Evaluating the performance and cost of accelerating seismic processing with cuda, opencl, openacc, and openmp. In *2018 IEEE International Parallel and Distributed Processing Symposium (IPDPS)*, pages 399–408. IEEE.

Guan, F., Moore, I. D., and Spyrakos, C. C. (1998). Two dimensional transient fundamental solution due to suddenly applied load in a half-space. *Soil Dynamics and Earthquake Engineering*, 17(4):269–277. Publisher: Elsevier.

Guasch, L., Calderón Agudo, O., Tang, M.-X., Nachev, P., and Warner, M. (2020). Full-waveform inversion imaging of the human brain. *NPJ digital medicine*, 3(1):1–12. Publisher: Nature Publishing Group.

Hashash, Y. M., Hook, J. J., Schmidt, B., John, I., and Yao, C. (2001). Seismic design and analysis of underground structures. *Tunnelling and Underground Space Technology*, 16(4):247–293. Publisher: Elsevier.

Hasheminejad, S. M. and Avazmohammadi, R. (2007). Harmonic wave diffraction by two circular cavities in a poroelastic formation. *Soil Dynamics and Earthquake Engineering*, 27(1):29–41. Publisher: Elsevier.

Hasheminejad, S. M. and Kazemirad, S. (2008). Dynamic response of an eccentrically lined circular tunnel in poroelastic soil under seismic excitation. *Soil Dynamics and Earthquake Engineering*, 28(4):277–292. Publisher: Elsevier.

Hirai, H. (1988). Analysis of transient response of SH wave scattering in a half space by the boundary element method. *Engineering analysis*, 5(4):189–194. Publisher: Elsevier.

Hisada, Y. (1994). An efficient method for computing Green's functions for a layered half-space with sources and receivers at close depths. *Bulletin of the Seismological Society of America*, 84(5):1456–1472. Publisher: The Seismological Society of America.

Hisada, Y. (1995). An efficient method for computing Green's functions for a layered half-space with sources and receivers at close depths (Part 2). *Bulletin of the Seismological Society of America*, 85(4):1080–1093. Publisher: The Seismological Society of America.

Hisada, Y., Aki, K., and Teng, T.-L. (1993). 3-D simulations of surface wave propagation in the Kanto sedimentary basin, Japan Part 2: Application of the surface wave BEM. *Bulletin of the Seismological Society of America*, 83(6):1700–1720. Publisher: The Seismological Society of America.

Hisada, Y., Yamamoto, S., and Tani, S. (1992). The BEM based on the Green's function of the layered half-space and the normal mode solution. In *Proc. of Int. Symp. on The Effects of Surface Geology on Seismic Motion, Japan, I*, pages 185–189.

Hooke, J. (1962). Green's Function for Axially Symmetric Elastic Waves in Unbounded Inhomogeneous Media Having Constant Velocity Gradients. *J. Appl. Mech., Trans. ASME, Ser. E*, 29:293–298.

Hoop, A. (1959). The surface line source problem. *Appl. Sci. Res.*, 8:349–356.

Hu, Y.-Y., Wang, L.-Z., Chen, Y.-M., Wu, S.-M., and Zhang, Z.-M. (1998). Scattering and refracting of plane strain wave by a cylindrical inclusion in fluid-saturated soils. *Acta Seismologica Sinica*, 11(3):355–363. Publisher: Springer.

Itzá, R., Iturrarán-Viveros, U., and Parra, J. O. (2016). Optimal implicit 2-D finite differences to model wave propagation in poroelastic media. *Geophysical Journal International*, 206(2):1111–1125. Publisher: Oxford University Press.

Jaberipour, M., Khorram, E., and Karimi, B. (2011). Particle swarm algorithm for solving systems of nonlinear equations. *Computers & Mathematics with Applications*, 62(2):566–576.

Jaswon, M. A. (1963). Integral equation methods in potential theory. I. *Proceedings of the Royal Society of London. Series A. Mathematical and Physical Sciences*, 275(1360):23–32. Publisher: The Royal Society London.

Jean, P. (2015). A 3D FEM/BEM code for ground–structure interaction: Implementation strategy including the multi-traction problem. *Engineering Analysis with Boundary Elements*, 59:52–61. Publisher: Elsevier.

Jeong, W., Lee, H.-Y., and Min, D.-J. (2012). Full waveform inversion strategy for density in the frequency domain: Elastic waveform inversion for density. *Geophysical Journal International*, 188(3):1221–1242.

Jiang, J. and Zhu, P. (2018). Acceleration for 2D time-domain elastic full waveform inversion using a single GPU card. *Journal of Applied Geophysics*, 152:173–187. Publisher: Elsevier.

Jiang, L.-F., Zhou, X.-L., and Wang, J.-H. (2009). Scattering of a plane wave by a lined cylindrical cavity in a poroelastic half-plane. *Computers and Geotechnics*, 36(5):773–786. Publisher: Elsevier.

Jo, C., Shin, C., and Suh, J. H. (1996). An optimal 9-point, finite-difference, frequency-space, 2-D scalar wave extrapolator. *Geophysics*, 61(2):529–537.

Kamalian, M., Gatmiri, B., and Sohrabi Bidar, A. (2003). On time-domain two-dimensional site response analysis of topographic structures by BEM. *Journal of seismology and earthquake engineering*, 5(2):35–45. Publisher: International Institute of Seismology and Earthquake Engineering.

Kaplanvural, , Pekşen, E., and Özkap, K. (2020). 1D waveform inversion of GPR trace by particle swarm optimization. *Journal of Applied Geophysics*, 181:104157.

Karabalis, D. L. and Beskos, D. E. (1984). Dynamic response of 3-D rigid surface foundations by time domain boundary element method. *Earthquake engineering & structural dynamics*, 12(1):73–93. Publisher: Wiley Online Library.

Kattis, S., Beskos, D., and Cheng, A. (2003). 2D dynamic response of unlined and lined tunnels in poroelastic soil to harmonic body waves. *Earthquake Engineering & Structural Dynamics*, 32(1):97–110. Publisher: Wiley Online Library.

Kausel, E. (1981). *An explicit solution for the Green functions for dynamic loads in layered media*. Department of Civil Engineering, School of Engineering, Massachusetts ....

Kelly, K. R., Ward, R. W., Treitel, S., and Alford, R. M. (1976). Synthetic seismograms: A finite-difference approach. *Geophysics*, 41(1):2–27. Publisher: Society of Exploration Geophysicists.

Kennedy, J. and Eberhart, R. (1995). Particle swarm optimization. In *Proceedings of ICNN'95-international conference on neural networks*, volume 4, pages 1942–1948. IEEE.

Kim, Y., Cho, H., Min, D.-J., and Shin, C. (2011). Comparison of frequency-selection strategies for 2D frequency-domain acoustic waveform inversion. *Pure and Applied Geophysics*, 168(10):1715–1727.

Kitahara, M., Nakagawa, K., and Achenbach, J. D. (1989). Boundary-integral equation method for elastodynamic scattering by a compact inhomogeneity. *Computational Mechanics*, 5(2):129–144. Publisher: Springer.

Kobayashi, S. (1980). Green's tensors for elastic half-spaces. An application of boundary integral equation method.

Kobayashi, S. (1983). Some problems of the boundary integral equation method in elastodynamics. *Boundary elements*, pages 775–784. Publisher: Springer-Verlag, Berlin.

Kobayashi, S. (1987). Elastodynamics, Chapter 4 in Boundary Element Methods in Mechanics, edited by D. E. Beskos.

Kolb, P., Collino, F., and Lailly, P. (1986). Pre-stack inversion of a 1-D medium. *Proceedings of the IEEE*, 74(3):498–508.

Komatitsch, D. and Martin, R. (2007). An unsplit convolutional perfectly matched layer improved at grazing incidence for the seismic wave equation. *Geophysics*, 72(5):SM155–SM167. Publisher: Society of Exploration Geophysicists.

Konagai, K., Takatsu, S., Kanai, T., Fujita, T., Ikeda, T., and Johansson, J. (2009). Kizawa tunnel cracked on 23 October 2004 Mid-Niigata earthquake: An example of earthquake-induced damage to tunnels in active-folding zones. *Soil Dynamics and Earthquake Engineering*, 29(2):394–403. Publisher: Elsevier.

Kuvshinov, B. N. and Mulder, W. A. (2006). The exact solution of the time-harmonic wave equation for a linear velocity profile. *Geophysical Journal International*, 167(2):659–662. Publisher: Blackwell Publishing Ltd Oxford, UK.

Köhn, D. (2011). *Time domain 2D elastic full waveform tomography*. PhD Thesis.

Köhn, D., De Nil, D., and Rabbel, W. (2017). Introduction to frequency domain modelling and FWI of georadar data with GERMAINE.

Köhn, D., Kurzmann, A., De Nil, D., and Groos, L. (2014). DENISE-User manual.

Lamb, H. (1903). On the Propagation of Tremors over the Surface of an Elastic Solid. *Proceedings of the royal society of London*, 72:128–130. Publisher: JSTOR.

Lee, J. and Ha, W. (2019). Laplace-domain waveform inversion using the l-BFGS method. *Geosystem Engineering*, 22(4):214–224.

Leung, K. L., Vardoulakis, I. G., Beskos, D. E., and Tassoulas, J. L. (1991). Vibration isolation by trenches in continuously nonhomogeneous soil by the BEM. *Soil Dynamics and Earthquake Engineering*, 10(3):172–179. Publisher: Elsevier.

Levander, A. R. (1988). Fourth-order finite-difference P-SV seismograms. *Geophysics*, 53(11):1425–1436. Publisher: Society of Exploration Geophysicists.

Li, A., Liu, H., Yuan, Y., Hu, T., and Guo, X. (2018). Modeling of frequency-domain elastic-wave equation with a general optimal scheme. *Journal of Applied Geophysics*, 159:1–15.

Li, L., Tan, J., Schwarz, B., Staněk, F., Poiata, N., Shi, P., Diekmann, L., Eisner, L., and Gajewski, D. (2020). Recent advances and challenges of waveform-based seismic location methods at multiple scales. *Reviews of Geophysics*, 58(1):e2019RG000667. Publisher: Wiley Online Library.

Li, W. and Zhao, C. (2008). An analytical solution for the scattering of plane SV-waves around cylindrical cavity in a fluid-saturated porous media half-space. *Journal of Earthquake Engineering and Engineering Vibration*, 6:002.

Li, W.-H. and Zhang, Z. (2013). Scattering of transient plane waves by deep buried cylindrical lining cavity in saturated soil. *Diqiu Wuli Xuebao*, 56(1):325–334. Publisher: Kexue Chubanshe, 16 Donghuangchenggen North Street Beijing 100717 journalspg. net http://www. geophysics. ac. cn.

Li, Y., Li, Z., Zhang, K., and Lin, Y. (2016). Frequency-domain full waveform inversion. *Journal of Seismic Exploration*, 25:543–559.

Liang, J., Ba, Z., and Lee, V. W. (2006). Diffraction of plane SV waves by a shallow circular-arc canyon in a saturated poroelastic half-space. *Soil Dynamics and Earthquake Engineering*, 26(6):582–610. Publisher: Elsevier.

Liang, J. and Liu, Z. (2009). Diffraction of plane SV waves by a cavity in poroelastic half-space. *Earthquake Engineering and Engineering Vibration*, 8(1):29–46. Publisher: Springer.

Lin, C.-H., Lee, V. W., and Trifunac, M. D. (2005). The reflection of plane waves in a poroelastic half-space saturated with inviscid fluid. *Soil Dynamics and Earthquake Engineering*, 25(3):205–223.

Liu, Z., Ju, X., Wu, C., and Liang, J. (2017). Scattering of plane P1 waves and dynamic stress concentration by a lined tunnel in a fluid-saturated poroelastic half-space. *Tunnelling and Underground Space Technology*, 67:71–84.

Liu, Z., Liang, J., and Huang, Y. (2015). The IBIEM solution to the scattering of plane SV waves around a canyon in saturated poroelastic half-space. *Journal of Earthquake Engineering*, 19(6):956–977. Publisher: Taylor & Francis.

Liu, Z., Liu, L., Liang, J., and Zhou, Y. (2016). An indirect boundary element method to model the 3-D scattering of elastic waves in a fluid-saturated poroelastic half-space. *Engineering Analysis with Boundary Elements*, 66:91–108. Publisher: Elsevier.

Love, A. E. H. (1944). *A Treatise on the Mathematical Theory of Elasticity*. Courier Corporation.

Lu, J.-F., Jeng, D.-S., and Lee, T.-L. (2007). Dynamic response of a piecewise circular tunnel embedded in a poroelastic medium. *Soil Dynamics and Earthquake Engineering*, 27(9):875–891. Publisher: Elsevier.

Lubich, C. (1988). Convolution quadrature and discretized operational calculus. II. *Numerische Mathematik*, 52(4):413–425. Publisher: Springer.

Lubich, C. (1994). On the multistep time discretization of linear$\backslash$newline initial-boundary value problems and their boundary integral equations. *Numerische Mathematik*, 67(3):365–389. Publisher: Springer.

Luco, J. E. and Apsel, R. J. (1983). On the Green's functions for a layered half-space. Part I. *Bulletin of the Seismological Society of America*, 73(4):909–929. Publisher: The Seismological Society of America.

Luco, J. E. and de Barros, F. C. P. (1994). Dynamic displacements and stresses in the vicinity of a cylindrical cavity embedded in a half-space. *Earthquake Engineering & Structural Dynamics*, 23(3):321–340.

Luzon, F., Ramirez, L., Sánchez-Sesma, F., and Posadas, A. (2004). Simulation of the seismic response of sedimentary basins with vertical constant-gradient velocity for incident SH waves. In *Geodetic and Geophysical Effects Associated with Seismic and Volcanic Hazards*, pages 1533–1547. Springer.

Luzon, F., Ramırez, L., Sanchez-Sesma, F., and Posadas, A. (2003). Propagation of SH elastic waves in deep sedimentary basins with an oblique velocity gradient. *Wave Motion*, 38(1):11–23. Publisher: Elsevier.

Luzón, F., Sánchez-Sesma, F. J., Pérez-Ruiz, J. A., Ramírez-Guzmán, L., and Pech, A. (2009). In-plane seismic response of inhomogeneous alluvial valleys with vertical gradients of velocities and constant Poisson ratio. *Soil Dynamics and Earthquake Engineering*, 29(6):994–1004. Publisher: Elsevier.

Lysmer, J. and Drake, L. A. (1972). A finite element method for seismology. *Methods in computational physics*, 11:181–216. Publisher: Academic Press New York.

Malinowski, M., Operto, S., and Ribodetti, A. (2011). High-resolution seismic attenuation imaging from wide-aperture onshore data by visco-acoustic frequency-domain full-waveform inversion. *Geophysical Journal International*, 186(3):1179–1204. Publisher: Blackwell Publishing Ltd Oxford, UK.

Manolis, G., Dineva, P., and Rangelov, T. (2004). Wave scattering by cracks in inhomogeneous continua using BIEM. *International Journal of Solids and Structures*, 41(14):3905–3927. Publisher: Elsevier.

Manolis, G. and Shaw, R. (1996a). Harmonic wave propagation through viscoelastic heterogeneous media exhibiting mild stochasticity-I. Fundamental solutions. *Soil Dynamics and Earthquake Engineering*, 15(2):119–127. Publisher: Elsevier.

Manolis, G. and Shaw, R. (1996b). Harmonic wave propagation through viscoelastic heterogeneous media exhibiting mild stochasticity-II. Applications. *Soil Dynamics and Earthquake Engineering*, 15(2):129–139. Publisher: Elsevier.

Manolis, G. D. (1983). A comparative study on three boundary element method approaches to problems in elastodynamics. *International Journal for Numerical Methods in Engineering*, 19(1):73–91. Publisher: Wiley Online Library.

Manolis, G. D. and Beskos, D. E. (1988). *Boundary element methods in elastodynamics*. Taylor & Francis.

Manolis, G. D. and Dineva, P. S. (2015). Elastic waves in continuous and discontinuous geological media by boundary integral equation methods: A review. *Soil Dynamics and Earthquake Engineering*, 70:11–29. Publisher: Elsevier.

Manolis, G. D., Dineva, P. S., and Rangelov, T. V. (2012). Dynamic fracture analysis of a smoothly inhomogeneous plane containing defects by BEM. *Engineering analysis with boundary elements*, 36(5):727–737. Publisher: Elsevier.

Manolis, G. D., Dineva, P. S., Rangelov, T. V., and Wuttke, F. (2017). *Seismic Wave Propagation in Non-Homogeneous Elastic Media by Boundary Elements*, volume 240 of *Solid Mechanics and Its Applications*. Springer International Publishing, Cham.

Manolis, G. D. and Kausel, E. (2000). *Wave motion in earthquake engineering*. WIT Press.

Manolis, G. D., Parvanova, S. L., Makra, K., and Dineva, P. S. (2015). Seismic response of buried metro tunnels by a hybrid FDM-BEM approach. *Bulletin of Earthquake Engineering*, 13(7):1953–1977.

Manolis, G. D. and Shaw, R. P. (1996c). Green's function for the vector wave equation in a mildly heterogeneous continuum. *Wave Motion*, 24(1):59–83. Publisher: Elsevier.

Mansur, W. J. (1983). *A time-stepping technique to solve wave propagation problems using the boundary element method*. PhD Thesis, University of Southampton.

Mansur, W. J. and Brebbia, C. A. (1982a). Formulation of the boundary element method for transient problems governed by the scalar wave equation. *Applied Mathematical Modelling*, 6(4):307–311. Publisher: Elsevier.

Mansur, W. J. and Brebbia, C. A. (1982b). Numerical implementation of the boundary element method for two dimensional transient scalar wave propagation problems. *Applied Mathematical Modelling*, 6(4):299–306. Publisher: Elsevier.

Martin, R. and Komatitsch, D. (2009). An unsplit convolutional perfectly matched layer technique improved at grazing incidence for the viscoelastic wave equation. *Geophysical Journal International*, 179(1):333–344. Publisher: Blackwell Publishing Ltd Oxford, UK.

Martin, R., Komatitsch, D., and Ezziani, A. (2008). An unsplit convolutional perfectly matched layer improved at grazing incidence for seismic wave propagation in poroelastic media. *Geophysics*, 73(4):T51–T61. Publisher: Society of Exploration Geophysicists.

Maruyama, T. (1963). On the Force Equivalents of Dynamical Elastic Dislocations with Reference to the Earthquake Mechanism.

Masson, Y. and Pride, S. (2010). Finite-difference modeling of Biot's poroelastic equations across all frequencies. *Geophysics*, 75(2):N33–N41, https://doi.org/10.1190/1.3332589. Publisher: Society of Exploration Geophysicists.

Matharu, G. and Sacchi, M. (2019). A subsampled truncated-Newton method for multiparameter full-waveform inversion. *GEOPHYSICS*, 84(3):R333–R340.

Mei, C. C., Si, B. I., and Cai, D. (1984). Scattering of simple harmonic waves by a circular cavity in a fluid-infiltrated poro-elastic medium. *Wave Motion*, 6(3):265–278. Publisher: Elsevier.

Memeti, S., Li, L., Pllana, S., Ko\lodziej, J., and Kessler, C. (2017). Benchmarking OpenCL, OpenACC, OpenMP, and CUDA: programming productivity, performance, and energy consumption. In *Proceedings of the 2017 Workshop on Adaptive Resource Management and Scheduling for Cloud Computing*, pages 1–6.

Michéa, D. and Komatitsch, D. (2010). Accelerating a three-dimensional finite-difference wave propagation code using GPU graphics cards. *Geophysical Journal International*, 182(1):389–402. Publisher: Blackwell Publishing Ltd Oxford, UK.

Miranda, L. J. V. (2018). PySwarms, a research-toolkit for Particle Swarm Optimization in Python. *Journal of Open Source Software*, 3(21).

Moczo, P. (1998). *Introduction to Modeling Seismic Wave Propagation by the Finite-Difference Methods*. Disaster Prevention Research Institute, Kyoto University.

Moczo, P., Robertsson, J. O., and Eisner, L. (2007). The finite-difference time-domain method for modeling of seismic wave propagation. *Advances in geophysics*, 48:421–516. Publisher: Elsevier.

Mora, P. (1987). Nonlinear two-dimensional elastic inversion of multioffset seismic data. *Geophysics*, 52(9):1211–1228. Publisher: Society of Exploration Geophysicists.

Morency, C. and Tromp, J. (2008). Spectral-element simulations of wave propagation in porous media. *Geophysical Journal International*, 175(1):301–345. Publisher: Blackwell Publishing Ltd Oxford, UK.

Morse, P. M. and Feshbach, H. (1954). Methods of theoretical physics. *American Journal of Physics*, 22(6):410–413. Publisher: American Association of Physics Teachers.

Moura, F. A., Silva, S. A., de Araújo, J. M., and Lucena, L. S. (2020). Progressive matching optimisation method for FWI. *Journal of Geophysics and Engineering*, 17(2):357–364. _eprint: https://academic.oup.com/jge/article-pdf/17/2/357/32900931/gxz121.pdf.

Métivier, L., Brossier, R., Virieux, J., and Operto, S. (2013). Full Waveform Inversion and the Truncated Newton Method. *SIAM Journal on Scientific Computing*, 35(2):B401–B437.

Nakagawa, K. and Kitahara, M. (1986). Transient analysis in three dimensional elastodynamics. *Innovative numerical methods in engineering*, pages 367–377.

Nardini, D. and Brebbia, C. A. (1983). A new approach to free vibration analysis using boundary elements. *Applied mathematical modelling*, 7(3):157–162. Publisher: Elsevier.

Niwa, Y. (1975). An analysis of transient stresses produced around cavities of arbitrary shape during the passage of traveling waves.

Niwa, Y. (1980). An application of the integral equation method to two-dimensional elastodynamics. *Theoretical and applied mechanics*, 28:281–290. Publisher: University of Tokyo Press.

Niwa, Y., Kobayashi, S., and Fukui, T. (1976). Applications of integral equation method to some geomechanical problems.

Nocedal, J. and Wright, S. J. (2006). *Numerical optimization*. Springer series in operations research. Springer, New York, 2nd ed edition. OCLC: ocm68629100.

Nur, A., Mavko, G., Dvorkin, J., and Galmudi, D. (1998). Critical porosity: A key to relating physical properties to porosity in rocks. *The Leading Edge*, 17(3):357–362. Publisher: Society of Exploration Geophysicists.

Operto, S., Gholami, Y., Prieux, V., Ribodetti, A., Brossier, R., Metivier, L., and Virieux, J. (2013). A guided tour of multiparameter full-waveform inversion with multicomponent data: From theory to practice. *The leading edge*, 32(9):1040–1054. Publisher: Society of Exploration Geophysicists.

Operto, S., Miniussi, A., Brossier, R., Combe, L., Métivier, L., Monteiller, V., Ribodetti, A., and Virieux, J. (2015). Efficient 3-D frequency-domain mono-parameter full-waveform inversion of ocean-bottom cable data: application to Valhall in the visco-acoustic vertical transverse isotropic approximation. *Geophysical Journal International*, 202(2):1362–1391. Publisher: Oxford University Press.

Operto, S., Virieux, J., Ribodetti, A., and Anderson, J. E. (2009). Finite-difference frequency-domain modeling of viscoacoustic wave propagation in 2D tilted transversely isotropic (TTI) media. *Geophysics*, 74(5):T75–T95.

Pak, R. and Guzina, B. (2002). Three-Dimensional Green's Functions for a Multilayered Half-Space in Displacement Potentials. *Journal of Engineering Mechanics-asce - J ENG MECH-ASCE*, 128.

Pakbaz, M. C. and Yareevand, A. (2005). 2-D analysis of circular tunnel against earthquake loading. *Tunnelling and Underground Space Technology*, 20(5):411–417. Publisher: Elsevier.

Pan, L., Rizzo, F., and Martin, P. (1998). Some efficient boundary integral strategies for time-harmonic wave problems in an elastic halfspace. *Computer Methods in Applied Mechanics and Engineering*, 164:207–221.

Pan, W., Innanen, K. A., and Liao, W. (2017). Accelerating Hessian-free Gauss-Newton full-waveform inversion via l-BFGS preconditioned conjugate-gradient algorithm. *Geophysics*, 82(2):R49–R64.

Pan, W., Innanen, K. A., and Wang, Y. (2020). SeisElastic2D: An open-source package for multiparameter full-waveform inversion in isotropic-, anisotropic-and visco-elastic media. *Computers & Geosciences*, 145:104586. Publisher: Elsevier.

Panji, M., Kamalian, M., Marnani, J., and Jafari, M. K. (2013a). Antiplane seismic response from semi-sine shaped valley above embedded truncated circular cavity: A time-domain half-plane BEM. *Int. J. Civil Eng.*, 12.

Panji, M., Kamalian, M., Marnani, J. A., and Jafari, M. K. (2013b). Transient analysis of wave propagation problems by half-plane BEM. *Geophysical Journal International*, 194(3):1849–1865. Publisher: Oxford University Press.

Panza, G. F., Paskaleva, I., Dineva, P., and La Mura, C. (2009). Earthquakes site effects modeling by hybrid MS-BIEM: the case study of Sofia, Bulgaria. *RENDICONTI LINCEI*, 20(2):91–116.

Partridge, P., Brebbia, C., and Wrobel, L. (1992). *The Dual Reciprocity Boundary Element Method*. Journal Abbreviation: Computational Mechanics Publications Publication Title: Computational Mechanics Publications.

Parvanova, S., Dineva, P., and Manolis, G. D. (2014). Elastic wave fields in a half-plane with free-surface relief, tunnels and multiple buried inclusions. *Acta Mechanica*, 225(7):1843–1865.

Pekşen, E., Yas, T., and Kıyak, A. (2014). 1-D DC Resistivity Modeling and Interpretation in Anisotropic Media Using Particle Swarm Optimization. *Pure and Applied Geophysics*, 171(9):2371–2389.

Pica, A., Diet, J. P., and Tarantola, A. (1990). Nonlinear inversion of seismic reflection data in a laterally invariant medium. *Geophysics*, 55(3):284–292. Publisher: Society of Exploration Geophysicists.

Plessix, R.-E. and Perkins, C. (2010). Thematic Set: Full waveform inversion of a deep water ocean bottom seismometer dataset. *First Break*, 28.

Plessix, R.- (2009). Three-dimensional frequency-domain full-waveform inversion with an iterative solver. *Geophysics*, 74(6):WCC149–WCC157. Publisher: Society of Exploration Geophysicists.

Pratt, R. G. (1990a). Frequency-domain elastic wave modeling by finite differences: A tool for crosshole seismic imaging. *GEOPHYSICS*, 55(5):626–632.

Pratt, R. G. (1990b). Inverse theory applied to multi-source cross-hole tomography. Part 2: elastic wave-equation method. *Geophysical Prospecting*, 38(3):311–329. Publisher: European Association of Geoscientists & Engineers.

Pratt, R. G. (1999). Seismic waveform inversion in the frequency domain, Part 1: Theory and verification in a physical scale model. *Geophysics*, 64(3):888–901. Publisher: Society of Exploration Geophysicists.

Pratt, R. G., Gao, F., Zelt, C., and Levander, A. (2002). The limits and complementary nature of traveltime and waveform tomography. In *Journal of Conference Abstracts*, volume 7, pages 181–182. Issue: 2.

Pratt, R. G., Shin, C., and Hicks (1998). Gauss-Newton and full Newton methods in frequency-space seismic waveform inversion. *Geophysical Journal International*, 133(2):341–362.

Pratt, R. G. and Shipp, R. M. (1999). Seismic waveform inversion in the frequency domain, Part 2: Fault delineation in sediments using crosshole data. *Geophysics*, 64(3):902–914. Publisher: Society of Exploration Geophysicists.

Pratt, R. G. and Worthington, M. H. (1990). Inverse theory applied to multi-source cross-hole tomography. Part 1: acoustic wave-equation method. *Geophysical Prospecting*, 38(3):287–310.

Rajapakse, R. and Senjuntichai, T. (1995). An indirect boundary integral equation method for poroelasticity. *International Journal for Numerical and Analytical methods in Geomechanics*, 19(9):587–614. Publisher: Wiley Online Library.

Ramanathan, R. M. (2006). Intel multi-core processors: Making the move to quad-core and beyond. *Technology@ Intel Magazine*, 4(9):2–4.

Rangelov, T., Manolis, G., and Dineva, P. (2005). Elastodynamic fundamental solutions for certain families of 2D inhomogeneous anisotropic domains: basic derivations. *European Journal of Mechanics-A/Solids*, 24(5):820–836. Publisher: Elsevier.

Rangelov, T. V. and Manolis, G. D. (2014). Point force and dipole solutions in the inhomogeneous half-plane under time-harmonic conditions. *Mechanics Research Communications*, 56:90–97. Publisher: Elsevier.

Rizvi, Z. H., Akhtar, S. J., Haider, H., Follmann, J., and Wuttke, F. (2020). Estimation of seismic wave velocities of metamorphic rocks using artificial neural network. *Materials Today: Proceedings*, 26:324–330. Publisher: Elsevier.

Rizzo, F. J., Shippy, D. J., and Rezayat, M. (1985). A boundary integral equation method for radiation and scattering of elastic waves in three dimensions. *International journal for numerical methods in engineering*, 21(1):115–129. Publisher: Wiley Online Library.

Robey, R. and Zamora, Y. (2021). *Parallel and high performance computing*. Simon and Schuster.

Romero, A., Galvín, P., and Domínguez, J. (2013). 3D non-linear time domain FEM–BEM approach to soil–structure interaction problems. *Engineering Analysis with Boundary Elements*, 37(3):501–512. Publisher: Elsevier.

Ross, P. E. (2008). Why cpu frequency stalled. *IEEE Spectrum*, 45(4):72–72. Publisher: IEEE.

Saitoh, T., Chikazawa, F., and Hirose, S. (2014). Convolution quadrature time-domain boundary element method for 2-D fluid-saturated porous media. *Applied Mathematical Modelling*, 38(15):3724–3740. Publisher: Elsevier.

Sanchez-Sesma, F. and Campillo, M. (1991). Diffraction of P, SV and Rayleigh waves by topographic features: a boundary integral formulation. *Bulletin - Seismological Society of America*, 81:2234–2253.

Santamarina, J. C., Rinaldi, V. A., Fratta, D., Klein, K. A., Wang, Y.-H., Cho, G. C., Cascante, G., and others (2005). A survey of elastic and electromagnetic properties of near-surface soils. *Near-surface geophysics*, 1:71–87. Publisher: Society Exploration Geophysics Tulsa, OK.

Schanz, M. (2001). Application of 3D time domain boundary element formulation to wave propagation in poroelastic solids. *Engineering Analysis with Boundary Elements*, 25(4):363–376. Publisher: Elsevier.

Schanz, M. (2009). Poroelastodynamics: linear models, analytical solutions, and numerical methods. *Applied Mechanics Reviews*, 62(3):030803,doi:10.1115/1.3090831. Publisher: American Society of Mechanical Engineers.

Schanz, M. and Antes, H. (1997a). Application of 'operational quadrature methods' in time domain boundary element methods. *Meccanica*, 32(3):179–186. Publisher: Springer.

Schanz, M. and Antes, H. (1997b). A new visco-and elastodynamic time domain boundary element formulation. *Computational Mechanics*, 20(5):452–459. Publisher: Springer.

Shaw, R. and Srivastava, S. (2007). Particle swarm optimization: A new tool to invert geophysical data. *GEOPHYSICS*, 72(2):F75–F83.

Shi, L., Wang, P., Cai, Y., and Cao, Z. (2016). Multi-transmitting formula for finite element modeling of wave propagation in a saturated poroelastic medium. *Soil Dynamics and Earthquake Engineering*, 80:11–24. Publisher: Elsevier.

Shin, C. and Ha, W. (2008). A comparison between the behavior of objective functions for waveform inversion in the frequency and Laplace domains. *Geophysics*, 73(5):VE119–VE133. Publisher: Society of Exploration Geophysicists.

Sirgue, L. and Pratt, R. G. (2004). Efficient waveform inversion and imaging: A strategy for selecting temporal frequencies. *Geophysics*, 69(1):231–248.

Smith, M. (2009). *ABAQUS/Standard User's Manual, Version 6.9*. Dassault Systèmes Simulia Corp, United States.

Sourbier, F., Operto, S., Virieux, J., Amestoy, P., and L'Excellent, J.-Y. (2009a). FWT2D: A massively parallel program for frequency-domain full-waveform tomography of wide-aperture seismic data—Part 1: Algorithm. *Computers & Geosciences*, 35(3):487–495. Publisher: Elsevier.

Sourbier, F., Operto, S., Virieux, J., Amestoy, P., and L'Excellent, J.-Y. (2009b). FWT2D: A massively parallel program for frequency-domain full-waveform tomography of wide-aperture seismic data—Part 2: Numerical examples and scalability analysis. *Computers & Geosciences*, 35(3):496–514. Publisher: Elsevier.

Stokes, G. G. (1849). On the dynamical theory of diffraction. *Transactions of the Cambridge Philosophical Society*, 9:1–48.

Symm, G. T. (1963). Integral equation methods in potential theory. II. *Proceedings of the Royal Society of London. Series A. Mathematical and Physical Sciences*, 275(1360):33–46. Publisher: The Royal Society London.

Sánchez-Sesma, F. J., Madariaga, R., and Irikura, K. (2001). An approximate elastic two-dimensional Green's function for a constant-gradient medium. *Geophysical Journal International*, 146(1):237–248. Publisher: Blackwell Publishing Ltd Oxford, UK.

Tadeu, A. and Kausel, E. (2000). Green's functions for two-and-a-half-dimensional dlastodynamic problems. *Journal of Engineering Mechanics-asce - J ENG MECH-ASCE*, 126.

Tape, C., Liu, Q., Maggi, A., and Tromp, J. (2010). Seismic tomography of the southern California crust based on spectral-element and adjoint methods. *Geophysical Journal International*, 180.

Tarantola, A. (1984a). Inversion of seismic reflection data in the acoustic approximation. *Geophysics*, 49(8):1259–1266. Publisher: Society of Exploration Geophysicists.

Tarantola, A. (1984b). Linearized inversion of seismic reflection data. *Geophysical prospecting*, 32(6):998–1015. Publisher: Wiley Online Library.

Tarantola, A. (1988). Theoretical background for the inversion of seismic waveforms, including elasticity and attenuation. In *Scattering and attenuations of seismic waves, part i*, pages 365–399. Springer.

Trinh, P.-T., Brossier, R., Métivier, L., Tavard, L., and Virieux, J. (2019). Efficient time-domain 3D elastic and viscoelastic full-waveform inversion using a spectral-element method on flexible Cartesian-based mesh. *Geophysics*, 84(1):R61–R83. Publisher: Society of Exploration Geophysicists.

Turek, S., Obaid, A., and Markert, B. (2013). On a fully implicit, monolithic finite element method-multigrid solution approach for dynamic porous media problems. *Journal of Coupled Systems and Multiscale Dynamics*, 1(2):224–240. Publisher: American Scientific Publishers.

Van Rossum, G. and others (2007). Python Programming Language. In *USENIX Annual Technical Conference*, volume 41, page 36.

Vasilev, G., Parvanova, S., Dineva, P., and Wuttke, F. (2015). Soil-structure interaction using BEM–FEM coupling through ANSYS software package. *Soil Dynamics and Earthquake Engineering*, 70:104–117.

Virieux, J. (1986). P-SV wave propagation in heterogeneous media: Velocity-stress finite-difference method. *Geophysics*, 51(4):889–901. Publisher: Society of Exploration Geophysicists.

Volterra, V. (1894). Sur les vibrations des corps élastiques isotropes. *Acta Mathematica - ACTA MATH*, 18:161–232.

Von Estorff, O. and Hagen, C. (2005). Iterative coupling of FEM and BEM in 3D transient elastodynamics. *Engineering Analysis with Boundary Elements*, 29(8):775–787. Publisher: Elsevier.

Wang, B., Gao, J., Zhang, H., and Zhao, W. (2011). CUDA-based acceleration of full waveform inversion on GPU. In *SEG Technical Program Expanded Abstracts 2011*, pages 2528–2533. Society of Exploration Geophysicists.

Wang, J., Zhou, X., and Lu, J. (2005). Dynamic stress concentration around elliptic cavities in saturated poroelastic soil under harmonic plane waves. *International Journal of Solids and Structures*, 42(14):4295–4310. Publisher: Elsevier.

Wang, K., Guo, M., Xiao, Q., Ma, C., Zhang, L., Xu, X., Li, M., and Li, N. (2021). Frequency Domain Full Waveform Inversion Method of Acquiring Rock Wave Velocity in Front of Tunnels. *Applied Sciences*, 11(14):6330.

Watanabe, K. (1982). Transient Response of an Inhomogeneous Elastic Solid to an Impulsive SH-source: Variable SH-wave Velocity. *Bulletin of JSME*, 25(201):315–320. Publisher: The Japan Society of Mechanical Engineers.

Watanabe, K. and Payton, R. G. (2004). Green's function and its non-wave nature for SH-wave in inhomogeneous elastic solid. *International journal of engineering science*, 42(19-20):2087–2106. Publisher: Elsevier.

Watanabe, K. and Takeuchi, T. (2003). Green's function for two-dimensional waves in a radially inhomogeneous elastic solid. In *IUTAM symposium on dynamics of advanced materials and smart structures*, pages 459–468. Springer.

Wei, Z.-F., Gao, H.-W., and Zhang, J.-F. (2014). Time-domain full waveform inversion based on an irregular-grid acoustic modeling method. *Chinese Journal of Geophysics*, 57(2):586–594. Publisher: Chinese Journal of Geophysics.

Wenzlau, F. and Müller, T. M. (2009). Finite-difference modeling of wave propagation and diffusion in poroelastic media. *Geophysics*, 74(4):T55–T66. Publisher: Society of Exploration Geophysicists.

Wong, H. L. (1982). Effect of surface topography on the diffraction of P, SV, and Rayleigh waves. *Bulletin of the Seismological Society of America*, 72(4):1167–1183. Publisher: The Seismological Society of America.

Wong, H. L. and Jennings, P. C. (1975). Effects of canyon topography on strong ground motion. *Bulletin of the seismological Society of America*, 65(5):1239–1257. Publisher: The Seismological Society of America.

Wuttke, F., Dineva, P., and Schanz, T. (2011). Seismic wave propagation in laterally inhomogeneous geological region via a new hybrid approach. *Journal of Sound and Vibration*, 330(4):664–684. Publisher: Elsevier.

Wuttke, F., Fontara, I.-K., Dineva, P., and Rangelov, T. (2015). SH-wave propagation in a continuously inhomogeneous half-plane with free-surface relief by BIEM. *ZAMM-Journal of Applied Mathematics and Mechanics/Zeitschrift für Angewandte Mathematik und Mechanik*, 95(7):714–729. Publisher: Wiley Online Library.

Wuttke, F., Lyu, H., Sattari, A. S., and Rizvi, Z. H. (2021). Wave based damage detection in solid structures using spatially asymmetric encoder–decoder network. *Scientific reports*, 11(1):1–15. Publisher: Nature Publishing Group.

Yang, P., Brossier, R., Métivier, L., Virieux, J., and Zhou, W. (2018). A time-domain preconditioned truncated Newton approach to visco-acoustic multiparameter full waveform inversion. *SIAM Journal on Scientific Computing*, 40(4):B1101–B1130. Publisher: SIAM.

Yeh, C.-S., Teng, T.-J., Liao, W.-I., and Chai, J.-F. (2007). The transition matrix for the scattering of elastic waves in a half-space. *Journal of the Chinese Institute of Engineers*, 30(6):983–996. Publisher: Taylor & Francis.

Yu, C.-W. and Dravinski, M. (2009). Scattering of plane harmonic P, SV or Rayleigh waves by a completely embedded corrugated cavity. *Geophysical Journal International*, 178(1):479–487. Publisher: Blackwell Publishing Ltd Oxford, UK.

Yuan, S., Wang, S., and Tian, N. (2009). Swarm intelligence optimization and its application in geophysical data inversion. *Applied Geophysics*, 6(2):166–174.

Zeng, Y. Q. and Liu, Q. H. (2001). A staggered-grid finite-difference method with perfectly matched layers for poroelastic wave equations. *The Journal of the Acoustical Society of America*, 109(6):2571–2580. Publisher: ASA.

Zhou, X.-L., Wang, J.-H., and Jiang, L.-F. (2009). Dynamic response of a pair of elliptic tunnels embedded in a poroelastic medium. *Journal of Sound and Vibration*, 325(4):816–834. Publisher: Elsevier.

Zhu, H., Bozdağ, E., Peter, D., and Tromp, J. (2012). Structure of the European upper mantle revealed by adjoint tomography. *Nature Geoscience*, 5(7):493–498. Publisher: Nature Publishing Group.

Zimmerman, C. and Stern, M. (1993). Boundary element solution of 3-D wave scatter problems in a poroelastic medium. *Engineering Analysis with Boundary Elements*, 12(4):223–240. Publisher: Elsevier.

Álvarez Rubio, S., Sánchez-Sesma, F. J., José Benito, J., and Alarcón, E. (2004). The direct boundary element method: 2D site effects assessment on laterally varying layered media (methodology). *Soil Dynamics and Earthquake Engineering*, 24(2):167–180.

Štekl, I. and Pratt, R. G. (1998). Accurate viscoelastic modeling by frequency-domain finite differences using rotated operators. *Geophysics*, 63(5):1779–1794.

Appendix A

Finite difference discretization of elastic wave equation

A.1 Finite difference scheme of wave equation

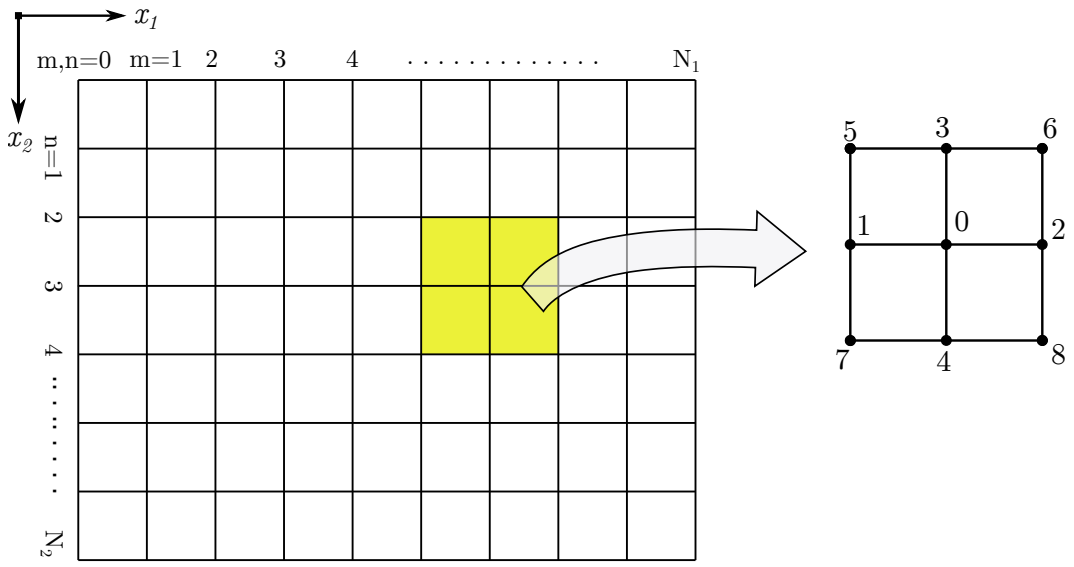

Fig. A.1 A nine-point finite difference stencil.

Chen and Cao (2016) proposed an average derivative optimal scheme for finite difference wave equation which, for a nine-point scheme as shown in Figure A.1, can be written as follows:

$$
\begin{aligned}
&A_0\, v_{m,n} + A_1\, v_{m-1,n} + A_2\, v_{m+1,n} + A_3\, v_{m,n-1} + A_4\, v_{m,n+1} \\
&+A_5\, v_{m-1,n-1} + A_6\, v_{m+1,n-1} + A_7\, v_{m-1,n+1} + A_8\, v_{m+1,n+1} \\
&+\tilde{B}_5 w_{m-1,n-1} + \tilde{B}_6 w_{m+1,n-1} + \tilde{B}_7 w_{m-1,n+1} + \tilde{B}_8 w_{m+1,n+1} = 0
\end{aligned} \tag{A.1}
$$

$$
\begin{aligned}
&B_0\, w_{m,n} + B_1\, w_{m-1,n} + B_2\, w_{m+1,n} + B_3\, w_{m,n-1} + B_4\, w_{m,n+1} \\
&+B_5\, w_{m-1,n-1} + B_6\, w_{m+1,n-1} + B_7\, w_{m-1,n+1} + B_8 w_{m+1,n+1} \\
&+\tilde{A}_5\, v_{m-1,n-1} + \tilde{A}_6\, v_{m+1,n-1} + \tilde{A}_7\, v_{m-1,n+1} + \tilde{A}_8\, v_{m+1,n+1} = 0
\end{aligned} \tag{A.2}
$$

Where: $v = u_1$ and $w = u_2$ components of displacement $u(u_1, u_2)$; The constant terms $A_0 - A_8$, $B_0 - B_8$, $\tilde{A}_5 - \tilde{A}_8$ and $\tilde{B}_5 - \tilde{A}_B$ are given in Equations (A.5−A.30); the subscripts $0-8$ denote the local node numbers in the nine-point stencil, and (m,n) represent the global node indices in the respective Cartesian directions (m,n).

Perfectly matched layers: ξ_{x_m} and ξ_{z_n} are the PML function values at the corresponding horizontal and vertical grid locations, respectively. The continuous function values of PML, given by Equations (A.3) and (A.4), are taken at the grid points and half grid points in the PML region. For simplicity in the algorithm, one-dimensional arrays are used in each direction for full and half grids, where the values in the region not in PML zone to be 1.

$$
\xi_x(x) = 1 - \frac{ic_x}{\omega} \cos\frac{\pi}{2}\frac{x}{L_x} \tag{A.3}
$$

$$
\xi_z(z) = 1 - \frac{ic_z}{\omega} \cos\frac{\pi}{2}\frac{z}{L_z} \tag{A.4}
$$

where, $\xi_x(x)$ and $\xi_z(z)$ are PML functions along the respective axes in the local coordinate system, whose origin is located at the outer edges of the PML layers. L_x and L_z are the length of the PML layers in respective directions. c_x and c_z are the scalar values determined by trial and error. For the simulations in this thesis $c_x = c_z = 90$ is used.

$$A_0 = -\frac{1}{\xi_{x_m}\Delta x^2}\left(\frac{\eta_{m-\frac{1}{2},n}}{\xi_{x_{m-\frac{1}{2}}}} + \frac{\eta_{m+\frac{1}{2},n}}{\xi_{x_{m+\frac{1}{2}}}}\right)\gamma_1 - \frac{1}{\xi_{z_n}\Delta z^2}\left(\frac{\mu_{m,n-\frac{1}{2}}}{\xi_{z_{n-\frac{1}{2}}}} + \frac{\mu_{m,n+\frac{1}{2}}}{\xi_{z_{n+\frac{1}{2}}}}\right)\gamma_2 + \rho_{m,n}\omega^2 c; \tag{A.5}$$

$$A_1 = \frac{1}{\xi_{x_m}\Delta x^2}\frac{\eta_{m-\frac{1}{2},n}}{\xi_{x_{m-\frac{1}{2}}}}\gamma_1 - \frac{1}{\xi_{z_n}\Delta z^2}\left(\frac{\mu_{m,n-\frac{1}{2}}}{\xi_{z_{n-\frac{1}{2}}}} + \frac{\mu_{m,n+\frac{1}{2}}}{\xi_{z_{n+\frac{1}{2}}}}\right)\left(\frac{1-\gamma_2}{2}\right) + \rho_{m,n}\omega^2 d; \tag{A.6}$$

$$A_2 = \frac{1}{\xi_{x_m}\Delta x^2}\frac{\eta_{m+\frac{1}{2},n}}{\xi_{x_{m+\frac{1}{2}}}}\gamma_1 - \frac{1}{\xi_{z_n}\Delta z^2}\left(\frac{\mu_{m,n-\frac{1}{2}}}{\xi_{z_{n-\frac{1}{2}}}} + \frac{\mu_{m,n+\frac{1}{2}}}{\xi_{z_{n+\frac{1}{2}}}}\right)\left(\frac{1-\gamma_2}{2}\right) + \rho_{m,n}\omega^2 d; \tag{A.7}$$

$$A_3 = -\frac{1}{\xi_{x_m}\Delta x^2}\left(\frac{\eta_{m-\frac{1}{2},n}}{\xi_{x_{m-\frac{1}{2}}}} + \frac{\eta_{m+\frac{1}{2},n}}{\xi_{x_{m+\frac{1}{2}}}}\right)\left(\frac{1-\gamma_1}{2}\right) + \frac{1}{\xi_{z_n}\Delta z^2}\frac{\mu_{m,n-\frac{1}{2}}}{\xi_{z_{n-\frac{1}{2}}}}\gamma_2 + \rho_{m,n}\omega^2 d; \tag{A.8}$$

$$A_4 = -\frac{1}{\xi_{x_m}\Delta x^2}\left(\frac{\eta_{m-\frac{1}{2},n}}{\xi_{x_{m-\frac{1}{2}}}} + \frac{\eta_{m+\frac{1}{2},n}}{\xi_{x_{m+\frac{1}{2}}}}\right)\left(\frac{1-\gamma_1}{2}\right) + \frac{1}{\xi_{z_n}\Delta z^2}\frac{\mu_{m,n+\frac{1}{2}}}{\xi_{z_{n+\frac{1}{2}}}}\gamma_2 + \rho_{m,n}\omega^2 d; \tag{A.9}$$

$$A_5 = \frac{1}{\xi_{x_m}\Delta x^2}\frac{\eta_{m-\frac{1}{2},n}}{\xi_{x_{m-\frac{1}{2}}}}\left(\frac{1-\gamma_1}{2}\right) + \frac{1}{\xi_{z_n}\Delta z^2}\frac{\mu_{m,n-\frac{1}{2}}}{\xi_{z_{n-\frac{1}{2}}}}\left(\frac{1-\gamma_2}{2}\right) + \rho_{m,n}\omega^2 e; \tag{A.10}$$

$$A_6 = \frac{1}{\xi_{x_m}\Delta x^2}\frac{\eta_{m+\frac{1}{2},n}}{\xi_{x_{m+\frac{1}{2}}}}\left(\frac{1-\gamma_1}{2}\right) + \frac{1}{\xi_{z_n}\Delta z^2}\frac{\mu_{m,n-\frac{1}{2}}}{\xi_{z_{n-\frac{1}{2}}}}\left(\frac{1-\gamma_2}{2}\right) + \rho_{m,n}\omega^2 e; \tag{A.11}$$

$$A_7 = \frac{1}{\xi_{x_m}\Delta x^2}\frac{\eta_{m-\frac{1}{2},n}}{\xi_{x_{m-\frac{1}{2}}}}\left(\frac{1-\gamma_1}{2}\right) + \frac{1}{\xi_{z_n}\Delta z^2}\frac{\mu_{m,n+\frac{1}{2}}}{\xi_{z_{n+\frac{1}{2}}}}\left(\frac{1-\gamma_2}{2}\right) + \rho_{m,n}\omega^2 e; \tag{A.12}$$

$$A_8 = \frac{1}{\xi_{x_m}\Delta x^2}\frac{\eta_{m+\frac{1}{2},n}}{\xi_{x_{m+\frac{1}{2}}}}\left(\frac{1-\gamma_1}{2}\right) + \frac{1}{\xi_{z_n}\Delta z^2}\frac{\mu_{m,n+\frac{1}{2}}}{\xi_{z_{n+\frac{1}{2}}}}\left(\frac{1-\gamma_2}{2}\right) + \rho_{m,n}\omega^2 e; \tag{A.13}$$

$$B_5 = \frac{1}{4\xi_{x_m}\Delta x\Delta z}\frac{\lambda_{m-1,n}}{\xi_{z_n}} + \frac{1}{4\xi_{z_n}\Delta x\Delta z}\frac{\mu_{m,n-1}}{\xi_{x_m}}; \tag{A.14}$$

$$B_6 = -\frac{1}{4\xi_{x_m}\Delta x\Delta z}\frac{\lambda_{m+1,n}}{\xi_{z_n}} - \frac{1}{4\xi_{z_n}\Delta x\Delta z}\frac{\mu_{m,n-1}}{\xi_{x_m}}; \tag{A.15}$$

$$B_7 = -\frac{1}{4\xi_{x_m}\Delta x\Delta z}\frac{\lambda_{m-1,n}}{\xi_{z_n}} - \frac{1}{4\xi_{z_n}\Delta x\Delta z}\frac{\mu_{m,n+1}}{\xi_{x_m}}; \tag{A.16}$$

$$B_8 = \frac{1}{4\xi_{x_m}\Delta x\Delta z}\frac{\lambda_{m+1,n}}{\xi_{z_n}} + \frac{1}{4\xi_{z_n}\Delta x\Delta z}\frac{\mu_{m,n+1}}{\xi_{x_m}} \tag{A.17}$$

$$\tilde{B}_0 = -\frac{1}{\xi_{x_m}\Delta x^2}\left(\frac{\mu_{m-\frac{1}{2},n}}{\xi_{x_{m-\frac{1}{2}}}} + \frac{\mu_{m+\frac{1}{2},n}}{\xi_{x_{m+\frac{1}{2}}}}\right)\gamma_1 - \frac{1}{\xi_{z_n}\Delta z^2}\left(\frac{\eta_{m,n-\frac{1}{2}}}{\xi_{z_{n-\frac{1}{2}}}} + \frac{\eta_{m,n+\frac{1}{2}}}{\xi_{z_{n+\frac{1}{2}}}}\right)\gamma_2 + \rho_{m,n}\omega^2 c; \tag{A.18}$$

$$\tilde{B}_1 = \frac{1}{\xi_{x_m}\Delta x^2}\frac{\mu_{m-\frac{1}{2},n}}{\xi_{x_{m-\frac{1}{2}}}}\gamma_1 - \frac{1}{\xi_{z_n}\Delta z^2}\left(\frac{\eta_{m,n-\frac{1}{2}}}{\xi_{z_{n-\frac{1}{2}}}} + \frac{\eta_{m,n+\frac{1}{2}}}{\xi_{z_{n+\frac{1}{2}}}}\right)\left(\frac{1-\gamma_2}{2}\right) + \rho_{m,n}\omega^2 d; \tag{A.19}$$

$$\tilde{B}_2 = \frac{1}{\xi_{x_m}\Delta x^2}\frac{\mu_{m+\frac{1}{2},n}}{\xi_{x_{m+\frac{1}{2}}}}\gamma_1 - \frac{1}{\xi_{z_n}\Delta z^2}\left(\frac{\eta_{m,n-\frac{1}{2}}}{\xi_{z_{n-\frac{1}{2}}}} + \frac{\eta_{m,n+\frac{1}{2}}}{\xi_{z_{n+\frac{1}{2}}}}\right)\left(\frac{1-\gamma_2}{2}\right) + \rho_{m,n}\omega^2 d; \tag{A.20}$$

$$\tilde{B}_3 = -\frac{1}{\xi_{x_m}\Delta x^2}\left(\frac{\mu_{m-\frac{1}{2},n}}{\xi_{x_{m-\frac{1}{2}}}} + \frac{\mu_{m+\frac{1}{2},n}}{\xi_{x_{m+\frac{1}{2}}}}\right)\left(\frac{1-\gamma_1}{2}\right) + \frac{1}{\xi_{z_n}\Delta z^2}\frac{\mu_{m,n-\frac{1}{2}}}{\xi_{z_{n-\frac{1}{2}}}}\gamma_2 + \rho_{m,n}\omega^2 d; \tag{A.21}$$

$$\tilde{B}_4 = -\frac{1}{\xi_{x_m}\Delta x^2}\left(\frac{\mu_{m-\frac{1}{2},n}}{\xi_{x_{m-\frac{1}{2}}}} + \frac{\mu_{m+\frac{1}{2},n}}{\xi_{x_{m+\frac{1}{2}}}}\right)\left(\frac{1-\gamma_1}{2}\right) + \frac{1}{\xi_{z_n}\Delta z^2}\frac{\eta_{m,n+\frac{1}{2}}}{\xi_{z_{n+\frac{1}{2}}}}\gamma_2 + \rho_{m,n}\omega^2 d; \tag{A.22}$$

$$\tilde{B}_5 = \frac{1}{\xi_{x_m}\Delta x^2}\frac{\mu_{m-\frac{1}{2},n}}{\xi_{x_{m-\frac{1}{2}}}}\left(\frac{1-\gamma_1}{2}\right) + \frac{1}{\xi_{z_n}\Delta z^2}\frac{\mu_{m,n-\frac{1}{2}}}{\xi_{z_{n-\frac{1}{2}}}}\left(\frac{1-\gamma_2}{2}\right) + \rho_{m,n}\omega^2 e; \tag{A.23}$$

$$\tilde{B}_6 = \frac{1}{\xi_{x_m}\Delta x^2}\frac{\mu_{m+\frac{1}{2},n}}{\xi_{x_{m+\frac{1}{2}}}}\left(\frac{1-\gamma_1}{2}\right) + \frac{1}{\xi_{z_n}\Delta z^2}\frac{\eta_{m,n-\frac{1}{2}}}{\xi_{z_{n-\frac{1}{2}}}}\left(\frac{1-\gamma_2}{2}\right) + \rho_{m,n}\omega^2 e; \tag{A.24}$$

$$\tilde{B}_7 = \frac{1}{\xi_{x_m}\Delta x^2}\frac{\mu_{m-\frac{1}{2},n}}{\xi_{x_{m-\frac{1}{2}}}}\left(\frac{1-\gamma_1}{2}\right) + \frac{1}{\xi_{z_n}\Delta z^2}\frac{\eta_{m,n+\frac{1}{2}}}{\xi_{z_{n+\frac{1}{2}}}}\left(\frac{1-\gamma_2}{2}\right) + \rho_{m,n}\omega^2 e; \tag{A.25}$$

$$\tilde{B}_8 = \frac{1}{\xi_{x_m}\Delta x^2}\frac{\mu_{m+\frac{1}{2},n}}{\xi_{x_{m+\frac{1}{2}}}}\left(\frac{1-\gamma_1}{2}\right) + \frac{1}{\xi_{z_n}\Delta z^2}\frac{\eta_{m,n+\frac{1}{2}}}{\xi_{z_{n+\frac{1}{2}}}}\left(\frac{1-\gamma_2}{2}\right) + \rho_{m,n}\omega^2 e; \tag{A.26}$$

$$\tilde{A}_5 = \frac{1}{4\xi_{x_m}\Delta x\Delta z}\frac{\mu_{m-1,n}}{\xi_{z_n}} + \frac{1}{4\xi_{z_n}\Delta x\Delta z}\frac{\lambda_{m,n-1}}{\xi_{x_m}} \tag{A.27}$$

$$\tilde{A}_6 = -\frac{1}{4\xi_{x_m}\Delta x\Delta z}\frac{\mu_{m+1,n}}{\xi_{z_n}} - \frac{1}{4\xi_{z_n}\Delta x\Delta z}\frac{\lambda_{m,n-1}}{\xi_{x_m}} \tag{A.28}$$

$$\tilde{A}_7 = -\frac{1}{4\xi_{x_m}\Delta x\Delta z}\frac{\mu_{m-1,n}}{\xi_{z_n}} - \frac{1}{4\xi_{z_n}\Delta x\Delta z}\frac{\lambda_{m,n+1}}{\xi_{x_m}} \tag{A.29}$$

$$\tilde{A}_8 = \frac{1}{4\xi_{x_m}\Delta x\Delta z}\frac{\mu_{m+1,n}}{\xi_{z_n}} + \frac{1}{4\xi_{z_n}\Delta x\Delta z}\frac{\lambda_{m,n+1}}{\xi_{x_m}} \tag{A.30}$$

A.2 Partial derivative of Impedance

The partial derivatives of the impedance matrix are obtained by taking the partial derivative of Equations (A.1-A.2) with respect to each parameter in the node. As the linear operators are used and they are averaged only between the neighboring nodes, the partial derivative of impedance with respect to a nodal parameter $\frac{\partial \mathbf{S}}{\partial p_k}$ consists of very few non-zero elements localized around the node. Additionally, for the parameters that do not lie in the PML zone $\xi_x = \xi_z = 1$. The partial derivatives are taken separately for each nodal parameter λ_k, μ_k and ρ_k for the set of nodes where parameters are required to be inverted. All the partial derivative terms except the following relations are zero.

$$\frac{\partial \eta_{m\pm\frac{1}{2},n}}{\partial \lambda_{m,n}} = \frac{\partial \eta_{m,n\pm\frac{1}{2}}}{\partial \lambda_{m,n}} = \frac{1}{2} \tag{A.31}$$

$$\frac{\partial \eta_{m\pm\frac{1}{2},n}}{\partial \mu_{m,n}} = \frac{\partial \eta_{m,n\pm\frac{1}{2}}}{\partial \mu_{m,n}} = 1 \tag{A.32}$$

$$\frac{\partial \mu_{m\pm\frac{1}{2},n}}{\partial \lambda_{m,n}} = \frac{\partial \mu_{m,n\pm\frac{1}{2}}}{\partial \lambda_{m,n}} = 0 \tag{A.33}$$

$$\frac{\partial \mu_{m\pm\frac{1}{2},n}}{\partial \mu_{m,n}} = \frac{\partial \mu_{m,n\pm\frac{1}{2}}}{\partial \mu_{m,n}} = \frac{1}{2} \tag{A.34}$$

$$\frac{\partial \lambda_{m,n}}{\partial \lambda_{m,n}} = \frac{\partial \mu_{m,n}}{\partial \mu_{m,n}} = \frac{\partial \rho_{m,n}}{\partial \rho_{m,n}} = 1 \tag{A.35}$$

It is also to be noted that there are N_k number of $\frac{\partial \mathbf{S}}{\partial p_k}$ matrices where the total number of nodal parameters to be inverted, N_k is given by:

$$N_k = N_p \times N_n \tag{A.36}$$

where, N_p is the number of parameters to be inverted per node, for example, if the parameters λ_k, μ_k, and ρ_k are to be inverted $N_p = 3$; and N_n is the number of nodes in which the parameters are to be inverted.

Appendix B

Free-field wave motion in a homogeneous elastic isotropic half-plane

Free field displacements and traction in a homogeneous elastic isotropic half-plane are analytically derived (see Achenbach et al. (1973), Dominguez (1993) and various other books and articles). The free field motion for the case of incident P and SV waves in 2-D in-plane problems is given by the following formulae for the observer point $X(x_1, x_2)$:

- ***Incident P-wave:***

$$\begin{aligned}\begin{pmatrix} u_1^{ff}(X,\omega) \\ u_2^{ff}(X,\omega) \end{pmatrix} &= A_p^{in} \begin{pmatrix} k/k_p \\ -iv/k_p \end{pmatrix} e^{(-vx_2 - ikx_1)} \\ &+ A_p^{in} R_{pp} \begin{pmatrix} k/k_p \\ -iv/k_p \end{pmatrix} e^{(vx_2 - ikx_1)} \\ &+ A_p^{in} R_{ps} \begin{pmatrix} iv'/k_P \\ -k/k_p \end{pmatrix} e^{(v'x_2 - ikx_1)}\end{aligned} \tag{B.1}$$

Where, k_p *and* k_s are the wave numbers of P and SV waves, respectively, and

$$\begin{aligned} & k = k_p cos\theta; \;\; v = ik_p sin\theta; \; v' = \sqrt{k^2 - k_s^2}; \\ & \Delta(k) = (2k^2 - k_s^2)^2 - 4k^2 vv'; \\ & R_{pp} = -\lfloor (2k^2 - k_s^2)^2) + 4k^2 vv' \rfloor / \Delta(k); \\ & R_{ps} = -4ikv(2k^2 - k^2)/\Delta(k); \\ & k_p = \frac{\omega}{C_{P0}}; \;\; k_s = \frac{\omega}{C_{S0}}; \end{aligned}$$

- ***Incident SV-wave:***

$$\begin{aligned}\begin{pmatrix} u_1^{ff}(X,\omega) \\ u_2^{ff}(X,\omega) \end{pmatrix} &= A_{SV}^{in} \begin{pmatrix} -iv'/k_s \\ -k/k_s \end{pmatrix} e^{(-v'x_2 - ikx_1)} \\ &+ A_{SV}^{in} R_{SS} \begin{pmatrix} iv/k_s \\ -k/k_s \end{pmatrix} e^{(v'x_2 - ikx_1)} \\ &+ A_{SV}^{in} R_{SP} \begin{pmatrix} k/k_s \\ iv/k_s \end{pmatrix} e^{(vx_2 - ikx_1)} \end{aligned} \tag{B.2}$$

Where, k_p *and* k_s are the wave numbers of P and SV waves, respectively, and

$$\begin{aligned} &k = k_s cos\theta; \quad v = \sqrt{k^2 - k_s^2}; \;\; v' = ik_s sin\theta; \\ &\Delta(k) = (2k^2 - k_s^2)^2 - 4k^2 vv'; \\ &R_{ss} = -\lfloor (2k^2 - k_s^2)^2) - 4k^2 vv' \rfloor / \Delta(k); \\ &R_{sp} = -4ikv'(2k^2 - k^2)/\Delta(k); \\ &k_p = \frac{\omega}{C_{P0}}; \;\; k_s = \frac{\omega}{C_{S0}}; \end{aligned}$$

The corresponding traction at any point X in the half-plane is computed by:

$$t_i^{ff}(X,\omega) = \lfloor \lambda_0 u_{k,k}^{ff} \delta_{ij} + \mu_0 \left(u_{i,j}^{ff} + u_{j,j}^{ff} \right) \rfloor n_j; \quad i,j,k = 1,2 \tag{B.3}$$

Appendix C

A review of fundamental solutions and Green's functions in elastodynamics

The mathematical sense of the term fundamental solution of 2D elastodynamic governing equation for elastic isotropic continua is defined as a particular solution of the corresponding differential operator for a point force with magnitude F_0 in space and time in the form $f(x,t) = F_0\hat{f}\delta(x-x_0)\delta(t-t_0)$ which is applied in an unbounded domain, where $\hat{f}$ defines the force direction and two Dirac delta functions δ attest to the location and impulsive nature of the source. The mechanical sense of this term provides the response (displacement, stress, traction) at an observation point $x(x_1,x_2)$ in the plane and at running time t due to unit force acting at source point $x_0(x_{01},x_{02})$ with initial time t_0. In BEM, the fundamental solution serves as a kernel in integral equations formulations and is redefined for a source (where the load is applied) and receiver or field point (where the response is measured). The key role played by the fundamental solution in BEM is to reduce a boundary-value problem formulated by the governing partial differential equation together with the boundary and initial conditions into a system of boundary integral equations via the use of reciprocal theorems. The literature corresponding to the development of fundamental solutions and Green's functions in elastodynamics and their BIEM application are given in Table (C.1−C.3).

Table C.1 Fundamental solutions and Green's functions for homogeneous elastic isotropic continua and the earliest BIEM applications

Subject	**Out-of-plane wave motion**	**In-plane wave motion**	**3D wave motion**
Fundamental solution in time domain	Morse and Feshbach (1954), Eringen and Suhubi (1975), Cole et al. (1978), Mansur and Brebbia (1982a,b), Mansur (1983)	Volterra (1894), Eason et al. (1956), Achenbach et al. (1973), Antes (1985)	Stokes (1849), Love (1944), Morse and Feshbach (1954), Maruyama (1963), Achenbach et al. (1973), Niwa (1980), Karabalis and Beskos (1984)
Fundamental solution in frequency domain	Morse and Feshbach (1954), Eringen and Suhubi (1975)	Doyle (1966), Cruse and Rizzo (1968), Kitahara et al. (1989), Dominguez (1993), Barra and Telles (1999)	Doyle (1966), Cruse and Rizzo (1968), Kitahara et al. (1989), Dominguez (1993)
Green's function in time domain	Hirai (1988), Panji et al. (2013a,b)	Hoop (1959), Guan et al. (1998)	
Green's function in frequency domain	Lamb (1903), Achenbach et al. (1973), Wong and Jennings (1975), Kobayashi (1983)	Kobayashi (1980), Pan et al. (1998)-comparison between BIEM based on fundamental solutions and Green's function.	Luco and Apsel (1983), Apsel and Luco (1983)-stratified half space; Banerjee and Mamoon (1990); Hisada (1994, 1995) - stratified half space; Tadeu and Kausel (2000) - 2.5D elastodynamic problem; Pak and Guzina (2002) - stratified half space; Kausel (1981) - stratified half space.

Continued on next page

Table C.1 – *Continued from previous page*

Subject	**Out-of-plane wave motion**	**In-plane wave motion**	**3D wave motion**
BIEM based on fundamental solutions in time domain	Friedman and Shaw (1962), Mansur and Brebbia (1982a), Manolis and Beskos (1988), Beskos (1987a,b, 1997).	Niwa (1980), Manolis (1983), Antes (1985), Antes and Von Estorff (1989), Manolis and Beskos (1988), Beskos (1987a,b, 1997)	Karabalis and Beskos (1984), Banerjee et al. (1986), Beskos (1987a,b, 1997)
BIEM based on fundamental solutions in frequency domain	Banaugh and Goldsmith (1963b), Manolis and Beskos (1988), Beskos (1987a,b, 1997)	Banaugh and Goldsmith (1963a), Cruse and Rizzo (1968)- Laplace domain, Niwa (1975), Niwa et al. (1976) - FFT, Dominguez (1993) - FFT, Manolis (1983), Manolis and Beskos (1988), Beskos (1987a,b, 1997)	Rizzo et al. (1985), Nakagawa and Kitahara (1986) - transient by FFT, Kitahara et al. (1989), Beskos (1987a,b, 1997)
Dual reciprocity based on elastostatic fundamental solutions		Nardini and Brebbia (1983), Partridge et al. (1992)	
BIEM based on Convolution Quadrature Method			Schanz and Antes (1997a,b)

Table C.2 Fundamental solutions and Green's functions for inhomogeneous elastic isotropic continua with constant velocity profile

	Type of the model	**References**
A. Antiplane case		
Fundamental solution in time domain	exponential, trigonometric	Daros (2008)
Fundamental solution in frequency domain	exponential	Manolis et al. (2012)
	exponential, trigonometric	Daros (2008)
Green's function in frequency domain	exponential and quadratic	Rangelov and Manolis (2014)
BIEM formulation in frequency domain	quadratic (Green's functions)	Wuttke et al. (2015), Fontara et al. (2014a,b,c)
	exponential, trigonometric	Daros (2010) - direct traction BEM, by fundamental solutions in Daros (2008)
B. Inplane case		
Fundamental solution in frequency domain	quadratic	Manolis et al. (2004), Dineva et al. (2006)
	quadratic, exponential, trigonometric	Rangelov et al. (2005) - anisotropic
	exponential, trigonometric	Daros (2009)-transversely isotropic
	exponential	Dineva et al. (2007)
BIEM formulation in frequency domain	quadratic and exponential	Dineva et al. (2008), direct BEM
C. 3D case		
Fundamental solution in frequency domain	quadratic ($\nu = 0.25$)	Manolis and Shaw (1996c)
	stratified half-space	Hisada (1994, 1995)
BIEM formulation in time domain	based on Hisada (1994, 1995)	Hisada et al. (1992, 1993)
BIEM formulation in frequency domain	based on fundamental solutions in Manolis and Shaw (1996c)	Daros and Mesquita (2006), direct BEM

Table C.3 Fundamental solutions and Green's functions for inhomogeneous elastic isotropic continua with variable velocity profile

	Type of velocity profile	**References**
Fundamental solution in time domain	linear	Watanabe (1982)
	linear function of depth in the Cartesian coordinates and a **power function** of radial distance in the polar coordinate system	Watanabe and Payton (2004)
	linear/ constant	Daros (2008) - anisotropic
	power function + linear in one space variable: one of the elastic moduli has a quadratic variation, whilst the other elastic modulus and the density have the same power function profile.	Daros (2013) - anisotropic
	linear	Sánchez-Sesma et al. (2001) - approximate fundamental solutions based on the asymptotic ray theory
Fundamental solution in frequency domain	**linear function** of depth in the Cartesian coordinates and a **power function** of radial distance in the polar coordinate system	Watanabe and Payton (2004)
	linear	Daros (2008) - anisotropic
	linear	Sánchez-Sesma et al. (2001)-approximate fundamental solutions based on the asymptotic ray theory, Luzón et al. (2009)-improvement of the formulae in Sánchez-Sesma et al. (2001), Kuvshinov and Mulder (2006)
	depth dependent described by a special frequency dependent relation	Manolis and Shaw (1996a,b)

Continued on next page

Table C.3 – *Continued from previous page*

	Type of velocity profile	**References**
BIEM formulation in time domain	**Line in depth:** in the inhomogeneous basin is used frequency dependent fundamental solutions in Sánchez-Sesma et al. (2001), while in a homogeneous half-plane frequency dependent fundamental solutions for homogeneous case	Luzon et al. (2004)-continuously inhomogeneous semi-circular sedimentary basin rested in a homogeneous half-plane under SH transient wave by **indirect BEM**, solution in time by FFT.
	line in arbitrary direction: (Vary in the horizontal and vertical direction). In the inhomogeneous basin used frequency dependent fundamental solutions in Sánchez-Sesma et al. (2001), while in a homogeneous half-plane-freq. dependent fundamental solutions for homogeneous case.	Luzon et al. (2003)-continuously inhomogeneous semi-circular sedimentary basin rested in a homogeneous half-plane under SH transient wave by **indirect BEM**, solution in time by FFT.
	line in arbitrary direction (Vary in the horizontal and vertical direction).	Ge (2010)-direct BEM by frequency-dependent fundamental solutions in Sánchez-Sesma et al. (2001), use FFT, Ricker signal. Consider sedimentary basins above a half-space for vertical incidence of SH plane waves.
BIEM formulation in frequency domain	**Line in depth:** in the inhomogeneous basin is used frequency dependent fundamental solutions in Sánchez-Sesma et al. (2001), while in a homogeneous half-plane-freq. dependent fundamental solutions for homogeneous case	Luzon et al. (2004)-continuously inhomogeneous semi-circular sedimentary basin rested in a homogeneous half-plane under SH transient wave by **indirect BEM**, solution in time by FFT.

Continued on next page

Table C.3 – *Continued from previous page*

	Type of velocity profile	**References**
	line in arbitrary direction: (Vary in the horizontal and vertical direction). In the inhomogeneous basin used frequency dependent fundamental solutions in Sánchez-Sesma et al. (2001), while in a homogeneous half-plane-freq. dependent fundamental solutions for homogeneous case.	Luzon et al. (2004)-continuously inhomogeneous semi-circular sedimentary basin rested in a homogeneous half-plane under SH transient wave by **indirect BEM**, solution in time by FFT. Ge (2010)-the same problem but by direct BEM
B. In-plane case		
Fundamental solution in time domain	linear	Hooke (1962)
	linear	Watanabe and Takeuchi (2003)
	linear with the depth, ν = constant	Sánchez-Sesma et al. (2001)-approximate fundamental solutions based on the asymptotic ray theory
Fundamental solution in frequency domain	linear	Watanabe and Takeuchi (2003)
	linear with the depth, ν = constant	Sánchez-Sesma et al. (2001)-approximate fundamental solutions based on the asymptotic ray theory, Luzón et al. (2009)-improvement of the formulae in Sánchez-Sesma et al. (2001)
BIEM formulation in time domain	linear velocity profile improvement of the fundamental solutions in Sánchez-Sesma et al. (2001)	Luzón et al. (2009)-**indirect BEM** for seismic response of sedimentary alluvial valleys with semicircular shape under transient of Ricker type P/SV wave, FFT is used.

Continued on next page

Table C.3 – *Continued from previous page*

	Type of velocity profile	**References**
BIEM formulation in frequency domain	by Green's function of Kausel-Peek-Hull for layered half-plane.	Leung et al. (1991)
	linear velocity profile improvement of fundamental solutions in Sánchez-Sesma et al. (2001)	Luzón et al. (2009) - **indirect BEM** for seismic response of sedimentary alluvial valleys with semi-circular shape under time-harmonic P/SV wave.

Appendix D

Elastodynamic fundamental solutions and its derivatives for elastic isotropic continuum

D.1 Elastodynamic fundamental solutions

The frequency-dependent displacement elastodynamic fundamental solution for in-plane wave field and its corresponding traction is given by Equations (D.1) and (D.2), respectively, see Dominguez (1993).

$$u^*_{lk}(x,\xi,\omega) = \frac{1}{2\pi\rho c_2^2}\left[\psi\ \delta_{lk} - \chi\ r_{,k}\ r_{,l}\right] \tag{D.1}$$

$$\begin{aligned}\tau^*_{lk}(x,\xi,\omega)\ =\ & \frac{1}{2\pi}\left[\left(\frac{\partial\psi}{\partial r}-\frac{1}{r}\chi\right)\left(\delta_{lk}\frac{\partial r}{\partial n}+r_{,k}\ n_{,l}\right)\ -\frac{2}{r}\chi\left(r_{,l}\ n_k - 2r_{,l}\ r_{,k}\frac{\partial r}{\partial n}\right)\right.\\ & \left.-\ 2\frac{\partial\chi}{\partial r}\ r_{,l}\ r_{,k}\frac{\partial r}{\partial n}+\left(\frac{c_1^2}{c_2^2}-2\right)\left(\frac{\partial\psi}{\partial r}-\frac{\partial\chi}{\partial r}-\frac{1}{r}\chi\right)r_{,l}\ n_k\right]\end{aligned} \tag{D.2}$$

Where the functions ψ and χ and their derivatives with respect to the distance between the source and the collocation point r are given by:

$$\psi = K_0(z_2) + \frac{1}{z_2}\left[K_1(z_2) - \tfrac{c_2}{c_1}\, K_1(z_1)\right] \tag{D.3}$$

$$\chi = K_2(z_2) - \frac{c_1^2}{c_2^2}\, K_2(z_1) \tag{D.4}$$

$$\frac{\partial \psi}{\partial r} = \frac{1}{r}\left[\frac{c_2}{c_1}\left(\frac{z_1}{z_2}K_0(z_1) + \frac{2}{z_2}K_1(z_1)\right) - K_0(z_2) - \left(z_2 + \frac{2}{z_2}\right)\, K_1(z_2)\right] \tag{D.5}$$

$$\frac{\partial \chi}{\partial r} = \frac{1}{r}\left[\frac{c_2^2}{c_1^2}\left(z_1\, K_1(z_1) + 2\, K_2(z_1)\right) - z_2\, K_1(z_2) - 2K_2(z_2)\right] \tag{D.6}$$

$c_1 = \sqrt{(\lambda + 2\mu)/\rho}$ and $c_2 = \sqrt{\mu/\rho}$ are longitudinal and shear wave velocities of the medium, respectively; λ and μ are Lame constants and ρ is the mass density of the medium; i and j are the principle directions of applied unit loads and observed responses respectively; $r = |x - \xi|$ is the distance between the collocation (source) point and the integration (field) point along the element; $z_1 = i\omega r/c_1$, $z_2 = i\omega r/c_2$, $K_n(z)$ and $K_n(z)$ are the modified Bessel functions of the second type of order n for imaginary argument z, see Bateman (1953). The asymptotic expression for Bessel functions at $r \to 0$ can be found in Bateman (1953) and the asymptotic expressions for reciprocal displacement and traction can be found in Dominguez (1993).

D.2 Derivatives of the fundamental solutions

Using the partial derivatives of the modified Bessel's functions of the second kind and product rules for derivatives, the following expressions can be obtained for the derivatives of u^* and τ^* in Equations (D.1−D.4), with respect to the parameters c_1, c_2 and ρ.

Partial derivatives with respect to c_1:

$$\frac{\partial u_{lk}^*}{\partial c_1} = \frac{1}{2\pi\rho c_2^2}\left[\frac{\partial \psi}{\partial c_1}\delta_{lk} - \frac{\partial \chi}{\partial c_1}\, r_{,k}\, r_{,l}\right] \tag{D.7}$$

$$\begin{aligned}\frac{\partial \tau^*_{lk}}{\partial c_1} &= \frac{1}{2\pi}\left[\left(\frac{\partial^2\psi}{\partial c_1 \partial r} - \frac{1}{r}\frac{\partial \chi}{\partial c_1}\right)\left(\delta_{lk}\frac{\partial r}{\partial n} + r_{,k}\, n_{,l}\right) - \frac{2}{r}\frac{\partial \chi}{\partial c_1}\left(r_{,l}\, n_k - 2r_{,l}\, r_{,k}\frac{\partial r}{\partial n}\right)\right. \\ &- 2\frac{\partial^2 \chi}{\partial c_1 \partial r}\, r_{,l}\, r_{,k}\frac{\partial r}{\partial n} + \frac{2c_1}{c_2^2}\left(\frac{\partial \psi}{\partial r} - \frac{\partial \chi}{\partial r} - \frac{1}{r}\chi\right) r_{,l}\, n_k \\ &+ \left.\left(\frac{c_1^2}{c_2^2} - 2\right)\left(\frac{\partial^2\psi}{\partial c_1 \partial r} - \frac{\partial^2 \chi}{\partial c_1 \partial r} - \frac{1}{r}\frac{\partial \chi}{\partial c_1}\right) r_{,l}\, n_k\right]\end{aligned} \tag{D.8}$$

Where,

$$\frac{\partial \psi}{\partial c_1} = -\frac{z_1}{z_2}\frac{c_2}{c_1^2}\, K_0(z_1) \tag{D.9}$$

$$\frac{\partial \chi}{\partial c_1} = -\frac{c_1}{c_2^2}\left[z_1\, K_1(z_1) + 4\, K_2(z_1)\right] \tag{D.10}$$

$$\frac{\partial^2 \psi}{\partial c_1 \partial r} = \frac{1}{r}\frac{c_2}{c_1^2}\left[z_1\, K_0(z_1) + \frac{z_2}{c_2}\, K_1(z_1)\right] \tag{D.11}$$

$$\frac{\partial^2 \chi}{\partial c_1 \partial r} = \frac{1}{r}\frac{c_2^2}{c_1^3}\left[z_1^2\, K_0(z_1) - 2\, K_1(z_1)\right] \tag{D.12}$$

$$\tag{D.13}$$

Partial derivatives with respect to c_2:

$$\frac{\partial u^*_{lk}}{\partial c_2} = \frac{1}{2\pi\rho c_2^2}\left[\frac{\partial \psi}{\partial c_2}\delta_{lk} - \frac{\partial \chi}{\partial c_2}\, r_{,k}\, r_{,l}\right] - \frac{1}{\pi\rho c_2^3}\left[\psi\, \delta_{lk} - \chi\, r_{,k}\, r_{,l}\right] \tag{D.14}$$

$$\begin{aligned}\frac{\partial \tau^*_{lk}}{\partial c_2} &= \frac{1}{2\pi}\left[\left(\frac{\partial^2\psi}{\partial c_2 \partial r} - \frac{1}{r}\frac{\partial \chi}{\partial c_2}\right)\left(\delta_{lk}\frac{\partial r}{\partial n} + r_{,k}\, n_{,l}\right) - \frac{2}{r}\frac{\partial \chi}{\partial c_2}\left(r_{,l}\, n_k - 2r_{,l}\, r_{,k}\frac{\partial r}{\partial n}\right)\right. \\ &- 2\frac{\partial^2 \chi}{\partial c_2 \partial r}\, r_{,l}\, r_{,k}\frac{\partial r}{\partial n} - \frac{2c_1^2}{c_2^3}\left(\frac{\partial \psi}{\partial r} - \frac{\partial \chi}{\partial r} - \frac{1}{r}\chi\right) r_{,l}\, n_k \\ &+ \left.\left(\frac{c_1^2}{c_2^2} - 2\right)\left(\frac{\partial^2\psi}{\partial c_2 \partial r} - \frac{\partial^2 \chi}{\partial c_2 \partial r} - \frac{1}{r}\frac{\partial \chi}{\partial c_2}\right) r_{,l}\, n_k\right]\end{aligned} \tag{D.15}$$

Where,

$$\frac{\partial \psi}{\partial c_2} = \frac{1}{z_2\, c_2}\left[z_2\, K_0(z_2) - \left(1+\frac{c_2}{c_1}\right)\, K_1(z_1) + \left(z_2^2+2\right) K_1(z_2)\right] \tag{D.16}$$

$$\frac{\partial \chi}{\partial c_2} = \frac{1}{c_2}\left[z_2\, K_1(z_2) + 2\, K_2(z_2)\, + 2\frac{c_1^2}{c_2^2}\, K_2(z_1)\right] \tag{D.17}$$

$$\frac{\partial^2 \psi}{\partial c_2 \partial r} = \frac{1}{r}\left[\frac{2}{z_2\, c_2} K_1(z_1) - \frac{2}{z_2\, c_2}\left(z_2+\frac{2}{z_2}\right)\, K_0(z_2) + \left(4-\frac{z_2}{c_2}\right) K_1(z_2)\right] \tag{D.18}$$

$$\frac{\partial^2 \chi}{\partial c_2 \partial r} = \frac{1}{r}\left[2\frac{c_2^3}{c_1^2}\left[z_1\, K_1(z_1) + 2\, K_2(z_1)\right] - \frac{1}{c_2}\left[z_2^2\, K_0(z_2) - 4\, z_2\, K_1(z_2) - 4\, K_2(z_2)\right]\right] \tag{D.19}$$

Partial derivatives with respect to ρ:

$$\frac{\partial u_{lk}^*}{\partial \rho} = -\frac{1}{2\pi\rho^2 c_2^2}\left[\psi\, \delta_{lk} - \chi\, r_{,k}\, r_{,l}\right] \tag{D.20}$$

$$\frac{\partial \tau_{lk}^*}{\partial \rho} = 0 \tag{D.21}$$

Appendix E

Enclosed publications

Chapter 5

Basnet, M. B., Aji, H. D., Wuttke, F., and Dineva, P. (2018). Wave propagation through poroelastic soil with underground structures via hybrid BEM-FEM, *ZAMM-Journal of Applied Mathematics and Mechanics/Zeitschrift für Angewandte Mathematik und Mechanik*, 98(8) 1390-1411.

Abstract

A hybrid model for evaluation of the seismic response of a complex poroelastic soil region containing an underground structure is developed. The model is based on an efficient computational technique unifying the benefits of both boundary element method (BEM) and finite element method (FEM). The mechanical model takes the whole seismic wave path from the seismic source, through the heterogeneous geological saturated deposits, till the local site with underground structure into consideration. The seismic load comprises time-harmonic or transient P- and SV-wave, thus covering the plane strain case. A viscoelastic isomorphism to Biot's equations of dynamic poroelasticity presented by Bardet's model is used. The direct BEM is applied for the unbounded part of the geological region, while the FEM is used for the local finite geological profile containing an underground structure. The BEM model is inserted as a macro finite element in commercial program ABAQUS used for solution of the entire problem. The simulation results reveal that the seismic response is sensitive to the site conditions such as the existence of surface relief and layers, to soil inhomogeneity and poroelasticity, and most importantly to the soil-underground structure interaction.

Chapter 6

Basnet, M. B., Anas, M., Rizvi, Z. H., Ali, A. H., Zain, M., Cascante, G., and Wuttke, F. (2022). Enhancement of In-Plane Seismic Full Waveform Inversion with CPU and GPU Parallelization. *Applied Sciences,* 12(17), 8844.

Abstract

Full waveform inversion is a widely used technique to estimate the subsurface parameters with the help of seismic measurements on the surface. Due to the amount of data, model size and non-linear iterative procedures, the numerical computation of Full Waveform Inversion are computationally intensive and time-consuming. This paper addresses the parallel computation of seismic full waveform inversion with Graphical Processing Units. Seismic full-waveform inversion of in-plane wave propagation in the finite difference method is presented here. The stress velocity formulation of the wave equation in the time domain is used. A four nodded staggered grid finite-difference method is applied to solve the equation, and the perfectly matched layers are considered to satisfy Sommerfeld's radiation condition at infinity. The gradient descent method with conjugate gradient method is used for adjoined modelling in full-waveform inversion. The host code is written in C++, and parallel computation codes are written in CUDA C. The computational time and performance gained from CUDA C and OpenMP parallel computation in different hardware are compared to the serial code. The performance improvement is enhanced with increased model dimensions and remains almost constant after a certain threshold. A GPU performance gain of up to 90 times is obtained compared to the serial code.